

# FATIGUE LIFE ASSESSMENT OF RAILWAY AXLE: A COMPARATIVE STUDY



A THESIS SUBMITTED IN FULFILLMENT  
OF THE REQUIREMENT FOR THE DEGREE OF  
DOCTOR OF ENGINEERING IN MECHANICAL ENGINEERING  
SCHOOL OF ENGINEERING  
KING MONGKUT'S INSTITUTE OF TECHNOLOGY LADKRABANG  
2024  
KMITL-2024-EN-D- 058-182

This material is reserved for educational use only, not allowed for commercial use.

Forbidden to modify the content, and cite the document when use.



**COPYRIGHT 2024**

**SCHOOL OF ENGINEERING**

**KING MONGKUT'S INSTITUTE OF TECHNOLOGY LADKRABANG**

This material is reserved for educational use only, not allowed for commercial use.

Forbidden to modify the content, and cite the document when use.

<b>Thesis Title</b>	Fatigue Life Assessment of Railway Axle: A Comparative Study
<b>Student Name</b>	Ms. Theingi Nwe
<b>Student ID.</b>	62601033
<b>Degree</b>	Doctor of Engineering
<b>Program</b>	Mechanical Engineering
<b>Year</b>	2024
<b>Thesis Advisor</b>	Asst.Prof.Dr.Monsak Pimsarn

## ABSTRACT

Railway axles play a pivotal role in the safe and efficient functioning of rail transportation systems, bearing heavy loads and enduring various operational conditions. Understanding the factors influencing the fatigue life of railway axles is crucial for ensuring the reliability and safety of rail networks. This dissertation presents a comprehensive study that delves into several aspects of fatigue life assessment and prediction models for railway axles.

The study begins by investigating the effect of press-fitting interference on railway wheel and axle assemblies. Detailed examinations of press-fitting force characteristics and holding torque capacity provide insights into the assembly process, contributing to improved design and manufacturing practices. This work establishes a foundation for enhancing the structural integrity of axle systems.

Multiaxial fatigue-life prediction is essential in railway axle engineering. The research addresses this by considering the complex effects of braking on axle fatigue life. By incorporating multiaxial fatigue-life prediction models, the study offers a deeper understanding of the interplay between multiple load components, enabling the development of more accurate and reliable axle systems.

The study further explores the deterministic stress intensity factor (SIF) under adverse running conditions. By focusing on critical SIF values, it identifies potential failure points in railway axles, thereby informing maintenance strategies to mitigate the impact of adverse running conditions on structural integrity.

Additionally, this dissertation assesses the impact of braking and axle hot box bearing temperature on the stress intensity factor (SIF) and residual lifetime of railway axles.

Through rigorous simulations and analyses, it highlights the significance of considering these effects when evaluating axle integrity under real-world conditions.

In pursuit of lightweight axle design, a multi-objective optimization approach is introduced. This novel method aims to balance the structural and weight requirements of inboard bearings in high-speed railway axles, offering more efficient and sustainable solutions.

The collective research contributes to the field of railway axle engineering by advancing knowledge, introducing innovative solutions, and highlighting the importance of predictive models in fatigue life assessment. The implications of this research are significant for enhancing railway safety, improving maintenance practices, and extending the durability of axle systems.

Though the study acknowledges certain limitations, it paves the way for future research in railway axle engineering, offering potential areas for further exploration. In conclusion, this dissertation emphasizes the significance of its findings and their potential impact on the railway industry, underscoring the necessity of comprehensive studies to ensure the reliability and safety of rail transportation networks.

## ACKNOWLEDGEMENTS

I extend my deepest appreciation to Assistant Professor Dr. Monsak Pimsarn, my esteemed supervisor, for his unwavering support throughout my Ph.D. study and associated research endeavors. Prof. Dr.Monsak's continuous guidance, patience, and enthusiasm have been invaluable sources of motivation. His profound expertise in the field, coupled with his intelligence and compassionate personality, make him an exceptional supervisor. Working under his mentorship has been a great honor, and I am grateful for the opportunity to have collaborated with such a distinguished professional. I am indebted to Prof. Dr. Monsak for his contributions to my research, and I will forever cherish the experience of working with a supervisor of his caliber.

Special thanks are extended to King Mongkut's Institute of Technology Ladkrabang for providing scholarships, covering tuition fees, and offering support for living expenses. This support has been crucial in enabling me to engage in continuous research, ultimately leading to the successful completion of the doctoral program.

I would like to express my gratitude to my family, particularly Father U Khin Maung Lay and Mother Daw Hla Aye, as well as my elder sister and younger sister. Their encouragement has been a constant source of motivation.

Finally, I dedicate this doctoral dissertation to all benefactors, seeking the blessings of the Triple Gem. With reverence, I wish that the outcomes of this research become a source of enduring benefit to the broader community. May the ripple effect of this work extend far and wide, fostering positive change and enlightenment for the betterment of humanity. In the spirit of interconnectedness, I express my sincere appreciation for the support that has allowed this research to manifest.

## TABLE OF CONTENTS

	PAGE
ABSTRACT.....	i
ACKNOWLEDGEMENTS .....	iii
TABLE OF CONTENTS .....	iv
LIST OF TABLES .....	xiii
LIST OF FIGURES.....	xiv
CHAPTER 1.....	25
INTRODUCTION.....	25
1.1 Background.....	25
1.2 Research Problem.....	26
1.3 Significant of the Research.....	27
1.4 Outline of the Dissertation.....	27
CHAPTER 2.....	30
LITERATURE REVIEW.....	30
2.1 Introduction.....	30
2.2 Historical Perspective .....	30
2.2.1 Railway Disasters Caused by Axle Failures .....	31
2.3 Comprehensive Review of Railway Axle Failures .....	36
2.4 Railway international standards.....	37
2.5 Review of High-Speed Rail.....	38

This material is reserved for educational use only, not allowed for commercial use.

Forbidden to modify the content, and cite the document when use.

2.5.1 Technologies of High-speed Train .....	40
2.5.2 Function and Composition of High-Speed Train Bogie.....	41
2.5.3 Axle System Function .....	42
2.5.4 Structural Characteristics and Requirements of High-Speed Train Wheels .....	44
2.5.5 Function and Manufacture of Framework.....	46
2.5.6 Function, Classification, and Composition of Suspension System .....	46
2.5.7 Function and Composition of Foundation Brake System.....	48
2.5.8 Test and Standard for Bogies of High-Speed Trains.....	50
2.5.9 Basic Concepts of Car Bodies.....	52
2.5.10 Train Monitoring and Diagnosis Technology .....	54
2.5.11 Performance Parameters of Vehicles.....	54
2.5.12 Railway Clearance.....	55
2.5.13 Line structure of HSR.....	56
2.5.14 Line parameters of HSR .....	59
CHAPTER 3.....	62
METHODOLOGY.....	62
3.1 Press-Fitting of Railway Wheelset.....	62
3.1.1 Theoretical Analysis of Press-Fitting.....	64
3.1.2 Characteristics of the Press-Fitting Curve.....	67

This material is reserved for educational use only, not allowed for commercial use.

Forbidden to modify the content, and cite the document when use.

3.1.3 Determination of the Press-Fitting Force.....	68
3.1.4 Holding Torque Capacity Evaluation.....	68
3.2 Analytical Strength Evaluation of Railway Axles.....	69
3.2.1 Loads Acting on an Axle.....	70
3.2.2 Stress Evaluation along an Axle.....	71
3.3 Multiaxial Fatigue Analysis.....	74
3.3.1 Brown-Miller method.....	76
3.3.2 Infinite Fatigue Life Analysis.....	78
3.4 Numerical Approaches of Evaluation Stress Intensity Factor.....	79
3.4.1 The Analytical Method of Evaluation the SIFs of Elliptical Surface Cracked Subjected to Bending.....	80
3.5 Lightweight Bearing Design Optimization.....	82
3.5.1 Multi-Objective Optimization Method.....	83
CHAPTER 4.....	85
EFFECT OF INTERFERENCE WITH THE PRESS-FITTING OF RAILWAY WHEEL AND AXLE ASSEMBLIES.....	85
4.1 Overview.....	85
4.1.1 Press-Fitting in Railway Axle Assemblies.....	85
4.2 Numerical Simulation.....	86
4.2.1 Variations in Interference Fit.....	88

4.3 Discussion .....	88
4.4 Conclusions.....	92
4.4.1 Summary of Key Findings .....	92
4.4.2 Achieving Optimal Interference Fit.....	93
4.4.3 Practical Implications .....	93
CHAPTER 5.....	94
RAILWAY AXLE AND WHEEL ASSEMBLY PRESS-FITTING FORCE CHARACTERISTICS AND HOLDING TORQUE CAPACITY.....	94
5.1 Overview.....	94
5.1.1 Press-Fitting in Railway Axle and Wheel Assemblies .....	94
5.2 Numerical Simulation .....	94
5.2.1 Materials.....	94
5.2.2 Modelling and Simulation of Press-Fitting.....	95
5.2.3 Finite Element Analysis of the Holding Torque Capacity .....	97
5.3 Discussion.....	97
5.3.1 Comparison between the FEA and Theoretical Results .....	97
5.3.2 Effect of the Interference and Friction Coefficient on Press-Fitting Curves .....	99
5.3.3 Contact Strength Analysis.....	101
5.3.4 Holding Torque Behavior .....	103
5.4 Conclusions.....	107
5.4.1 Summary of Key Findings .....	107

This material is reserved for educational use only, not allowed for commercial use.

Forbidden to modify the content, and cite the document when use.

5.4.2 Recommendations and Applications .....	108
CHAPTER 6 .....	110
MULTIAXIAL FATIGUE-LIFE PREDICTION OF RAILWAY AXLES WITH CONSIDERATION OF PRESS-FITTING AND BRAKING EFFECTS .....	110
6.1 Overview .....	110
6.1.1 Press-Fitting Impact on Fatigue Life .....	110
6.1.2 Importance of Understanding the Effects of Assembly Processes on Structural Durability .....	110
6.1.3 Multiaxial Fatigue-Life Prediction with Braking .....	111
6.2 Numerical Analysis of the Influence of Press-Fitting on the Fatigue Life of Railway Axle .....	111
6.2.1 Numerical Simulation for Press-Fitting Influence .....	111
6.2.2 Bending Stress Variation under Different Running Conditions .....	113
6.2.3 Press-Fitting Effect on Stress Distribution .....	114
6.2.4 Relationship Between Fatigue Life and Overloading Repeated Cycles ..	116
6.3 Numerical Simulation with Braking Considerations .....	117
6.4 Discussion .....	118
6.4.1 Effect of loading cases on the stress concentration of a railway axle ...	119
6.4.2 Multiaxial fatigue-life prediction of a railway axle .....	122
6.5 Conclusions .....	126
CHAPTER 7 .....	127

ASSESSING THE IMPACT OF PRESS-FITTING, RUNNING CONDITIONS, BRAKING AND AXLE HOT BOX BEARING TEMPERATURE ON THE STRESS INTENSITY FACTOR AND RESIDUAL LIFETIME OF RAILWAY AXLES.....	127
7.1 Overview.....	127
7.1.1 The Impact of Press-Fitting and Running Condition on Stress Intensity Factor (SIF).....	127
7.1.2 The Impact of Braking and Axle Hot Box Bearing Temperature on Stress Intensity Factor (SIF).....	128
7.2 Numerical Simulation .....	128
7.2.1 Finite Element Modelling and Simulation.....	128
7.2.2 Mesh Sensitivity Analysis.....	129
7.2.3 Residual Lifetime Prediction and Fatigue Crack Growth Estimation.....	131
7.3 Findings .....	132
7.3.1 Verification of the SIF Evaluation Results with FEM And Theory.....	133
7.3.2 Effect of Stable and Adverse Running Conditions on SIF Solutions .....	135
7.3.3 Effects of Press-Fitting on SIF.....	137
7.3.4 Studying the Rotary Bending Effect on SIF Solutions .....	137
7.3.5 Effects of Thermal Loading and Breaking .....	140
7.3.6 Effect of crack shape on the stress intensity factor.....	138
7.3.7 Crack Growth and Residual Lifetime.....	140
7.4 Discussion .....	144
7.4.1 Impact of Running Conditions .....	145

This material is reserved for educational use only, not allowed for commercial use.

Forbidden to modify the content, and cite the document when use.

7.4.2 Press Fitting Effect.....	145
7.4.3 Effect of Crack Shape.....	145
7.4.4 Braking Effect.....	146
7.4.5 Influence of Thermal Load.....	146
7.4.6 Further Research.....	146
7.5 Conclusion.....	147
CHAPTER 8.....	148
MULTI-OBJECTIVE OPTIMIZATION OF LIGHTWEIGHT INBOARD BEARING DESIGN FOR HIGH-SPEED RAILWAY AXLE.....	148
8.1 Overview.....	148
8.1.1 Introduction to Inboard Bearing Design.....	148
8.1.2 Multi-Objective Optimization.....	149
8.1.3 Finite element model.....	150
8.1.4 Parametric design optimization algorithm.....	151
8.2 Findings.....	152
8.2.1 Analysis of an inboard and outboard bearing wheelset FEA results.....	152
8.2.2 Identification of optimal design.....	153
8.2.3 Assessment of infinite life.....	155
8.3 Discussion.....	156
8.4 Conclusions.....	156
8.4.1 Key Insights from Multi-Objective Optimization.....	156

This material is reserved for educational use only, not allowed for commercial use.

Forbidden to modify the content, and cite the document when use.

8.4.2 Recommendations for High-Speed Rail Industry.....	157
CHAPTER 9.....	158
CONCLUSION.....	158
9.1 Summary of Key Findings.....	158
9.1.1 Effect of Press-Fitting Interference on Railway Wheel and Axle Assemblies.....	158
9.1.2 Press-Fitting Force Characteristics and Holding Torque Capacity .....	158
9.1.3 Influence of Press-Fitting on Fatigue Life.....	158
9.1.4 Multiaxial Fatigue-Life Prediction Considering Braking Effects .....	158
9.1.5 Assessing the Impact of Press-Fitting, Running Conditions, Braking and Axle Hot Box Bearing Temperature on the Stress Intensity Factor and Residual Lifetime of Railway Axles .....	159
9.1.6 Multi-Objective Optimization of Lightweight Inboard Bearing Design.....	159
9.2 Contributions to Knowledge.....	159
9.2.1 Advances in Railway Axle Engineering .....	159
9.2.2 Innovative Solutions.....	159
9.3 Implications for the Railway Industry .....	160
9.3.1 Safety Enhancements .....	160
9.3.2 Maintenance and Durability .....	160
9.4 Limitations and Future Research.....	160
9.4.1 Study Limitations .....	160
9.4.2 Areas for Future Research.....	160

This material is reserved for educational use only, not allowed for commercial use.

Forbidden to modify the content, and cite the document when use.

9.5 Concluding Remarks .....	160
REFERENCES.....	162
APPENDICES .....	165
Appendix A: Publications .....	166
AUTHOR'S BIOGRAPHY .....	223

«



This material is reserved for educational use only, not allowed for commercial use.

Forbidden to modify the content, and cite the document when use.

## LIST OF TABLES

	PAGE
Table 3.1 Loads for an axle of a motor bogie.....	71
Table 3.2 Stress concentration factor in various axle sections. ....	72
Table 3.3 Load case vs. load ratio.....	76
Table 3.4 Fatigue properties of the EA4T material.....	77
Table 5.1. Press-fitting curve for a railway wheelset: force vs axial displacement [13].....	94
Table 5.2 Press-fitting curve for a railway wheelset: force vs axial displacement [13].....	95
Table 5.3 Maximum holding torque capacity—theory and finite element versus interference.....	106
Table 6.1 Loads for an axle of a motor bogie.....	113
Table 6.2 Comparison of fatigue life of the motor bogie axles.....	116
Table 8.1. Objective, constraint, and design variable at initial design (all dimensions in mm).....	151
Table 8.2 Comparison of the starting design points and optimum design points of inboard bearing axle.....	155

## LIST OF FIGURES

	PAGE
Figure 2.1 Sketch of the derailment and fire in the 1841 Versailles Train Disaster, France - the first railway accident resulting in major loss of life [3].	32
Figure 2.2 The 1998 Eschede Train Disaster, Germany [4].	33
Figure 2.3 Collision of Metrolink Train 111 with Union Pacific Train LOF65-12 [5].	33
Figure 2.4 The 2013 Lac-Mégantic Train derailment and fire [6].	34
Figure 2.5 Eastward view of the derailed cars (Source: Interior News, with TSB annotations)	35
Figure 2.6 Mating fracture surface from the broken axle at the L1 bearing (view toward end of axle) [7].	36
Figure 2.7 Mating fracture surface from the broken axle at the L1 bearing (view toward centre of axle) [7]	36
Figure 2.8 History of railway speed [8]	39
Figure 2.9 Key technologies of high-speed train.	41
Figure 2.10 Railway bogie composition	42
Figure 2.11 CR300AF motor wheelset.	43

This material is reserved for educational use only, not allowed for commercial use.

Forbidden to modify the content, and cite the document when use.

Figure 2.12 Motor axle.....	44
Figure 2.13 Trailer axle.....	44
Figure 2.14 Wheels of different spoke types.....	45
Figure 2.15 Profile of standard conical tread.....	45
Figure 2.16 Worn profile tread.....	45
Figure 2.17 Composition and installation interface of the framework.....	46
Figure 2.18 Suspension systems of bogie.....	47
Figure 2.19 Primary suspension system.....	48
Figure 2.20 Secondary suspension system.....	48
Figure 2.21 Foundation brake device.....	49
Figure 2.22 Bogie test type.....	51
Figure 2.23 Hunting limit cycle diagram.....	51
Figure 2.24 Structure of a leading vehicle in high-speed trains.....	53
Figure 2.25 Railway clearance (a) Vehicle gauge (b) Equipment gauge (c) Construction gauge.....	55
Figure 2.26 Rail.....	56

Figure 2.27 Intermediate connector.....	57
Figure 2.28 Sleeper.....	57
Figure 2.29 Track bed.....	58
Figure 2.30 Roadbed .....	58
Figure 2.31 Turnout .....	59
Figure 2.32 Track gauge .....	59
Figure 2.33 Rail cant .....	60
Figure 2.34 Curved track superelevation.....	60
Figure 3.1 Common locations of damage accumulation on railway axles.....	63
Figure 3.2 Circumferential crack under wheel press-fit.....	63
Figure 3.3 Stresses in a thick-walled cylinder element.....	65
Figure 3.4 Assembly of an axle and a wheel.....	66
Figure 3.5 Simplified model of a wheelset for theoretical analysis [20].....	66
Figure 3.6 Press-fitting curve for a railway wheelset: force vs axial displacement [13]. ....	68
Figure 3.7 A schematic free-body diagram of a motor bogie wheelset due to masses in motion (measurements are in mm).....	69

Figure 3.8 A schematic free-body diagram of a motor bogie wheelset due to braking (measurements are in mm).....	70
Figure 3.9 Expression of a stress concentration factor (a) bottom of the transition between two cylindrical parts and (b) groove bottom [1, 2] .....	71
Figure 3.10 Fatigue analysis procedure. ....	75
Figure 3.11 Load spectra for fatigue prediction (R=-1) .....	76
Figure 3.12 Load spectra for fatigue prediction (R=0).....	76
Figure 3.13 The Dang Van plot for the endurance limit. ....	79
Figure 3.14 Contour for J-integral evaluation [25].....	79
Figure 3.15 Local orthogonal Cartesian coordinates are defined at point s on the crack front.[25].....	79
Figure 3.16 Semi-elliptical crack in cylindrical bar.....	81
Figure 3.17 Structural analysis and optimization process workflows chart.....	82
Figure 4.1 Press-fitting assembly machine .....	85
Figure 4.2 Geometry of the wheel and axle assembly .....	86
Figure 4.3 Finite Element Mesh of Wheelset.....	87
Figure 4.4 Boundary conditions for wheel and axle assembly.....	87

Figure 4.5 Von Mises stress along the centre of the wheelset radial axis.....89

Figure 4.6 Radial stress distribution along the centre of the wheelset radial axis.....89

Figure 4.7 Tangential stress distribution along the centre of the wheelset radial axis.....89

Figure 4.8 Von Mises stress distribution along the centre of the wheelset radial axis.....89

Figure 4.9 Axial stress distribution for wheel and axle assembly along the radial axis. ....90

Figure 4.10 Radial stress distribution for wheel and axle assembly along the radial axis..90

Figure 4.11 Tangential stress distribution for wheel and axle assembly along the radial axis.....90

Figure 4.12 Contact pressure at axle wheel seat.....90

Figure 4.13 Contact pressure distribution along the contact length vs interference clearance.....90

Figure 4.14 Von Mises stress distribution along the contact length vs interference clearance.....90

Figure 4.15 Axial stress distribution along the contact length vs interference clearance. .91

Figure 4.16 Radial stress distribution along the contact length vs interference clearance.....91

Figure 5.1 Stress–plastic strain curve for EA4T steel.....95

Figure 5.2 Dimensions of the wheelset [17].	96
Figure 5.3 Boundary conditions.	96
Figure 5.4 Mesh used by the finite element model.	96
Figure 5.5 Loading and boundary conditions for the torque analysis.	97
Figure 5.6 Contact pressure distribution along the contact length.	98
Figure 5.7 Press-fitting curves obtained from the finite element model (FEM) and Lamé's theory (straight green line).	99
Figure 5.8 Press-fitting curves vs interference derived from the finite element simulations.	100
Figure 5.9 Maximum press-fitting force vs interference.	100
Figure 5.10 Press-fitting curves with friction coefficient as a parameter.	101
Figure 5.11 Maximum press-fitting force vs coefficient of friction.	101
Figure 5.13 Von Mises stress distribution during simulation (a) axial displacement of 30 mm, (b) axial displacement of 100 mm, and (c) axial displacement of 180 mm.	102
Figure 5.14 Von Mises stress of the wheel and axle due to radial interference (MPa).	103
Figure 5.15 Equivalent plastic strain on the wheel.	103
Figure 5.16 Holding torque capacity vs contact length.	104

Figure 5.17 Torque vs. the rotation angle for 240 $\mu\text{m}$ interference.....	105
Figure 5.18 Torque vs rotation angle for four interferences. ....	105
Figure 5.19 The relation between the interferences and maximum holding torque capacity .....	106
Figure 6.1 Meshing and boundary conditions of the motor bogie wheelset for stable condition.....	112
Figure 6.2 Meshing and boundary conditions of the motor bogie wheelset for adverse condition.....	112
Figure 6.3 Comparison of bending stress along the axial direction of the motor bogie axle.....	113
Figure 6.4 Moment diagram of the axle along the longitudinal axis .....	114
Figure 6.5 Comparison of von Mises stress along the axial direction of the motor bogie axle.....	115
Figure 6.6 Comparison of the maximum von Mises stress for the motor bogie axle.....	115
Figure 6.7 Fatigue-life assessment of the motor bogie wheelset.....	116
Figure 6.8 Safety factor assessment of the motor bogie wheelset.....	116
Figure 6.9 FE meshing model of the wheelset.....	117

Figure 6.10 Boundary condition of the FE model wheelset. ....	118
Figure 6.11 von Mises stress variation of an axle along the longitudinal axis generated by Loading Case 1 .....	119
Figure 6.12 von Mises stress variation of an axle along the longitudinal axis generated by Loading Case 2 .....	120
Figure 6.13 von Mises stress variation of an axle along the longitudinal axis generated by Loading Case 4 .....	120
Figure 6.14 von Mises stress variation of an axle along the longitudinal axis generated by Loading Case 3 .....	121
Figure 6.15 Comparison of von Mises stress variation of an axle along the longitudinal axis .....	121
Figure 6.16 Estimated fatigue life of a railway axle .....	123
Figure 6.17 Estimated factor of strength of railway axle.....	124
Figure 6.18 The estimated fatigue damage of railway axle.....	125
Figure 7.1 Boundary condition of the railway wheelset under braking forces .....	130
Figure 7.2 3D finite element model of high-speed wheelset.....	131
Figure 7.3 The procedure of the determination of crack growth rate.....	132

Figure 7.4 Comparison of Stress Intensity Factors (SIFs) between the BS 7910 standard and Finite Element method.....	133
Figure 7.5 Comparison of Stress Intensity Factors (SIFs) in relation to various crack front contours.....	134
Figure 7.6 Comparison of Stress Intensity Factors (K) in relation to various crack modes (I, II, and III).....	135
Figure 7.7 Comparison of stress intensity factor for stable and adverse running conditions.....	136
Figure 7.8 Distribution of the longitudinal stress for the semi-elliptical crack under combined press-fitting and the bending load of a wheelset in FEM.....	136
Figure 7.9 Stress intensity factor comparison for the press-fitting effect.....	137
Figure 7.10 Stress intensity factor of the finite element model versus rotation angle.....	138
Figure 7.11 The longitudinal stress distribution near the crack with different crack geometries Case (a) $a=15\text{mm}$ , $c=20\text{mm}$ , Case (b) $a=20\text{mm}$ , $c=20\text{mm}$ , Case (c) $a=20\text{mm}$ , $c=15\text{mm}$ .....	139
Figure 7.12 Comparison of the distribution of the Stress Intensity Factor (SIF) along the crack front based on the crack shape.....	140
Figure 7.13 Comparison of Stress Intensity Factor (SIF) along the crack front under the different loading conditions.....	141

This material is reserved for educational use only, not allowed for commercial use.

Forbidden to modify the content, and cite the document when use.

Figure 7.14 Comparison of Stress Intensity Factor (SIF) along the crack front under the different temperature load. ....	141
Figure 7.15 Fatigue crack life prediction diagrams based on the crack shape (a) along depth direction and (b) along length direction.....	142
Figure 7.16 The comparison of the crack growth rate as a function of stress intensity factor upon different loading conditions (a) crack deepest point A and (b) crack surface point C.....	143
Figure 7.17 The comparison of the predicted life of the axle upon different loading conditions (a) crack deepest point A and (b) crack surface point C.....	144
Figure 8.1 Mesh, loading and boundary conditions of FE model.....	150
Figure 8.2 Comparison of longitudinal stresses of calculated and FEM (a) inboard bearing axle and (b) outboard bearing axle.....	153
Figure 8.3 Comparison the deflection of the axle under the loading (a) for the assembled inside axle boxes (b) for the assembled outside axle boxes.....	153
Figure 8.4 Pareto plot of $S_{mises\_max}$ vs. mass from optimization. ....	154
Figure 8.5 3D contour graph of design feasibility vs mass, $S_{mises\_max}$ .....	154
Figure 8.6 Correlation map of input and output parameters.....	154
Figure 8.7 History of design variable optimization process (a) F1, (b) F2, (c) Ri, (d) Ro.....	155

Figure 8.8 Radial FRF contour of (a) before optimization and (b) after optimization.....156



This material is reserved for educational use only, not allowed for commercial use.

Forbidden to modify the content, and cite the document when use.

# CHAPTER 1

## INTRODUCTION

### 1.1 Background

The operation of railway systems is highly dependent on the integrity and performance of their axle components. These axles play a pivotal role in supporting rotating elements, transmitting rotational motion, and managing power transfer in locomotive systems' rolling stock. The railway axles are subjected to a wide range of dynamic loads and environmental conditions that can cause extensive fatigue damage over their operational lifespan. Such loads include vertical forces resulting from the wagon's mass and payload, lateral forces during turns, and the crucial braking forces necessary for controlling vehicle speed. Railway axles must absorb these braking forces while maintaining a known fatigue life to ensure the safety and efficiency of railway operations.

The assembly of railway wheel and axle systems through press fitting is a fundamental practice in the railway industry. This process serves as a cornerstone in ensuring the reliable operation of trains. However, the complexities and challenges associated with press fitting extend beyond the basic joining of components. Railway axles are subjected to various dynamic forces, thermal loads, and environmental conditions that necessitate a comprehensive understanding of the entire assembly process.

There are two common types of brakes used in railway systems: adhesion-dependent and independent brakes. These brakes, consisting of a tread and brake disc, can be mounted on either the axle or the wheel. The choice of brake system depends on the specific rail vehicle and its intended use. The forces generated during traction and braking are not usually applied simultaneously to the axle, and as such, the effects of traction forces are not considered in this analysis. Fatigue due to cyclic loading is a prevalent cause of railway axle failure. Even well-designed axles may experience mechanical failure when subjected to repeated loading or overloading. To evaluate and enhance product designs, fatigue-life prediction is a crucial technique that requires comprehensive data about the component's shape, material properties, load conditions, working environment, and limitations. Traditional uniaxial fatigue models are insufficient in

This material is reserved for educational use only, not allowed for commercial use.

Forbidden to modify the content, and cite the document when use.

addressing the actual loading conditions of railway axles, as they experience combined multiaxial loading involving direct and shear stresses under service conditions.

In response to these challenges, this research focuses on examining the fatigue behavior of railway axles under variable amplitude cyclic overloading. This study pays particular attention to the effects of track irregularities, including curves, alignment, longitudinal level, switches, and crossovers, using a strain-life method. Surprisingly, the influence of braking effects has been largely underexplored in contemporary literature. Therefore, the research aims to investigate the impact of braking forces on the fatigue life and structural integrity of railway axles. The collective study encompasses an exploration of press-fitting curve characteristics, predictions of fatigue life under the influence of press fitting, the effects of braking, variations in running conditions, weight reduction strategies achieved by comparing inboard and outboard bearing designs, the analysis of stress intensity factors (SIF) under diverse conditions, and the implications of thermal loading and braking effects.

## 1.2 Research Problem

The central objective of this dissertation is to provide a comprehensive understanding of the intricate dynamics that affect railway axle systems. While press fitting serves as the focal point, it is inextricably linked with various factors that collectively contribute to the structural integrity and operational effectiveness of these critical components.

The primary objectives of this research are as follows:

- To analyze the effects of interference fit, represented by press-fitting, on the stress and fatigue life of railway axles.
- To investigate the combined influences of braking and thermal loading on stress intensity factor and crack propagation in railway axles.
- To predict multiaxial fatigue behavior and remaining service life of railway axles under various loading conditions.
- To explore the delicate balance between reducing axle weight and preserving structural integrity

Hypotheses guiding this research include:

- Press-fitting has a significant impact on the fatigue life of railway axles.
- Braking forces combined with thermal loading exacerbate stress concentrations, leading to increased crack propagation.

This material is reserved for educational use only, not allowed for commercial use.

Forbidden to modify the content, and cite the document when use.

- Accurate multiaxial fatigue analysis can reliably predict the remaining service life of railway axles.
- It compares inboard and outboard bearing designs, conducting comprehensive finite element simulations to optimize axle design while promoting weight reduction and enhancing fatigue resistance.

### 1.3 Significant of the Research

The research conducted in this dissertation contributes significantly to the advancement of railway transportation systems by addressing critical issues in railway axle assembly, operation, and structural integrity. The significance of this research encompasses several key areas:

- A comprehensive understanding of stress distribution, deformation, and fatigue life during the press-fitting process, which is pivotal in railway axle design.
- Practical guidelines for determining interference limits and classifying press-fitting curves based on industry standards, enhancing the practicality of their application.
- A quantified understanding of the effects of press fitting on stress concentration, fatigue life, and stress distribution within axles, directly influencing axle design.
- The incorporation of the effects of braking into axle design to ensure safety and robustness under dynamic loading conditions.
- The importance of considering thermal and braking effects in stress intensity factor (SIF) assessments to ensure the longevity and reliability of railway axles.
- A focus on weight reduction strategies using the multi-objective optimization techniques for reducing axle mass while preserving structural integrity, a critical factor in high-speed axle design.

By addressing these multifaceted challenges and considering the interplay of these factors, this research significantly contributes to the advancement of railway transportation systems.

### 1.4 Outline of the Dissertation

Chapter 2 undertakes an extensive exploration of the existing body of knowledge related to the dissertation's research topic. Starting with a contextual introduction, the chapter

This material is reserved for educational use only, not allowed for commercial use.

Forbidden to modify the content, and cite the document when use.

proceeds to examine the historical perspective of railway axle failures, specifically those caused by axle failures. A thorough review of railway axle failures and an examination of railway bogies follow, laying the groundwork for subsequent analytical and numerical investigations. This chapter serves as a critical foundation for understanding the context and gaps in the existing literature.

Chapter 3 is dedicated to elucidating the research methodology employed in the study. It systematically discusses the press-fitting of railway wheelsets, encompassing theoretical analyses, characteristics of the press-fitting curve, determination of press-fitting force, and the evaluation of holding torque capacity. Additionally, the chapter covers analytical strength evaluations of railway axles, multiaxial fatigue analyses, and numerical approaches for evaluating stress intensity factors. The methodology section is comprehensive, providing a clear roadmap for the analytical and numerical investigations undertaken in the subsequent chapters.

Chapter 4 focuses on investigating the repercussions of interference with the press-fitting of railway wheel and axle assemblies. It begins with an overview of press-fitting in railway axle assemblies and employs numerical simulations to analyze variations in interference fit. The findings are discussed in detail, leading to comprehensive conclusions that not only summarize key findings but also provide insights into achieving optimal interference fit and practical implications for the railway industry.

Chapter 5 homes in on the characteristics of press-fitting force and holding torque capacity in railway axle and wheel assemblies. Offering an in-depth overview, the chapter includes numerical simulations, comparing finite element analysis and theoretical results. The discussion encompasses the effect of interference and friction coefficient on press-fitting curves, contact strength analysis, and holding torque behavior. The conclusions drawn from this chapter summarize key findings and present practical recommendations for applications in the railway industry.

Chapter 6 ventures into the realm of predicting the fatigue life of railway axles under multiaxial loading conditions. It establishes the context by highlighting the impact of press-fitting on fatigue life and emphasizing the importance of understanding assembly processes

This material is reserved for educational use only, not allowed for commercial use.

Forbidden to modify the content, and cite the document when use.

on structural durability. The chapter then delves into numerical simulations, providing insights into stress distribution, variations under different running conditions, and the relationship between fatigue life and overloading repeated cycles. The chapter concludes by summarizing the findings derived from the multiaxial fatigue-life predictions.

Chapter 7 critically assesses the impact of various factors on the stress intensity factor (SIF) and residual lifetime of railway axles. The chapter commences with an overview, emphasizing the impact of press-fitting and running conditions on SIF, as well as the influence of braking and axle hot box bearing temperature. Employing numerical simulations, the findings are detailed, covering the effects of stable and adverse running conditions, press-fitting, rotary bending, thermal loading, and crack shape on SIF. The chapter concludes with a comprehensive discussion, shedding light on the implications of the research and proposing avenues for further study.

Chapter 8 shifts the focus to the optimization of the lightweight inboard bearing design for high-speed railway axles. The chapter introduces the inboard bearing design, outlines the optimization process, and discusses the finite element model and parametric design optimization algorithm. Findings from the analysis of inboard and outboard bearing wheelset finite element analysis results are presented, along with the identification of optimal designs and the assessment of infinite life. The chapter concludes with a comprehensive discussion, summarizing key insights from the optimization process and providing practical recommendations for the high-speed rail industry.

Chapter 9 offers a comprehensive synthesis of the entire dissertation. It begins with a summary of key findings, systematically addressing the effects of press-fitting interference, press-fitting force characteristics, and multiaxial fatigue-life predictions on railway axles. The contributions to knowledge are expounded upon, highlighting advances in railway axle engineering and innovative solutions. Implications for the railway industry, including safety enhancements and considerations for maintenance and durability, are thoroughly outlined. Acknowledging study limitations and identifying areas for future research, the chapter concludes with a set of final remarks, providing a well-rounded closure to the dissertation.

This material is reserved for educational use only, not allowed for commercial use.

Forbidden to modify the content, and cite the document when use.

# CHAPTER 2

## LITERATURE REVIEW

### 2.1 Introduction

The fatigue life assessment and prediction of railway axles play a pivotal role in ensuring the safety, reliability, and efficiency of railway systems. This comprehensive study seeks to explore, analyze, and synthesize the body of knowledge surrounding the fatigue-related aspects of railway axles. By understanding the factors influencing the fatigue life of these critical components, this research aims to contribute to the development of enhanced maintenance practices and innovative axle designs, ultimately leading to safer and more sustainable railway operations.

Typically, railway axles are in service for more than thirty years. This increased service life equates to a substantial number of loading cycles, typically on the order of  $10^9$  cycles. Despite being designed for long-lasting and dependable operation, railway axles are not immune to failure. Most of these failures are attributable to flaws that show during operation and serve as the source from which cracks propagate to critical sizes [1]. Railway axles, as essential structural elements of rolling stock, are subjected to a complex set of mechanical forces and environmental conditions during their operational life. Failures or unexpected damage to axles can have terrible consequences, not only in terms of safety but also in terms of economic and operational disruptions. Consequently, it is of utmost importance to assess the fatigue life of railway axles accurately. Therefore, a profound comprehension of the factors that influence axle fatigue life is indispensable for the railway industry. This literature review aims to provide a comprehensive overview of existing research, highlighting the key factors, theories, and methodologies that have been explored in the domain of railway axle fatigue life assessment and prediction.

### 2.2 Historical Perspective

The historical trajectory of railway axles is replete with a persistent commitment to enhancing their fatigue resistance and overall performance. The emergence of railway systems in the early 19th century marked the inception of a new era in transportation, accompanied by a host of engineering challenges. During this nascent period of rail travel,

This material is reserved for educational use only, not allowed for commercial use.

Forbidden to modify the content, and cite the document when use.

limited knowledge of material science, manufacturing techniques, and inspection methods led to recurrent axle failures. Engineers and designers were confronted with the formidable task of understanding and mitigating these early failures.

In the 20th century, significant advancements in both material science and assessment methodologies led to a substantial reduction in the incidence of railway axle failures. These innovations heralded a new era in railway safety and reliability. As evidence of this improved safety record, the European Railway Agency (ERA) produced a comprehensive safety performance report in 2011 [1,2]. According to this report, the total number of broken axles in the European Union from 2006 to 2009 amounted to a mere 329 instances. When considering this figure in the context of the approximately  $1.66 \times 10^{10}$  train kilometers covered during these four years, it becomes apparent that the incidence of axle fractures was exceedingly rare, occurring at a rate of just one fracture event per 50.45 million train kilometers.

### *2.2.1 Railway Disasters Caused by Axle Failures*

This section delves into a historical analysis of significant railway disasters caused by axle failures, highlighting key incidents year by year. These events have played a pivotal role in shaping the understanding of axle failure mechanisms and the evolution of safety measures in the railway industry.

#### **Case 1: 1841 - Versailles Train Disaster, France:**

One of the earliest recorded railway accidents related to axle failure occurred in France. On May 8, 1841, the Versailles train disaster took place. A train traveling from Paris to Versailles experienced an axle failure, causing a catastrophic derailment (Figure 2.1). The failure was attributed to a manufacturing defect in the axle. This incident underscored the importance of quality control in axle production and marked an early recognition of the dangers of axle-related failures.

This material is reserved for educational use only, not allowed for commercial use.

Forbidden to modify the content, and cite the document when use.



Figure 2.1 Sketch of the derailment and fire in the 1841 Versailles Train Disaster, France - the first railway accident resulting in major loss of life [3].

### **Case 2. 1967 - Hither Green Rail Crash, United Kingdom:**

The Hither Green Rail Crash in the United Kingdom occurred on November 5, 1967, and was attributed to a fractured axle. A freight train's axle failure caused a derailment, leading to the collision of several tank cars containing petrol and subsequent fires. This accident resulted in the deaths of 49 people and numerous injuries. The incident prompted a reevaluation of axle manufacturing, inspection, and maintenance practices in the UK.

### **Case 3. 1998 - Eschede Train Disaster, Germany:**

The Eschede train disaster is one of the most notable railway accidents in recent history. On June 3, 1998, a high-speed InterCityExpress (ICE) train derailed near the town of Eschede, Germany (Figure 2.2). The disaster was attributed to a fatigue-induced fracture in a wheel axle, which resulted in the derailment and the subsequent destruction of the train. The crash led to 101 fatalities and 88 injuries, making it one of the deadliest accidents caused by axle failure. This tragedy prompted significant advancements in axle materials, maintenance procedures, and non-destructive testing technologies.

This material is reserved for educational use only, not allowed for commercial use.

Forbidden to modify the content, and cite the document when use.



Figure 2.2 The 1998 Eschede Train Disaster, Germany [4].

#### **Case 4. 2008 - Chatsworth Train Collision, USA:**

The Chatsworth train collision in the United States occurred on September 12, 2008, and was a result of an axle failure (Figure 2.3). A Metrolink commuter train collided head-on with a Union Pacific freight train in Chatsworth, California. Investigations revealed that the Metrolink train had derailed due to a fatigue-induced fracture in its axles. This accident resulted in 25 fatalities and many injuries, highlighting the ongoing challenges associated with axle integrity in the rail industry and the need for rigorous inspection and maintenance practices.



Figure 2.3 Collision of Metrolink Train 111 with Union Pacific Train LOF65-12 [5].

This material is reserved for educational use only, not allowed for commercial use.

Forbidden to modify the content, and cite the document when use.

These historical incidents represent significant milestones in the understanding of railway disasters caused by axle failures. They have contributed to the development of improved safety standards, inspection techniques, and materials for axles in the railway industry. Subsequent sections of this dissertation will further explore the causes and consequences of axle failures and the measures in place to prevent them.

#### **Case 5. Lac-Mégantic, Canada (2013):**

On July 6, 2013, in Lac-Mégantic, Quebec, a train carrying crude oil derailed, resulting in a massive explosion and fire that killed 47 people (Figure 2.4). While the primary cause was not an axle failure, the incident highlighted the importance of transportation safety in railways, including the secure transport of hazardous materials, which can be exacerbated by axle failures.



Figure 2.4 The 2013 Lac-Mégantic Train derailment and fire [6].

#### **Case 6. 2018, New Hazelton, British Columbia:**

On January 19, 2018, Canadian National Railway Company freight train C76751-17 experienced a train-initiated emergency brake application near New Hazelton, British Columbia (Figure 2.5). The train was carrying 27 gondola cars loaded with thermal coal, which derailed, with some coal spilled into a nearby waterway. No injuries or dangerous goods were involved.

This material is reserved for educational use only, not allowed for commercial use.

Forbidden to modify the content, and cite the document when use.

The investigation revealed that the 52nd car sustained a broken axle, leading to the derailment of 27 cars. The axle broke due to fatigue cracking in the journal fillet radius, but the exact cause could not be determined. Fatigue cracks from multiple origins merged, forming two large cracks that met at the middle of the axle cross-section. When the small remaining axle cross-section could no longer support the load, the axle failed in overstress.

The damaged axle from car CNA 194141 underwent metallurgical examination at the TSB Engineering Laboratory. The fracture occurred between the L1 bearing seal wear ring and the backing ring, precisely at the point where the axle journal transitions into the fillet. This resulted in the separation of the journal, along with the bearing, from the rest of the assembly (see Figure 2.6). The fracture was attributed to fatigue cracking in the journal near the fillet, evidenced by the presence of crack arrest lines, or beach marks, on the smooth areas of the fracture surface (refer to Figure 2.7). Multiple ratchet marks along the edge of the fracture surface indicated several fatigue origins on opposite sides of the axle journal cylindrical surface.



Figure 2.5 Eastward view of the derailed cars (Source: Interior News, with TSB annotations)

This material is reserved for educational use only, not allowed for commercial use.

Forbidden to modify the content, and cite the document when use.



Figure 2.6 Mating fracture surface from the broken axle at the L1 bearing (view toward end of axle) [7]



Figure 2.7 Mating fracture surface from the broken axle at the L1 bearing (view toward centre of axle) [7]

### 2.3 Comprehensive Review of Railway Axle Failures

The investigation into railway axle failures is imperative due to the critical safety role of wheelsets, with potential consequences ranging from derailments to fatalities and injuries. The inability to duplicate wheelsets underscores the necessity for a rigorous inspection plan utilizing non-destructive testing technologies like Visual Inspection (VI), Magnetic Particles testing, and Ultra-Sonic testing. Acknowledging the inherent impossibility of achieving "zero risk" in mechanical systems, the emphasis on risk management is paramount, particularly for safety-critical components like axles.

Despite the potentially long useful life of wheelsets, failures in wheels, axles, or bearings necessitate regular checks, as the failure of a running axle can lead to derailments. Historically, axles have been identified as the weakest component of wheelsets [1], tracing back to the Meudon accident in 1842, which instigated research by August Wöhler, forming the basis of material fatigue knowledge. The cyclic nature of "rotating bending" stresses, with stresses reversing every half cycle, renders axles prone to in-service failures. Regulations impose limits on maximum stresses, and materials with well-known crack propagation rules are mandated.

Despite nearly two centuries of development, broken axles remain a common occurrence, as indicated by statistics such as 78 broken axles in 2006, 103 in 2007, and 104 in 2008, according to the ESIS/TC24 report [2]. James and Galton's tests in 1848 on large iron bars subjected to alternating loads, along with Wöhler's subsequent test series

This material is reserved for educational use only, not allowed for commercial use.

Forbidden to modify the content, and cite the document when use.

between 1858 and 1871 [3], [4], laid the groundwork for the development of the S-N curve, a vital tool for fatigue design in railway applications and engineering at large.

Wöhler's studies identified the fatigue limit for steels, with evidence suggesting that the safe stress range erodes for lives longer than the conventional  $10^6$  to  $10^7$  cycles. Gradual transitions in profile and fretting-initiated failures due to micro-slip between press-fitted wheels and axles were among Wöhler's observations [4].

Contemporary research, such as the analysis of axle failure causes, comparisons of European and Japanese fatigue design strategies, and proposals for standard axle stress analysis methods, contributes to improving axle manufacture and in-service inspection [5]. Studies on scale effects in fatigue limit and crack growth rate for high-strength steel used in high-speed railway axles, as well as examinations of failures in axles and cylindrical roller bearings of freight wagons, provide valuable insights into fatigue mechanisms [6].

Research methodologies extend to the study of failed wheel-drive shaft components in unmanned military vehicles, fatigue life prediction for railway vehicles through computer simulation, and design-driven validation approaches using Bayesian methods and reliability design optimization formulations [7]. The need for axle examination arises from their safety-critical nature and exposure to repeated loading cycles, where factors such as loading geometry, surface quality, corrosion effects, and material heterogeneity introduce stress concentrations, leading to fatigue fractures.

The periodic variation (load cycle) of stress, rather than maximum stress values, is deemed crucial. European Community Standards for railway axle design further underscore the importance of comprehensive research in addressing the safety and reliability of railway axles.

## 2.4 Railway international standards

Railway international standards, crucial for ensuring the safety and reliability of railway vehicles, are established by entities such as the International Union of Railways (UIC), European Standards (EN), and Japanese Industrial Standards (JIS). These standards encompass a variety of aspects related to railway components, including wheelsets, wheel-axles, and wheels.

For the design and calculation of railway axles, European standards EN13103 and EN13104 provide essential procedures. These standards, denoted as EN 13 103 and EN 13 104, respectively, detail the methods for calculating bending strains and stresses based on

This material is reserved for educational use only, not allowed for commercial use.

Forbidden to modify the content, and cite the document when use.

loading forces. The fatigue assessment for railway axles, often employing a constant amplitude approach under extreme load conditions, is outlined in these standards.

European standards EN 13 260 and EN 13 261 are integral components in the regulatory framework governing the design and manufacturing of railway components. EN 13 260 specifically outlines the requirements for wheelsets, establishing criteria related to geometrical accuracy, thermo-mechanical resilience, and mechanical strength. This standard ensures that wheelsets meet stringent specifications, contributing to the overall safety and performance of railway systems. Complementary to this, EN 13 261 addresses the design and manufacturing standards for wheel-axles, focusing on aspects such as material properties, load-bearing capacities, and dimensional accuracy. Together, these standards play a crucial role in maintaining the integrity of railway components, providing guidelines that prioritize safety, reliability, and adherence to stringent quality standards within the rail industry.

Addressing the structural requirements of bogie frames, EN13749 (EN 13 715) codifies assumptions, calculations, and test methods for verifying both static and fatigue resistance. Notably, EN13749 mandates that fatigue life be evaluated through track tests, ensuring a comprehensive assessment of bogie frame durability.

In summary, adherence to a comprehensive set of international railway standards, including EN 13 103, EN 13 104, EN 13 979-1, EN 13 715, UIC 510-5, EN 13 260, EN 13 261, and EN 13 262, is essential for the robust design and manufacturing of critical components like axles and wheels, with a strong emphasis on safety, reliability, and fatigue resistance.

## 2.5 Review of High-Speed Rail

The development of high-speed rail (HSR) represents a remarkable integration of various technical components, encompassing infrastructure, rolling stock, signaling systems, operations, maintenance systems, and cross-sectoral issues. According to the International Union of Railways (UIC) [8], HSR is defined by new lines designed for speeds of at least 250 km/h, or upgraded existing lines capable of speeds up to 200 km/h. The history of railways reflects a constant pursuit of speed, from the inaugural "Rocket" locomotive in 1829 to the birth of High-Speed Rail with the Tokaido Shinkansen reaching 210 km/h in 1964.

Two primary strategies for enhancing commercial speed involve upgrading existing lines and constructing new dedicated lines. This approach has been embraced globally,

This material is reserved for educational use only, not allowed for commercial use.

Forbidden to modify the content, and cite the document when use.

with notable milestones such as the TGV's introduction in 1981 and subsequent global proliferation in countries like Italy, Germany, Spain, Korea, China, Turkey, Morocco, Saudi Arabia, and the United States. Japan's Shinkansen lines have consistently exceeded speeds of 260 km/h, while China's high-speed conventional rail lines operate at an impressive top speed of 350 km/h as shown in Figure 2.8. The CRH380AL in China set a world record, reaching 486.1 km/h, highlighting the continuous evolution and achievements in high-speed rail technology. Notably, the V150, a specially configured version of Alstom's TGV, holds the world record for high-speed rail at an astonishing 574.8 km/h achieved during a test run. This collective progress underscores the ongoing commitment to advancing rail technology and pushing the boundaries of speed on the tracks.

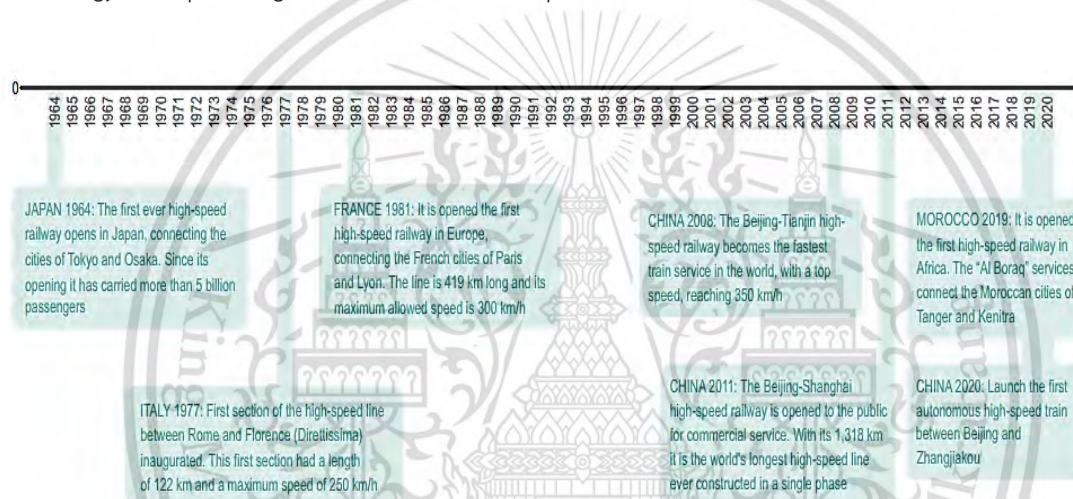


Figure 2.8 History of railway speed [8]

High-speed trains exhibit remarkable characteristics that make them a superior mode of transportation. With a maximum test speed reaching a staggering 574.8 km/h, exemplified by the TGV in France in 2007, and an operational speed of 350 km/h achieved by CRH and CR in China, these trains are synonymous with speed and efficiency. The safety record of high-speed trains is commendable, boasting significantly fewer operation accidents compared to cars, buses, and airplanes. Operating on completely enclosed lines with advanced automatic control systems, high-speed trains are renowned for their punctuality in all weather conditions. Beyond speed and safety, these trains demonstrate low energy consumption, occupy less land, and boast a high capacity, exemplified by the Beijing-Shanghai High-speed Railway's annual one-way capacity of approximately 58 million people. This capacity surpasses that of air transportation and expressways, making high-speed rail a more efficient and environmentally friendly choice. Furthermore, the

This material is reserved for educational use only, not allowed for commercial use.

Forbidden to modify the content, and cite the document when use.

economic and social benefits of high-speed trains are substantial, with a proven direct investment income above 12% and a social benefit rate exceeding 20%, ensuring a positive return on investment within a decade. In summary, high-speed trains represent a paradigm shift in transportation, offering unparalleled speed, safety, efficiency, and sustainability.

### 2.5.1 Technologies of High-speed Train

The technologies that propel high-speed trains into the forefront of modern rail transportation are both diverse and integrated, showcasing a harmonious blend of innovation across key components (Figure 2.9). The key technologies of High-speed trains are:

- System integration
- Car body
- Bogie
- Traction and transmission system
- Breaking system
- Train communication network and control system

System integration serves as the foundation, encompassing critical aspects such as the wheel-rail relation, pantograph-catenary interaction, fluid-structure dynamics, electromechanical coupling, and electromagnetic compatibility. The car body is engineered for lightweight efficiency and aerodynamic shaping, with the streamlined head playing a pivotal role in determining aerodynamic resistance, lift, lateral forces, and air pressure pulses during crossings. The bogie, a linchpin in high-speed train technology, assumes a multifaceted role in guiding, loading, vibration reduction, and providing traction and braking functions, thereby determining operational safety and dynamic performance. The traction and transmission system, powered by transformers, converters, and traction motors, is central to driving force provision, with a focus on increasing power to enhance speed by reducing air resistance. The braking system, featuring electric, air, and regenerative braking, is meticulously designed to optimize energy feedback, reduce mechanical wear, and ensure safe and stable parking within specified distances. Complementing these elements, the train control network system integrates operation monitoring, failure detection and diagnosis, and a robust communication network. Chinese high-speed trains have led in system innovations across various domains, including system integration, streamlined head design, lightweight car bodies, advanced bogie technologies,

This material is reserved for educational use only, not allowed for commercial use.

Forbidden to modify the content, and cite the document when use.

vibration and noise reduction, efficient traction systems, streamlined pantograph-catenary current collection, braking innovations, and enhanced passenger interfaces. This comprehensive approach to technological advancements underscores the holistic nature of high-speed train development, where each element plays a crucial role in achieving the pinnacle of efficiency, safety, and speed in rail transportation.

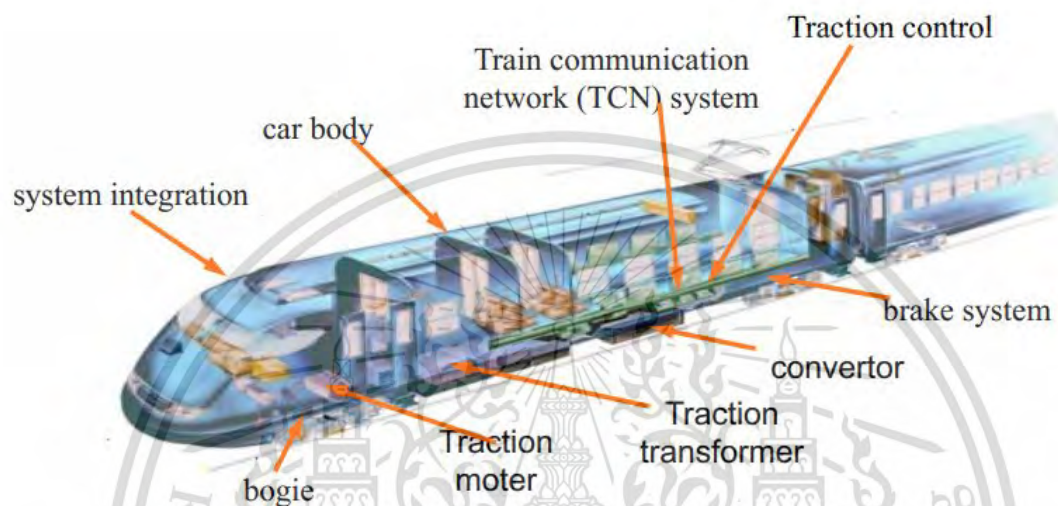


Figure 2.9 Key technologies of high-speed train.

### 2.5.2 Function and Composition of High-Speed Train Bogie

Railway bogies, fundamental components of rail vehicles, play a crucial role in maintaining vehicle stability, safe navigation during curves, and passenger comfort during journeys. A central concern in bogie design is addressing the fatigue loads generated by repetitive vibrations and landing forces during service, underscoring the necessity of ensuring structural strength to withstand both static and fatigue loads. Typically, bogie frames employ structural steels to meet these requirements [8].

In order to meet the need of high-speed operation of trains, high-speed train bogies must have sufficient strength and rigidity, high motion stability and ride quality, good curve passage ability, low wheel-rail force, so as to maximize the adhesion potential between the wheel and the rail. Additionally, the structure must be simple, reliable and low maintenance. Bogies of high-speed trains are equipped with the integral rolled steel small-diameter wheels, hollow axles, light metal axle boxes, lightweight axle box bearings, and the technology of frame or body suspension is adopted for the traction motor to comprehensively reduce the unsprung weight.

This material is reserved for educational use only, not allowed for commercial use.

Forbidden to modify the content, and cite the document when use.

The weight of bogies constitutes approximately 37% of a rail vehicle's total weight. Consequently, the reduction of bogie component weight is a priority for companies striving to achieve lightweight vehicle designs. Reducing the unsprung weight of bogies is also essential for mitigating rail loads, minimizing dynamic variations in wheel loads (a factor in track deformation), and reducing noise and vibration. Bogies are comprised of several key components (as illustrated in Figure 2.10). Notably, there are various types of bogies, categorized based on their applications, such as passenger, semitrailer, locomotive, metro, and tram bogies [9].

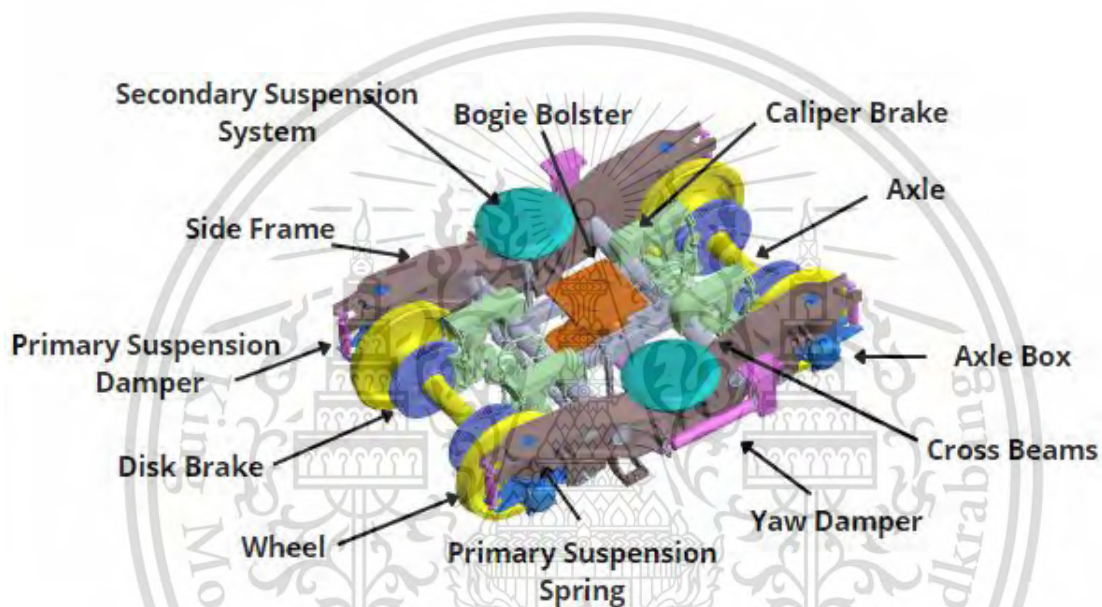


Figure 2.10 Railway bogie composition

### 2.5.3 Axle System Function

The axle system of a rolling stock serves a pivotal role in ensuring the smooth and efficient operation of trains, with its functions distinctly categorized into three key aspects (Figure 2.11). Firstly, the axle system bears the weight of the entire rolling stock and absorbs the impacts generated during train movement, providing structural integrity and stability. Secondly, the system produces traction or braking force by leveraging adhesion with the rail. This adhesion allows the wheels to grip the track, enabling the transfer of power from the locomotive to the wheels for acceleration or, conversely, facilitating controlled deceleration through braking. Finally, the rolling of the wheelset, a collective term for the wheels and axle, actively propels the entire rolling stock forward. As the wheelset rotates along the tracks, the kinetic energy generated is harnessed to move the

This material is reserved for educational use only, not allowed for commercial use.

Forbidden to modify the content, and cite the document when use.

train, illustrating the dynamic interplay between the axle system and the railway infrastructure. In essence, the axle system's multifaceted functions are instrumental in ensuring the operational efficiency, safety, and controlled movement of trains within the railway network.



Figure 2.11 CR300AF motor wheelset

The structural characteristics and requirements of high-speed train axles are essential considerations in ensuring the robustness and reliability of these critical components. High-speed train axles typically serve two primary roles: motor axles and trailer axles (Figures 2.12 and 2.13). Regardless of their specific designation, the working conditions for axles are among the most challenging among all parts of the train. Motor axles play a key role in providing the driving force, while trailer axles bear the load without actively contributing to propulsion. Both types of axles must withstand significant loads and forces, making their structural integrity crucial for the overall performance and safety of the high-speed train. The design of high-speed train axles must carefully balance factors such as material strength, weight distribution, and resistance to wear and fatigue to ensure they meet the demanding operational requirements of high-speed rail travel. The rigorous working conditions necessitate a focus on precision engineering and high-quality materials to guarantee the durability and efficiency of these axles in the demanding environment of high-speed rail transportation.

This material is reserved for educational use only, not allowed for commercial use.

Forbidden to modify the content, and cite the document when use.

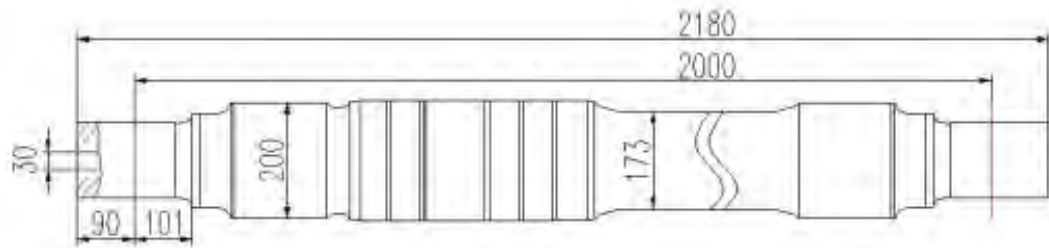


Figure 2.12 Motor axle

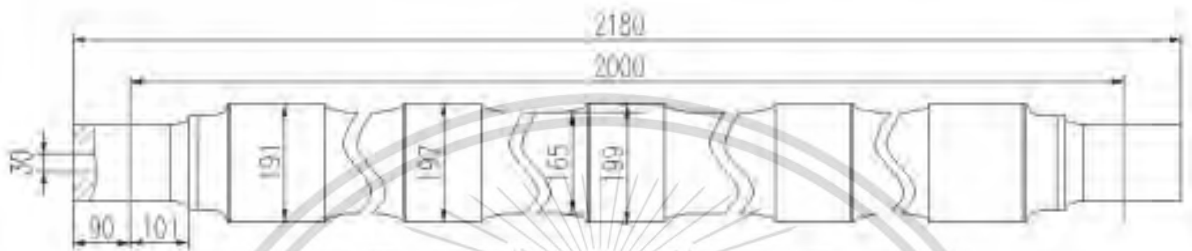


Figure 2.13 Trailer axle.

#### 2.5.4 Structural Characteristics and Requirements of High-Speed Train Wheels

The structural characteristics of high-speed train wheels play a crucial role in ensuring optimal performance and safety. Two common spoke types are utilized in wheel designs: straight spokes and curved spokes (Figure 2.14). Straight spokes are typically adopted when wheel-mounted brake discs are employed, while curved spokes are preferred in cases where the lateral distance between the hub and rim is considerable. The choice between these designs is influenced by functional requirements and practical considerations. Additionally, the flange and tread profiles are essential elements in wheel design. The conical tread, with its distinct profile, serves multiple functions, including facilitating the automatic centering of the wheelset during straight riding and enabling smooth passage through curves (Figure 2.15). The worn profile tread, which mimics the standard conical tread after wear, offers advantages such as extended wheel lathing life, increased permissible axle weight, and reduced flange wear on curves (Figure 2.16). However, it comes with the disadvantage of a larger equivalent gradient, impacting hunting stability. The careful consideration of these structural characteristics and their requirements is paramount in achieving the balance between performance enhancements and potential drawbacks in the design of high-speed train wheels.

This material is reserved for educational use only, not allowed for commercial use.

Forbidden to modify the content, and cite the document when use.



(a) Straight spoke wheel

(b) Curved spoke wheel

Figure 2.14 Wheels of different spoke types.

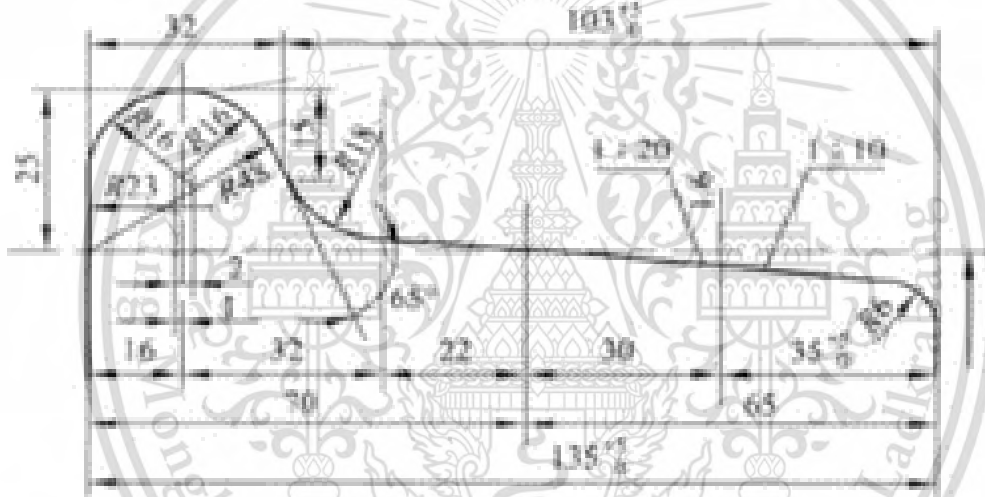


Figure 2.15 Profile of standard conical tread

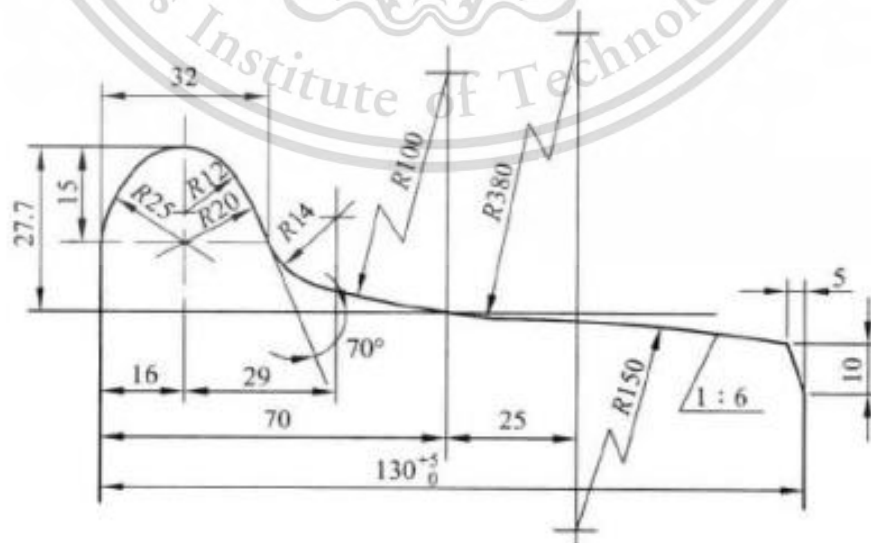


Figure 2.16 Worn profile tread.

This material is reserved for educational use only, not allowed for commercial use.

Forbidden to modify the content, and cite the document when use.

### 2.5.5 Function and Manufacture of Framework

The bogie frame is a critical component in the construction of railway bogies, serving several essential functions (Figure 2.17). Primarily, it acts as the structural framework that connects and installs all components of the bogie. The frame is designed to efficiently transfer forces in all directions, ensuring the structural integrity and stability of the entire bogie system. One of its key roles is to maintain the proper position of the axles within the bogie, contributing to the smooth and controlled movement of the train. The manufacturing process of bogie frames typically involves welding, where various components are joined together. Once the welding process is complete, the entire frame undergoes an annealing process to relieve stresses and enhance the material's mechanical properties. Subsequently, the frame is machined to achieve precision and alignment. This meticulous manufacturing approach is crucial in producing bogie frames that meet the stringent standards required for the reliable and safe operation of high-speed trains. The well-designed and precisely manufactured bogie frame is fundamental to the overall performance and longevity of the train's bogie system.

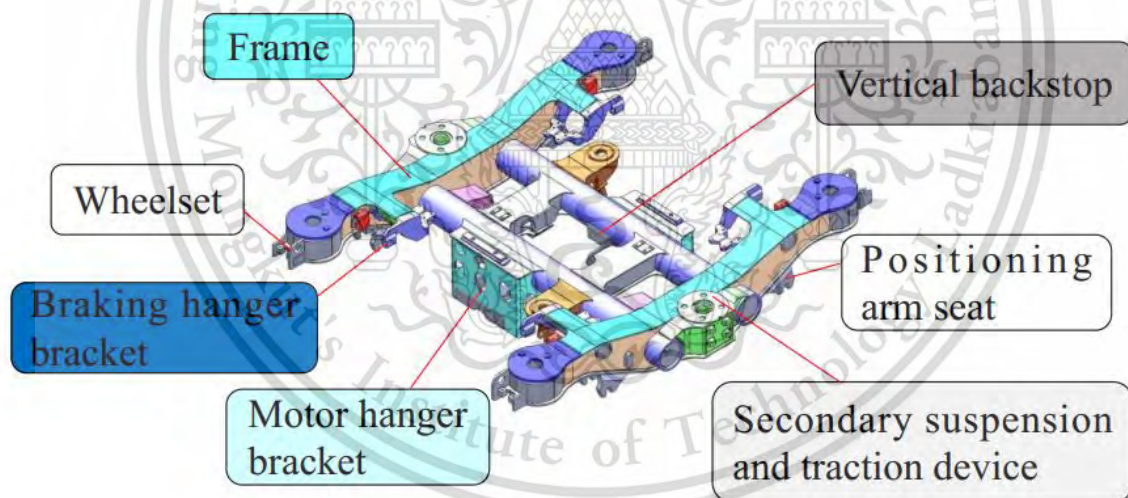


Figure 2.17 Composition and installation interface of the framework.

### 2.5.6 Function, Classification, and Composition of Suspension System

The suspension system in the context of high-speed trains serves a crucial role in ensuring the stability, balance, and smooth operation of the entire train assembly. The primary functions of the suspension system are threefold. Firstly, it allocates a specific load to each axle, maintaining a balanced distribution of weight to prevent uneven wear

This material is reserved for educational use only, not allowed for commercial use.

Forbidden to modify the content, and cite the document when use.



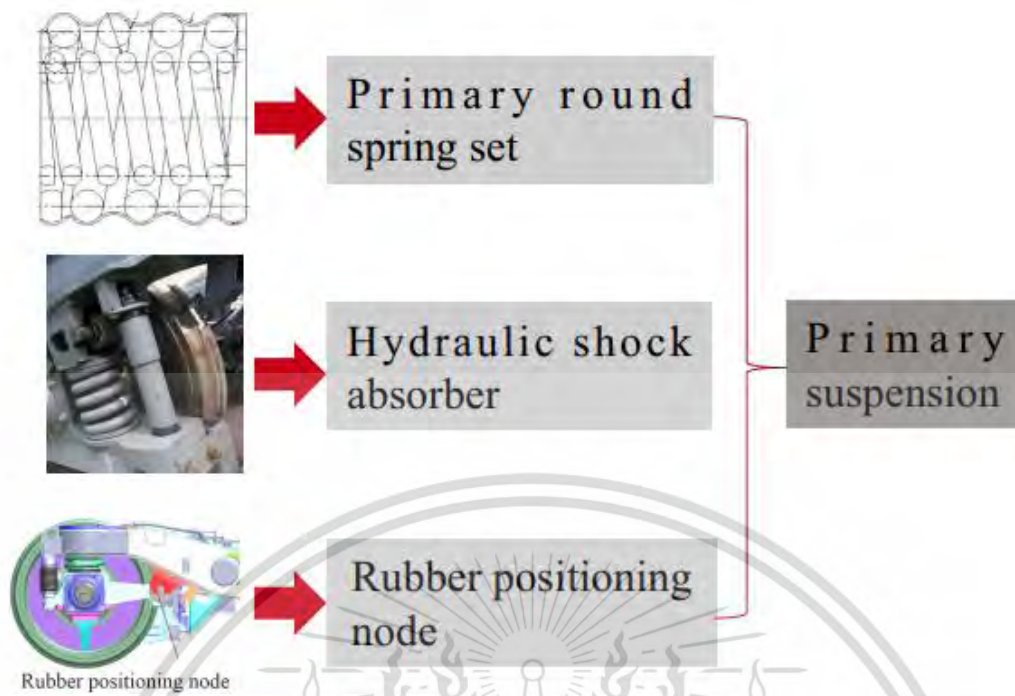


Figure 2.19 Primary suspension system.

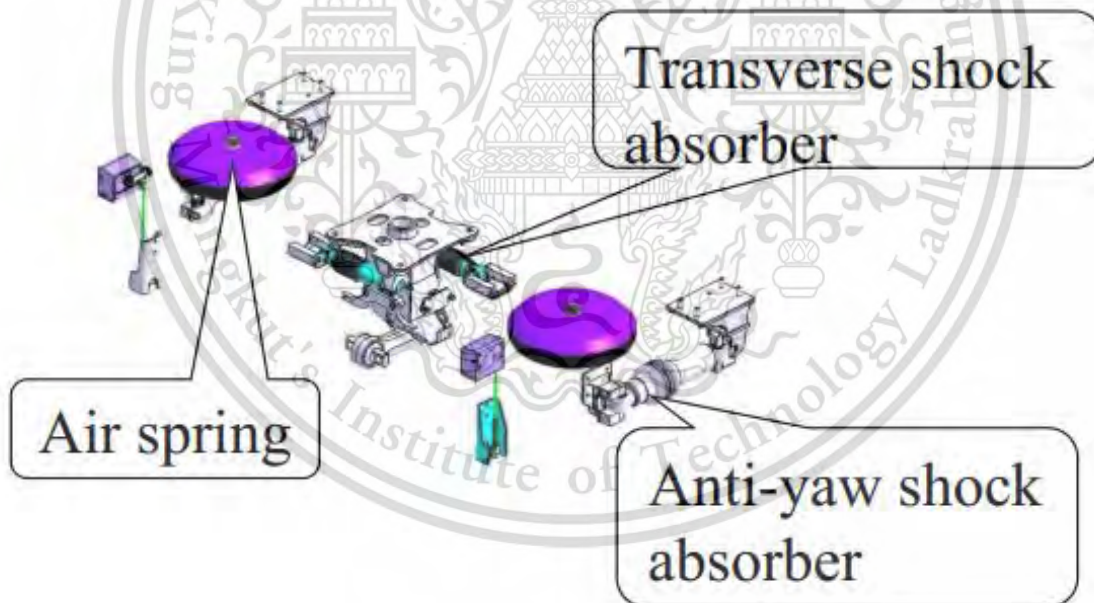


Figure 2.20 Secondary suspension system.

### 2.5.7 Function and Composition of Foundation Brake System

It generates a certain braking force to slow down or stop the train within a specified distance or time. The system mainly includes a mechanical part, an air pipeline part and

This material is reserved for educational use only, not allowed for commercial use.

Forbidden to modify the content, and cite the document when use.

an electrical control part. The foundation brake system of a high-speed train is a critical component responsible for ensuring effective braking performance and safety. Its primary tasks can be summarized into several key functions. Firstly, it transmits the piston force generated by each brake cylinder to each brake shoe or brake lining. Secondly, it multiplies this piston force, enhancing the braking effect. Lastly, it ensures that the pressure applied to each brake shoe or brake lining is essentially equal, promoting balanced and uniform braking across the entire system.

The composition of the foundation brake system includes two main types: caliper disc brakes for motor car wheels and trailer axle disc brakes. The wheel disc, installed on each wheel, serves both motor car and trailer wheels, while the axle disc is specifically designed for trailer axles, with two discs on each axle (Figure 2.21).

It requires huge energy for high-speed trains to brake, so it is necessary to adopt a composite braking mode combining multiple braking methods and equipped with electronic anti-skid devices to improve the wheel-rail adhesion utilization. Dynamic braking (rheostatic and regenerative braking) shall be applied with friction braking (disc braking) wherever possible on the motor bogie. On the trailer bogie, non-adhesion braking (eddy current braking and magnetic braking) shall be applied in addition to the disc braking.



Figure 2.21 Foundation brake device.

Generally, an electric instruction straight-through electro-pneumatic brake control system is adopted, with the microprocessor as the control center and dynamic braking. This material is reserved for educational use only, not allowed for commercial use.

Forbidden to modify the content, and cite the document when use.

preferred. When dynamic braking is insufficient, the brake control unit issues an electric instruction, and the EP electro-pneumatic unit operates the brake cylinder to generate air braking to supplement the shortage.

The foundation brake device is further composed of a caliper braking device and an automatic brake adjuster, among other parts. The caliper braking device, equipped with components like the caliper body, brake linings, brake adjuster, support pins (upper and lower), and mounting seat, operates by changing air pressure. This change in air pressure causes the lever to hang, and the brake linings on both sides clamp the brake disc together, generating the necessary clamping force to initiate the braking action. Simultaneously, the automatic brake adjuster continuously and steplessly adjusts the gap between the brake pads and the brake disc, ensuring optimal and consistent braking performance. Overall, the foundation brake system plays a pivotal role in maintaining the train's braking efficiency, contributing significantly to the safety and reliability of high-speed rail travel.

#### *2.5.8 Test and Standard for Bogies of High-Speed Trains*

In the comprehensive evaluation of high-speed train bogies, a rigorous testing regimen is imperative, encompassing both component and complete bogie assessments (Figure 2.22). The complete bogie test is further subdivided into Bench test and Line test, each serving distinct purposes. Within the Bench test, crucial evaluations include the Running-in test, Stability test, and Stationary test. Notably, the Stability test aims to determine the critical speed by assessing the critical velocity of hunting instability. This evaluation involves both pure rolling tests on the test bed and simulated rolling vibration tests reflecting line operations.

Bench tests of key components include routine tests and type tests like the Bogie, Frame, Axle, and Wheel, each subjected to specific evaluations, such as Rolling and Vibration tests, Static Strength, Fatigue Strength tests, and more. The test standards for these assessments adhere to established protocols, such as the "Dynamic Test Evaluation Method and Evaluation Standard" (Annex 2 of EMU tender documents), GB5599-85 "Railway Vehicle Dynamic Performance Evaluation and Test Evaluation Specification," "Test method for locomotive and vehicle dynamic performance bench test" (TB/T3115-2005), and the "High-speed EMU Vehicle Test Specification" (Tieyun (2008) No. 28).

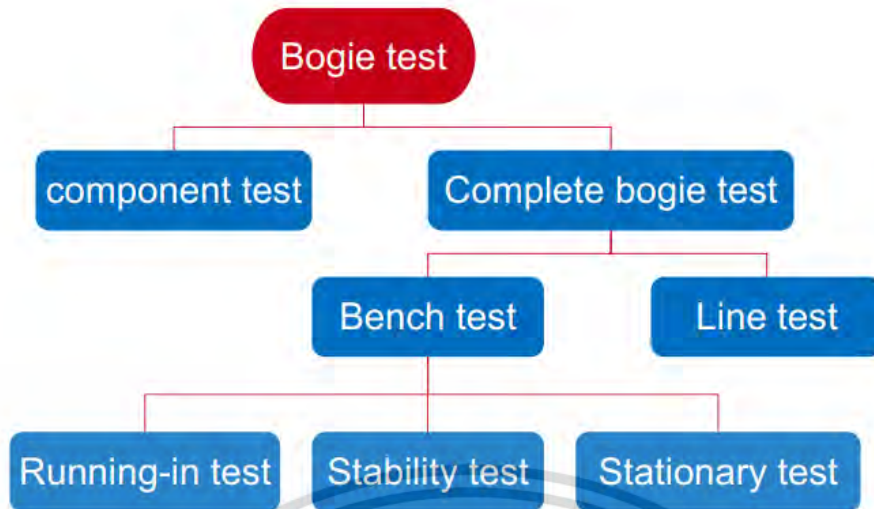


Figure 2.22 Bogie test type

The test requirements are rigorous, encompassing a speed range of 0 to 400 km/h, with a total running time of 10 hours. Specific speed phases are addressed, including a 0 to 300 km/h phase-excitation simulation line spectrum lasting 6 hours, and a 300 to 400 km/h stage pure rolling test lasting 4 hours.

Stability tests are critical components of the bench test, aiming to determine the critical speed and evaluate running stability. This involves defining and assessing the critical velocity hunting limit cycle diagram and employing methods such as pure rolling tests on the test bed or simulating rolling vibration tests of rolling stock line operation. The evaluation method considers the hunting unstable critical velocity, including  $V_{c1}$  when instability occurs, and  $V_{c2}$  after stability is restored (Figure 2.23).

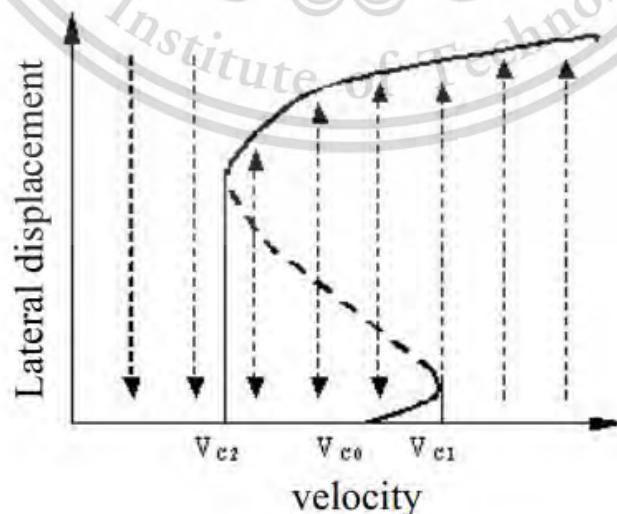


Figure 2.23 Hunting limit cycle diagram.

This material is reserved for educational use only, not allowed for commercial use.

Forbidden to modify the content, and cite the document when use.

The stationary test, as per GB5599-85 specifications, evaluates running stability through comfort index NMV and stability index W. For the line test, the functional objective is to investigate whether the EMU's performance indices align with contractual requirements, focusing on operational stability, lateral stability, and operational smoothness. These meticulous and standardized tests contribute to the comprehensive evaluation of high-speed train bogies, ensuring that they meet the stringent criteria necessary for safe and efficient rail travel.

### *2.5.9 Basic Concepts of Car Bodies*

The design and construction of the carbody in high-speed trains are integral to the overall performance and safety of the train system. The primary function of the carbody is to carry passengers or goods and house essential traction equipment. It is crucial for protecting the payload and providing a comfortable environment. The carbody structure can be categorized based on materials, with options such as carbon steel, stainless steel, and aluminum alloy, each offering unique advantages. The high-speed train body is mainly made of stainless steel and aluminum alloy. Fiber reinforced plastics have been applied for the streamlined part of the train head and the interior decoration of the carbody. The high-speed train body adopts a low body (less than 4000mm) and a drum-shaped section to reduce the body weight and aerodynamic resistance. In order to realize the specified functions of the carbody with minimum volume, the high-speed train is also modular and integrated.

In order to reduce aerodynamic resistance and interference, high-speed trains must have perfect aerodynamic shape, i.e. slender and streamlined head and tail, to reduce the pressure resistance. The surface must also be smooth to reduce the skin friction resistance. In addition, streamlined fairings are arranged at the bottom and top of the car to eliminate interference drag of exposed accessories on high-speed trains, and to reduce aerodynamic resistance during trains crossing, tunnel operation and strong crosswind.

In order to keep a basically stable pressure and reduce the noise in the car, the doors and windows installed on the carbody must also be kept sealed like the carbody itself. Connecting devices (vestibules) between the cars are enclosed with an elastic inner windshield. The inner door leading to the vestibule should be automatic to ensure that it is normally closed.

Load-carrying structures of the carbody can be borne by underframes, sidewalls, or a barrel-type monocoque structure. The latter, consisting of plate-girder, thin extrusion (single-shell), or hollow extrusion (double-shell) structures, is widely utilized in modern EMU train sets due to its enhanced load-bearing capacity, lightweight properties, and energy efficiency.

The carbody configuration varies based on the type of passenger carriages, including leading vehicles, middle vehicles, and coupling devices. For instance, the hollow extrusion structure in aluminum alloy car bodies provides advantages such as increased load-bearing capacity, lightweight construction, and reduced operational costs.

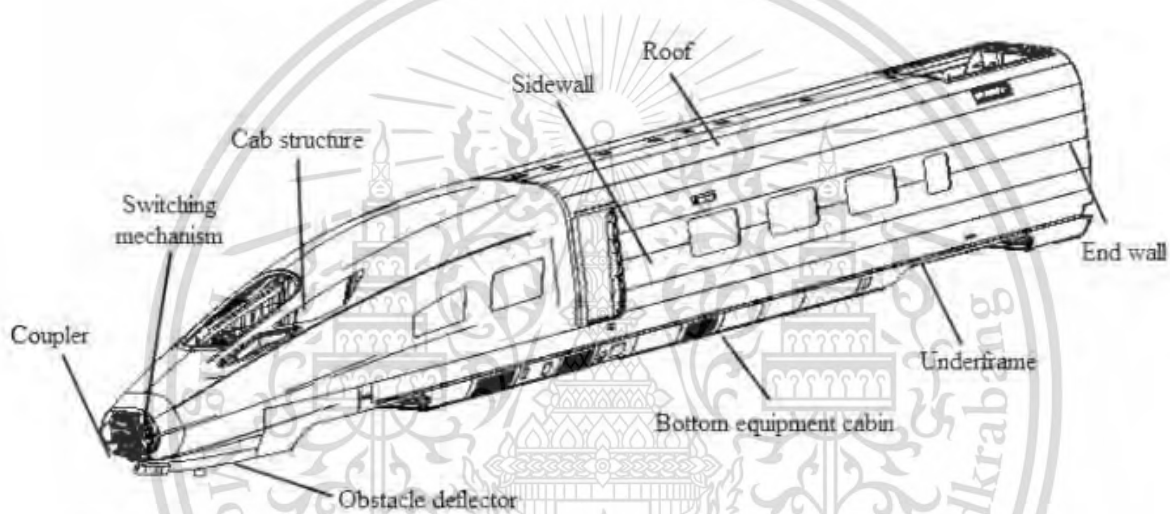


Figure 2.24 Structure of a leading vehicle in high-speed trains.

Detailed attention is given in Figure 2.24 to the design of specific components such as the cab, underframe, sidewall, roof, endwall, and doors, ensuring a balance between structural strength, aerodynamics, and passenger comfort. The aluminum alloy carbody, in particular, leverages hollow extrusion profiles and an integral barrel-type load-bearing structure, contributing to its durability, weight efficiency, and cost-effectiveness.

To validate structural integrity and performance, rigorous testing procedures are employed, including strength, stiffness, and stability assessments. Various standards and specifications, such as EN12663 and TB/T 1335-1996, guide these evaluations, addressing issues like vertical, longitudinal, lateral, airtight, and torsional loads.

Moreover, the carbody design incorporates measures for passive safety, vibration, and noise reduction. Fire prevention considerations adhere to standards like EN 45545-

2013, ensuring the safety of passengers and personnel during any potential fire-related incidents.

In summary, the comprehensive design and evaluation of high-speed train carriages involve a meticulous balance of factors, including material selection, load-bearing structures, aerodynamics, safety, comfort, and maintenance considerations. These considerations collectively contribute to the efficiency, safety, and overall success of high-speed train operations.

#### *2.5.10 Train Monitoring and Diagnosis Technology*

Automatic train protection (ATP) and automatic train supervision (ATS) are adopted to monitor the operation safety of high-speed trains. They can ensure the safety of the train operation to the greatest extent, prevent the train from speeding or entering dangerous areas, i.e. operating without permission. Fault diagnosis of high-speed trains is to correctly locate the fault through correct fault identification (inspection and detection) and isolate the parts that need to be repaired or replaced, thus greatly shortening the maintenance process and downtime.

The control instruction, operation monitoring, fault detection and diagnosis information of the high-speed train are all transmitted through its communication network. All computer-controlled components are networked and exchange information through network communication. Backed by network technology, not only can train connection be saved and train weight be reduced, but also the integration, reliability and maintainability of the system can be improved.

#### *2.5.11 Performance Parameters of Vehicles*

In the realm of vehicle performance, several critical parameters play pivotal roles in ensuring safety, efficiency, and adherence to design standards. The dead weight of a vehicle represents its total self-weight, while the permissible load indicates the maximum weight it can carry. Maximum operating speed is a crucial criterion, requiring the vehicle to sustain optimal performance during continuous operation at this specified velocity. The average braking deceleration, from maximum speed to a complete stop under rated load, is essential for assessing stopping capabilities. On the acceleration front, the maximum starting acceleration and average starting acceleration are key metrics, highlighting a

This material is reserved for educational use only, not allowed for commercial use.

Forbidden to modify the content, and cite the document when use.

vehicle's ability to initiate movement smoothly. Axle load is a critical consideration, dictating the maximum mass an axle can bear within a designated speed range. Track load per linear meter is indicative of bridge and line strength, with implications for station line utilization and overall transport capacity.

The configuration of train formations, encompassing vehicle type, quantity, and the motor-to-trailer ratio, plays a pivotal role in operational efficiency. Lastly, the minimum curve radius is a safety parameter, ensuring that a vehicle, equipped with a specific type of bogie, can navigate curves without risking derailment or other accidents. In the intricate design and operation of vehicles, these parameters collectively define the performance characteristics that govern their safe and effective utilization in diverse transportation scenarios.

### 2.5.12 Railway Clearance

In order to prevent vehicles from making contact with various buildings and equipment when running on straight lines or curves, and to ensure the absolute safety of driving, railway clearances are set, mainly including gauges of vehicles, equipment and buildings.

1. Vehicle gauge: a profile that limits the maximum allowable cross section of the vehicle. Whether empty or loaded, the vehicle shall have all protruding and suspended parts accommodated in the gauge profile.

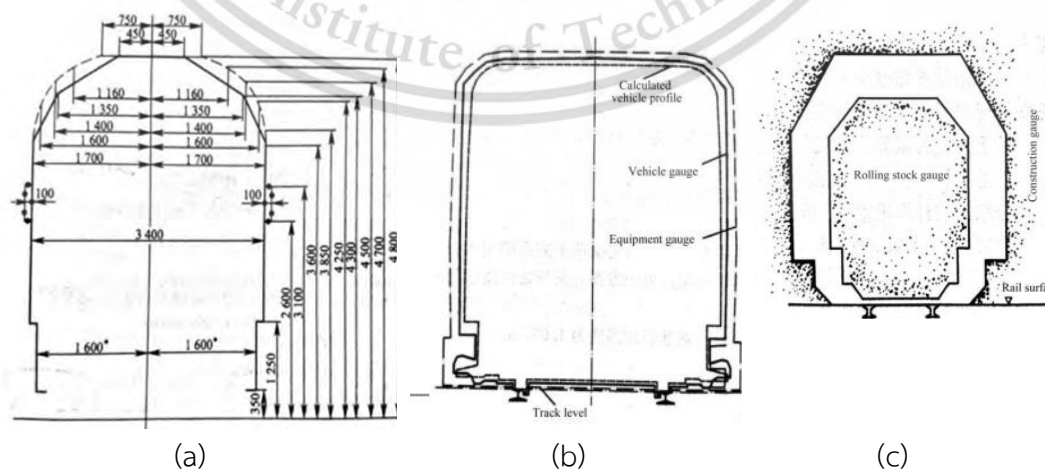


Figure 2.25 Railway clearance (a) Vehicle gauge (b) Equipment gauge (c) Construction gauge

This material is reserved for educational use only, not allowed for commercial use.

Forbidden to modify the content, and cite the document when use.

2. **Equipment gauge:** Any part of the stationary equipment (such as the signal device), including their rigid and flexible movements, shall not intrude into this gauge. The equipment gauge is a profile outside the vehicle gauge.
3. **Construction gauge:** the minimum size of buildings invading the line in the direction of its cross section, i.e. the minimum space cross section that each line must maintain, and buildings close to the line shall not invade the construction gauge under any circumstances.

### 2.5.13 Line structure of HSR

1. **Rail:** As the main component of the track, the rail is designed to guide the wheels of the rolling stock to move forward, to bear the huge pressure of the wheels, and to transmit the load to the sleeper, track bed and roadbed. In addition, the rail must provide continuous and smooth rolling surface with minimum resistance for the wheel (Figure 2.26).



Figure 2.26 Rail

2. **Intermediate connector:** The intermediate connector is a component connecting the rails or connecting the rail with the sleeper (Figure 2.27). It is used to effectively ensure the reliable connection between the rails or between the rail and the sleeper, maintain the best possible continuity and integrity of the rail, prevent the vertical and horizontal movement of the rail relative to the sleeper, ensure the

This material is reserved for educational use only, not allowed for commercial use.

Forbidden to modify the content, and cite the document when use.

normal gauge, buffer and damp the dynamic action of the rolling stock, and delay the accumulation of residual deformation of the line.

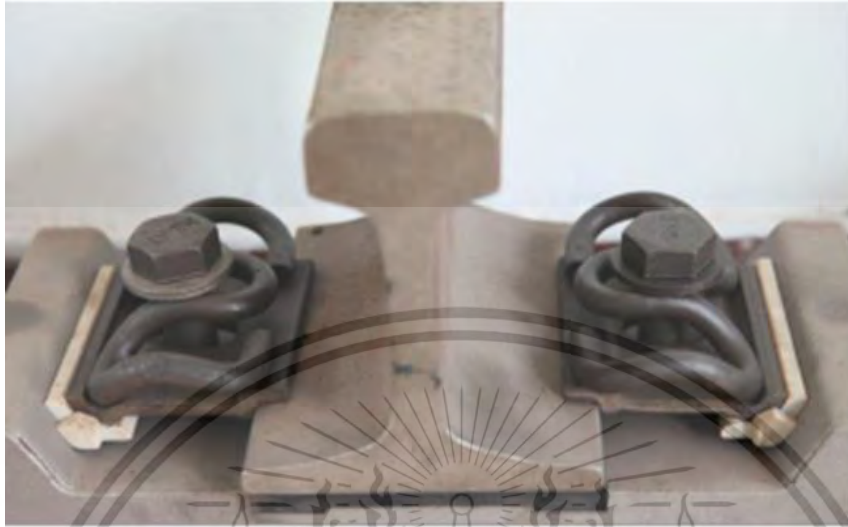


Figure 2.27 Intermediate connector

3. **Sleeper:** As an important part of the track structure, the sleeper is generally laid horizontally on the track bed beneath the rail to withstand and elastically spread all directions of pressure from the rail to the track bed, effectively maintaining the track geometry, especially the gauge and direction (Figure 2.28). Sleepers shall be necessarily firm, elastic and durable, and shall be convenient for fixing rails and able to resist longitudinal and transverse displacement.

4.



Figure 2.28 Sleeper

This material is reserved for educational use only, not allowed for commercial use.

Forbidden to modify the content, and cite the document when use.

5. **Track Bed:** On ballast tracks, the track bed is the foundation of sleepers, which are arranged at specified intervals with a certain number to increase the track elasticity and the resistance to vertical and horizontal movement, and to facilitate drainage and correct the plane and vertical sections of the track (Figure 2.29).



Figure 2.29 Track bed

6. **Roadbed:** The roadbed is a structure formed by filling or excavation to directly support the track (Figure 2.30). It is also called the substructure of the line and is a crucial work to ensure the high speed, safe and comfortable operation of trains. The function of railroad bed is to bear not only the weight of track structure, i.e. static load, but also the dynamic load transmitted through the track when the train is running. The line structure formed by the roadbed and the track is relatively loosely connected with weak resistance to dynamic load. For HSR, the roadbed should also be reasonably rigid to ensure stability and comfort during train running at high speed.



Figure 2.30 Roadbed

7. **Turnout:** Turnouts are essential line equipment when the rolling stock transfers from one track to another or crosses another track (Figure 2.31). As an important part of railway tracks, they are characterized by large quantity, complex structure,

This material is reserved for educational use only, not allowed for commercial use.

Forbidden to modify the content, and cite the document when use.

short service life, limited train speed, low traffic safety, large maintenance investment etc.



Figure 2.31 Turnout

#### 2.5.14 Line parameters of HSR

1. **Gauge:** The gauge is the minimum distance between the two rail action edges within 16mm below the top surface of the rail, as shown in Figure 2.32. The standard gauge size is 1435mm. Those larger than the standard gauge are called broad gauge, mainly including 1524mm, 1600mm, 1670mm, etc. Those smaller than the standard gauge is called narrow gauge, mainly including 1000mm, 1067mm, 762mm, 610mm, etc.

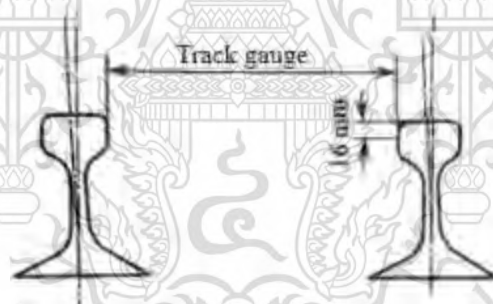


Figure 2.32 Track gauge

2. **Rail Cant:** Since the main contact part between the wheel tread and the rail top surface has a certain inclination, the rail should also have an inward inclination to ensure that the wheel load of the tapered tread acts on the symmetry axis of the rail section, and a transverse gradient, called rail cant, is thus formed between the rail bottom and the track plane (Figure 2.33). The rail is provided with a rail cant, so that the wheel-rail contact can be concentrated in the middle of the rail top, the lateral stability of the rail can be improved, and uneven wear of the rail head can be reduced. Analysis shows that the accumulation of plastic deformation in the middle of the rail head is slower than that on both sides, so a rail cant is also

beneficial to reduce the plastic deformation of the rail head and prolong its service life.

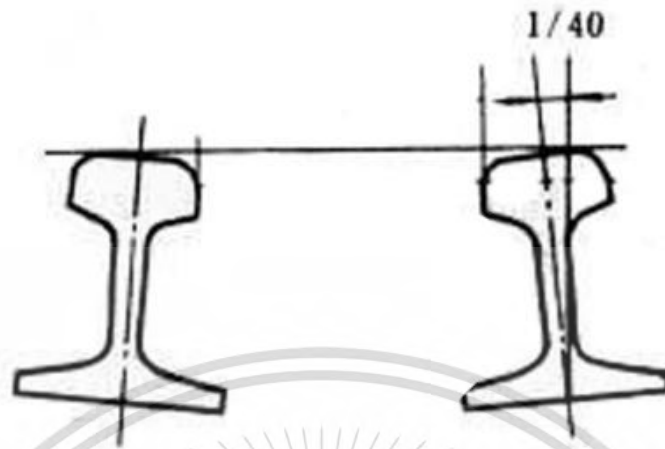


Figure 2.33 Rail cant

3. **Curved track superelevation:** When running on the curve, the rolling stock is pushed by the inertial centrifugal action to and increases the pressure of the outer rail, which makes passengers uncomfortable. Therefore, it is necessary to set superelevation on the curve. It refers to the horizontal height difference between top surfaces of the outer and inner rails of the curve. The gravity of the rolling stock will generate a centripetal horizontal component to offset the inertial centrifugal force due to the proper elevation of the curved outer rail, thus achieving uniform stress and equal vertical abrasion of the inner and outer rails, satisfying the comfort of passengers and improving the stability and safety of the line (Figure 2.34).

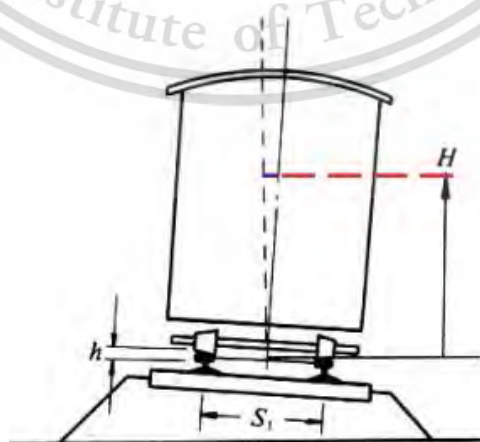


Figure 2.34 Curved track superelevation

This material is reserved for educational use only, not allowed for commercial use.

Forbidden to modify the content, and cite the document when use.

4. **Transition curve:** A curve with its radius and the outer rail's superelevation gradually changing is set up between the straight and circular part of the line, and it is called a transition curve. The transition curve has the following geometric characteristics: It connects a straight line and a circular curve with a radius of  $R$ , and its curvature gradually changes from 0 to  $1/R$ ; the outer rail superelevation of the transition curve gradually increases from zero on the straight line to and is connected with the superelevation of the circular curve.



## CHAPTER 3

# 3 METHODOLOGY

In this chapter, we elucidate the methodologies and techniques employed to conduct the research encompassed in the seven individual research papers. The methodologies presented herein aim to address the research objectives set forth, offering insights into the procedures followed, tools utilized, and the approach to analyzing data. The collective methodologies encompass a broad spectrum of techniques, including numerical simulations, and optimization processes. This chapter serves as a roadmap, providing a comprehensive overview of the research design and analytical approaches adopted.

### 3.1 Press-Fitting of Railway Wheelset

A railway wheelset is an assembly consisting of an axle and two wheels fitted with interference and, where necessary, applicable associated components, e.g., gear-shaft, bearing bushing, etc. Wheelsets need to be safe because failures could lead to derailment and potentially to major safety issues, including loss of life and heavy damage to railway vehicles. Therefore, it is important to assemble the wheelset correctly to reduce accidents and derailments. Wheelsets are assembled to remain attached to all components while in operation. Wheels may be press-fitted or shrink-fitted to the axles. Press-fit, or interference fit, tightens two parts together by relying on friction and joining the parts that can take a different form. This is commonly used in the industry because the process is reliable, simple, and does not require heating, cooling, or soldering. One problem with railway wheelsets is their failure due to excessive interference in press-fitting, and this can result in a slip between the wheel and axle. Fretting wear takes place at the interface of the axle wheel seat and the wheel hub surface, and it can cause surface fatigue, adhesion, oxidation, exfoliation, and scratching [1,2]. If a press-fit is used for assembling the wheels onto the axle, the wheel mounting peak press force limits and the press-fitting curve must be considered. Furthermore, many standards have been defined for railway wheelset assembly; for example, JIS E 4504 [12], EN 13260 [13], ISO 100-5 [14], and AAR [15]. Railways tend to follow national standards, so the authors followed the State Railway of Thailand's

This material is reserved for educational use only, not allowed for commercial use.

Forbidden to modify the content, and cite the document when use.

practice and used the European standard EN 13260 for the assembly of wheels and axles [13]. Following the standard improves the quality of the wheelset, and this would also help to standardise production.

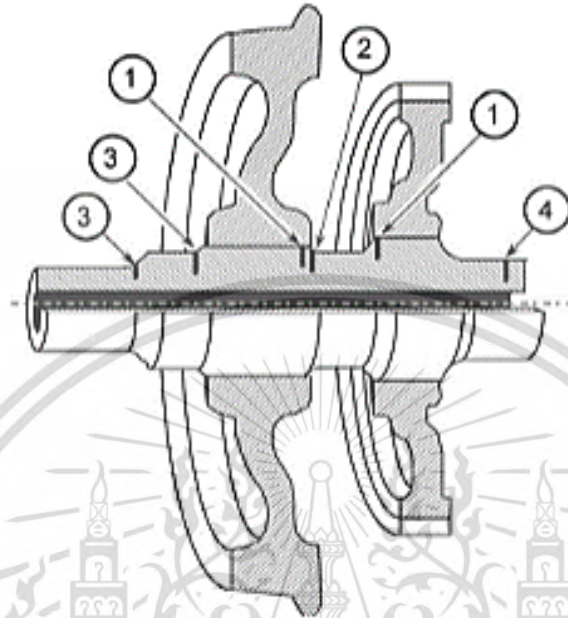


Figure 3.1 Common locations of damage accumulation on railway axles



Figure 3.2 Circumferential crack under wheel press-fit

Common sites of damage accumulation on railway axles are identifiable through a thorough investigation. Figure 3.1 highlights four prevalent locations for crack initiation, each shedding light on distinct challenges. Firstly, damage beneath the press-fitted

This material is reserved for educational use only, not allowed for commercial use.

Forbidden to modify the content, and cite the document when use.

sections is closely linked to fretting wear-induced surface damage (Figure 3.1, region 1). Another susceptible area is the contact edges (Figure 3.1, region 2), where material defects or surface irregularities can easily propagate due to stress concentration. Notably, the axle body, exposed to atmospheric conditions and physical impact, exhibits failures caused by ballast impact and corrosion damage in regions 3 and 4 of Figure 3.1. The assessment of damage accumulation beneath the press-fitted section is of paramount importance in the design of railway axles. Unlike other fatigue failures that initiate from a single point, fretting fatigue introduces challenges as it originates at multiple points, subject to similar multiaxial conditions along the press-fitted surface. The incorporation of individual fretting cracks gives rise to the formation of a major circumferential crack, leading to a rapid increase in fatigue crack propagation rate (Figure 3.2). This, in turn, results in the miscalculation of the remaining fatigue life and premature axle failure, necessitating more frequent inspection intervals and escalating operational costs. This highlights the critical role of axle design in press fitting assessment, posing a persistent challenge for railway operators in addressing wheel-axle contact interface issues.

### 3.1.1 Theoretical Analysis of Press-Fitting

In general, wheels and axles should meet the geometric requirements before being assembled, as defined in EN 13261 for axles and EN 13262 for wheels [16,17]. The wheelset can be formed by press-fitting or shrink-fitting. In press-fitting, pressure is applied to the wheel hub to force it onto a slightly larger diameter axle, thus leading to contact. External pressure acts on the axle wheel seat, and the internal pressure acts on the wheel hub. The maximum and a minimum interference between the axle wheel seat and wheel hub bore are as follows [13]:

For shrink fitting,

$$0.0009dm \leq 2\delta \leq 0.0015dm \quad (3.1)$$

For press-fitting,

$$0.001dm \leq 2\delta \leq 0.0015dm + 0.06 \quad (3.2)$$

where  $dm$  is the mean diameter and  $\delta$  is the radial interference in mm.

Assuming the cylinder subjected to internal pressure is the wheel hub bore and the cylinder subjected to external pressure is the axle wheel seat, the stresses can be calculated by Lamé's theory (Figure 3.3).

This material is reserved for educational use only, not allowed for commercial use.

Forbidden to modify the content, and cite the document when use.

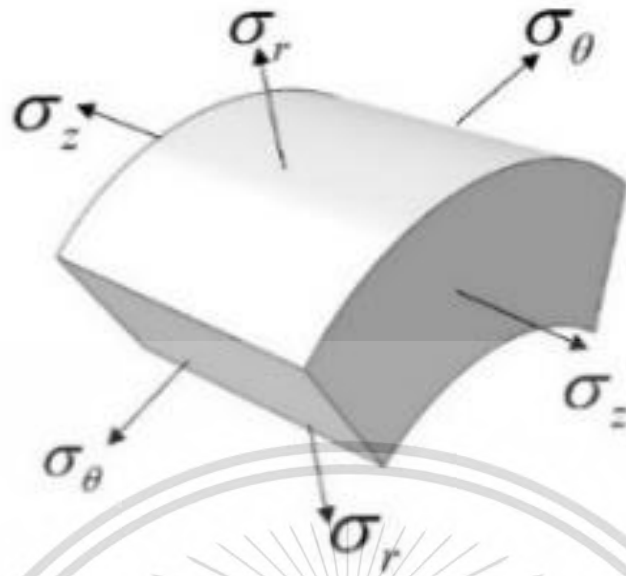


Figure 3.3 Stresses in a thick-walled cylinder element.

Consider a small section of the cylinder, radial stresses  $\sigma_r$  and  $\sigma_\theta$  tangential stresses can be achieved as a function of radius:

$$\sigma_r = \frac{r_i^2 P_i - r_o^2 P_o}{r_o^2 - r_i^2} - \frac{(P_i - P_o) r_i^2 r_o^2}{(r_o^2 - r_i^2) r^2} \quad (3.3)$$

$$\sigma_\theta = \frac{r_i^2 P_i - r_o^2 P_o}{r_o^2 - r_i^2} + \frac{(P_i - P_o) r_i^2 r_o^2}{(r_o^2 - r_i^2) r^2} \quad (3.4)$$

When the wheel and axle are press-fit assemblies, it can be assumed that pressure  $P$  is exerted all over the surface of the contact at the nominal radius,  $r$ . The magnitude of contact pressure, due to press-fitting assembly, can be calculated by summing the radial displacements of the inner and outer parts [18]. It was designated  $r_i$  is the inside radius of the cylinder,  $r_o$  is the outside radius,  $P_i$  is the inner pressure and  $P_o$  is the outer pressure. Where the subscripts  $o$  and  $i$  on Young's modulus  $E$  and Poisson's ratio  $\nu$  represent the inner and outer cylinder.

$$P = \frac{\delta}{r \left[ \frac{1}{E_o} \left( \frac{r_o^2 + r^2}{r_o^2 - r^2} \right) + \nu_o + \frac{1}{E_i} \left( \frac{r^2 + r_i^2}{r^2 - r_i^2} \right) - \nu_i \right]} \quad (3.5)$$

If the two members are the same material,  $E_o = E_i = E$ ,  $\nu_o = \nu_i$ , equation (3.5) simplifies to

$$P = \frac{E\delta}{2r^3} \left[ \frac{(r_o^2 - r^2)(r^2 - r_i^2)}{(r_o^2 - r_i^2)} \right] \quad (3.6)$$

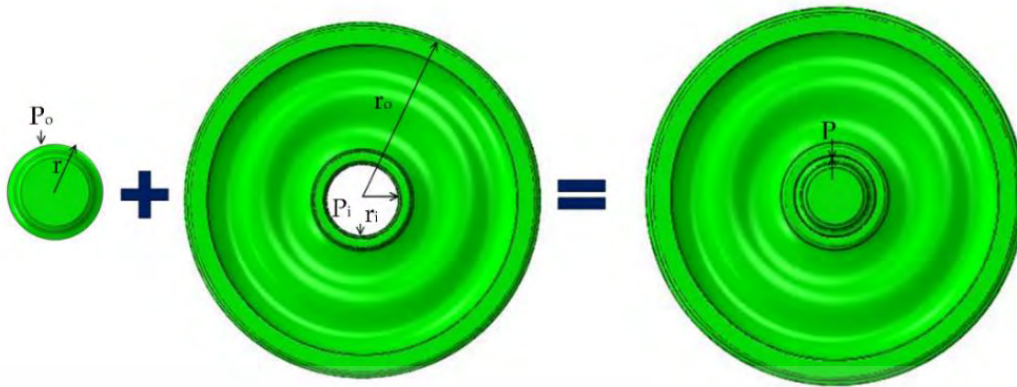


Figure 3.4 Assembly of an axle and a wheel.

As shown in Figure 3.4,  $P_i$  and  $P_o$  are equal and opposite at the contact surface in the wheelset because it is assumed that the axle and wheel are composed of the same material. Lamé's equation for contact pressure distribution in thick-walled cylinders [19] was used for calculating the contact pressure,  $P$ .

The wheel and axle were idealized as thick-walled cylinders, and the wheel was divided into five sections (Figure 3.5). The average contact pressure was calculated using Equation (3.7).

$$\bar{P} = \frac{\sum_{i=1}^N P_i L_i}{\sum_{i=1}^N L_i} \quad (3.7)$$

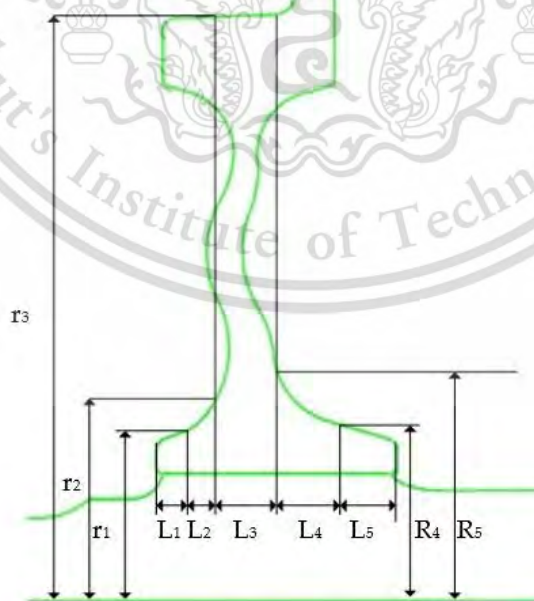


Figure 3.5 Simplified model of a wheelset for theoretical analysis [20].

This material is reserved for educational use only, not allowed for commercial use.

Forbidden to modify the content, and cite the document when use.

### 3.1.2 Characteristics of the Press-Fitting Curve

EN 13260 specified that the interference for press-fitting should be 0.2–0.36 mm, which was based on the geometric tolerances of the axle wheel seats. The factors that mainly influenced the maximum press-fitting force and characteristics of the press-fitting curve were the geometry, coefficient of friction, material strength, and operating conditions. During press-fitting, the wheelset could be damaged by insufficient or excessive press-fitting force. Therefore, the press-fitting curve is very important to determine that the assembly has not been damaged along the contact surfaces. If the press-fitting curve is not within the limits specified in the standard, the wheelset needs to be reassembled or rejected. Figure 3.6 depicts a press-fitting curve, showing the fitting force versus the displacement. In general, this displacement is the axial displacement of a wheel since the axle is fixed to the clamping head of a machine. The standard requires that the final fitting force lies in the range [13]

$$0.85 F < \text{Final Fitting Force} < 1.45 F$$

The axial force,  $F$ , in kN is

$$F = 4 d \quad (3.8)$$

where  $d$  is the mean diameter of the axle wheel seat (mm), and  $L$  is the axial displacement of the fitting (mm), which must be within the range

$$0.8 d < L < 1.1 d$$

The lines, AB, BC, HE, and ED define the boundaries of the press-fitting curve. The contact length is the X-axis, AG, in the diagram. The points labelled in Figure 3.6 can be found by using the following equations:

$$Y_H = 1.3 \phi;$$

$$Y_C = 0.85 F;$$

$$Y_D = Y_E = 1.45 F;$$

where  $\phi$  is the nominal diameter of the wheel seat in millimetres.

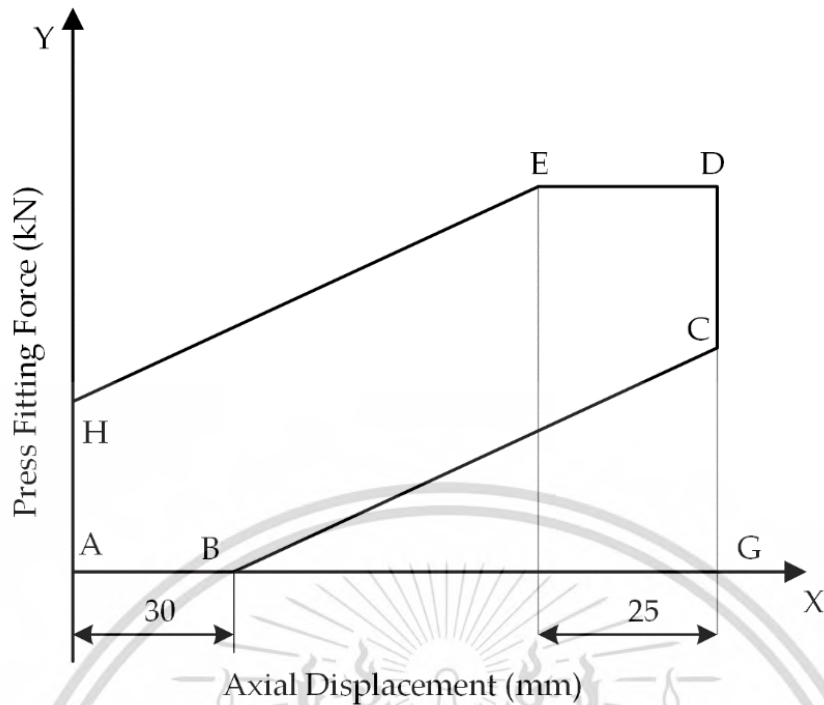


Figure 3.6 Press-fitting curve for a railway wheelset: force vs axial displacement [13].

### 3.1.3 Determination of the Press-Fitting Force

The press-fitting force is related to many factors, including interference, friction coefficient, and elasticity of the assembled parts. These factors could significantly change the press-fitting force. The press-fitting force to the wheel on the axle,  $F_p$ , can be calculated from

$$F_p = \mu \int_A P dA \quad (3.9)$$

where  $P$  = contact pressure ( $\text{N/m}^2$ ),  $\mu$  = coefficient of friction, and  $A$  = contact surface area ( $\text{m}^2$ ). Thus, to obtain the press-fit force, the contact pressure between the two assembly parts must be known.

### 3.1.4 Holding Torque Capacity Evaluation

Railway wheelsets are generally running under many loading conditions, for example, vertical statics forces of the vehicle, wheel and rail contact forces in longitudinal, vertical, and lateral directions, inertial forces, etc. In operation, the contact force, especially in the longitudinal direction, significantly increases as the train is accelerated (traction) or decelerated (braking). This leads to a torsional moment on the wheelset, which may cause slippage at the wheel hub and axle seat. The maximum holding torque capacity,  $T$ , is the torque required to predict the slip between the wheel and the axle, as

This material is reserved for educational use only, not allowed for commercial use.

Forbidden to modify the content, and cite the document when use.

it resists the motion of the wheelset at the contact surface. It is transmitted by frictional forces on the wheelset and can be evaluated using Lamé's equation. It was assumed that the contact pressure in the assembly was uniformly distributed. The radial interference was significant for the holding torque capacity since it was related to the contact pressure and frictional force. The holding torque capacity of the wheelset,  $T$ , was thus a function of the frictional coefficient, contact area, and contact pressure [18].

$$T = \mu \frac{D}{2} \int_A PdA \quad (3.10)$$

### 3.2 Analytical Strength Evaluation of Railway Axles

This study followed the EN 13104 standard for determining the bending moment and stress along an axle configuration using a specific load on a powered motor bogie wheelset. Figures 3.7 and 3.8 show schematic free-body diagrams of the wheelset induced by masses in motion and braking defined by the EN standards.

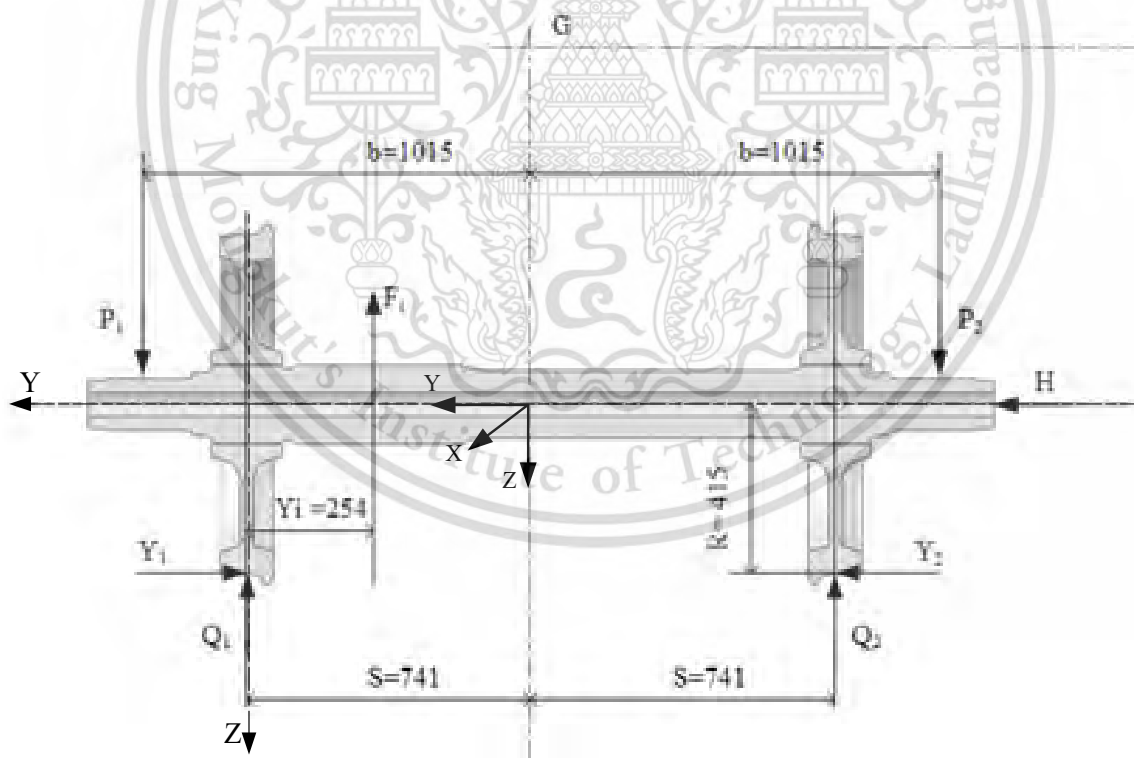


Figure 3.7 A schematic free-body diagram of a motor bogie wheelset due to masses in motion (measurements are in mm)

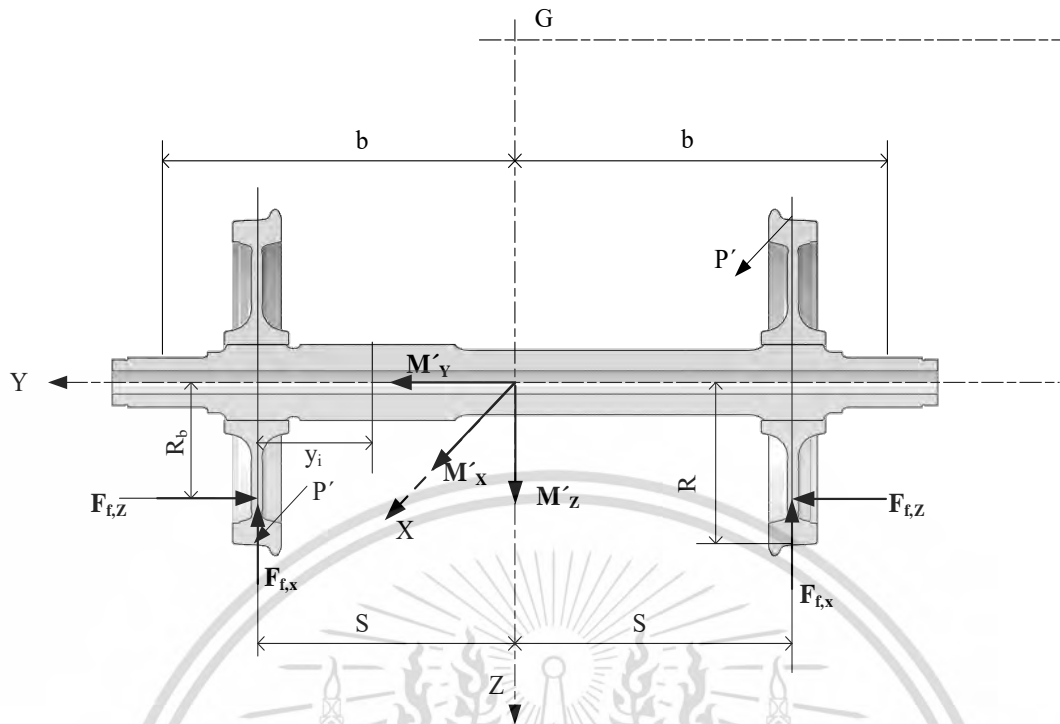


Figure 3.8 A schematic free-body diagram of a motor bogie wheelset due to braking (measurements are in mm)

### 3.2.1 Loads Acting on an Axle

An operating wheelset experiences three forces, those generated by masses in motion, braking and traction. For a powered motor bogie axle with an asymmetric vertical force loaded on its journal bearings, the force due to the masses of the unsprung parts, wheel-rail contact force, lateral force and braking are the most prominent acting on an axle. An axle can be subjected to torsional loading during driving, accelerating, and braking. A railway axle with two brake discs attached to its wheel hub is considered in the calculations of the current study. Type of the rolling stock used in this study is high-speed motor bogies and long-distance trains. The maximum normal design payload for a vehicle is 239.136 kN, and the weight of the vehicle body is 283.755 kN. The maximum braking force used in this study is for emergency braking under a deceleration of  $1.25 \text{ m/s}^2$ . The specific load values used to calculate the internal and external stresses on a motor bogie axle are shown in Table 3.1 [20].

This material is reserved for educational use only, not allowed for commercial use.

Forbidden to modify the content, and cite the document when use.

Table 3.1 Loads for an axle of a motor bogie.

Load	Magnitude (kN)
Vertical force on the more loaded side= $P_1$	101.300
Vertical force on the less loaded side= $P_2$	75.528
Wheel-rail horizontal contact force on the more loaded side= $Y_1$	49.509
Wheel-rail horizontal contact force on the less loaded side= $Y_2$	24.754
Vertical rail contact reaction force on the more loaded side= $Q_1$	112.430
Vertical rail contact reaction force on the less loaded side= $Q_2$	63.171
Balancing force between $Y_1$ and $Y_2=H$	24.775
Un-sprung force= $F_i$	-1.215
Friction force between the wheel and brake disk= $\Gamma$	0.250
Maximum braking force= $F_f$	39.200
The proportion of P braked by the braking system= $P'$	75.000

### 3.2.2 Stress Evaluation along an Axle

The stress concentration factor of an axle,  $K$ , is proportional to the ratio of the fillet or groove radius, the diameter of a cylindrical part, and the ratio of two different adjacent cylindrical parts at the transition fillet or groove (Figure 3.9). In the current study, these parameters were calculated according to the appropriate standards [3, 4]. Table 2 shows the stress concentration factor at various transition zones of a motor bogie axle. The bore of the hollow axle and other parts that did not change the section and the stress concentration factor was 1.

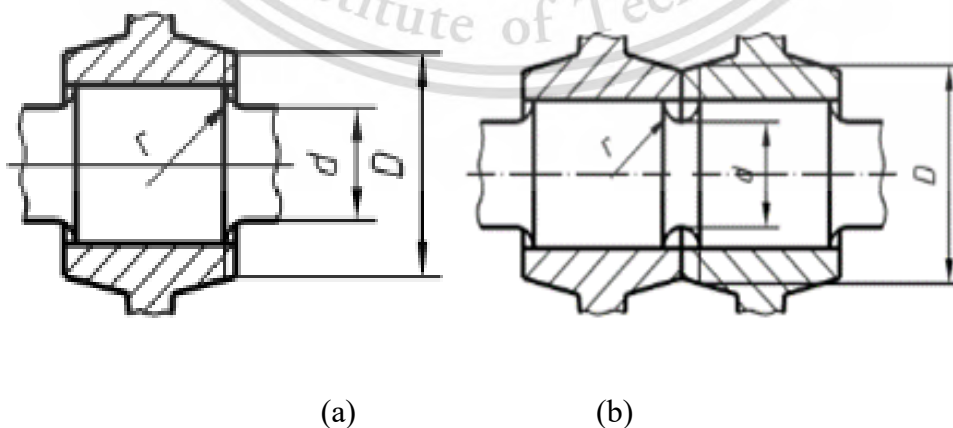
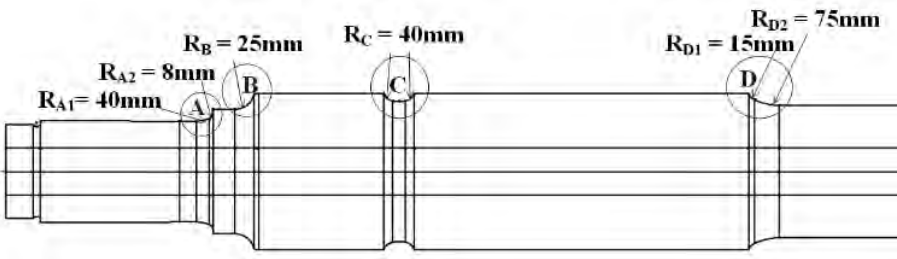


Figure 3.9 Expression of a stress concentration factor (a) bottom of the transition between two cylindrical parts and (b) groove bottom [1, 2]

This material is reserved for educational use only, not allowed for commercial use.

Forbidden to modify the content, and cite the document when use.

Table 3.2 Stress concentration factor in various axle sections.



Region	A1	A2	B	C	D1	D2
R (mm)	40	8	25	40	15	75
d (mm)	130	130	160	180	184	170
D (mm)	138	152	266	266	200	200
K	1.01	1.16	1.19	1.21	1.06	1.02

The bending and torsional moments generated by the vertical reaction and braking forces acting on the wheelset were calculated using beam theory. Eqns. (3.11) and (3.12) [3, 4] are the bending moments generated by the masses acting on the journal bearings and braking forces acting between the load plane and wheel.

$$M_x = P_1 y \quad (3.11)$$

$$M'_x = F_{f,x} \Gamma y \quad (3.12)$$

where,  $M_x$  is the bending moment generated by masses in motion,  $M'_x$  is the bending moment caused by braking forces acting on the x axis,  $F_{f,x}$  is the maximum braking force acting vertically,  $\Gamma$  is the friction force between the brake disk and wheel, and  $y$  is the distance for any axle section from the vertical force  $P_1$ .

Eqns. (3.13) and (3.14) [3, 4] are the bending moments generated by the masses in motion and braking forces between two wheels.

$$M_x = P_1 y - Q_1 (y - b + S) + Y_1 R - \sum_i F_i (y - b + S - y_i) \quad (3.13)$$

$$M'_x = F_{f,x} \Gamma (b - S + y_i) \quad (3.14)$$

where,  $b$  is the distance between the vertical centerline and the vertical force on axle journals,  $S$  is the distance between the wheel tread and the vertical centerline,  $R$  is the nominal radius of the wheel tread, and  $y_i$  is the distance between one wheel's tread and the force  $F_i$ .

Eq. (3.15) is the torsional moment between two wheels generated by braking forces acting tangentially to the wheels. The torsional moment between the vertical force load plane and the wheel is zero.

$$M'_y = 0.3P'R \quad (3.15)$$

where,  $M'_y$  is the torsional moment due to braking,  $P'$  is the proportion of  $P$  from the braking system, and  $R$  is the nominal wheel radius.

Eq. (3.16) is the bending moment between the vertical force load plane and wheel generated by braking forces acting along the x-axis.

$$M'_z = F_{f,z}\Gamma \frac{R_b}{R} y \quad (3.16)$$

Eq. (3.17) is the bending moment between two wheels generated by braking forces acting along the x-axis.

$$M'_z = F_{f,z}\Gamma(b-S) \frac{R_b}{R} \quad (3.17)$$

where,  $M'_z$  is the bending moment due to braking acting on the z axis,  $F_{f,z}$  is the maximum braking force acting horizontally and  $R_b$  is the radius of applied brake force.

The resultant moment,  $M_R$ , is given by Eq. 3.18.

$$M_R = \sqrt{MX^2 + MY^2 + MZ^2} \quad (3.18)$$

where,  $MX$  is the sums of the bending moment acting on the x axis and  $MZ$  are the sums of the bending moments acting on the z axis,  $MY$  is the summation of torsional moments. The current study considered normal, shear, and equivalent stresses at various sections along a hollow axle. The normal and shear stresses are respectively expressed by Eqns. (3.19) and (3.20).

$$\sigma_n = \frac{32 \times \sqrt{MX^2 + MZ^2} d}{\pi(d^4 - d'^4)} \quad (3.19)$$

This material is reserved for educational use only, not allowed for commercial use.

Forbidden to modify the content, and cite the document when use.

$$\tau = \frac{16 \times MY \times d}{\pi(d^4 - d'^4)} \quad (3.20)$$

Eq. (3.21) [3, 4] is the equivalent stress on the surface of an axle.

$$\sigma = \frac{K \times 32 \times MR \times d}{\pi(d^4 - d'^4)} \quad (3.21)$$

where,  $K$  is the stress concentration factor,  $d$  is the external diameter for an axle section and  $d'$  is the bore diameter of a hollow axle.

Eq. (3.22) [3, 4] is the equivalent stress on the bore surface of an axle.

$$\sigma = \frac{K \times 32 \times MR \times d'}{\pi(d^4 - d'^4)} \quad (3.22)$$

Eqns. 3.23 and 24 [3, 4] are the stress concentration factor of the bottom of the transition between two cylindrical parts and groove bottom.

$$K = \frac{(4 - D/d)(D/d - 1)}{5(10(r/d))^{(2.5(r/d)+1.5-0.5(D/d))}} + 1 \quad (3.23)$$

$$K = \left[ \frac{(4 - D/d)(D/d - 1)}{5(10(r/d))^{(2.5(r/d)+1.5-0.5(D/d))}} \right] \left[ \frac{-1.2(r/d)^2 + 37(r/d)}{(D/d)^6} + 1.74 \right] + 1 \quad (3.24)$$

where,  $r$  is the transition fillet or groove radius,  $d$  is the diameter of the axle in which the stress concentration is calculated,  $D$  is the diameter of the wheel hub as shown in Figure 3.9.

### 3.3 Multiaxial Fatigue Analysis

A multiaxial strain-life method was used in the current study. It is applicable to both high- and low-cycle fatigue problems with complicated forces and moments that produce multiaxial stress and strain states. The fatigue performance of the axle was examined under various loading conditions to investigate the discrepancy between the results of considering braking effect and not. A typical strain-life analysis has several basic steps. First, the stress determined from numerical analysis using the ABAQUS program is

This material is reserved for educational use only, not allowed for commercial use.

Forbidden to modify the content, and cite the document when use.

necessary. It is important in obtaining actual fatigue-life estimates. These FE results are then imported into fe-safe. The fatigue material properties, loading history, fatigue algorithm selection, and mean stress correction all have a significant impact on fatigue-life prediction. Figure 3.10 illustrates the fatigue analysis procedure used in this investigation.

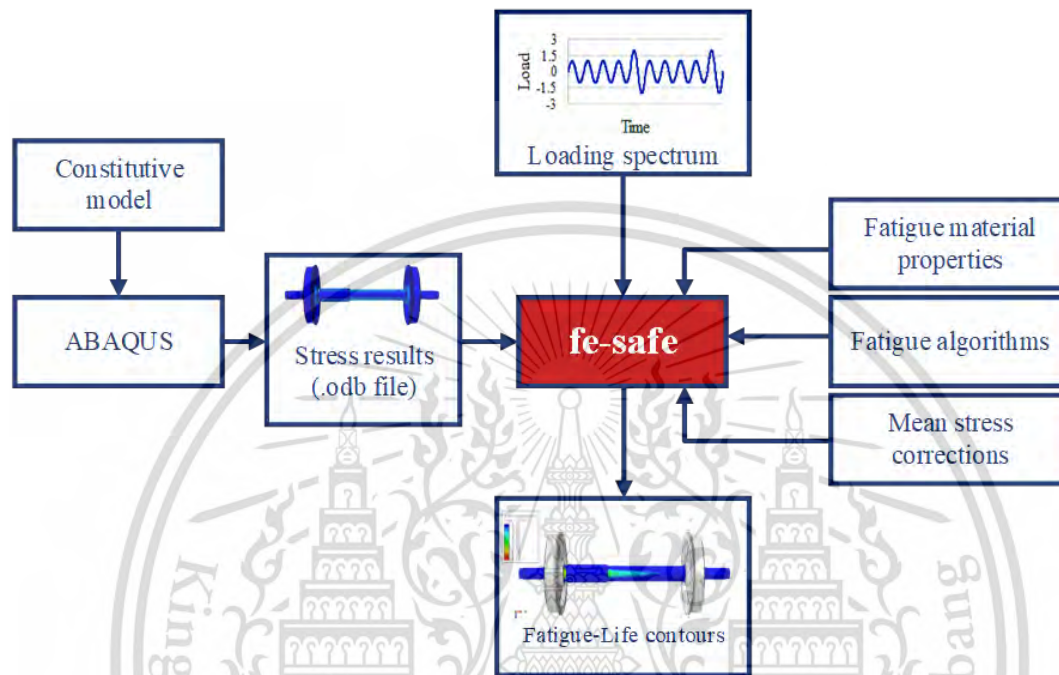


Figure 3.10 Fatigue analysis procedure.

The loading history to which the component has been subjected affects the fatigue-life prediction model. Imported FE results contain multiple linear elastic stress datasets. Each dataset contains the results of a unit-load scenario for a specific load direction. The estimated stress tensor at each node is multiplied by the load history in fe-safe. Moreover, the load ratios are easily assignable. The load case per load ratio is shown in Table 3. Figures 3.11 and 3.12 give the loading history diagram applied to each stress dataset. The load histories are assumed to be repeated until the axle fails. Railway axles in service are exposed to variable amplitude loading, which causes variable fatigue damage and overloading due to additional dynamic forces. The bending stresses obtained from FE analysis were utilized as the base load and set with a cyclic amplitude of variable overloading that was applied every fifth cycle, both upward and downward, during axle rotation. A torsional stress load history was set up as a sinusoidal function with a magnitude range of 0 to 1, since torsion is steady [22]. Press fitting is a constant load ratio [23]. Under

This material is reserved for educational use only, not allowed for commercial use.

Forbidden to modify the content, and cite the document when use.

Neuber's law [24], elastic stress is converted into elastic-plastic stress-strains, which are then utilized in a strain-life fatigue calculation.

Table 3.3 Load case vs. load ratio.

Load Case	Load Ratio (R)
Press Fitting Force	Constant
Vertical Force	R=-1
Lateral Force	R=0
Braking Force	R=0
Torsional Moment	R=0

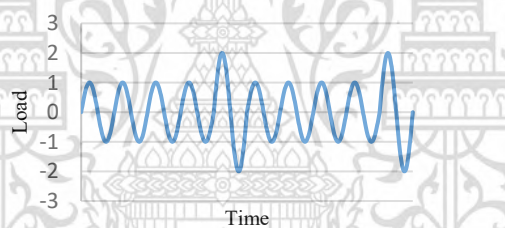


Figure 3.11 Load spectra for fatigue prediction (R=-1)

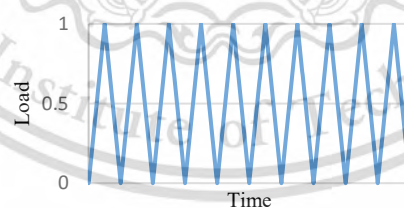


Figure 3.12 Load spectra for fatigue prediction (R=0)

### 3.3.1 Brown-Miller method

This study used the Brown-Miller method and Morrow mean stress correction with biaxial strain-life algorithm. The Brown-Miller criterion [25] is widely accepted for analysis of ductile metals and provides the highest accuracy estimates of fatigue-life. The Brown-

This material is reserved for educational use only, not allowed for commercial use.

Forbidden to modify the content, and cite the document when use.

Miller equation (Eq. (23)) states that the critical plane where maximum fatigue damage occurs is determined by the maximum shear strain amplitude ( $\Delta\gamma_{\max}/2$ ) and normal strain amplitude ( $\Delta\epsilon_{\max}/2$ ). Therefore, the Brown-Miller equation suggests that the combination of shear and normal strain is the primary cause of severe fatigue damage in materials. The complete Brown-Miller equation can be written as a result of the mean stress correlation.

$$\frac{\Delta\gamma_{\max}}{2} + \frac{\Delta\epsilon_{\max}}{2} = 1.65 \frac{\sigma'}{E} (2N_f)^b + 1.75 \epsilon'_f (2N_f)^c \quad (3.25)$$

where,  $N_f$ =the number of cycles to failure,  $\frac{\Delta\gamma_{\max}}{2}$ =shear strain amplitude,  $\frac{\Delta\epsilon_{\max}}{2}$ =normal strain amplitude.

Table 3.4 Fatigue properties of the EA4T material.

Ultimate tensile strength	650.0 MPa
Fatigue strength coefficient ( $\sigma'$ )	811.1 MPa
Cyclic yield strength ( $\sigma_{yc}$ )	385.2 MPa
Cyclic fatigue strength coefficient ( $K'$ )	806.3 MPa
Fatigue strength exponent (b)	-0.069
Fatigue ductility exponent (c)	-0.641
Fatigue ductility coefficient ( $\epsilon'_f$ )	0.658
Surface finish factor ( $K_f$ )	1

Fatigue damage is determined on each plane using a Rainflow cycle algorithm and Palmgrem-Miner rule [26]. For variable amplitude loading, fatigue damage is calculated by dividing the design life by its available life, and overall damage is summed up. The crack initiation plane is defined as the plane with the shortest life. Values greater than one indicate failure prior to reaching the design life. Table 4 provides information on the EA4T steel's fatigue materials properties.

This material is reserved for educational use only, not allowed for commercial use.

Forbidden to modify the content, and cite the document when use.

### 3.3.2 Infinite Fatigue Life Analysis

Railway axles experiencing multiaxial cyclic loading at high rotational speeds tend to reach their high cycle fatigue limit quickly during operation. Traditional fatigue analysis, which establishes a minimum number of cycles to failure, is inadequate for such scenarios. The focus is on determining the possibility of fatigue damage occurring during the component's entire loading history. The absence of damage indicates infinite life potential for the axle.

To address this, the Dang Van is an endurance criterion and employed for high cycle fatigue analysis subject to complex multiaxial stresses. In most cases, fatigue crack initiation takes place at stress concentration zones like fillets and notches. The Dang Van criterion has demonstrated considerable efficacy in assessing infinite fatigue life[21]. This methodology incorporates a multi-scale perspective, establishing a connection between the macroscopic stress derived from finite element analysis (FEA) and the microscopic stress within grain boundaries (Figure 3.13). Instead of directly calculating fatigue life, a novel approach involves the determination of the fatigue safety factor, denoted as the Fatigue Reverse Factor (FRF), utilizing a simplified pass/fail algorithm. Achieving an infinite life design necessitates ensuring that the FRF surpasses a value of 1 for all elements. To perform a Dang Van analysis, endurance limit stresses and corresponding R values need to be defined, the endurance stress is 375 MPa for constant amplitude testing at R=0 and the endurance stress is 290 MPa for R=-1 [22].

The Dang Van Criterion can be expressed as

$$\tau = \alpha S = \tau_o \quad (3.26)$$

Where

$\tau$  = local shear stress

$S$  = hydrostatic stress

$\alpha$  ,  $\tau_o$  are material-specific constants at a specific endurance.

The microscopic stress can be expressed as

$$\sigma_{ij}(P,t) = \sum_{ij}(P,t) + S_{ij}(P,t) \quad (3.27)$$

$\sigma_{ij}$  = microscopic stress tensor

$\sum_{ij}$  = macroscopic stress tensor

$S_{ij}$  = residual stress tensor

P,t are position and time co-ordinates.

This material is reserved for educational use only, not allowed for commercial use.

Forbidden to modify the content, and cite the document when use.

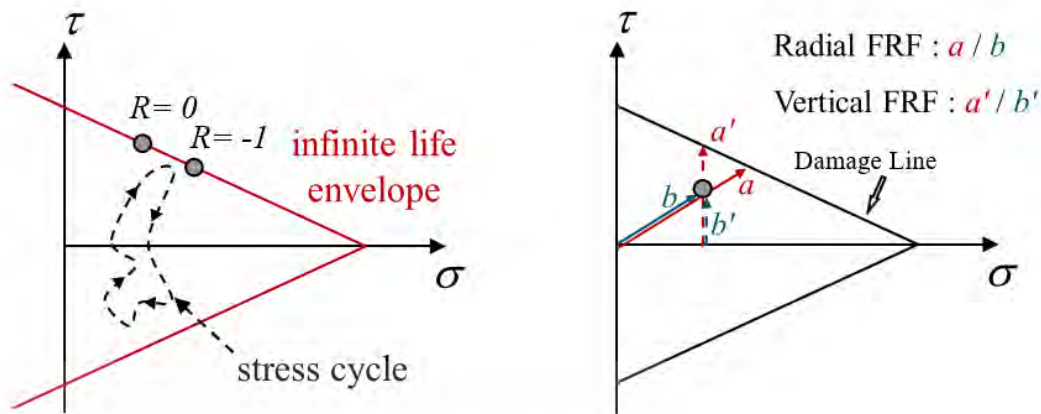


Figure 3.13 The Dang Van plot for the endurance limit.

### 3.4 Numerical Approaches of Evaluation Stress Intensity Factor

The numerical approaches for evaluating the SIF through the J-integral using the contour integral method provide a powerful tool for predicting the various crack geometries and loading conditions. The ABAQUS[23] finite element software package is capable of computing the stress intensity factor,  $K$ , and the J-Integral,  $J$  along paths that encircle a crack. The method involves defining a contour around the crack tip (Figure 3.14) and quantifying the energy absorbed by a crack and computing the stress field at the crack tip, was initially developed by Rice in 1968 [24].

$$J = \int_{\Gamma} (W dy - \vec{T} \frac{\partial \vec{u}}{\partial x} ds) \quad (3.28)$$

Where  $W$  is a strain energy density,  $\vec{T}$  is the traction vector,  $\vec{u}$  the displacement vector of a contour element  $ds$  respectively.

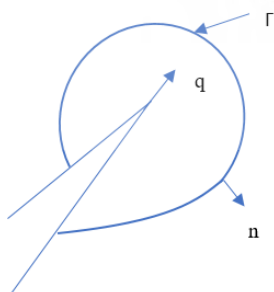


Figure 3.14 Contour for J-integral evaluation [25]

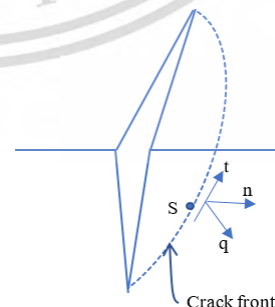


Figure 3.15 Local orthogonal Cartesian coordinates are defined at point  $s$  on the crack front.[25]

In order to extend the J-integral to three dimensions, it is necessary to examine a crack that has a tangential contour front, as illustrated in Figure 3.15. The direction of virtual crack propagation is denoted by  $q$ , which runs perpendicular to the local crack front and lies within the crack plane,  $n$  and  $t$  are assigned as normals and tangent of the crack front, respectively.

For homogeneous, isotropic materials, the crack front stress intensity factor,  $K$ , can be related to the J integral,  $J$ , using the following equation:

$$J = \frac{1}{E}(K_I^2 + K_{II}^2) + \frac{1}{2G}K_{III}^2 \quad (3.29)$$

where  $J$  is the J-integral,  $G$  is the shear modulus of a material,  $K_I$ ,  $K_{II}$ ,  $K_{III}$  are the three stress intensity factor modes for general crack opening.

For the plane stress,  $\bar{E} = E$  and the plane strain,  $\bar{E} = E/(1-\nu^2)$ , the conditions are axisymmetric, and three dimensions. Where  $E$  is the elastic modulus of the material,  $\nu$  is the Poisson ratio.

Regarding the linear elastic condition, the J-integral is equivalent to the rate of energy release when considering a single mode condition. Moreover, it is possible to calculate  $K$  from J-integral by using the following equation.

$$J = \frac{(1-\nu^2)K_I^2}{E} \quad (3.30)$$

### 3.4.1 The Analytical Method of Evaluation the SIFs of Elliptical Surface Cracked Subjected to Bending

The analytical method for SIF solutions typically involves mathematical modeling and solving equations that describe the physical behavior of the structure and the stress field around the crack tip. The solutions obtained can then be used to calculate the SIF, which is a measure of the stress intensity at the crack tip. Figure 3.16 shows the typical semi-elliptical crack in cylindrical bar.

The BS 7910 standard is a widely used code for assessing the integrity of structures containing cracks, and it provides a set of equations for calculating SIFs for various types of cracks and loading conditions. The standard uses a combination of analytical and empirical methods to derive the equations, which are based on the principles of linear elastic fracture mechanics. In this research, the analytical stress intensity factor (SIF)

solutions were determined by using the BS 7910 standard [9], referred to as K, expresses the stress state at a crack tip and is calculated with Eq. (3.31-38).

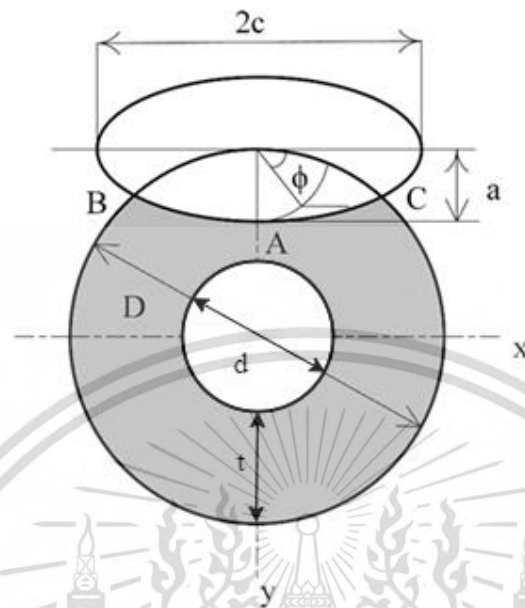


Figure 3.16 Semi-elliptical crack in cylindrical bar.

The general equation for the solution of the stress intensity factor is as described in the following:

$$K = Y\sigma\sqrt{\pi a} \quad (3.31)$$

where  $Y$  is a non-dimensional geometry factor,  $a$  is the crack length and  $\sigma$  is a nominal stress.

The following equation applies to the fracture evaluations:

$$Y\sigma = (Y\sigma)_p + (Y\sigma)_s \quad (3.32)$$

Where,  $(Y\sigma)_p$  is the primary stress and  $(Y\sigma)_s$  is the secondary stress. For simplicity, secondary stresses are ignored in this case. Therefore,

$$Y\sigma = (Y\sigma)_p \quad (3.33)$$

$$(Y\sigma)_p = Mf_w \{k_{tm}M_{km}M_m\sigma_m + k_{tb}M_{kb}M_b[\sigma_b + (k_m - 1)\sigma_m]\} \quad (3.34)$$

There are no welds, no misalignment, and no membrane loading for the semi-elliptical crack in cylindrical bar.

$$M = M_{km} = M_{kb} = f_w = 1 \quad (3.35)$$

It can be proceeded analogously to

This material is reserved for educational use only, not allowed for commercial use.

Forbidden to modify the content, and cite the document when use.

$$M_b = HM_m \quad (3.36)$$

Where:

$$M_m = (M_1 + M_2(a/B)^2 + M_3(a/B)^4) g.f_\theta / \phi \quad (3.37)$$

$$H = H_1 + (H_2 - H_1) \sin^4 \theta \quad (3.38)$$

The stress intensity factor can be determined at the deepest point on the crack front, ( $\phi = \pi/2$ ) and at the end of the crack corner point ( $\phi = 0$ ) as a function of a crack length.

### 3.5 Lightweight Bearing Design Optimization

The ABAQUS commercially available software, Abaqus/CAE, has been integrated into an Isight simulation workflow to achieve an optimized design focusing on both durability and weight performance. Figure 3.17 illustrates the schematic representation of the specific optimization workflow procedure. Initially, a Python script is employed to create a finite element model, subsequently executed in Abaqus/CAE as a pre- and post-processor. The Isight commercial optimization tool is then utilized for parametric design optimization, specifically targeting the inboard bearing wheelset model. The integration of Isight's Sim Code module facilitates the organization of input, output, and execution processes within the program [26]. This module operates by taking a Python script as input, capturing relevant parameters, and modifying the code to extract data from the generated file and output it in TXT format. Additionally, an Abaqus module takes the output file from Sim Code as input, generating an output database file. Optimization objectives aim for optimal values throughout the iteration process.

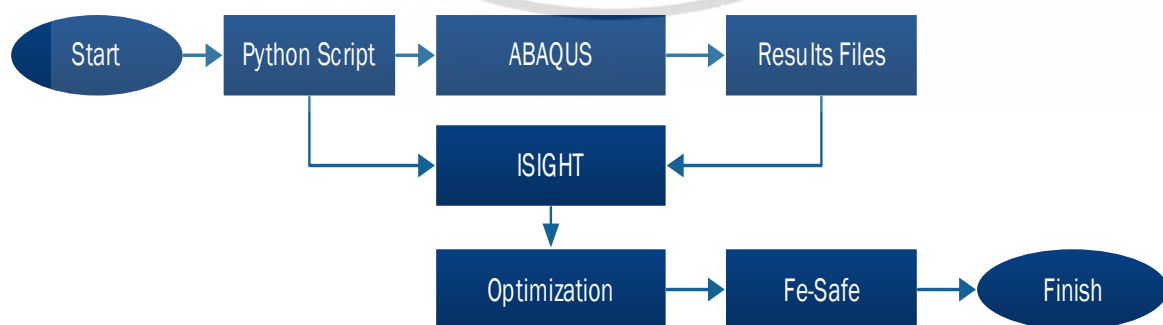


Figure 3.17 Structural analysis and optimization process workflows chart

This material is reserved for educational use only, not allowed for commercial use.

Forbidden to modify the content, and cite the document when use.

### 3.5.1 Multi-Objective Optimization Method

Optimization is applicable across various fields of engineering and science, involving the selection of the most favorable solution from a group of potential candidates based on specific criteria. Design optimization specifically entails the automatic variation of a predetermined set of input design variables using an algorithm to achieve more desirable outputs. These outputs typically represent variations from a target, minimal cost, and/or maximal performance.

To facilitate the automatic variation of design variables, algorithms that explore the design domain are necessary. Additionally, it is crucial to automatically compute the relevant outputs of interest. While the term "optimization" implies seeking the best solution, testing all possible combinations is the only way to ensure that the truly optimal design parameters are identified in a complex space. However, this exhaustive approach is impractical due to the significant time investment. For example, considering a straightforward problem with ten discrete values for five parameters and a five-minute analysis time, analyzing all combinations would require a year.

Optimization algorithms can be categorized into two main types: those relying on gradient methods and those employing non-gradient-based approaches. Initially, gradient-based algorithms were extensively utilized in the early stages of design optimization due to their rapid computational speed and low memory requirements. However, these algorithms face challenges in calculating the derivatives of dynamic responses to design parameters, especially when these derivatives are not easily determinable. Additionally, gradient-based methods prove less effective in handling multi-objective optimization. These drawbacks have constrained the widespread application of gradient-based optimization algorithms.

Non-gradient-based optimization algorithms can be further classified into local search and global search algorithms. Engineering optimization problems often lack derivative and gradient information, making them complex. With advancements in computer performance, global optimization methods have become prominent tools in design optimization, offering innovative approaches to address intricate problems. Among global optimization algorithms, genetic algorithms stand out as frequently employed [10].

This study utilized Pointer Automatic Optimizer for design optimization. Evolutionary Algorithm, based on biological evolutionary mechanisms, has gained popularity due to its synchronization and global search capabilities. MIGA, a modified

This material is reserved for educational use only, not allowed for commercial use.

Forbidden to modify the content, and cite the document when use.

version of parallel distributed genetic algorithms, demonstrates superior global solving capacity and computational efficiency compared to traditional genetic algorithms. MIGA divides populations into evolutionary groups or islands, enhancing global search and convergence capabilities.

Pointer functions as an automated optimization engine overseeing a set of conventional optimization techniques. Currently, it manages four distinct optimization methods: an evolutionary algorithm [11], the downhill simplex method by Nelder and Mead, sequential quadratic programming (SQP), a linear solver, and a TABU method[27]. This assortment of algorithms was chosen because each exhibits strengths and weaknesses in handling various topography features. The amalgamation of these methods in a hybrid form has proven effective in addressing a wide spectrum of design optimization problems. The Pointer Automatic Optimizer allows for the control of one algorithm at a time or all four simultaneously. Throughout the optimization process, the system evaluates the success of each algorithm and identifies optimal internal control parameter settings (such as step sizes, numbers of iterations, restarts, etc.). This decision-making process remains concealed from the user, aiming to empower non-optimization experts to successfully employ these methods.

## CHAPTER 4

# EFFECT OF INTERFERENCE WITH THE PRESS-FITTING OF RAILWAY WHEEL AND AXLE ASSEMBLIES

### 4.1 Overview

#### 4.1.1 Press-Fitting in Railway Axle Assemblies

Press-fitting is a widely adopted method in the assembly of mechanical components, particularly in the railway industry (Figure 4.1). The railway wheel and axle assembly process relies on press-fitting to securely connect these vital components. It is crucial to understand the dynamics of this assembly method as it has a direct impact on the structural integrity, longevity, and reliability of railway vehicles.

Interference fits play a pivotal role in press-fitting, and the success of this assembly process hinges on selecting the right interference values. Too much interference can lead to excessive stress concentrations, which may induce fatigue and potentially lead to catastrophic failure. Conversely, insufficient interference may result in a loose connection, jeopardizing the vehicle's operational safety. As such, the intricacies of interference fits in railway wheel and axle assemblies need to be examined closely.



Figure 4.1 Press-fitting assembly machine

This material is reserved for educational use only, not allowed for commercial use.

Forbidden to modify the content, and cite the document when use.

## 4.2 Numerical Simulation

The foundation of this research is the creation of numerical simulation models to simulate the press-fitting process. These models incorporate material properties, component dimensions, and boundary conditions, aiming to replicate real-world press-fitting scenarios accurately.

In this research, finite element analysis was employed to evaluate the stress distribution and deformation of the press fit interference on the railway wheel and axle. The geometric model of wheel and axle assembly is shown in Figure 4.2. The S1002 wheel profile and hollow axle were used in the analysis. The inside diameter of the axle is 60 mm and the wheel hub diameter is 190 mm. The axle length is 2300 mm and the wheel and axle contact length is 185 mm.

The wheel and axle quarter model were established using the symmetric boundary condition to reduce the running simulation time. A linear elastic material behavior with Young's modulus of 210 GPa and Poisson's ratio of 0.3 [28] is defined for both wheel and axle material properties. A three dimensional (C3D8R) 8-node linear brick (hexahedral), reduced integration, hourglass control was used for the element type (Figure 4.3). The wheel and axle contact area were meshed with a refine meshed until the stress and contact pressure changed lower than 1%. The total number of elements are 31,305 and 36,322, for the wheel and axle, respectively.

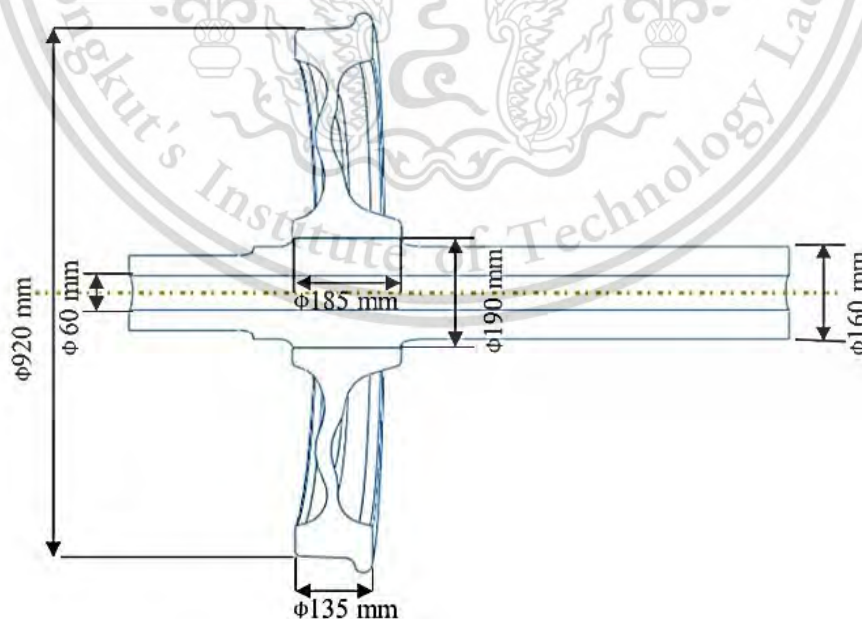


Figure 4.2 Geometry of the wheel and axle assembly

This material is reserved for educational use only, not allowed for commercial use.

Forbidden to modify the content, and cite the document when use.

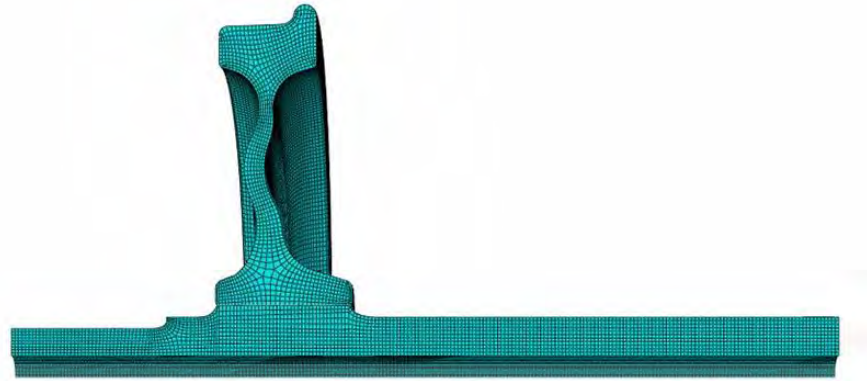
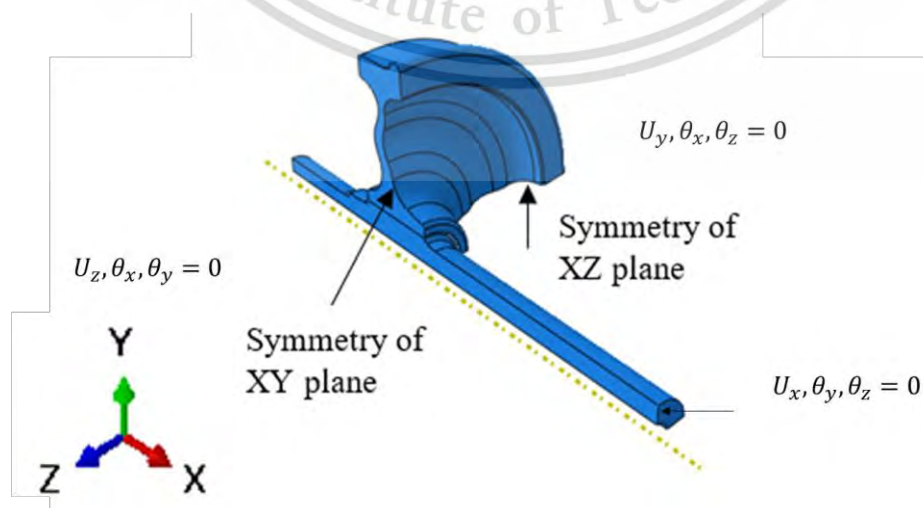


Figure 4.3 Finite Element Mesh of Wheelset

The contact surface interaction between the axle wheel seat and wheel hub was defined using a master-slave contact algorithm: the wheel hub surface was the master surface, and the axle wheel seat surface was the slave. A surface to surface interaction was defined with a finite sliding in the initial step. It is also required to be defined as an initial over-closure at the initial step. In the first step, the interference was resolved by automatic shrink-fit with a gradually removed slave node over closure during the step. A contact interaction property was defined as a penalty and the coefficient of friction was set to 0.6 to ensure tangential behavior. The sliding formulation was selected as “finite sliding” because the installation displacement was large. The flag indicating a non-linear geometry, Nlgeom, in the software, was set ON [29].

Figure 4.4 shows the boundary conditions of the symmetric finite element model: the symmetries of the wheel and axle assemblies used in the finite element analysis are: in the X-Y plane,  $U_z, \theta_x, \theta_y = 0$ , in the X-Z plane,  $U_y, \theta_x, \theta_z = 0$  and at the right end of the axle YZ plane was constrained in longitudinal direction,  $U_x, \theta_y, \theta_z = 0$ .



This material is reserved for educational use only, not allowed for commercial use.

Figure 4.4 Boundary conditions for wheel and axle assembly

Forbidden to modify the content, and cite the document when use.

### 4.2.1 Variations in Interference Fit

The central focus of this work is the investigation of various interference values. The central focus of this work is the investigation of various interference values. The range of interference fit clearances considered in the research represents a spectrum of conditions relevant to railway axle assembly. By varying the interference values, the study aims to offer a comprehensive analysis of the impact of interference on stress distribution, deformation, and, by extension, the structural soundness of these assemblies. The selected interference values are rooted in their significance to the railway industry and their potential effects on assembly integrity. To comprehensively address the research objectives, interference fit values ranging from 190  $\mu\text{m}$  to 345  $\mu\text{m}$  were considered. This wide range was chosen to represent practical scenarios and assess the full spectrum of interference effects.

### 4.3 Discussion

The discussion section delves into the pivotal balance between achieving a tight interference fit to enhance strength and mitigating the risk of stress concentrations. It further explores the practical implications of interference values in a real-world context.

This balance is exemplified by the various interference clearances studied, ranging from 190  $\mu\text{m}$  to 345  $\mu\text{m}$ , as derived from using EN 13261 standard. By comparing analytical results and finite element analysis outcomes, this section seeks to determine the reliability and accuracy of the finite element analysis method.

**Table 4.1.** Contact pressure and maximum deformations along the radial direction for various interferences by finite element method (FEM) and Lamé's theory.

Interference ( $\mu\text{m}$ )	Contact Pressure (MPa)		Relative Error %	Wheel Deformation ( $\mu\text{m}$ )		Axle Deformation ( $\mu\text{m}$ )	
	Lamé's Theory	FEM		Lamé's Theory	FEM	Lamé's Theory	FEM
200	95.7	107	11.08%	60.1	68.2	-30.3	-31.7
240	115	127	10.43%	72.1	77.3	-36	-38.1
280	134	132	1.64 %	84.2	85.7	-42	-38.1
320	153	168	9.8%	96.2	103	-48	-50.8

Table 4.1 offers a concise summary of the relative error in contact pressure for the different interference values, comparing results from finite element analysis and Lamé's theory. Additionally, it presents a comparison of the maximum deformations of the wheel and axle between modeling and theory. The striking observation is that as interference values increase, the deformations of both the wheel and axle intensify, indicating a direct correlation between interference levels and deformation.

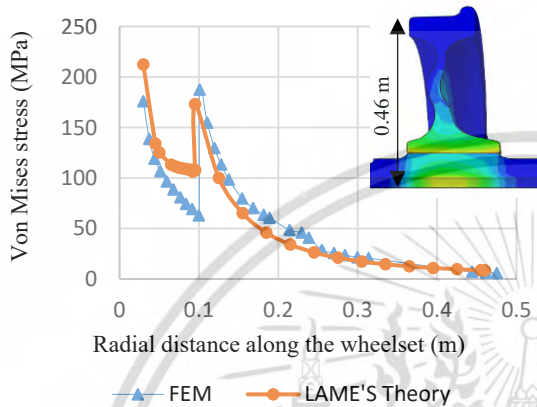


Figure 4.5 Von Mises stress along the centre of the wheelset radial axis.

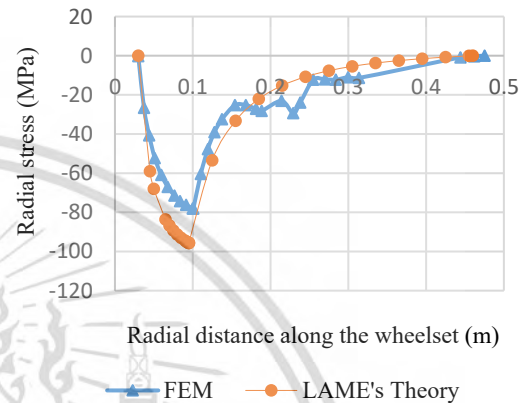


Figure 4.6 Radial stress distribution along the centre of the wheelset radial axis.

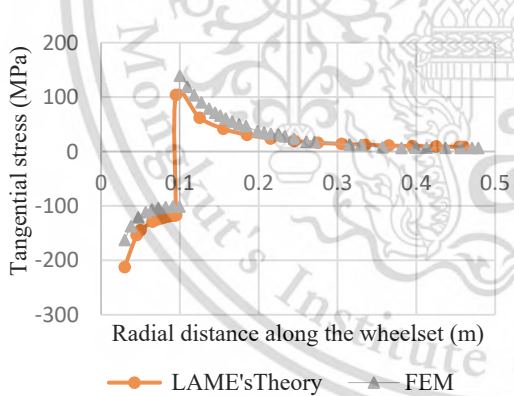


Figure 4.7 Tangential stress distribution along the centre of the wheelset radial axis.

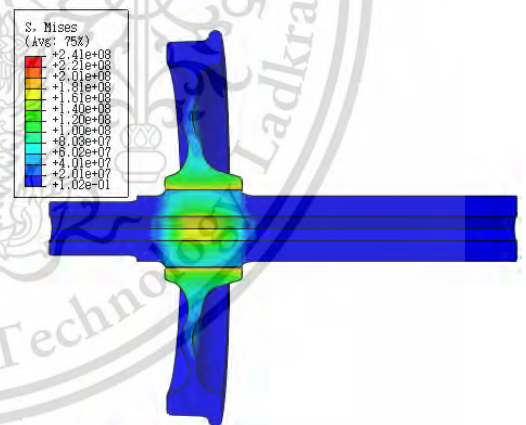


Figure 4.8 Von Mises stress distribution along the centre of the wheelset radial axis.

Figures 4.6 to 4.7 provide a visual representation of the Von Mises stress, radial and tangential distribution along the radial axis of the wheelset, comparing finite element and analytical results. It is evident that the Von Mises stress values closely correspond between the two methods. However, the finite element analysis identifies the maximum Von Mises stress at the wheel hub's inner surface, while the analytical results identify it at the axle's hollow inner surface.

This material is reserved for educational use only, not allowed for commercial use.

Forbidden to modify the content, and cite the document when use.

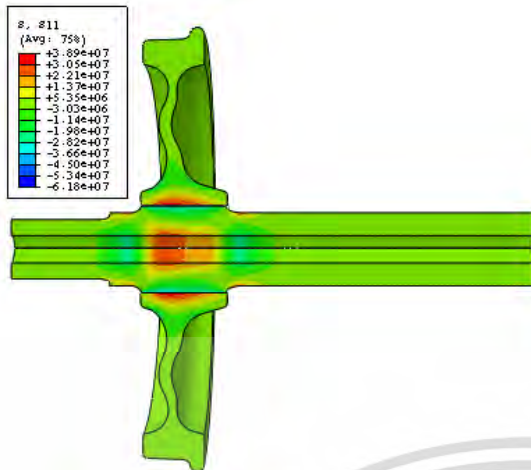


Figure 4.9 Axial stress distribution for wheel and axle assembly along the radial axis.

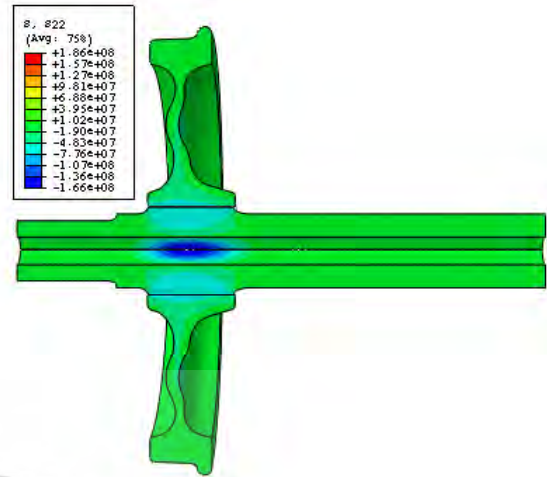


Figure 4.10 Radial stress distribution for wheel and axle assembly along the radial axis.

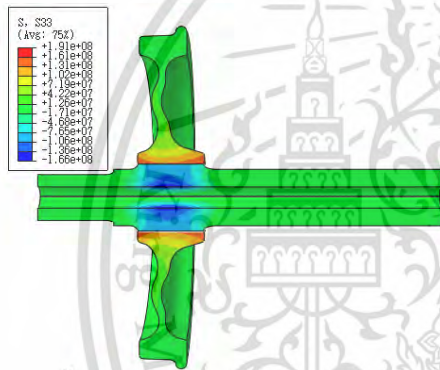


Figure 4.11 Tangential stress distribution for wheel and axle assembly along the radial axis.

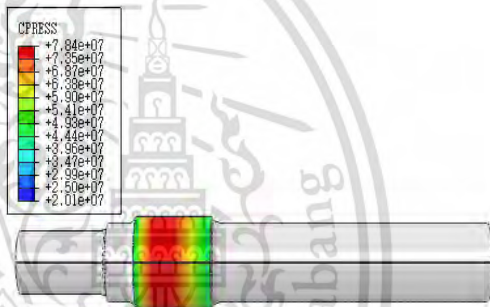


Figure 4.12 Contact pressure at axle wheel seat.

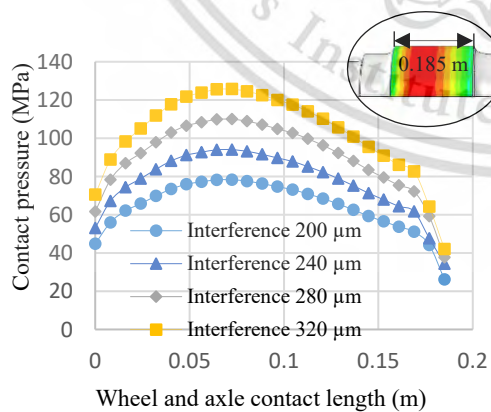


Figure 4.13 Contact pressure distribution along the contact length vs interference clearance.

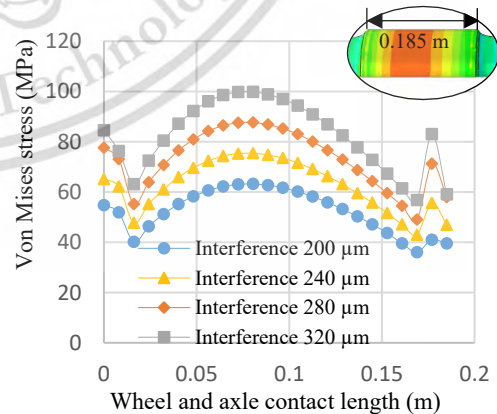


Figure 4.14 Von Mises stress distribution along the contact length vs interference clearance.

This material is reserved for educational use only, not allowed for commercial use.

Forbidden to modify the content, and cite the document when use.

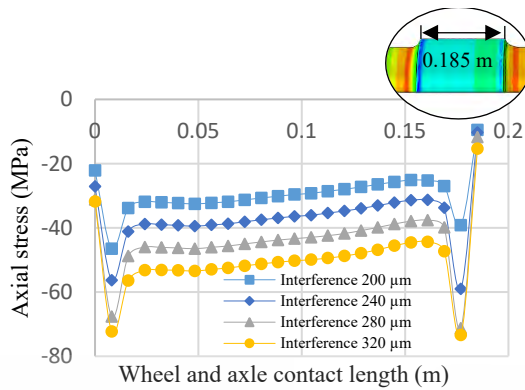


Figure 4.15 Axial stress distribution along the contact length vs interference clearance.

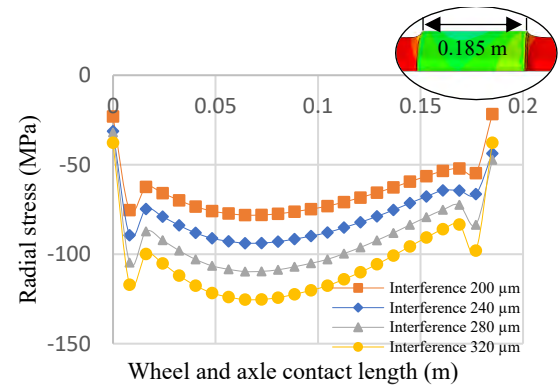


Figure 4.16 Radial stress distribution along the contact length vs interference clearance.

Figures 4.9 to 4.12 illustrate the Von Mises, radial, axial, and tangential stress distribution of the wheelset. These figures offer a comprehensive visual representation of how the interference values influence the distribution of stresses. The variations in contact pressure along the axle wheel seat length with changing interference values are shown in Figure 4.13. This visual representation indicates that increased interference values lead to higher contact pressure, maintaining the same mesh size. Notably, the distribution of contact pressure differs between finite element analysis and Lamé's theory, highlighting the complexities associated with interference fit. In Figure 4.14 to 4.17 the contact pressure, Von Mises, axial and radial stress distribution along the axle wheel seat is compared against interference values. These visual representations underscore the significant impacts of interference clearances on axial, radial, and Von Mises stresses.

The conclusion of this section emphasizes that the choice of interference fit values significantly affects the structural integrity and operational performance of railway wheel and axle assemblies. This research offers critical insights, suggesting that accounting for the press fit effect in railway axle design is vital for ensuring the long-term reliability of these components.

The interpretation of the findings is essential to extract meaning and implications. Understanding the implications of stress distribution patterns is pivotal to grasp how interference influences assembly integrity.

This section of the chapter critically examines the outcomes, shedding light on how different interference values affect the structural soundness of railway wheel and axle

assemblies. It underscores the intricate balance between the selected interference value and its effects on stress distribution.

## 4.4 Conclusions

### 4.4.1 Summary of Key Findings

The summary of key findings underscores the importance of the research and its implications for railway axle assembly practices. It recaps the most substantial results to serve as a reference point for future railway component assembly and design.

**Finite Element Method (FEM) vs. Lamé's Theory:** The study compared the FEM model with Lamé's theory for the analysis of wheel and axle press fitting. Results showed that the FEM model aligned well with the theory, with a maximum relative error of 11.08% and a minimum of 1.64%. This suggests that the results obtained are considered acceptable. However, the FEM method proved to be more accurate and comprehensive than Lamé's theory.

**Stress Distribution:** Critical stress points were identified at the contacting surfaces of the wheel hub. Among the three principal stresses, tangential stress emerged as the greatest contributor. Stress distribution was highly influenced by the level of interference in the press fitting.

**Deformation:** Deformation during press fitting, particularly along the radial axis, was adversely affected and strongly dependent on the contact pressure at the wheel and axle interface. Findings indicated that increasing interference led to more significant deformation, emphasizing the importance of selecting interference values carefully during railway axle design.

**Press Fit Impact:** The research underscores that the press fit assembly method has a substantial impact on the lifetime of wheelset components. It is crucial to consider the press fit effect when designing railway axles, as even slight variations in interference values can result in significant changes in stress distribution and deformation, which directly affect the structural integrity of the assemblies.

This material is reserved for educational use only, not allowed for commercial use.

Forbidden to modify the content, and cite the document when use.

#### *4.4.2 Achieving Optimal Interference Fit*

To conclude, this section reiterates the importance of achieving an optimal interference fit in railway wheel and axle assemblies. The research findings guide discussions on selecting the right interference values, striking a balance between structural robustness and the risk of stress concentration. This section serves as a practical reference for engineers and manufacturers, providing valuable guidance for maintaining the safety and reliability of railway axle assemblies.

In summary, this chapter offers a comprehensive understanding of the effects of interference in the press-fitting of railway wheel and axle assemblies. It not only presents the findings but also delves into the implications and practical applications of these findings in the railway industry.

#### *4.4.3 Practical Implications*

The results of this research are discussed in the context of real-world railway axle assembly procedures. This section provides practical insights for engineers and manufacturers, aiding them in making informed decisions regarding interference fit in railway assemblies. Considerations for balancing the advantages of tight interference for strength with the risk of stress concentrations are explored.

# CHAPTER 5

## RAILWAY AXLE AND WHEEL ASSEMBLY PRESS-FITTING

### FORCE CHARACTERISTICS AND HOLDING TORQUE

### CAPACITY

#### 5.1 Overview

##### 5.1.1 Press-Fitting in Railway Axle and Wheel Assemblies

Press-fitting is a critical process in the assembly of railway wheelsets, involving the precise fitting of wheels onto axles. This technique is vital for ensuring the safety and operational reliability of railway vehicles. Press-fitting offers a reliable and efficient means of assembly, which avoids the need for heat treatments, and is commonly used in industry.

The quality of the press-fitting assembly has a direct impact on the integrity and performance of railway wheel and axle assemblies. Failures or suboptimal press-fitting can lead to accidents, derailments, and significant safety concerns. Understanding the characteristics of press-fitting, including the force required and its relationship with interference and friction, is crucial for the railway industry.

#### 5.2 Numerical Simulation

##### 5.2.1 Materials

Following the EN standard, the EA1N and EA4T steel grades are widely used for railway axles. The chemical composition and mechanical characteristics of EA4T steel are in Tables 5.1 and 5.2. The materials of the wheel and axle were the same, homogeneous, and isotropic, with ideal elastic-plastic behaviour. The stress versus plastic strain graph for EA4T steel is shown in Figure 5.1.

Table 5.1. Press-fitting curve for a railway wheelset: force vs axial displacement [13].

Grade	C	Mn	Si	S	P	Cr	Cu	Ni	Mo	V
EA4T	0.29	0.8	0.4	0.015	0.02	1.2	0.3	0.3	0.3	0.06

This material is reserved for educational use only, not allowed for commercial use.

Forbidden to modify the content, and cite the document when use.

Table 5.2 Press-fitting curve for a railway wheelset: force vs axial displacement [13].

Material 1	Young's Modulus (GPa)	Poisson Ratio	Ultimate Tensile Strength (MPa)	Yield Strength (MPa)	Elongation n (%)	Absorbed Energy
EA4T	206	0.3	650–800	≥420	≥24	≥30

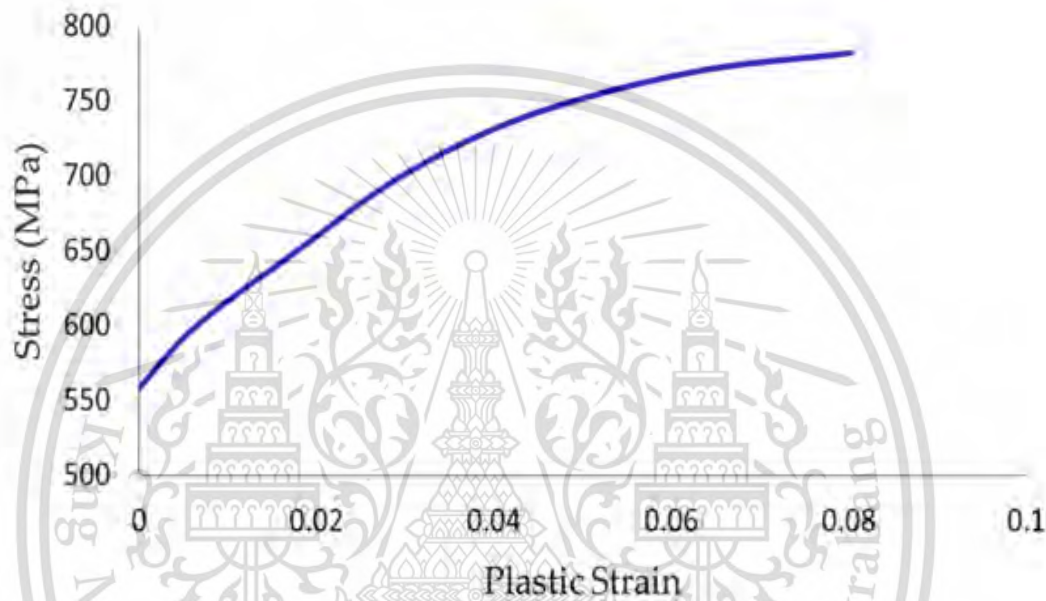


Figure 5.1 Stress-plastic strain curve for EA4T steel.

### 5.2.2 Modelling and Simulation of Press-Fitting

To determine the press-fitting force, a quarter 3D model of the wheel and axle assembly, their dimensions given in Figure 5.2, was made using Abaqus FEA (Figure 5.3). During assembly, the wheel was moved onto the axle wheel seat by a specialized assembly machine so that interference between the assembly was eliminated for the outer diameter of the axle wheel seat, which was larger than the inner diameter. A static structure was analysed, and the boundary conditions were used in the finite element analysis. Taking advantage of the symmetric boundary conditions, the XY and XZ planes were constrained in the finite element model. The end of the axle was fixed, and an axial displacement, 180 mm, was applied to the wheel hub towards the axle wheel seat. A contact pair was defined between the wheel- and axle-contacting surfaces. This analysis determined the press-fitting force and stress distribution at the contact surface between the wheel and axle. A 2 mm mesh was used for the contact surface of the wheelset, and a 10 mm mesh was used for the other surfaces (see

This material is reserved for educational use only, not allowed for commercial use.

Forbidden to modify the content, and cite the document when use.

Figure 5.4). The mesh type was a 20-node quadratic brick, reduced integration (C3D20R); 17,402 elements were used for the axle model, and 51,858 elements were used for the wheel model.

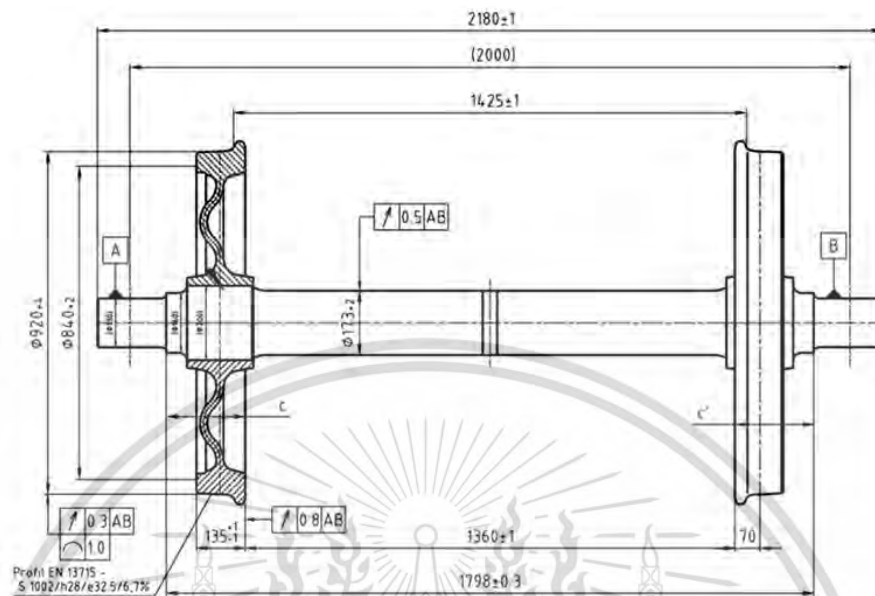


Figure 5.2 Dimensions of the wheelset [17].

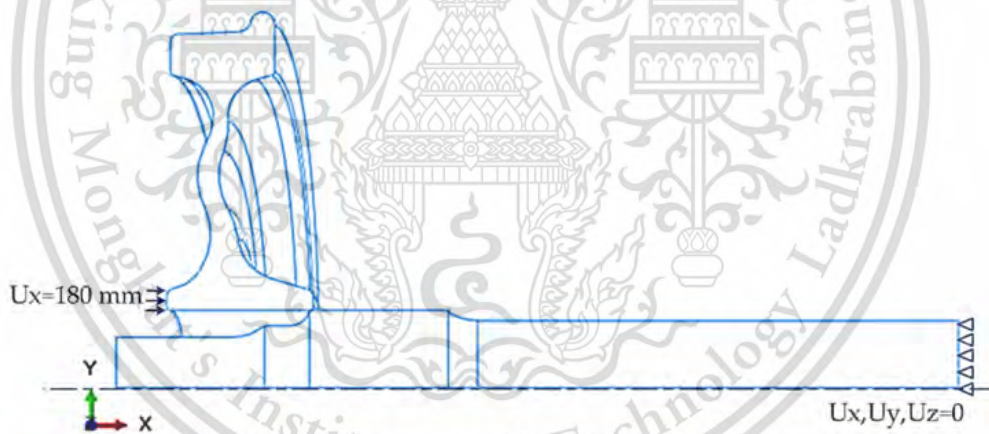


Figure 5.3 Boundary conditions.

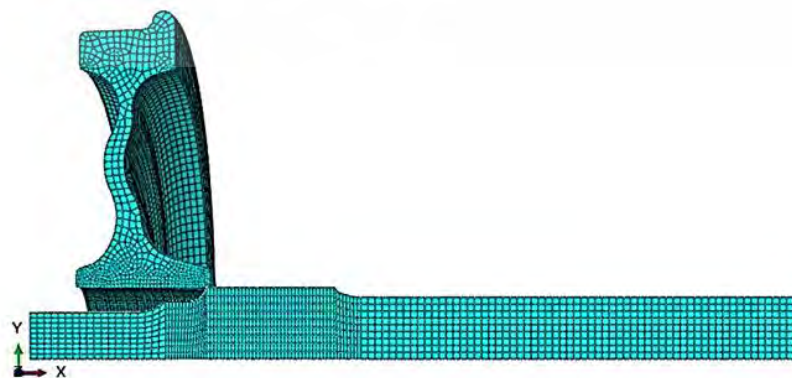


Figure 5.4 Mesh used by the finite element model.

### 5.2.3 Finite Element Analysis of the Holding Torque Capacity

Finite element analysis was used to examine the effect of the interference on the holding torque capacity for the wheel and axle assembly. The geometry of the 3D models and materials properties were similar to those for the press-fitting finite element analysis. During this analysis, surface-to-surface contact interaction was set between the wheel and axle interface with a contact interference fit option. A penalty frictional coefficient, 0.1, and hard contact were set as the contact properties. It was necessary to define the reference points on the axle at both end sides of the centre point and coupling to the surface that defined the coupling nodes. To obtain more accurate results, a refined mesh was used at the contact area with a coarse mesh for the other areas. The torque loading was applied to the reference node at the end of the axle, and the outer surface of the wheel was fixed (Figure 5.5). The value of the applied torque was increased until rotation or ‘slip’ occurred in the interface.

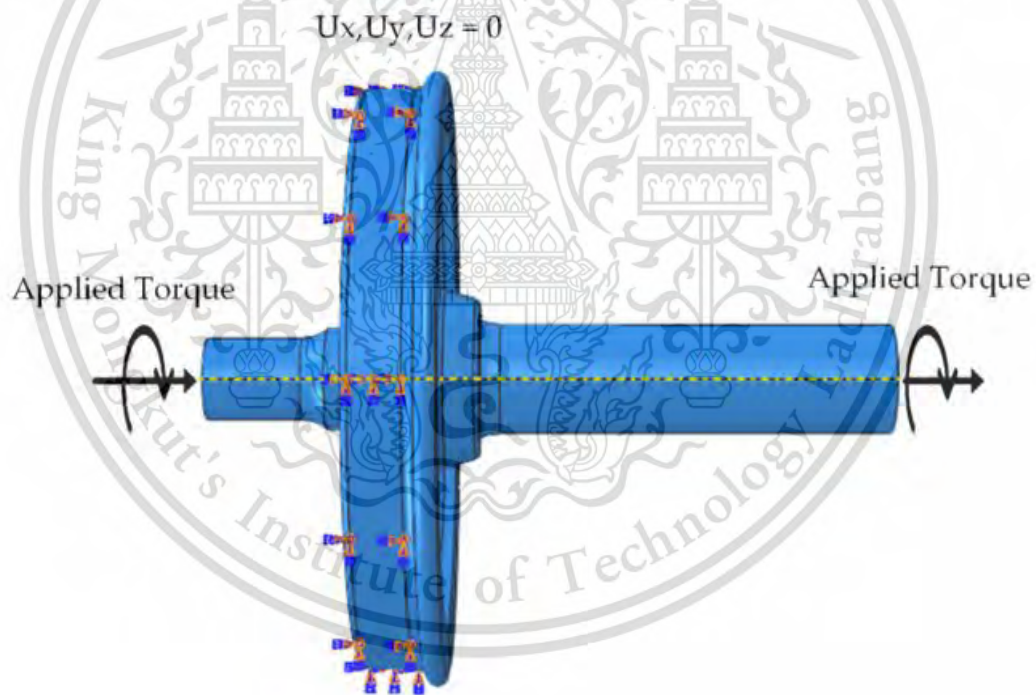


Figure 5.5 Loading and boundary conditions for the torque analysis.

## 5.3 Discussion

### 5.3.1 Comparison between the FEA and Theoretical Results

To verify the effectiveness of the numeric model, the finite element results were compared with the calculated theoretical results. The contact pressure between the wheel and axle wheel seat at different sections was determined from Equation (3.6), and the average

This material is reserved for educational use only, not allowed for commercial use.

Forbidden to modify the content, and cite the document when use.

contact pressure was calculated by Equation (3.7). In accordance with Lamé's theory, the contact pressure distribution on a wheel is influenced by its geometry, particularly the variation in radius along its circumference. As per this theory, the maximum contact pressure occurs at the middle section of the wheel, primarily due to the central position of the largest radius. The rationale behind this phenomenon lies in the geometric configuration of the wheel: the central region corresponds to the point of maximum radius, thus resulting in a higher contact pressure. Conversely, the contact pressure decreases towards the other sections of the wheel due to the diminishing radii compared to the center.

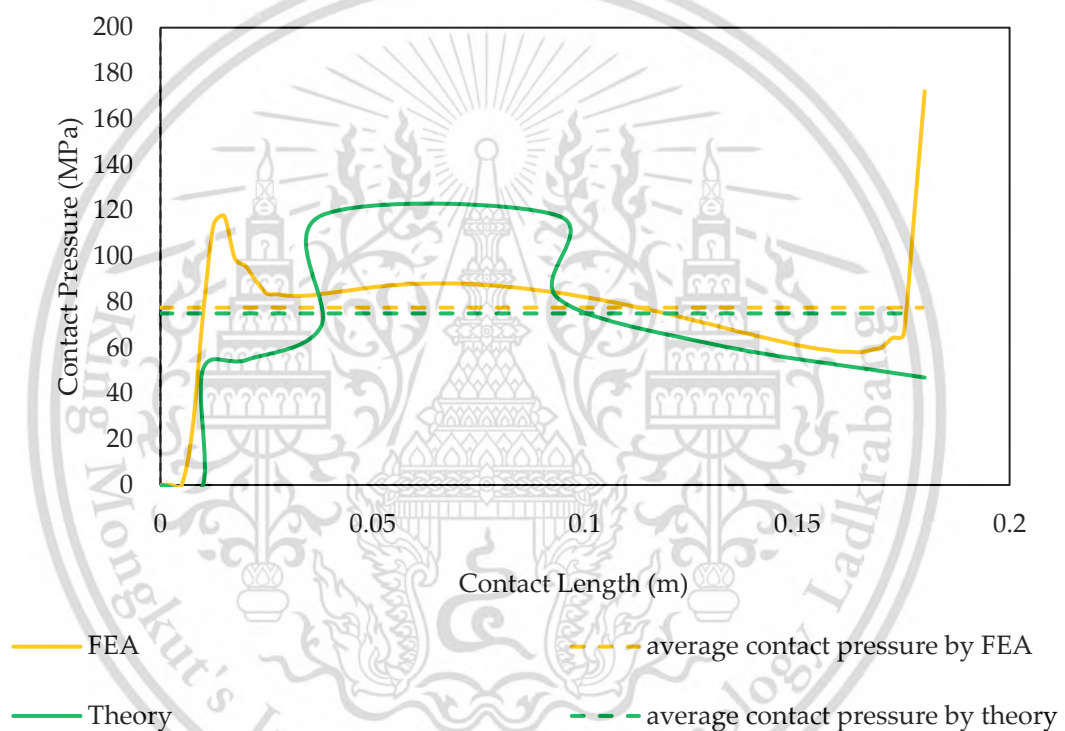


Figure 5.6 Contact pressure distribution along the contact length.

According to the FE analysis results, the contact pressure of the axle reached its maximum at the end of the contact edge. The distribution of the contact pressure and average contact pressure along the contact length of the wheelset is shown in Figure 5.6. The finite element analyses led to higher average contact pressure than the theoretical model because the volume of the 3D model used in the finite element simulation was greater than that of the theoretical model: the finite element results were 3% greater than the theoretical ones. At the start of the wheelset assembly, the two parts did not contact each other because of the taper of the axle. Therefore, the press-fitting force and contact pressure were zero until the end of the taper was reached, and then they suddenly increased. The theory showed

that the contact pressure was directly proportional to the outer radius or profile of the wheel and increased in the centre of the contact region. The contact pressure of the axle increased sharply at the start of the contact and decreased towards the centre of the contact length and maximum at the rear end of the edge. The press-fitting force was calculated from the contact length using Equation (3.9). Figure 5.7 compares the finite element and theoretical results. The maximum press-fitting force at the end of the assembly was 877 kN from the finite element analysis and 822 kN from the theory, when the interference was 240  $\mu\text{m}$ . The 7% difference between the results was considered acceptable.

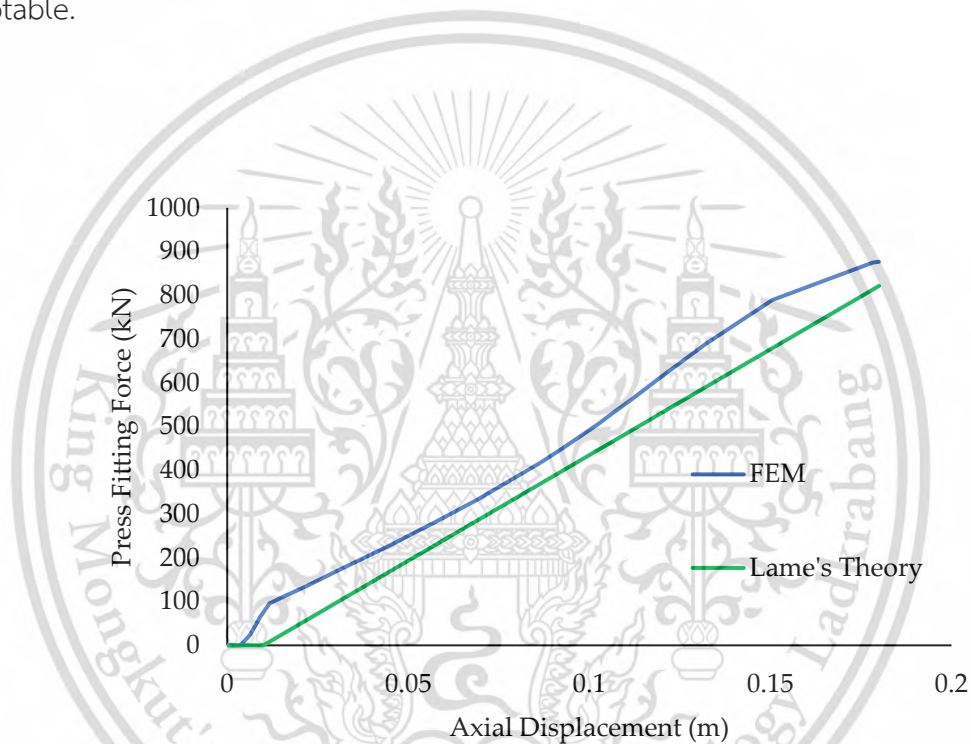


Figure 5.7 Press-fitting curves obtained from the finite element model (FEM) and Lame's theory (straight green line).

### 5.3.2 Effect of the Interference and Friction Coefficient on Press-Fitting Curves

The interference was a significant factor that affected the press-fitting curve. Simulations used interferences from 160 to 400  $\mu\text{m}$ . The curves are shown in Figure 5.8. The press-fitting force increased, as expected, with the interference. The boundary of the press-fitting curve was obtained from the EN 13260 standard. The press-fitting curves were used for monitoring the assembly and evaluating its quality. The curves for interferences of 160, 360, and 400  $\mu\text{m}$  did not qualify because they were outside the EN 13260 boundary. One key conclusion from the simulations was that the interferences, specified by the EN standard, fell within the boundary. When the interference increased by 20%, the maximum press-fitting

This material is reserved for educational use only, not allowed for commercial use.

Forbidden to modify the content, and cite the document when use.

force increased by 12% (Figure 5.9). Figure 5.10 shows the press-fitting forces and axial displacements from various friction coefficients obtained from the simulations. Friction coefficients in the range 0.08–0.13 were the only ones acceptable, i.e., led to forces within the boundary shown in Figure 5.10. Thus, it may be observed that the friction coefficient affected the press-fitting force during the assembly. In general, the greater the friction coefficient, the greater the maximum press-fitting force. Every 0.01 increment in the friction coefficient increased the maximum press-fitting force by 14% (Figure 5.11).

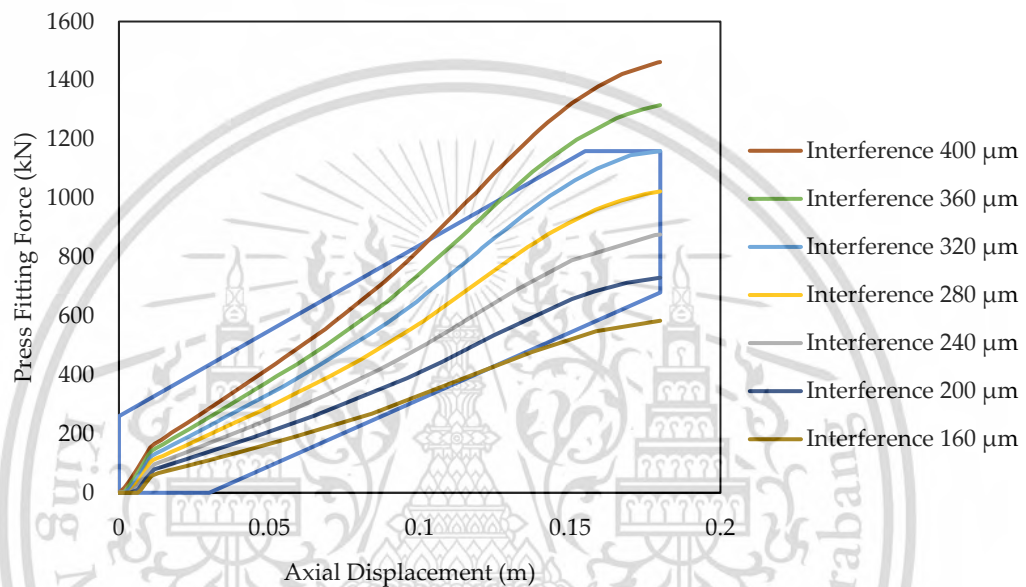


Figure 5.8 Press-fitting curves vs interference derived from the finite element simulations.

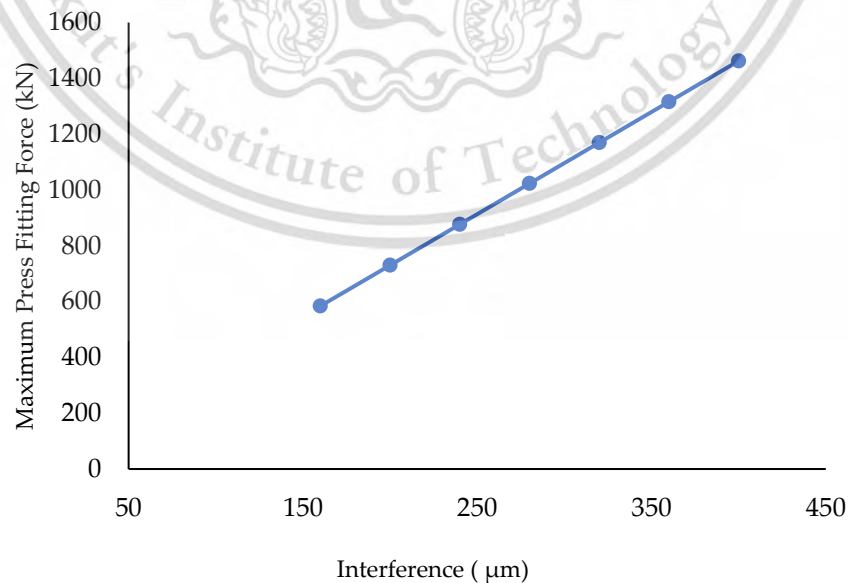


Figure 5.9 Maximum press-fitting force vs interference.

This material is reserved for educational use only, not allowed for commercial use.

Forbidden to modify the content, and cite the document when use.

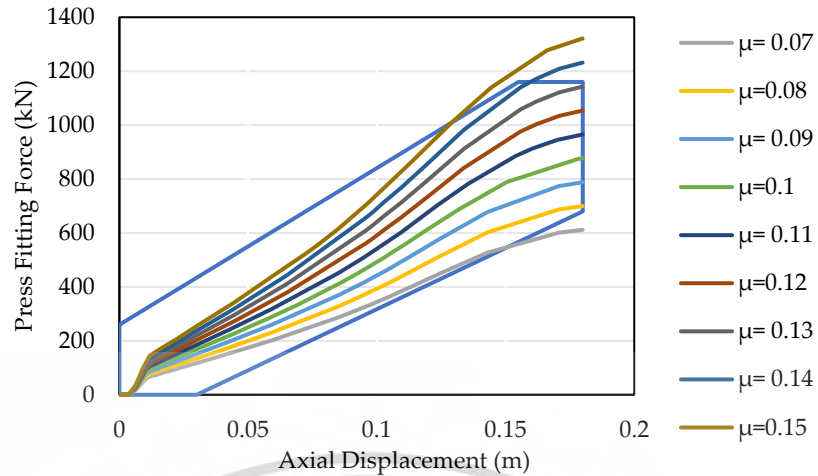


Figure 5.10 Press-fitting curves with friction coefficient as a parameter.

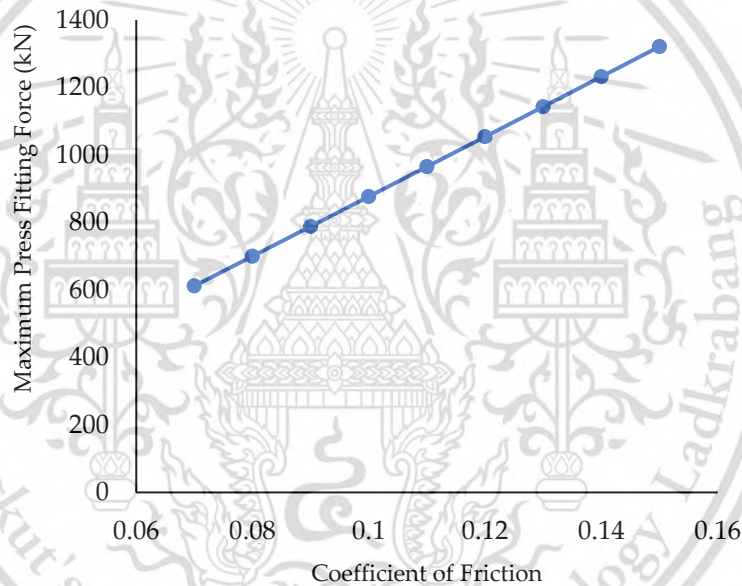


Figure 5.11 Maximum press-fitting force vs coefficient of friction.

### 5.3.3 Contact Strength Analysis

The simulations showed that the maximum von Mises stress took place at the wheel, in contact with the axle wheel seat taper area, in the first simulation time step. The changing of the value and location of the maximum von Mises stress versus the axial displacement and time increment is shown in Figure 5.12. The von Mises stress was distributed symmetrically on both sides of the wheelset; the maximum stress occurred at the wheel hub bore after assembly. For the axle, the peak stress occurred at the start of the axle wheel seat at the end of the taper area. The maximum stress concentration was localized at the edge of the wheel

hub because pressing the wheel to the axle induced critical stress due to the edge effect and abrupt transition in press-fitting. It can be minimized by some geometric characteristics, friction coefficient, contact pressure, and operation conditions. The maximum von Mises stress of the wheelset as a function of interference is shown in Figure 15.13. The simulations revealed that the interference value significantly affected the stress concentration.

To understand the effect of the interference on the deformation, note that for low values of the interference, up to 360  $\mu\text{m}$ , deformations in the assembly remained in the elastic range. However, for sufficiently large interferences, 380  $\mu\text{m}$  or more, elastoplastic deformation occurred in the wheel. Elastic plastic deformation began at the edge of the wheel hub bore first (Figure 5.14).

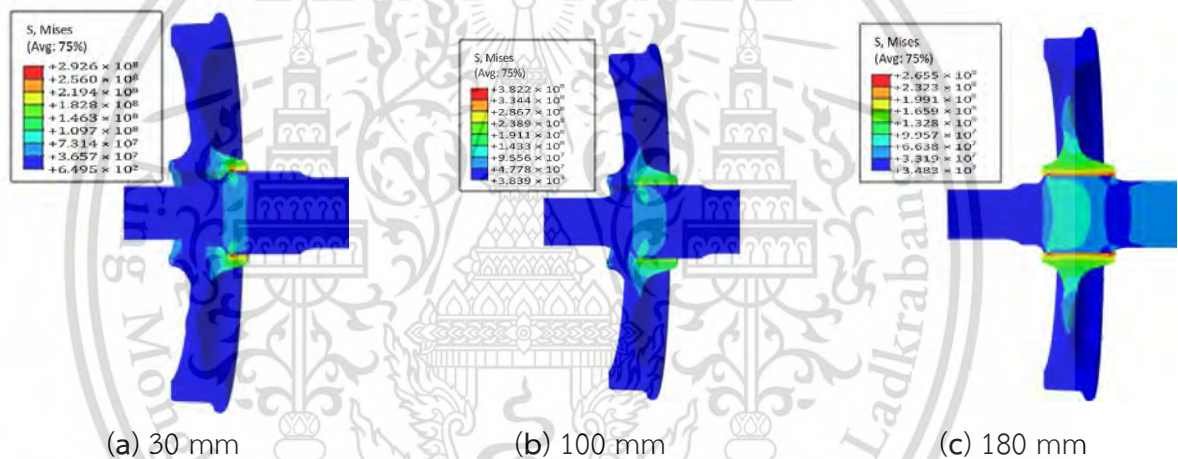
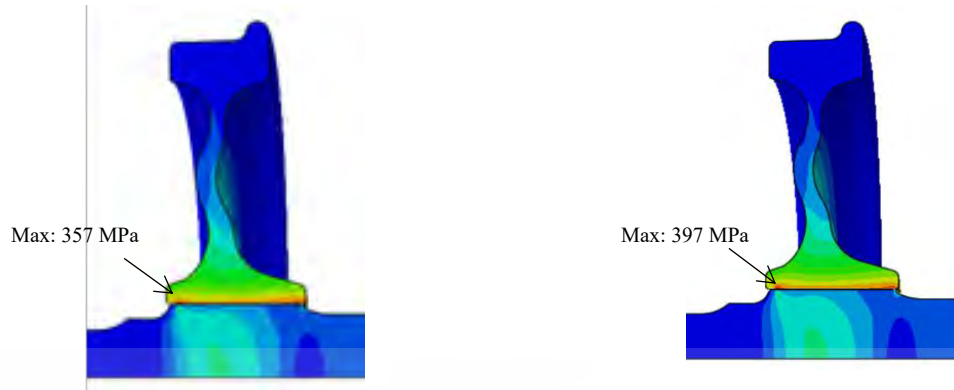


Figure 5.12 Von Mises stress distribution during simulation (a) axial displacement of 30 mm, (b) axial displacement of 100 mm, and (c) axial displacement of 180 mm.



(a) von Mises stress distribution for  $\delta$  240  $\mu\text{m}$ . (b) von Mises stress distribution for  $\delta$  280  $\mu\text{m}$ .



(c) von Mises stress distribution for  $\delta$  320  $\mu\text{m}$ . (d) von Mises stress distribution for  $\delta$  360  $\mu\text{m}$ .

Figure 5.13 Von Mises stress of the wheel and axle due to radial interference (MPa).

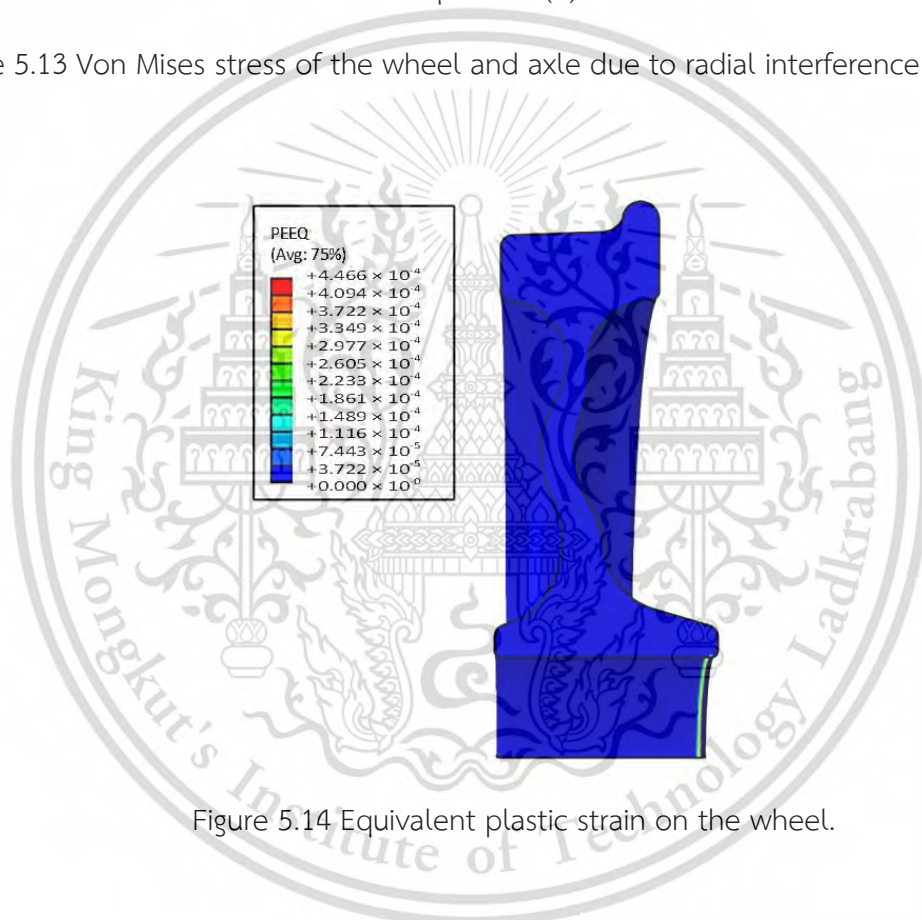


Figure 5.14 Equivalent plastic strain on the wheel.

### 5.3.4 Holding Torque Behavior

The discussion provides insights into the behavior of holding torque capacity under varying interferences. It elucidates the concept of plastic deformation and its implications for the assembly's ability to withstand operational torsional forces. The maximum holding torque capacities were 71 kNm for the interference of 200  $\mu\text{m}$ , 85 kNm for 240  $\mu\text{m}$ , 99 kNm for 280  $\mu\text{m}$ , and 113 kNm for 320  $\mu\text{m}$  (Figure 5.15). Clearly, the holding torque capacity increased with the interference.

This material is reserved for educational use only, not allowed for commercial use.

Forbidden to modify the content, and cite the document when use.

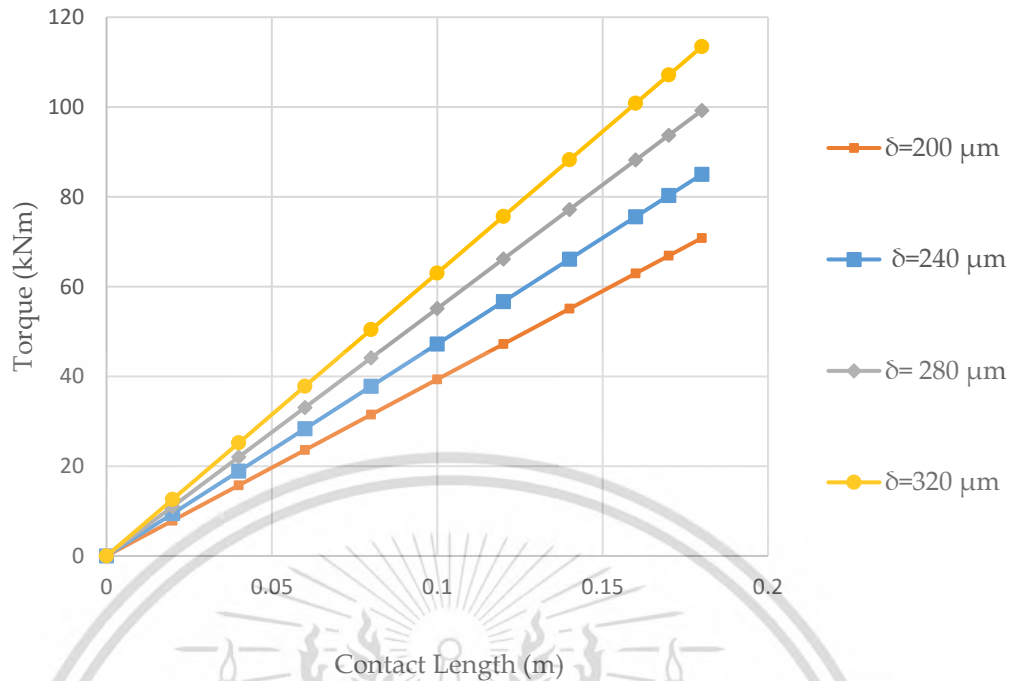


Figure 5.15 Holding torque capacity vs contact length.

The torque capacity analysis simulated the wheel and axle assemblies to obtain the curves of the torque and rotational angle, which determined the maximum holding torque capacity for different interference values. The torque and rotational angle curves were needed to decide the torque required to resist the slip between the interference assemblies. In Figure 5.16,  $T_E$  was the maximum elastic torque, and yielding started at that point. Within the elastic torque region, the shear stress in the axle varied linearly, and the axle showed only elastic deformation. When the torque increased to the plastic region,  $T_p$ , the axle rotated continuously with no further increase in the torque. The maximum elastic torque was equal to 75% of the maximum holding torque capacity at the fully plastic region [22,23]. Therefore, it was evident that the maximum holding torque capacity or plastic torque,  $T_p$ , before slipping was 75 kNm at the twist angle 0.15 rad, and the maximum elastic torque  $T_E$  was 56 kNm at the twist angle 0.029 rad for the interference of 240  $\mu\text{m}$ .  $T_E$  did not exceed the 75% of  $T_p$  for 240  $\mu\text{m}$ , and others were also less than 75% of the maximum holding torque capacity. When the torque increased beyond the maximum holding torque capacity, the axle started slipping. The curves for the torque capacity simulated with different interferences are shown in Figure 5.17. Table 5.3 compares the maximum holding torque capacity with theoretical and finite element results. The deviations between the estimated maximum holding torque capacities from the theory and finite element analyses were 15% for 200  $\mu\text{m}$  interference, 12% for 240

This material is reserved for educational use only, not allowed for commercial use.

Forbidden to modify the content, and cite the document when use.

$\mu\text{m}$ , 8% for 280  $\mu\text{m}$ , and 6% for 320  $\mu\text{m}$ . Thus, the finite element results agreed with the theory.

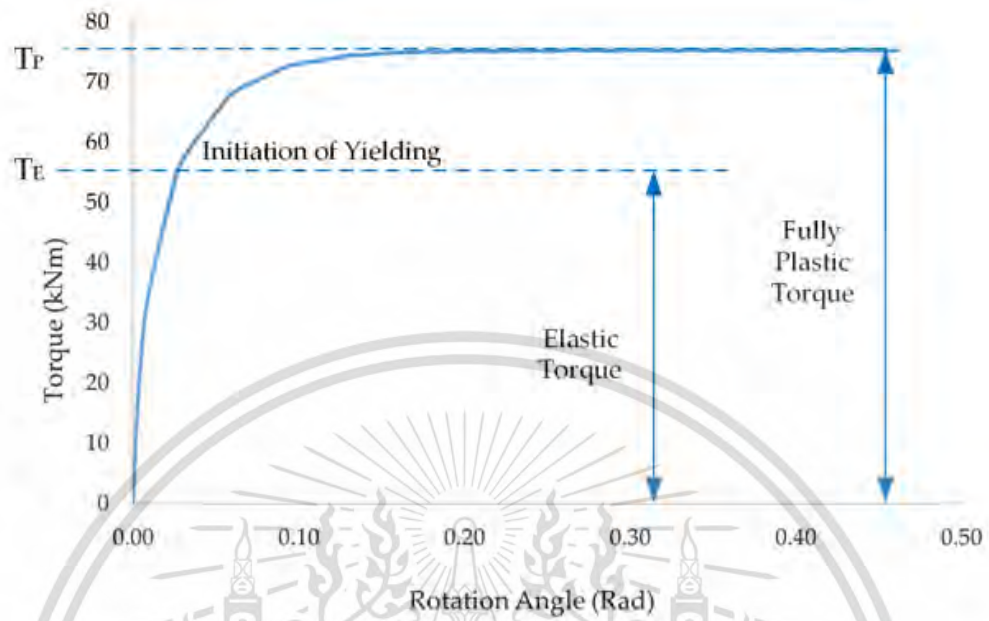


Figure 5.16 Torque vs. the rotation angle for 240  $\mu\text{m}$  interference.

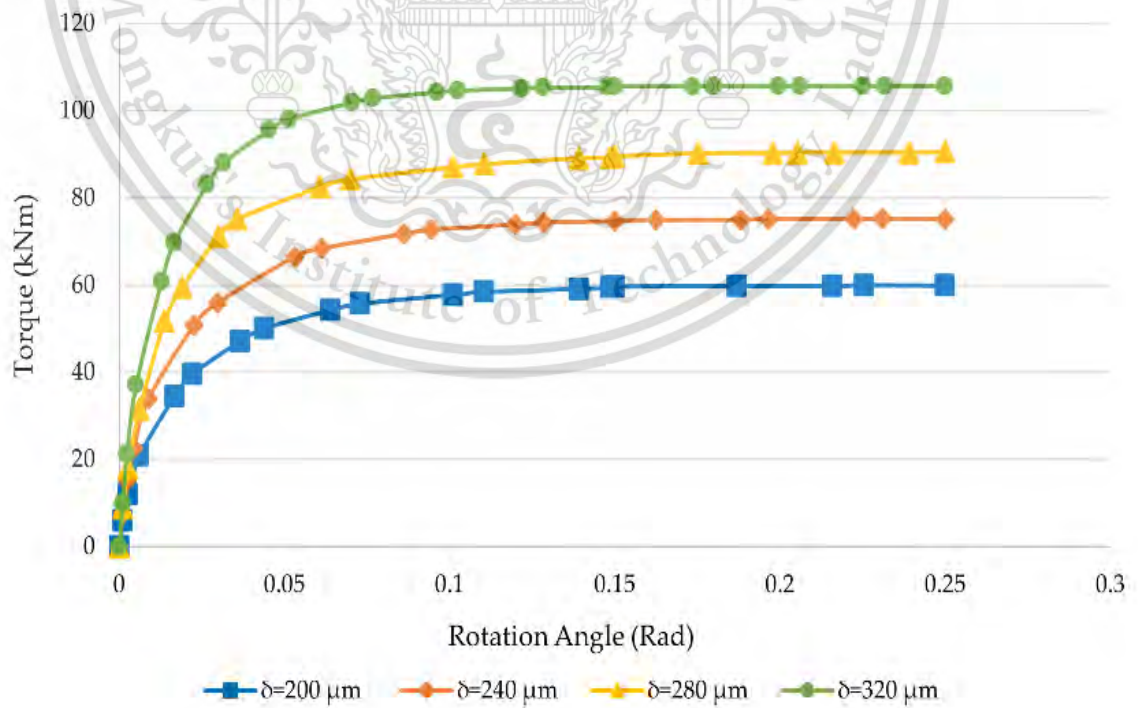


Figure 5.17 Torque vs rotation angle for four interferences.

This material is reserved for educational use only, not allowed for commercial use.

Forbidden to modify the content, and cite the document when use.

Table 5.3 Maximum holding torque capacity—theory and finite element versus interference.

Interference ( $\mu\text{m}$ )	Maximum Holding Torque Capacity		
	Theory (Equation (5)) (kNm)	Finite Element Method (kNm)	Percent Deviation (%)
200	71	60	15
240	85	75	12
280	99	91	8
320	113	106	6

Percent Deviation was calculated as  
Percent Deviation =  $[(\text{Theory}-\text{FEM})/\text{Theory}]*100\%$

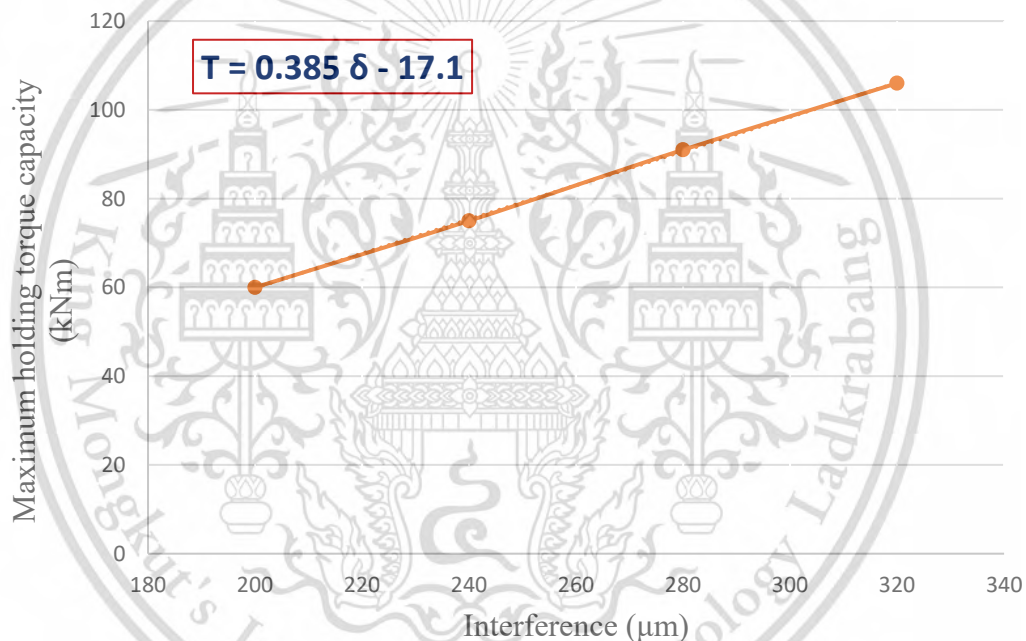


Figure 5.18 The relation between the interferences and maximum holding torque capacity

As illustrated in Figure 5.18, an increase in interference correlates with a general augmentation in the maximum holding torque capacity. However, exceeding the maximum holding torque capacity results in axle slipping. The observed relationship between interference and holding torque capacity exhibits a evident trend, providing an opportunity for design optimization. This relationship is succinctly captured by the equation:

maximum holding torque capacity ( $T$ ) =  $0.385 * \text{interference } (\delta) - 17.1$ ,  
which can be effectively utilized in the assembly process for optimal outcomes.

This material is reserved for educational use only, not allowed for commercial use.

Forbidden to modify the content, and cite the document when use.

## 5.4 Conclusions

The conclusion section summarizes the key findings of the research and their implications for the railway industry. It also provides recommendations and applications derived from the study.

### 5.4.1 Summary of Key Findings

The research has yielded valuable insights into the press-fitting force characteristics and holding torque capacity of railway axle and wheel assemblies. Key findings include the relationship between interference and press-fitting forces, the influence of friction coefficients, and the importance of complying with the EN 13260 standard. Additionally, the behavior of holding torque capacity, particularly the transition from elastic to plastic deformation, has been explored.

**Interference and Press-Fitting Force:** A key discovery was the direct correlation between the interference, the gap between the wheel hub and axle, and the press-fitting force. As the interference increased, the press-fitting force also exhibited a proportional rise. This relationship is crucial for understanding how variations in interference affect the assembly process. It was found that for interferences below 360  $\mu\text{m}$ , the assembly remained in the elastic range, with no plastic deformation.

**Friction Coefficient Influence:** Another significant finding was the impact of the friction coefficient on the press-fitting force. The research revealed that as the friction coefficient increased, the maximum press-fitting force also increased. The correlation between friction and force was not linear but displayed significant sensitivity. Even small increments in the friction coefficient resulted in substantial changes in the maximum press-fitting force.

**Adherence to EN Standard:** The findings demonstrated that adhering to the European Standard EN 13260 for railway wheelset assembly was crucial for maintaining press-fitting quality. Specifically, the research validated that the criteria outlined in this standard, specifying interferences in the range of 200  $\mu\text{m}$  to 320  $\mu\text{m}$  and friction coefficients between 0.08 and 0.13, ensured satisfactory press-fitting curves. Interferences beyond this range or friction coefficients outside the specified values resulted in suboptimal press-fitting, potentially compromising assembly integrity.

This material is reserved for educational use only, not allowed for commercial use.

Forbidden to modify the content, and cite the document when use.

**Interference and Holding Torque:** It was observed that the holding torque capacity was positively correlated with the interference in the elastic range. In practical terms, this means that a greater interference resulted in an increased ability of the assembly to resist torsional forces before slipping occurred. This information has critical implications for designing railway assemblies that can withstand varying operational loads and conditions.

**Plastic Deformation and Torque:** Beyond a certain interference threshold, the research indicated that plastic deformation occurred. At this stage, further increases in interference did not translate to higher holding torque capacity. Instead, the torque remained constant, indicating that the assembly underwent plastic deformation. The results showed that the maximum elastic torque typically did not exceed 75% of the maximum holding torque capacity, a critical insight into the assembly's behavior.

**Comparing Theory and Finite Element Analysis:** To validate the research outcomes, a comparison was made between the theoretical calculations and finite element analysis results. This comparison demonstrated a good level of agreement, with deviations ranging from 6% to 15%, depending on the interference level. The consistency between the theoretical and simulation-based findings reinforced the research's credibility.

#### *5.4.2 Recommendations and Applications*

Based on the research findings, several recommendations and applications arise:

**Optimizing Assembly Processes:** The insights into interference and friction sensitivity can inform railway assembly processes. It is recommended to carefully select interferences and friction coefficients within the recommended ranges to achieve efficient, reliable, and safe press-fitting.

**Assembly Design:** The research findings can guide the design of railway assemblies, taking into account the relationship between interferences and holding torque capacity. Designers can make informed decisions to ensure assemblies can withstand operational loads and maintain integrity.

This material is reserved for educational use only, not allowed for commercial use.

Forbidden to modify the content, and cite the document when use.

**Safety and Quality Assurance:** Railway companies can utilize the research outcomes to implement quality assurance measures. Compliance with standards, such as EN 13260, is crucial for ensuring the safety and quality of railway assemblies.

**Further Research:** The transition from elastic to plastic deformation is a critical area for further investigation. Future research can focus on optimizing assemblies to delay plastic deformation while maintaining safety and efficiency.

In conclusion, this research contributes significantly to the understanding of press-fitting in railway axle and wheel assemblies, offering practical insights for the railway industry to enhance safety, quality, and reliability.



# CHAPTER 6

## MULTIAXIAL FATIGUE-LIFE PREDICTION OF RAILWAY AXLES WITH CONSIDERATION OF PRESS-FITTING AND BRAKING EFFECTS

### 6.1 Overview

In this section, we will establish the context of the study and outline its objectives, focusing on the impact of press-fitting on the fatigue life of railway axles and the importance of accounting for braking effects in multiaxial fatigue-life prediction.

#### 6.1.1 *Press-Fitting Impact on Fatigue Life*

Press-fitting, a critical assembly process in the manufacture of railway axles, plays a significant role in the structural durability of these essential components. Understanding how the press-fitting process affects the fatigue life of railway axles is pivotal for ensuring their safe and reliable operation.

The press-fitting procedure involves the interference fit of a wheel hub onto an axle, creating an assembly that must withstand substantial cyclic loading, both during operation and in the assembly process itself. These dynamic forces can induce various stresses and strains on the axle, impacting its fatigue life. Therefore, gaining insights into the impact of press-fitting on fatigue life is essential for the design and maintenance of railway axles.

#### 6.1.2 *Importance of Understanding the Effects of Assembly Processes on Structural Durability*

The assembly process, particularly press-fitting, is a critical factor in ensuring the integrity of railway axles. Press-fitting impacts the stress concentration and distribution along the axle, which, in turn, influences the axle's fatigue life. Variations in the press-fitting process, including interferences, friction, and material properties, can result in substantial differences in the structural integrity of axles. Thus, understanding the effects of assembly processes is paramount for both the manufacturing industry and railway safety.

This material is reserved for educational use only, not allowed for commercial use.

Forbidden to modify the content, and cite the document when use.

### 6.1.3 Multiaxial Fatigue-Life Prediction with Braking

Braking forces are a significant component of the dynamic loads experienced by railway axles. Understanding the influence of braking effects on fatigue life is crucial because these forces can induce unique stress patterns and have a substantial impact on the overall structural durability. Although previous studies have not extensively explored the impact of braking on fatigue life, this research aims to bridge this gap in knowledge.

## 6.2 Numerical Analysis of the Influence of Press-Fitting on the Fatigue Life of Railway Axle

### 6.2.1 Numerical Simulation for Press-Fitting Influence

FEA is essential to compute the stress caused by applied loads while assessing the residual press-fitting effect on the axle. This study used two kinds of FE simulations to examine the effect of running conditions and press-fitting on axles stress concentration. There were two different contact techniques: tie contact for without press-fitting effect and interference fit contact for taking the press-fitting effect into account. For numerical simulation, this study used a linear elastic isotropic EA4T material which is commonly used in railway axles with a modulus of elasticity 206 GPa and a Poisson ratio of 0.3.

The 3D FE models of wheels and axles were created as a press-fitted assemblage. The refined mesh was used for a higher resolution at the contact area, fillet, and notch transition zone, where the stress is concentrated. The element size was 2 mm at the fillet, and the notch groove transition, 5 mm at the contact area of the wheel and axle, 10 mm at other parts of the axle, and 20 mm at the wheel is a 20 mm expected contact area (Figure 6.1 and 6.2). The element of the first-order-reduced integration hexagonal type (C3D8R) was used with a controlled hourglass effect [29].

The analysis consisted of two steps: press-fitting and applying the loading for the simulated case by taking into account the residual stress from the press-fitting. Surface-to-surface contact with an interference fit was used. For without press-fitting effect, the tie contact was used between two contact surfaces of the wheelset to ensure no relative motion between them. The master surface was the wheel bore, while the wheel seat of the axle's outer surface was the slave surface.

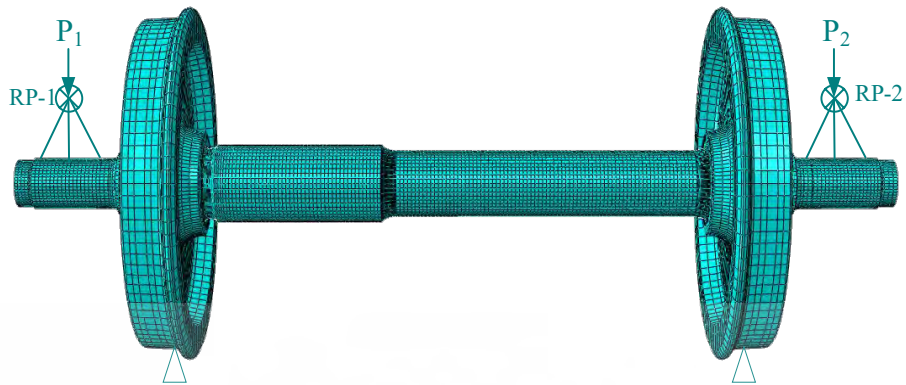


Figure 6.1 Meshing and boundary conditions of the motor bogie wheelset for stable condition.



Figure 6.2 Meshing and boundary conditions of the motor bogie wheelset for adverse condition.

The wheel and axle were press-fitted with an allowable radial interference value of 0.2 mm according to EN 13260 [32]. The frictional coefficient of 0.1 was assigned, encompassing the tangential behavior and the hard-contact model to ensure the normal behavior using the method of Augment Lagrange constraint enforcement. Besides, a small sliding was used to simulate the press-fitting. Figure. 6.1 and 6.2 shows the boundary conditions of the motor bogie wheelset based on the EN 13104 standard [33]. Table.I shows the specific load values used to calculate the internal and external stress on the motor bogie axle, and they were adopted from another study [34]. For stable condition with symmetric vertical forces (88.4 kN) loaded on the journal bearings, other forces are negligible.

This material is reserved for educational use only, not allowed for commercial use.

Forbidden to modify the content, and cite the document when use.

Table 6.1 Loads for an axle of a motor bogie.

Load	Magnitude (kN)
Vertical force on the more loaded side = $P_1$	101.300
Vertical force on the less loaded side = $P_2$	75.528
Wheel-rail horizontal contact force on more loaded side = $Y_1$	49.509
Wheel-rail horizontal contact force on less loaded side = $Y_2$	24.754
Vertical rail contact reaction force on more loaded side = $Q_1$	112.430
Vertical rail contact reaction force on less loaded side = $Q_2$	63.171
Balancing force between $Y_1$ and $Y_2$ = $H$	24.775
Un-sprung force = $F_i$	-1.215

### 6.2.2 Bending Stress Variation under Different Running Conditions

Figure 6.3 shows the bending stress variation of the motor bogie axle along the axial direction for stable and adverse conditions evaluated by the numerical FE simulation. The variation of bending stress was different for stable and adverse conditions. The maximum bending stress occurred on the surface of the axle farthest from the natural axis and notch groove, where the maximum stress concentration was. The maximum bending stress of the adverse condition was 72% higher than that of stability. Thus, it would be misleading to design the axle based on the stable condition.

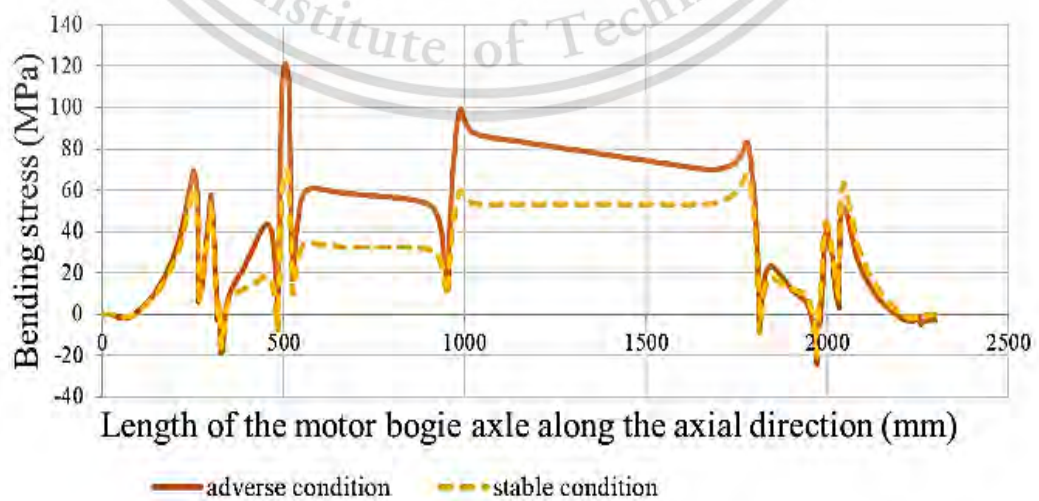


Figure 6.3 Comparison of bending stress along the axial direction of the motor bogie axle.

This material is reserved for educational use only, not allowed for commercial use.

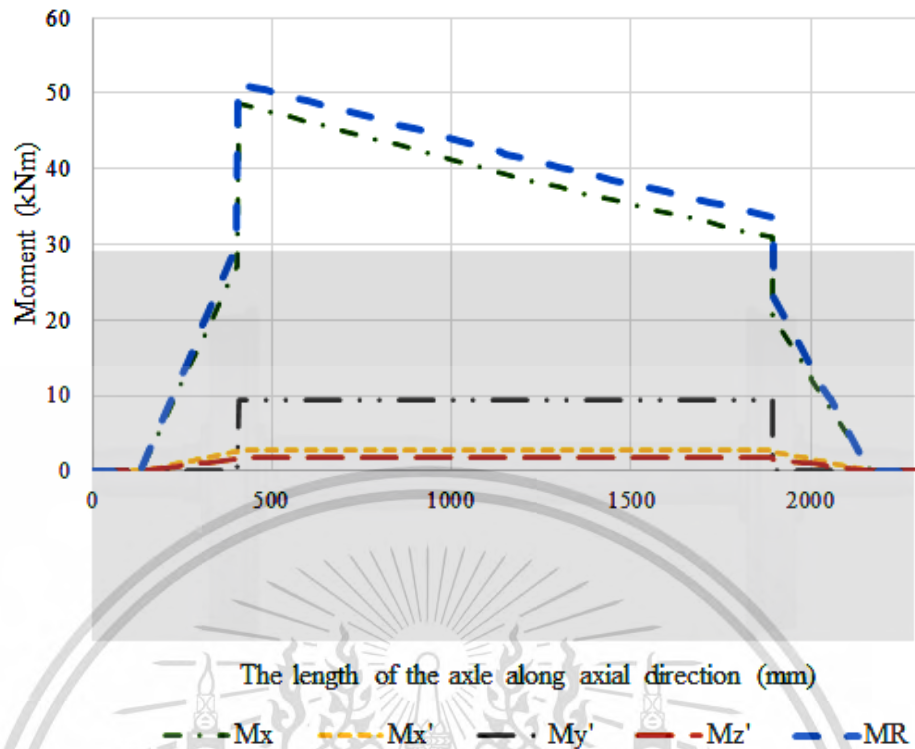


Figure 6.4 Moment diagram of the axle along the longitudinal axis

Figure 6.4 shows a moment diagram of an axle evaluated using the EN 13103/4 standard employing Eqns. (3.11) to (3.17). The wheelset was assumed to run on a curved track, considering lateral and braking forces. The bending moment  $M_x$  due to the vehicle's mass between the loading plane and the rolling wheel was also calculated using Eq. (3.18). It was computed between the two wheels using Eq. (3.19). The braking system generates moments as three components, x, y and z, which are calculated separately depending on the braking method. Brake imbalance, curvature effects and wheelset hunting generate torque along the y-axis. Frictional braking forces on the disc produce braking moments along the x- and z-axes. Bending moments of the x- and z-components are smaller than the torsional moment in the y-direction. The maximum moment occurred at the axle wheel seat with the transmission of track reaction forces to the axle through the wheel, causing the side of the axle to become more loaded.

### 6.2.3 Press-Fitting Effect on Stress Distribution

The press-fitting effect was studied under adverse running conditions. Figure. 6.5 shows the distribution of von Mises stress throughout the axles and the effects of press-fitting, tie contact type with loading and interference fit contact type with loading. In this study,

combining press-fitting and loading showed that press-fitting created the corresponding von Mises stress at the contact area of the wheelset and the transition zone near the wheel seat. However, the stress distribution of other parts remained constant. Therefore, the press-fitting substantially influenced the residual stresses of the wheelset's initial conditions. In other words, the residual stress of press-fitting remained vulnerable to cracking at places such as fillet, groove transition, and axle wheel seat.

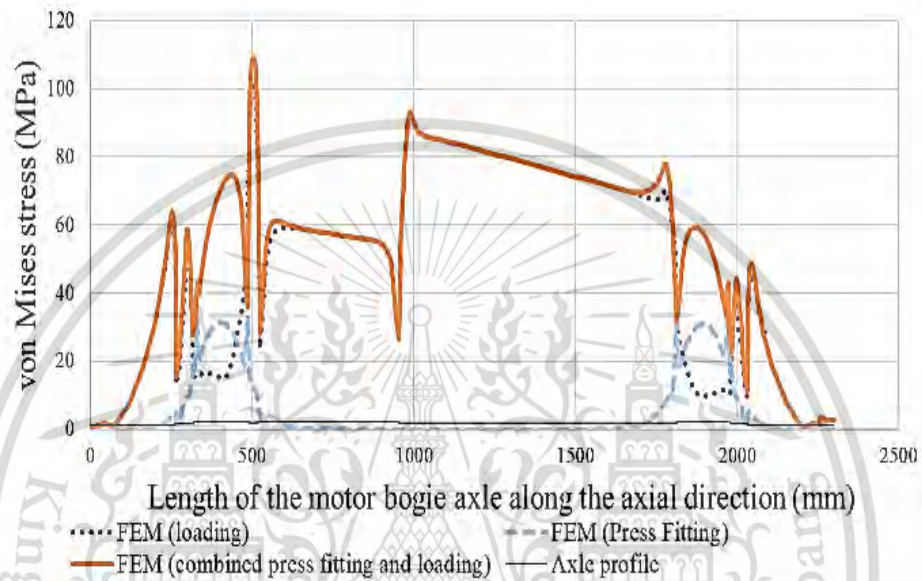
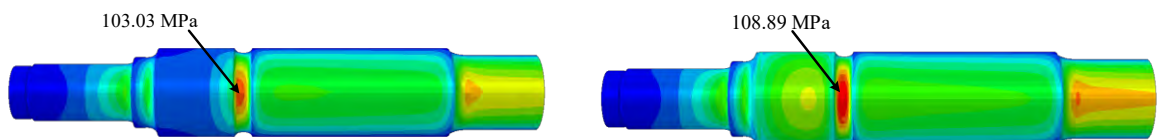


Figure 6.5 Comparison of von Mises stress along the axial direction of the motor bogie axle.

Figure. 6.6 shows that stresses at the contact of the wheel seat, fillet, and groove transition near the wheel seat from the finite element method differed between the with and without press-fitting effect. At the groove transition zone, the maximum von Mises stress occurred as expected, and the combined stress with the press-fitting effect was 6% higher than the value of applied loading without the press-fitting effect. The nature of interference fit and tie contacts differed substantially. Therefore, the stress distribution at the contact area of the wheel seat was different.



(a) Tie contact without press-fitting effect (b) Interference fit contact with press-fitting effect

This Figure 6.6 Comparison of the maximum von Mises stress for the motor bogie axle.

### 6.2.4 Relationship Between Fatigue Life and Overloading Repeated Cycles

To examine the press-fitting effect and impact of variable amplitude overload on the fatigue life, three loading scenarios are taken into consideration. The load scale factor 1 showed no damage in the motor axle design. The axle was designed to have an infinite life, and the working stress was below the permissible level. Therefore, it was necessary to scale the stress to almost yield stress. Expectedly, the fatigue life results showed that damage began at loading case 2, overloading applied every five cycles for the motor axle, and the fatigue life decreased when the overloading repeated cycle increased. Table III compares the shortest fatigue life and the safety factory between the interference fit and tie contact for motor bogie axles. The interference fit contact for the worst life-repeat cycle, and the safety factor was less than tie contact. The weakest failure position of the motor axle was the grooved notch. Figure. 6.13 and 6.14 show the fatigue life and factor of strength as a contour in the worst element.

Table 6.2 Comparison of fatigue life of the motor bogie axles.

Loading Case	Without press-fitting effect		With press-fitting effect	
	<i>Worst life- repeat cycle</i>	<i>FOS*</i>	<i>Worst life- repeat cycle</i>	<i>FOS*</i>
1	No damage	1.609	No damage	1.492
2	2.409E+7	0.935	1.513E+7	0.875
3	1.205E+7	0.889	7.568E+6	0.834

\* FOS = Factor of strength

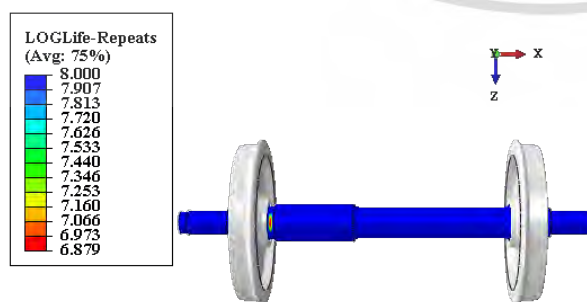


Figure 6.7 Fatigue-life assessment of the motor bogie wheelset.

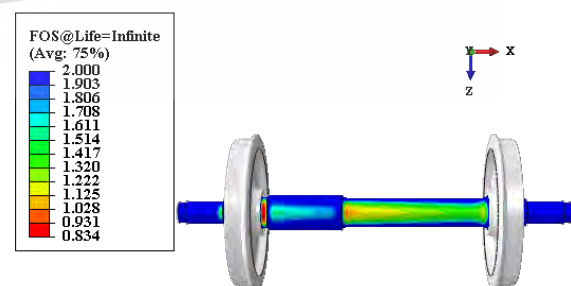


Figure 6.8 Safety factor assessment of the motor bogie wheelset.

### 6.3 Numerical Simulation with Braking Considerations

Finite element analysis of the railway motor bogie wheelset assembly was performed to examine stress history after press fitting and loading. A three-dimensional FE half-symmetry model of the wheelset was developed using ABAQUS software. As demonstrated in Figure 6.3, the FE model consists of two components, wheel and axle. A railway wheel and axle are press fitted with an interference 0.2 millimetres, calculated following EN 13260 [21]. The material used in this study is EA4T steel, Young's modulus ( $E$ ) is 206 GPa and Poisson's ratio ( $\nu$ ) is 0.3, which are frequently employed in railroad wheelsets. To achieve precise and accurate FE modelling results, the mesh sensitivity analysis was conducted, and the element size was carefully chosen. Based on the results of the comparison of different mesh sizes, we determined the optimal mesh size that provides a reasonable trade-off between accuracy and computational cost. Specifically, the element size was set to 2 mm at the fillet and notch groove transition, 5 mm at the contact area between the wheel and axle, 10 mm at other parts of the axle, and a 20 mm expected contact area for the wheel. This approach allows for accurate results with a minimal number of elements. The model consists of 256,456 elements (C3D8R), as demonstrated in Figure 6.10. First-order reduced integration elements are utilized by controlling the hourglass effect to improve the accuracy of results. This prevents potential singularities due to reduced integration and increases computational efficiency in numerical simulations.



Figure 6.9 FE meshing model of the wheelset.

The mating surface between the wheelset was defined as a surface-to-surface contact, where the wheel's contact surface was the master surface due to its greater stiffness. The master surface nodes could penetrate the slave surface, where the axle's contact surface was the slave. Small sliding contact formulation was used to ensure that motion between surfaces

was small and accurately simulated the press-fitting procedure. The coefficient of friction for the wheelset contact was 0.1 to account for tangential behaviour. A hard contact model was proposed to ensure normal behaviour.

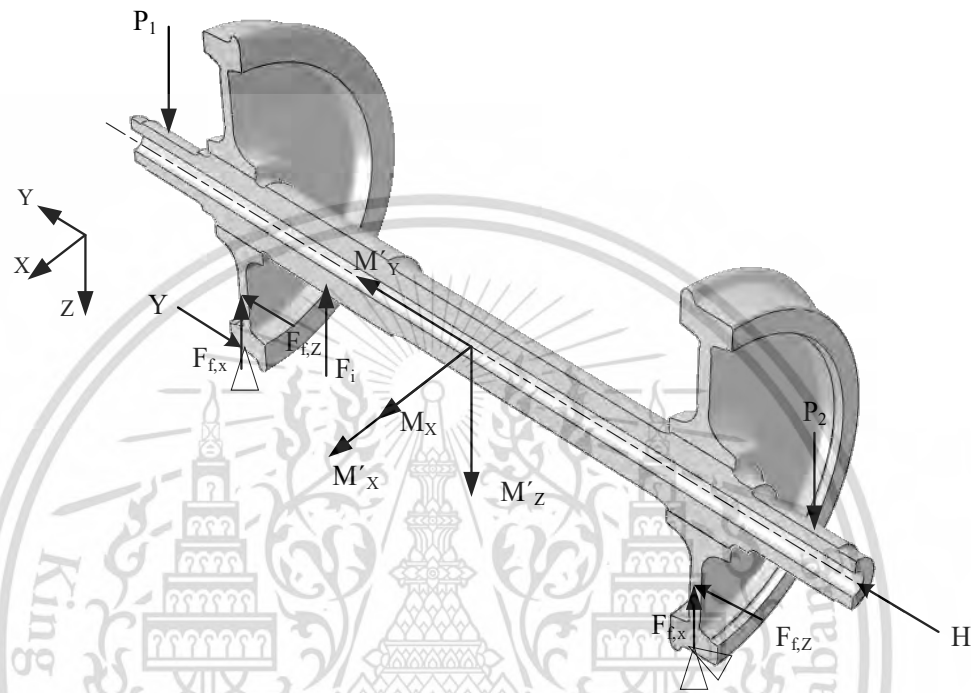


Figure 6.10 Boundary condition of the FE model wheelset.

The boundary conditions and loading of the wheelset were set following the EN 13103/4 design standard (Figure 6.11). The wheel-rail contact nodes were fixed,  $U_1, U_2=0$ , to the contact place of the wheel and track. In this analysis, the loading was applied in a multi-step case. We defined three load steps using a multi-load case function. Step 1 involves applying an interference fit. The second step is an analysis that adds vertical loading and lateral force to the model. Step 3 includes braking forces and torsion loading.

## 6.4 Discussion

The discussion section provides a thorough analysis of the research findings and their implications within the context of railway axle design and fatigue analysis. This section will delve into the significance of the findings, their alignment with existing literature, and potential areas of improvement or future research.

This material is reserved for educational use only, not allowed for commercial use.

Forbidden to modify the content, and cite the document when use.

#### 6.4.1 Effect of loading cases on the stress concentration of a railway axle

Several static stress analyses were performed and defined considering only the press fitting effect in Loading Case 1, combined press fitting and masses in motion in Loading Case 2, further combining them with the braking effect in Loading Case 3 and only masses in motion effect in Loading Case 4. Figures 6.11, 6.12, 6.13 and 6.14 present graphical representations of the corresponding von Mises stress variation and counter plot of the von Mises stress variation of the axle 3D model for each loading condition. The distribution of von Mises stress throughout the axles generated by press fitting is plotted in Figure 6.11. During the press fitting, displacement and deformation occur on the press fitted seats and wheel hub because the contact pressure increases, causing stress, and the stress concentration rises. The calculated von Mises stress distribution based on FE analysis was zero, except for the wheel seat contact areas, fillets, and groove transitions near the interference fit. As a result, press fitting significantly affected the wheelset's initial residual stresses.

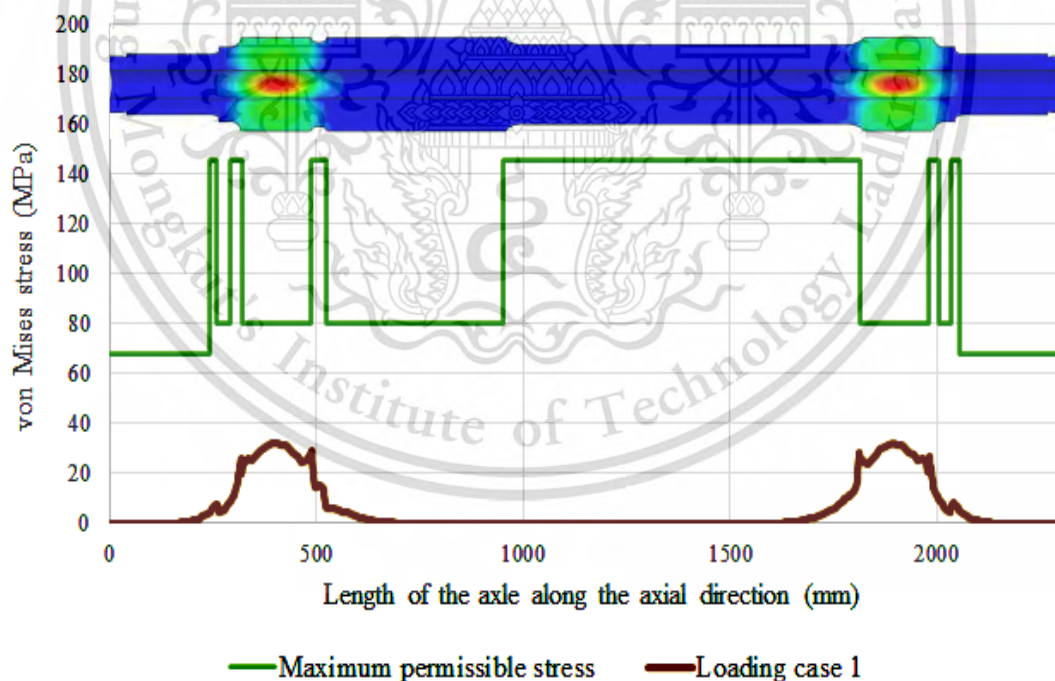


Figure 6.11 von Mises stress variation of an axle along the longitudinal axis generated by Loading Case 1

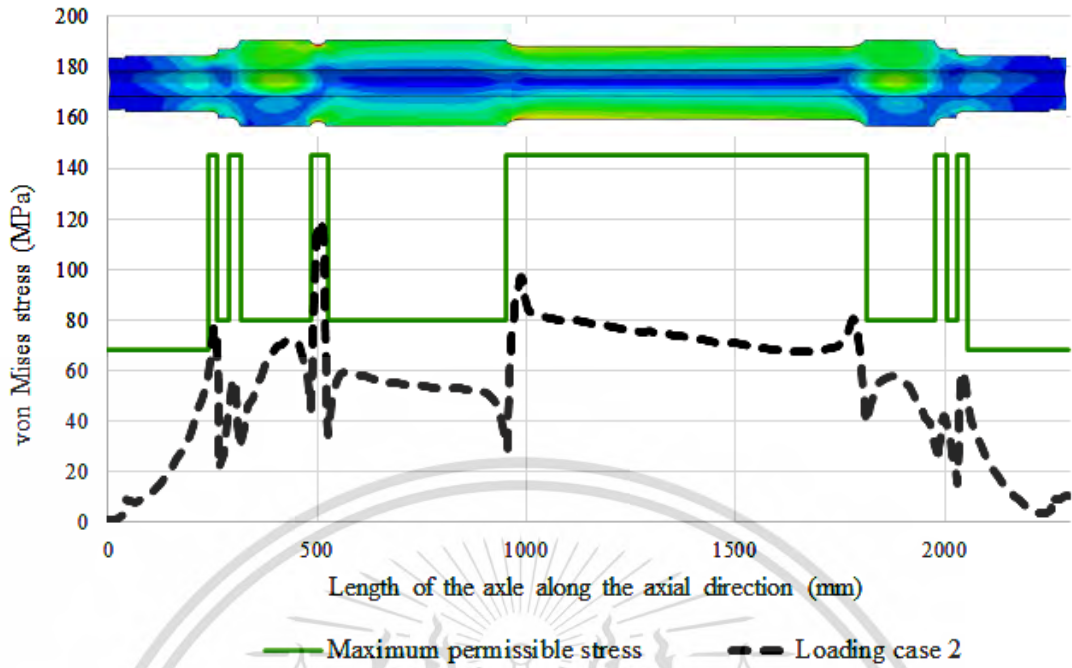


Figure 6.12 von Mises stress variation of an axle along the longitudinal axis generated by Loading Case 2

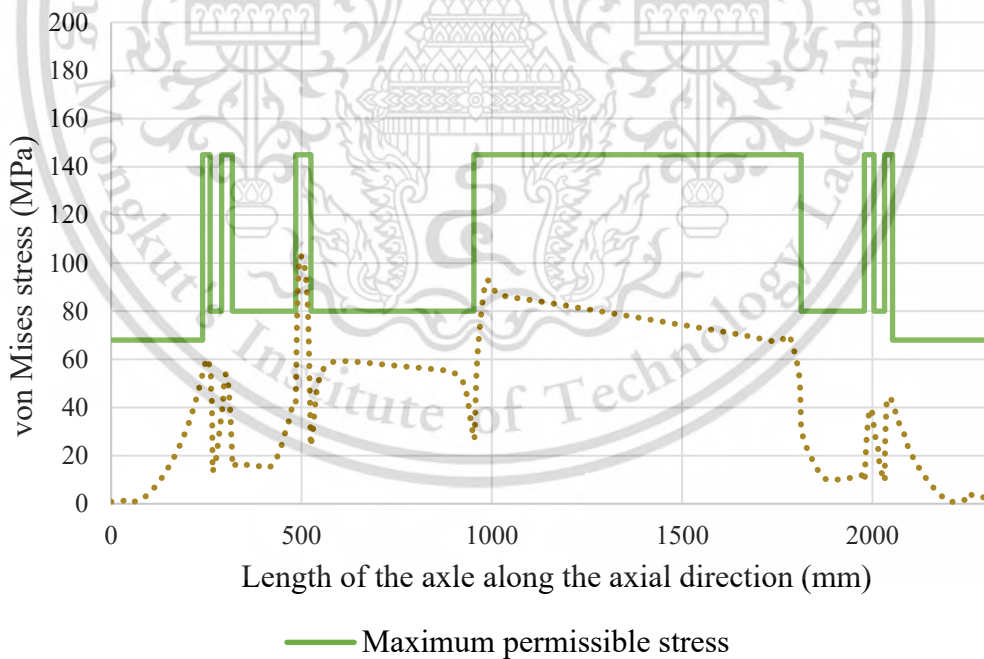


Figure 6.13 von Mises stress variation of an axle along the longitudinal axis generated by Loading Case 4

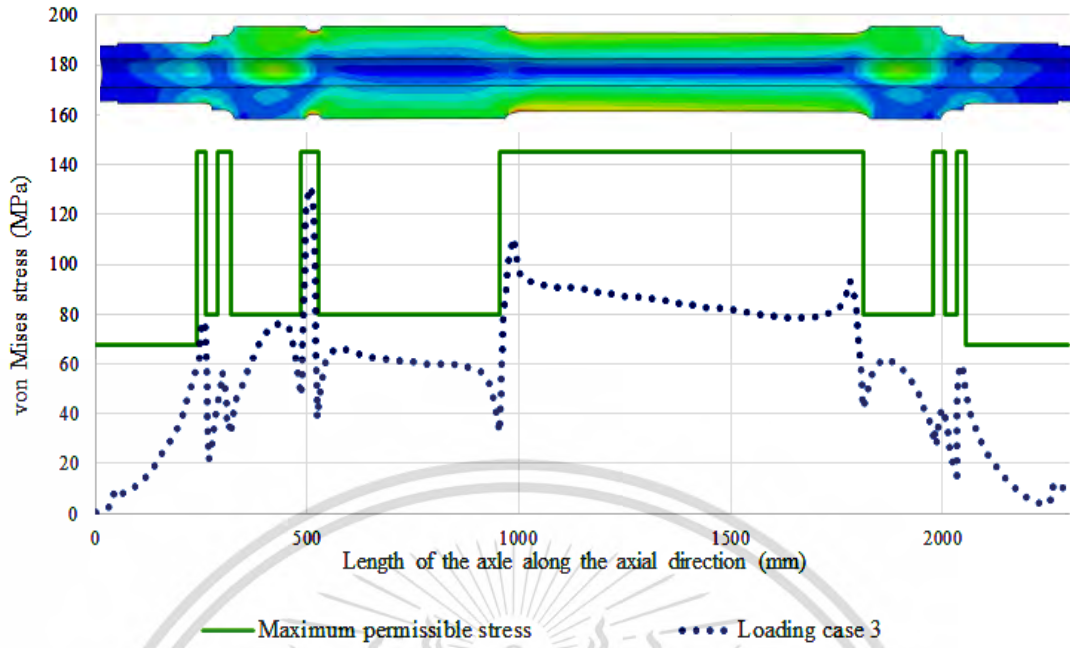


Figure 6.14 von Mises stress variation of an axle along the longitudinal axis generated by Loading Case 3

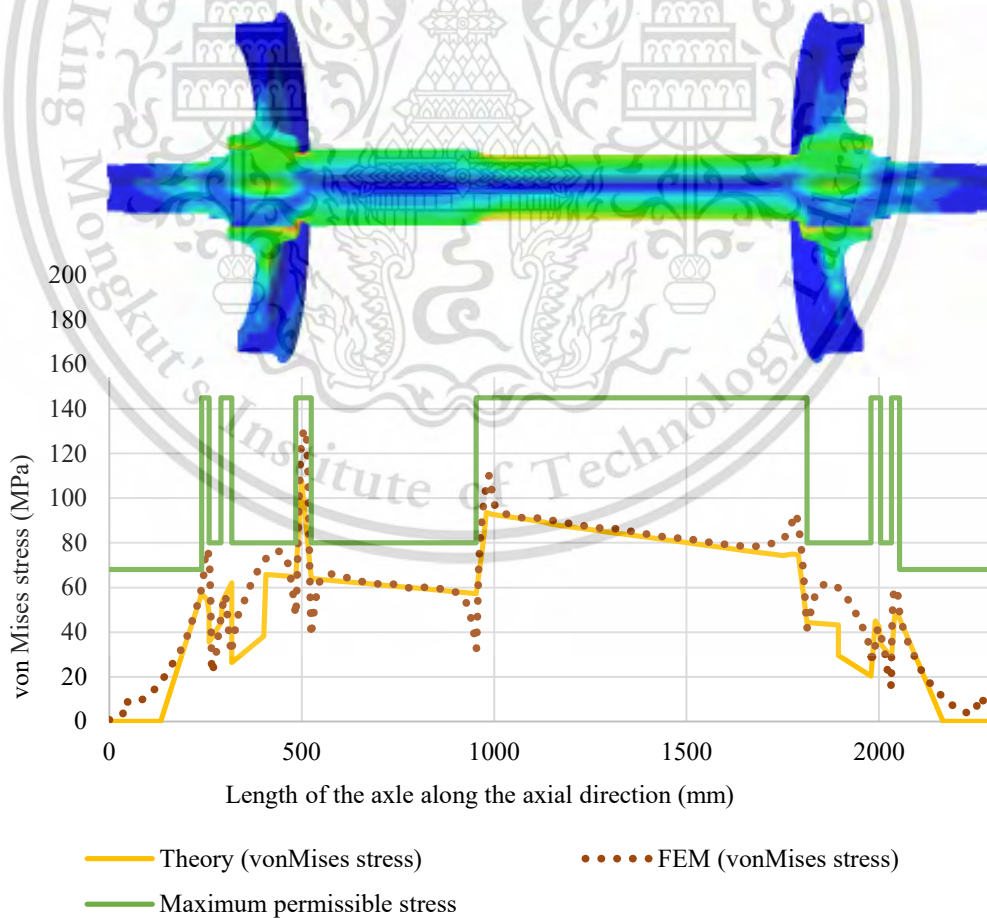


Figure 6.15 Comparison of von Mises stress variation of an axle along the longitudinal axis

This material is reserved for educational use only, not allowed for commercial use.

Forbidden to modify the content, and cite the document when use.

The von Mises stress from FE analysis throughout the axles generated by masses in motion and the combined loading cases is shown graphically in Figures 6.12, 6.13 and 6.14. The surface of the axle furthest from the natural axis and notch groove, where the most significant stress concentration resided, experienced the highest von Mises stress. In both loading cases (4, 2 and 3), the maximum stress concentration is located at the notch groove transition zone, with values of 108, 114 and 127 MPa. Comparing the analytical and FE analysis results (Figure 6.15), the maximum stress value of the notch groove transition from FE analysis was 43% higher than the value calculated using the EN standard. These values vary depending on various axle geometry parameters, as described in above section. Furthermore, the standard does not consider the press-fitting effect. The other sections of both results are very good agreements except for the location of the wheelset contact place and adjacent transitions places.

This was done to validate the safety factor following the EN 13013/4 standard, depending on the type and specific zone of the axle. The results from both theoretical and numerical methods indicate that the stress values are below the maximum permissible stress, as illustrated in Figure 6.15. Furthermore, the FE numerical method yielded a safety factor of 1.2 at the groove notch transition, indicating that the design is safe and can withstand the applied load. The combination of the braking effect increases stress to the axle by 10%. Thus, it would be misleading to design the axle based on only the masses in motion.

#### *6.4.2 Multiaxial fatigue-life prediction of a railway axle*

Multiaxial fatigue-life prediction was implemented in fe-safe, a commercial software that functions as a post-processor for structural FEA results, which reads data from a .odb file. Since fatigue cracks typically start at component surfaces, only surface nodes of the axle 3D model were examined. The FE analysis results are output as multiple load cases to accurately account for the effects of various stress histories on axle life. It was necessary to scale the stress to almost the yield-stress because the axle was designed to have an infinite life, and the working stress was below the permissible level.

Three loading scenarios were taken into consideration to examine the effects of loading conditions and impact of variable amplitude overload on the fatigue-crack initiation. Figure 6.16 compares the lowest fatigue life between four loading conditions (Loading case 4 only imposing mass in motions) is at specific locations with comparative results. The estimated fatigue safety factors show fatigue durability throughout an infinite life cycle in Figure 6.17. It

This material is reserved for educational use only, not allowed for commercial use.

was calculated as the product of the stress amplitude and the fatigue strength of the material. Figure 6.18 demonstrates the fatigue damage obtained through fatigue analysis using fe-safe.

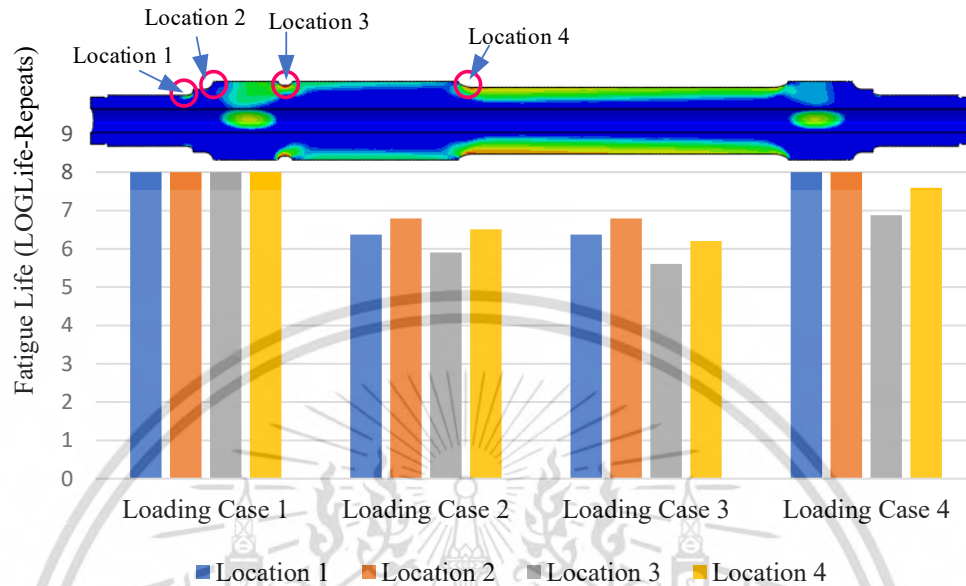


Figure 6.16 Estimated fatigue life of a railway axle

The effect of press fitting in Loading Case 1 showed no fatigue in the motor axle design. It has an infinite fatigue life because of endurance cycle reached  $10^7$ . Its factor of strength (FOS) was larger than 2 because the stress amplitude was below the permissible level, and the calculated life was greater than the design life. Figure 6.18 shows no damage will be caused due to that loading.

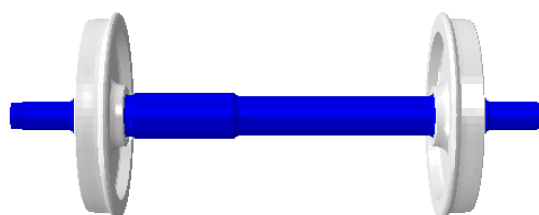
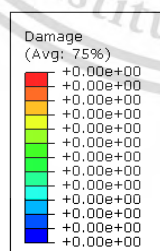
The generated fatigue-life results showed that fatigue began in Loading Case 2 at the groove notch, location 3, for the motor axle. It resulted from the combined press fitting and masses in motion with overloading applied every fifth cycle. Figure 6.16 shows the fatigue-life prediction results of axles as  $\log_{10}(\text{life})$  contours, where life is in cycles, and the minimum value is  $(10^{5.906}=8.05\text{E}+05)$  cycles). As is evident in Figure 6.16, at location 3, the groove notch region shows the minimum life, and crack initiation occurred here, at the highest stress level. This was determined by the stress at a node for all loading conditions. The crack initiation location is indicated by the red zone in the stress contour where the highest level of stress is present. The minimum factor of strength (FOS) was 0.715 at location 3. The damage contour plot gives the fatigue damage values of a specific plane at a given design life (Figure 6.18). It shows the maximum fatigue damage was  $3.830\text{E}-07$  and the crack initiation will occur when the fatigue damage is equal to 1 because fatigue life is inverse of the damage.



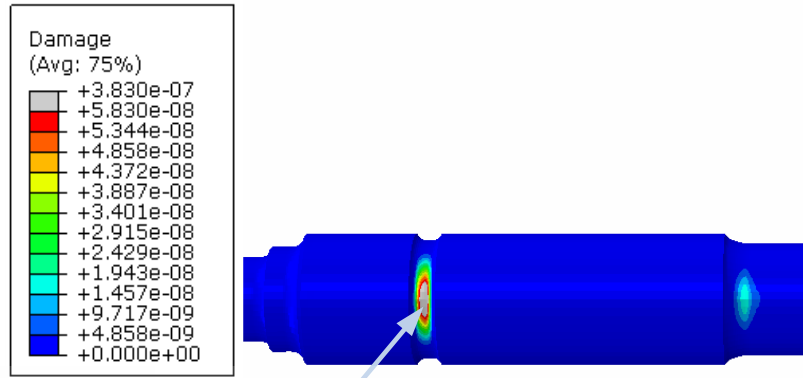
Figure 6.17 Estimated factor of strength of railway axle

For Loading Case 3, with three loading conditions, the lowest fatigue life will endure  $10^{5.609}=4.06E+05$  cycles at location 3 before failing. Loading Case 3 for of the log(life-repeat) cycle was 5% less that of Case 2 at location 3. The factor of strength (FOS) was 0.678 and the percentage difference between the two loading cases remained the same as the log(life-repeat) cycle. Additionally, in a specific scenario where braking is applied, the maximum damage value experienced a 70% increase (Figure 6.18).

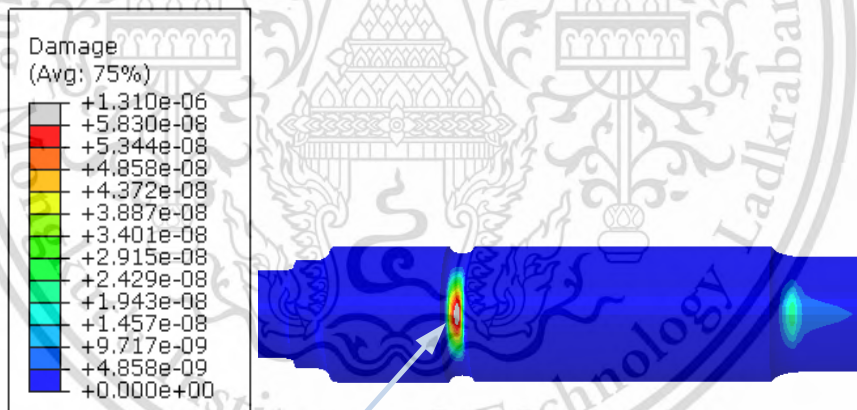
For Loading Case 4, with imposing only mass in motion conditions, fatigue life and safety factor increase showing a 14% higher than loading case 2 at location 3.



(a) Loading Case 1



(b) Loading Case 2



(c) Loading Case 3

This material is removed for educational use only, not allowed for commercial use.  
 Figure 6.18 The estimated fatigue damage of railway axle.  
 Forbidden to modify the content, and cite the document when use.

## 6.5 Conclusions

The conclusions of this research, based on the detailed findings and discussions, provide a comprehensive summary of the study's outcomes and their practical significance. The following key points are drawn from this research:

- Designing railway axles based on stable conditions is insufficient; a shift toward considering adverse conditions is essential for ensuring safety and reliability.
- Press-fitting significantly influences the stress concentration in axles, particularly at critical areas like the fillet, groove transition, and axle wheel seat.
- The maximum von Mises stress in the groove transition zone is 6% higher when press-fitting is considered, highlighting its importance in the design and analysis of axles.
- Fatigue life is closely related to the number of repeated overloading cycles, emphasizing the need for effective maintenance strategies.
- Numerical modeling plays a crucial role in assessing the impact of press-fitting and offers practical relevance for designing railway axles.
- The braking effect substantially increases stress on axles, reducing their fatigue life by 50%. Design and maintenance should account for this effect.
- Accurate fatigue-life predictions require the consideration of variable amplitude overload scenarios.

The safety factor validation and identification of the weakest failure point at the grooved notch further contribute to the safety and durability of railway axles.

In summary, this research enhances our understanding of railway axle design and fatigue analysis, providing insights that can guide the development of more robust and safer axles. It underscores the need to consider adverse operating conditions, the influence of press-fitting, and the impact of the braking effect in design and maintenance strategies. The practical relevance of this research to real-world railway operations cannot be understated, and it forms the basis for future work in this critical field. Ultimately, this study aids in the creation of railway axles with extended life cycles and enhanced safety.

## CHAPTER 7

# ASSESSING THE IMPACT OF PRESS-FITTING, RUNNING CONDITIONS, BRAKING AND AXLE HOT BOX BEARING TEMPERATURE ON THE STRESS INTENSITY FACTOR AND RESIDUAL LIFETIME OF RAILWAY AXLES

### 7.1 Overview

The structural integrity and performance of railway axles are of paramount importance for the safety, efficiency, and reliability of rail transport. These axles are subjected to a complex combination of loading conditions, including cyclic loading due to rolling contact fatigue, and various operational conditions. This complexity makes it imperative to assess their structural integrity accurately, particularly with regards to the risk of crack initiation, propagation, and subsequent failure. Stress intensity factor (SIF) plays a critical role in this assessment as it provides insights into the potential for crack growth and failure in structural components.

#### 7.1.1 *The Impact of Press-Fitting and Running Condition on Stress Intensity Factor (SIF)*

Stress Intensity Factor (SIF) is a fundamental parameter used to assess the potential for crack initiation and propagation in materials under stress. It is especially crucial for components subjected to cyclic and dynamic loading conditions, as is the case with railway axles. The SIF provides information about the maximum stress at the tip of a crack and helps in determining the rate of crack growth. Accurate SIF calculation is essential for predicting the remaining lifetime of railway axles and ensuring their safe operation.

A substantial body of previous research has addressed the issue of SIF in railway axles. Many of these studies have focused on symmetric loads and stable running conditions. These investigations have provided insights into SIF solutions for semi-elliptical cracks in railway axles and highlighted the significance of factors such as press-fitting effects, residual stresses, and manufacturing processes in SIF calculations. However, there is a notable gap in research regarding the effects of adverse running conditions on SIF. This research aims to bridge this

This material is reserved for educational use only, not allowed for commercial use.

Forbidden to modify the content, and cite the document when use.

gap by considering the impacts of adverse running conditions, press-fitting, and other factors on SIF, with a particular focus on asymmetrical loads and braking effects.

### *7.1.2 The Impact of Braking and Axle Hot Box Bearing Temperature on Stress Intensity Factor (SIF)*

During braking, railway axles experience dynamic loading conditions, including asymmetric forces due to the interaction between the wheel and rail. These forces create a twisting effect on the axle, leading to varying stress states and significant stress concentrations. Additionally, the temperature of axle hot box bearings can influence the stress state of axles, as the heat generated during braking is transferred to the axle. Therefore, it is crucial to investigate and understand how braking and axle hot box bearing temperature affect the stress state in railway axles.

The relationship between braking forces and axle hot box bearing temperature is a complex interplay of mechanical and thermal effects. Braking forces lead to both mechanical stress and heat generation, which can result in elevated temperatures at the axle hot box bearings. The temperature gradient, material properties, and thermal stresses that develop under these conditions can significantly impact the stress intensity factor and, consequently, the structural integrity of the railway axle.

This research aims to investigate these multifaceted impacts on SIF and provide a comprehensive understanding of how braking and axle hot box bearing temperature influence the structural integrity and remaining lifetime of railway axles. By bridging this gap in the existing literature, the study will contribute valuable insights for the safe and reliable performance of railway axles under diverse operational conditions.

## **7.2 Numerical Simulation**

### *7.2.1 Finite Element Modelling and Simulation*

The FE simulation presented in this research is an extension of previous work [17], utilizing the same dataset. The primary objective is to investigate the influence of braking on the stress intensity factor (SIF) and residual lifetime prediction of a railway axle using finite element analysis (FEA). The simulation represents the railway wheelset with a three-dimensional (3D) geometry and considering the linear elastic material properties of the axle (EA4T steel, Young's modulus (E) of 206 GPa and Poisson's ratio ( $\nu$ ) of 0.3). To simulate the

This material is reserved for educational use only, not allowed for commercial use.

Forbidden to modify the content, and cite the document when use.

braking effect, loads are applied to the axle to represent the actual braking forces experienced as shown in Figure 7.1.

The contact between the mating surfaces of the wheelset is modeled as a surface-to-surface interaction, where the wheel's bore surface is designated as the master surface due to its higher stiffness, while the axle surface is the slave. A small sliding approach is employed in the contact formulation to accurately simulate the press-fitting procedure, resulting in minimal motion between the surfaces. Tangential behavior is accounted for by assigning a coefficient of friction of 0.1 to the wheelset contact. Additionally, a hard contact model is implemented to accurately represent the normal behavior between the surfaces.

Furthermore, the loading and boundary conditions of the wheelset, as well as the placement of the semi-elliptical crack at the maximum stress concentration point, are depicted in Figures 3 and 4, respectively. The stress intensity factor (SIF) is calculated using the contour integral evaluation approach, which is a widely-used method for determining the SIF of structures subjected to variable loads.

### 7.2.2 Mesh Sensitivity Analysis

The symmetric boundary condition was applied to only half of the crack during the simulation of the semi-elliptical crack, as depicted in Figure 7.1. Careful definition and mesh design were necessary for the crack and its surrounding elements, particularly near the crack line and within the crack front tubes. To obtain the desired output for SIF (Stress Intensity Factor) and J-integral, different element types (WEDGE and HEX) were assigned to the elements sharing nodes with the crack line and those located on the crack front, respectively. The optimal number of elements in a radial direction within a slice of the crack front was determined to be seven. To allow for relative movement of the crack face nodes, a discontinuity in the mesh was introduced between the two crack surfaces. Additionally, a singularity was assigned at the crack tip to ensure compliance with the principles of linear elastic fracture mechanics.

For the analysis of an embedded penny crack, q-vectors (as shown in Figure 7.2) were specified to determine the direction of crack extension. To ensure accurate and convergent numerical values, eight contours were defined in the vicinity of the crack tip. A mesh sensitivity analysis was conducted to determine the optimal global mesh size of 0.05 mm, thereby validating and enhancing the accuracy of the model results.

This material is reserved for educational use only, not allowed for commercial use.

Forbidden to modify the content, and cite the document when use.

Refining the mesh in areas of interest, such as the crack tip, is a crucial aspect of finite element analysis aimed at improving accuracy. By employing finer meshes, local phenomena near the crack tip can be resolved with greater precision compared to coarse meshes. Moreover, increasing the number of elements in these regions allows for the accurate modeling and analysis of complex geometries without compromising accuracy or stability in other parts of the model.

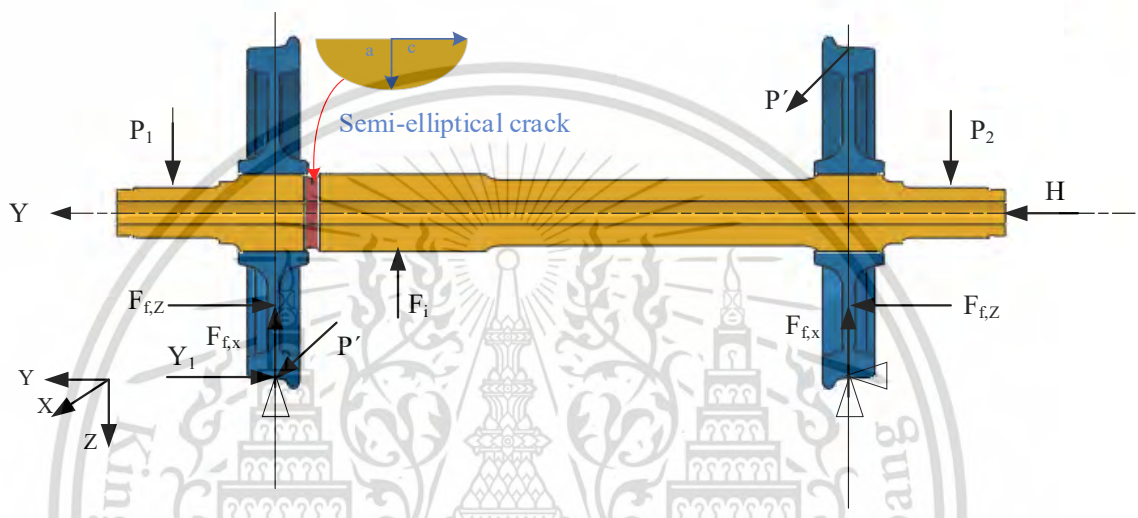
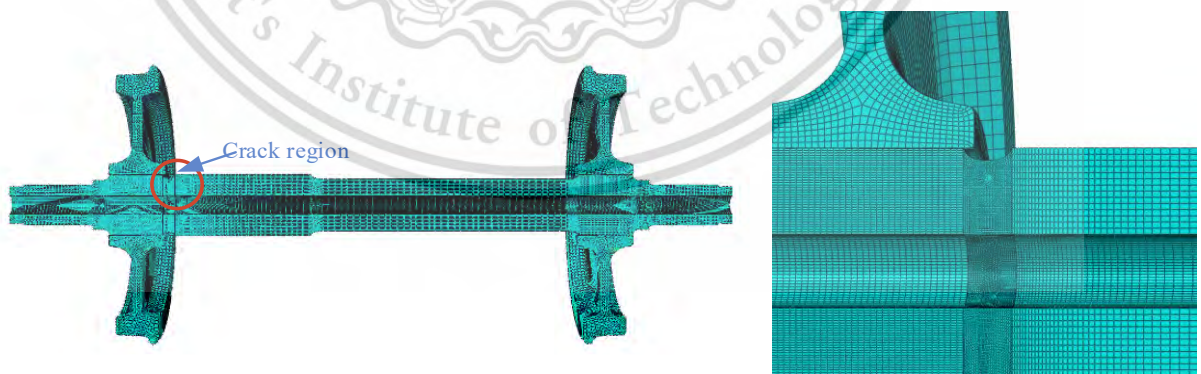


Figure 7.1 Boundary condition of the railway wheelset under braking forces



(a) Global mesh of the FE wheelset model with crack

(b) FE sub-model

This material is reserved for educational use only, not allowed for commercial use.

Forbidden to modify the content, and cite the document when use.

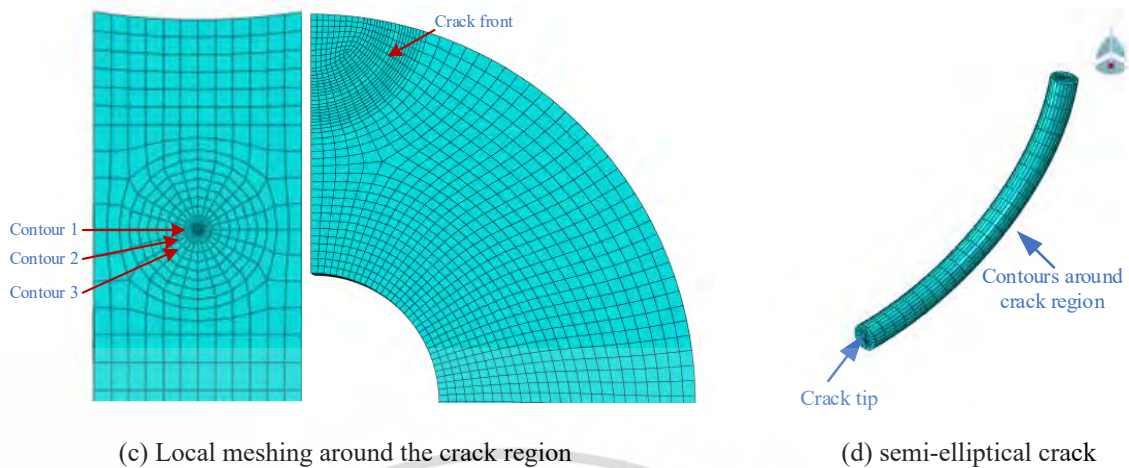


Figure 7.2 3D finite element model of high-speed wheelset.

### 7.2.3 Residual Lifetime Prediction and Fatigue Crack Growth Estimation

Residual lifetime prediction and fatigue crack growth estimation play a crucial role in assessing the remaining useful life of railway axle subjected to various loadings. This subsection focuses on the application of methodologies for accurately predicting the residual lifetime of railway axle and estimating the growth behavior of fatigue cracks using Paris law [35]. The Paris Law, developed by Paris and Erdogan in 1963, is widely used in fatigue analysis to predict the propagation of cracks over time under cyclic loading. It establishes a relationship between the crack growth rate ( $da/dN$ ) and the stress intensity factor range ( $\Delta K$ ). The equation can be represented as

$$da/dN = C(\Delta K)^m \quad (7.1)$$

where  $C$  and  $m$  are empirically determined constants. A fracture analysis typically starts with an initial crack size and propagates the crack until a critical stress intensity factor value  $K_{Ic}$ , which is  $86 \text{ MPam}^{0.5}$  and the threshold value is  $\Delta K_{th0} = 8.1 \text{ MPam}^{0.5}$  for a material EA4T steel when stress ratio  $R=0$ . The crack propagation analysis used in this article is a Paris law integration. It is chosen here for its simplicity and ease of implementation.

This material is reserved for educational use only, not allowed for commercial use.

Forbidden to modify the content, and cite the document when use.

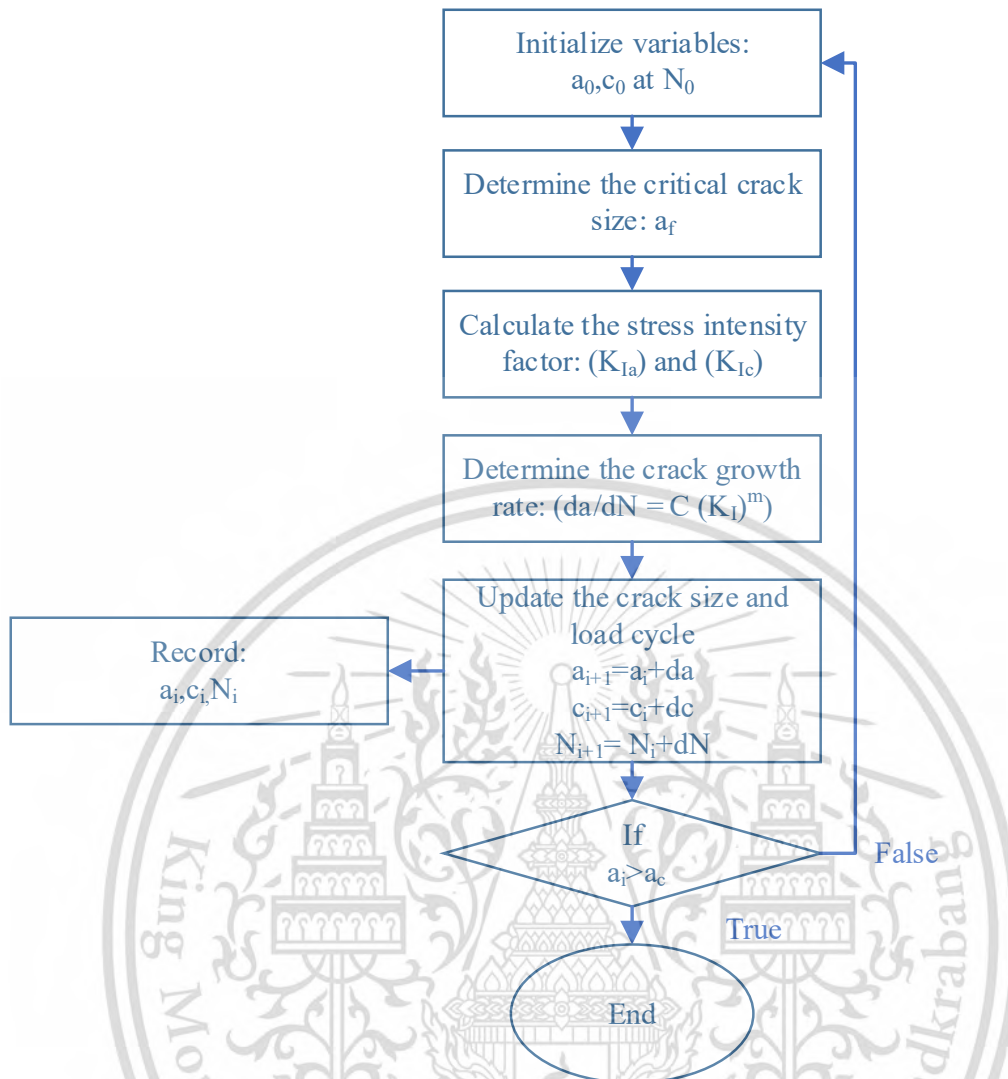


Figure 7.3 The procedure of the determination of crack growth rate.

Figure 7.3 illustrates the calculation procedure for determining the crack growth rate and the residual lifetime of railway axle. The flowchart outlines the steps involved, including determining the initial and final crack sizes, calculating the stress intensity factor solution, determining the stress range, dividing the crack path into steps, and calculating  $\Delta K$  and  $\Delta N$  for each step. The flowchart concludes with the summation of  $\Delta N$  for all steps to obtain the total number of cycles.

### 7.3 Findings

The extensive investigation into the impact of various operational conditions, crack shapes, and loading effects on the stress intensity factor (SIF) and residual lifetime of railway axles has yielded several significant findings. The findings are summarized as follows:

This material is reserved for educational use only, not allowed for commercial use.

Forbidden to modify the content, and cite the document when use.

### 7.3.1 Verification of the SIF Evaluation Results with FEM And Theory

Verification of the SIF evaluation results with FEM (finite element method) and theory (BS 7910 standard) is an important step in ensuring the accuracy and reliability of fracture mechanics analyses. In this study, we present the results of our verification process, which involved comparing the SIF values obtained from FEM simulations and theoretical calculations based on the BS 7910 standard. To analyze the SIF of a railway axle subjected to loading, the aspect ratio ( $a/c=0.75$ ) and relative crack depth ratio ( $a/t=0.25$ ) were respectively considered. As shown in Figure 7.4, the FE approach was employed to ascertain the SIF solution for a semi-elliptical crack occurring on an axle under bending and braking loads. This solution was subsequently compared to an analytical solution (BS 7920). The results indicated that the SIF value at the deepest point K(A) of the crack was lower than the SIF value at the surface point K(C) for both FEM simulations and theoretical calculations. The difference between the two values was approximately 10% for the FEM simulations and 8% for the theoretical calculations. The outcomes of the numerical simulation and the theory were in good accordance, with a maximum deviation of less than 10 percent.

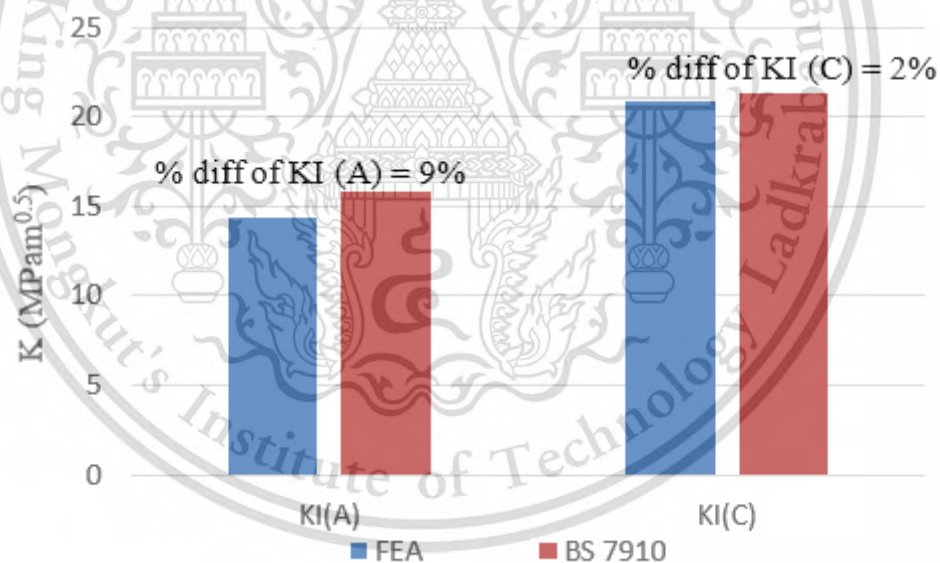


Figure 7.4 Comparison of Stress Intensity Factors (SIFs) between the BS 7910 standard and Finite Element method.

#### 7.3.1.1 Analyzing Crack Behavior and Modes

When extracting the SIF values along the crack front location from the FE simulation, it is observed that the results obtained from Contour 1 differ from other contours. However, it is notable that the other contours are identical (Figure 7.5).

The reason for neglecting the contour 1 results when averaging the SIF values lies in its specific characteristics. In regions where the stress distribution is likely to be highly concentrated and susceptible to numerical singularities, such as Contour 1, is commonly situated in the vicinity of the crack tip. This close proximity to the crack tip can lead to irregularities and inaccuracies in the computed SIF values, producing inconsistent or unreliable results.

However, Contours 2 to 7 are positioned at various distances from the crack tip. By choosing these contours, the stress distribution becomes more stable and less influenced by the localized stress concentration around the crack tip. Consequently, the computed SIF obtained from these contours tends to be more consistent and reliable.

To ensure the accuracy and validity of the SIF values, it is common practice to disregard the results from Contour 1 and instead focus on the averaged SIF obtained from the consistent and reliable results of Contours 2 to 7. This approach helps to mitigate the potential errors and uncertainties associated with the highly localized stress distribution near the crack tip, providing more robust and representative SIF values for further analysis and assessment of the crack behavior and structural integrity.

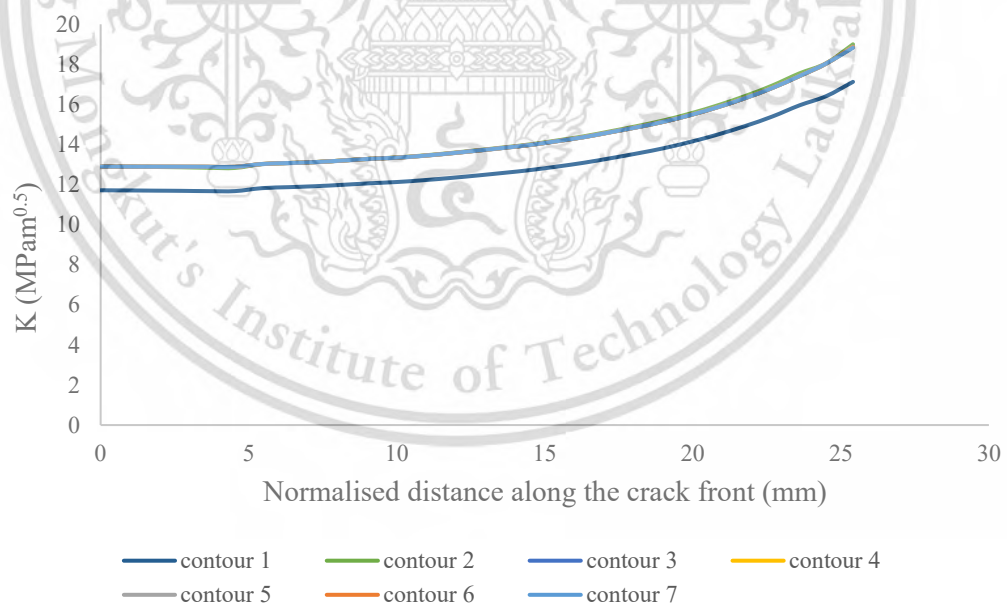


Figure 7.5 Comparison of Stress Intensity Factors (SIFs) in relation to various crack front contours.

The crack behavior under different crack mode shapes was analyzed by determining the SIFs, more precisely KI, KII, and KIII. Braking, press fitting, and masses in motion significantly contribute to the overall stress distribution and crack growth characteristics. While braking introduces both bending and torsional stresses on the axle, it specifically affects the SIF values associated with

torsional loading, namely KII and KIII. Nevertheless, according to the results of the analysis, KII and KIII are close to zero and can be disregarded, indicating that mode I loading is the major mode of operation on the crack (Figure 7.6).

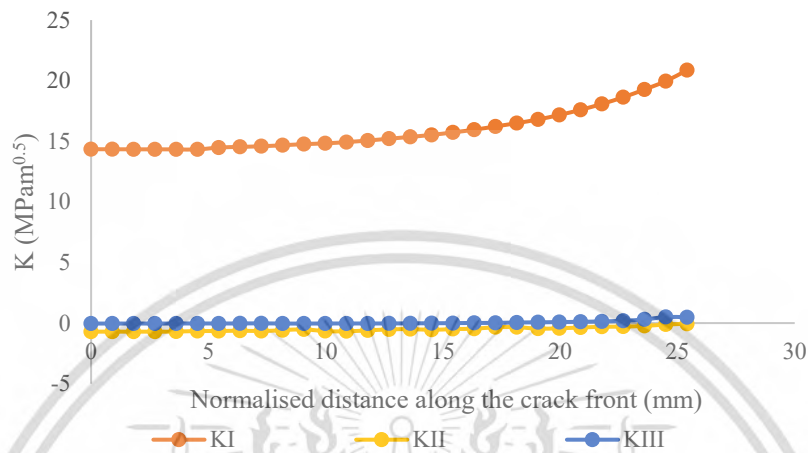


Figure 7.6 Comparison of Stress Intensity Factors (K) in relation to various crack modes (I, II, and III).

The negligible values of KII and KIII can be attributed to the specific combination of loading conditions. While braking induces both bending and torsional stresses, press fitting and masses in motion primarily contribute to bending stresses. As a result of the combined influence of these loading circumstances, mode I loading predominates, and shear and tearing effects are minor.

The prominence of mode I loading, represented by the significant KI component, highlights the importance of bending stresses in crack propagation. It indicates that crack growth primarily occurs due to opening and closing stresses, rather than shearing or tearing stresses. By understanding these findings, we can focus on mitigating mode I loading effects and developing appropriate measures to effectively prevent crack initiation and propagation.

### 7.3.2 Effect of Stable and Adverse Running Conditions on SIF Solutions

Figure 7.7 shows the variation of stress intensity factors along the crack front, which are determined under stable and adverse running conditions. As can be seen, the results show that SIF under adverse conditions is much greater than the stable condition. There is a remarkable finding that the maximum SIF takes place at the surface of crack point B and minimum at the deepest point A for relative depths ( $a/t=0.25$ ) and aspect ratios ( $a/c=0.75$ ), the SIF values decreased gradually as the distance from the crack tip increased. The SIF value

This material is reserved for educational use only, not allowed for commercial use.

Forbidden to modify the content, and cite the document when use.

of a railway axle under adverse running conditions is greater than under stable conditions due to several factors because of results in increased loads, including asymmetric bending loads, the contact lateral force between the wheel and the rail of the axle. These factors can lead to crack initiation and propagation in the axle, which can increase the SIF value. In Figure 7.8, the distribution of longitudinal stress for the semi-elliptical crack under combined press-fitting and the adverse loading of a wheelset is shown, and it is evident that the stress concentration is higher at the crack surface point B. The higher stress concentration at the crack tip can further increase the SIF value, resulting in a more critical structural state.

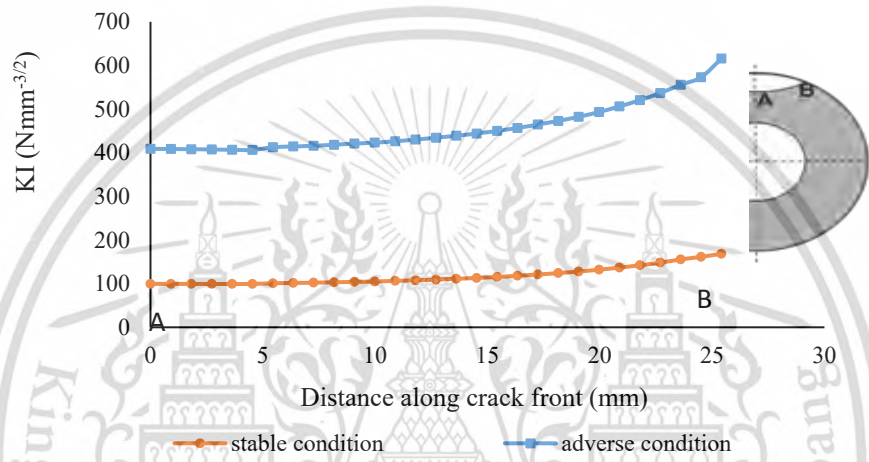


Figure 7.7 Comparison of stress intensity factor for stable and adverse running conditions.

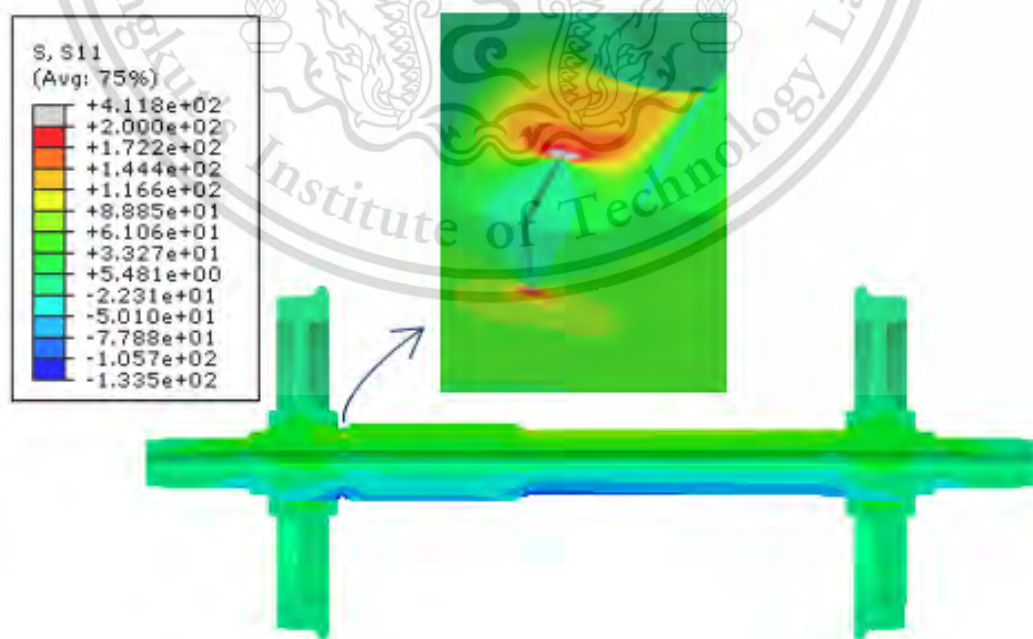


Figure 7.8 Distribution of the longitudinal stress for the semi-elliptical crack under combined press-fitting and the bending load of a wheelset in FEM.

This material is reserved for educational use only, not allowed for commercial use.

Forbidden to modify the content, and cite the document when use.

### 7.3.3 Effects of Press-Fitting on SIF

In Figure 7.9, the SIF values along the crack front are compared with and without the press-fitting effect of the wheelset assembly. The results indicate that the SIF value with the press-fitting effect is 13% greater than the one without it. The press fit creates contact stresses that cause the deformation of the components and that can lead to residual stresses. As a result, the press-fitting effect can increase the stiffness and strength of the component, which in turn increases the SIF values along the crack front. This suggests that the press-fitting effect should be considered in the design and analysis of the wheelset assembly to ensure its safe and reliable operation.

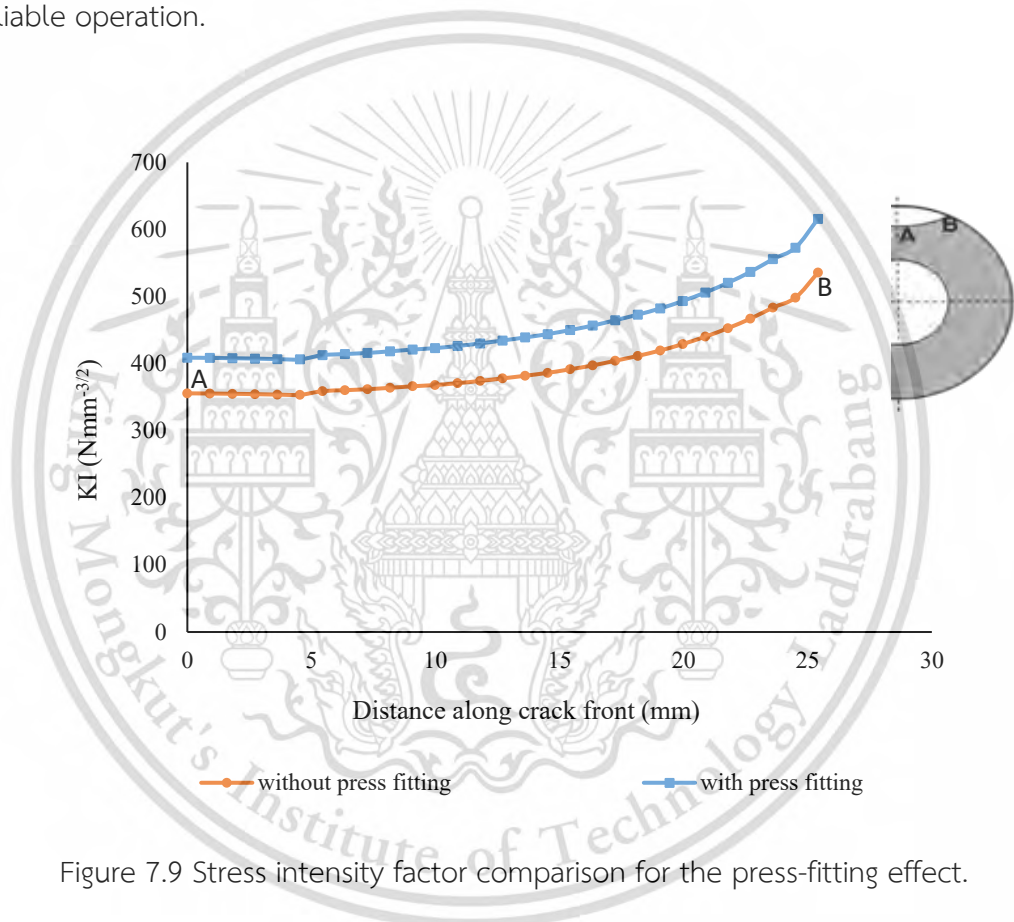


Figure 7.9 Stress intensity factor comparison for the press-fitting effect.

### 7.3.4 Studying the Rotary Bending Effect on SIF Solutions

In this section, stress intensity factors were evaluated under the rotation of the axle to understand the effect of rotary bending, according to the same procedure used for the previous section. Figure 7.10 shows the variation of the stress intensity factor as a function of rotational angle. It can be seen that when  $\theta = 0^\circ$ , the crack is fully open and positive because the maximum tensile stress is located at the crack front. On the other hand, the crack is fully closed when the rotation angle reaches the ( $\theta=180^\circ$ ), and the SIF is negative because of the

This material is reserved for educational use only, not allowed for commercial use.

Forbidden to modify the content, and cite the document when use.

maximum compressive stresses. This shows the principle of opening and closing the crack of the axle. The SIF values of crack surface point B are almost zero at  $\theta=90^\circ$ .

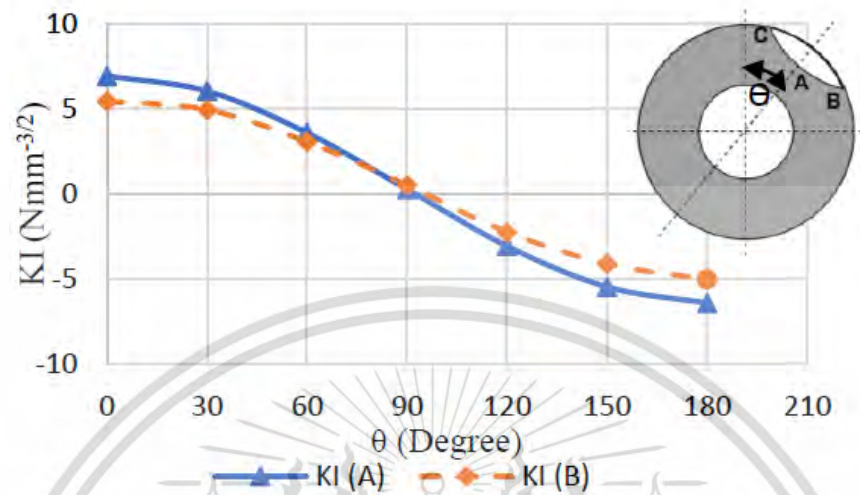


Figure 7.10 Stress intensity factor of the finite element model versus rotation angle.

### 7.3.5 Effect of crack shape on the stress intensity factor

The analysis of the impact of crack shape on the stress intensity factor (SIF) of a railway axle involves examining the longitudinal stress distribution near the crack with various crack geometries. Figure 7.11 displays the longitudinal stress distribution near the crack for three different crack configurations: (a) semi-elliptical crack with dimensions  $a=15\text{mm}$  and  $c=20\text{mm}$ , (b) circular crack with dimensions  $a=20\text{mm}$  and  $c=20\text{mm}$ , and (c) elongated semi-elliptical crack with dimensions  $a=20\text{mm}$  and  $c=15\text{mm}$ . The stress intensity factor distribution along the crack front based on the crack shape is compared in Figure 7.12.

First, in Case (a) representing the semi-elliptical crack ( $a=15\text{mm}$ ,  $c=20\text{mm}$ ), the stress intensity value at the deepest point A is higher than both Case (b), which represents a circular crack ( $a=20\text{mm}$ ,  $c=20\text{mm}$ ), and Case (c), which represents an elongated semi-elliptical crack ( $a=20\text{mm}$ ,  $c=15\text{mm}$ ). Additionally, the stress intensity factor at the deepest point A in Case (b) is higher than that in Case (c). These findings indicate that as the crack length ( $c$ ) increases, the stress intensity factor decreases. Conversely, when considering the SIF at the crack surface point C, Case (c) exhibits a higher value compared to the other two cases, with Case (a) having a higher SIF at surface point C compared to Case (b). Therefore, it can be concluded that as the crack depth ( $a$ ) increases, the stress intensity factor decreases.

The observed behavior can be explained by the redistribution of stress around the crack. As the crack deepens, the stress distribution becomes more evenly spread along the crack

front, leading to a reduction in stress concentration at the deepest point. Consequently, deeper cracks exhibit lower stress intensity factors at the deepest point. Similarly, as the crack length increases, the stress redistribution becomes more pronounced, resulting in a decrease in stress concentration at the crack surface point. As a result, the stress intensity factor decreases with increasing crack length. These findings underscore the significance of crack shape in determining the stress intensity factor and crack behaviour. Different crack geometries can substantially influence stress distribution and concentration, ultimately impacting the potential for crack growth and failure.

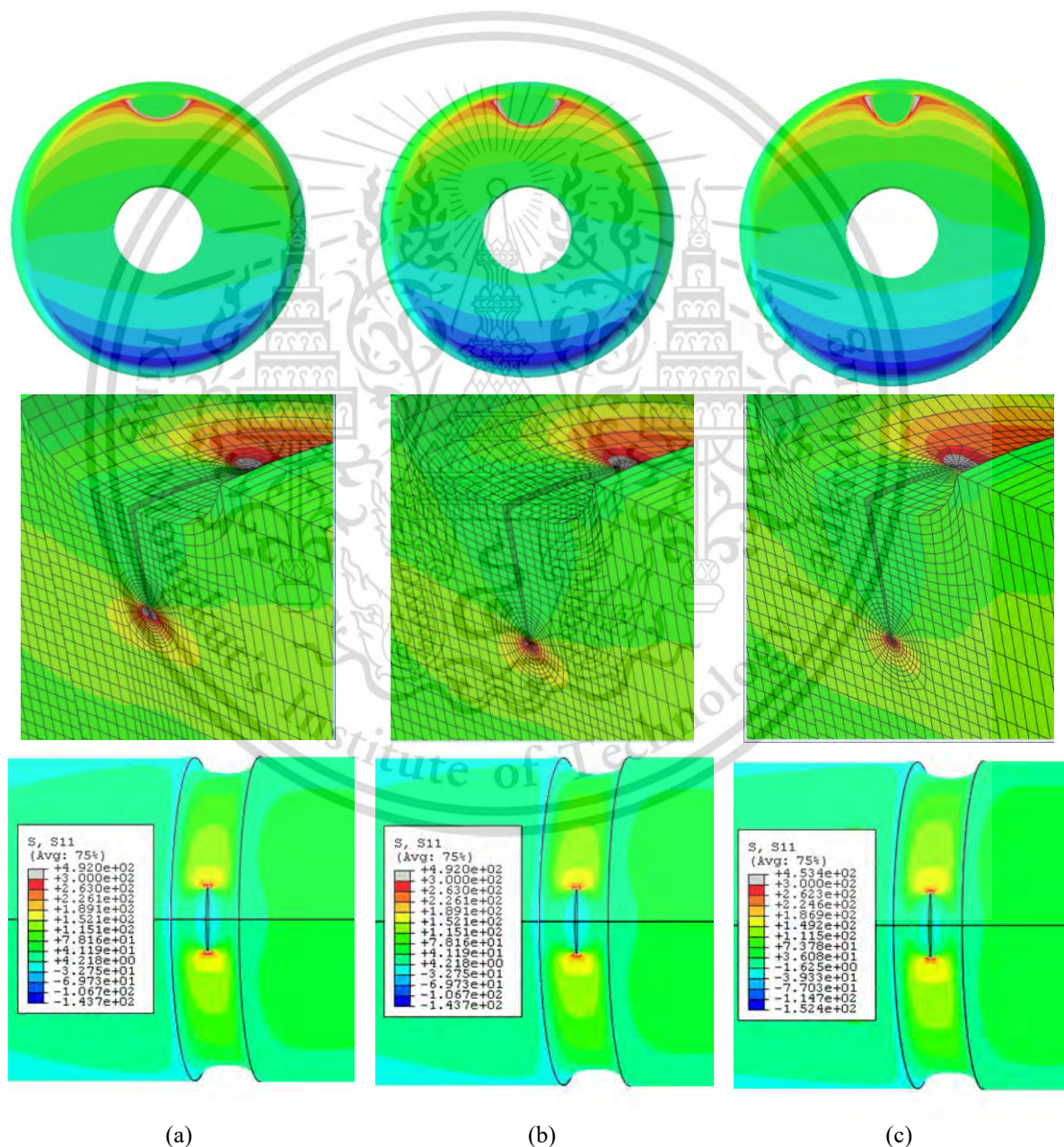


Figure 7.11 The longitudinal stress distribution near the crack with different crack geometries

Case (a)  $a=15\text{mm}$ ,  $c=20\text{mm}$ , Case (b)  $a=20\text{mm}$ ,  $c=20\text{mm}$ , Case (c)  $a=20\text{mm}$ ,  $c=15\text{mm}$ .

This material is reserved for educational use only, not allowed for commercial use.

Forbidden to modify the content, and cite the document when use.

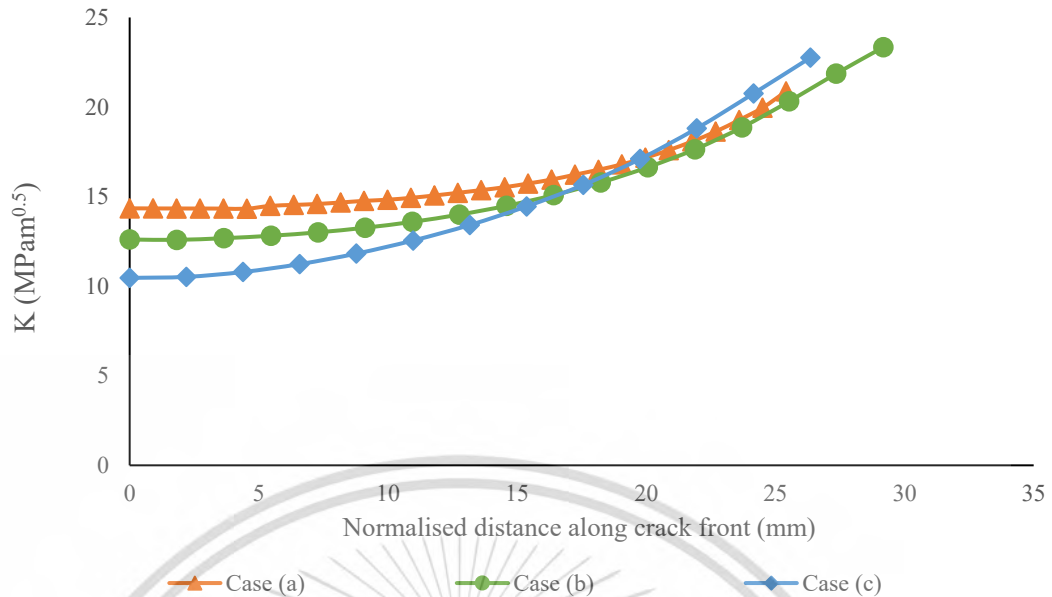


Figure 7.12 Comparison of the distribution of the Stress Intensity Factor (SIF) along the crack front based on the crack shape.

### 7.3.6 Effects of Thermal Loading and Braking

The study highlights the significant influence of combined loading conditions, including thermal loading, braking forces, press fitting, and the presence of masses in motion, on the Stress Intensity Factor (SIF) values of railway axles. The incorporation of braking forces in particular introduces additional bending and torsional stresses on the axle, resulting in an elevation of the KI component. This elevation is primarily attributed to the considerably higher magnitude of bending stresses induced by braking in comparison to those stemming from press fitting and masses in motion independently.

Figure 7.13 illustrates the combined loading conditions, categorized as follows: case 1 represents the combination of press fitting and masses in motion, case 2 involves the combined effect of braking, and case 3 focuses on the influence of thermal loading. Notably, the effect of braking on the SIFs stands out, with the results indicating a substantial 10% increase in the SIF value compared to the combination of press fitting and masses in motion.

Furthermore, the investigation into the influence of temperature on the Stress Intensity Factor (SIF) of railway axles revealed a significant increase of approximately 15% in the SIF at the surface point when subjected to temperature loading. This finding underscores the substantial role played by braking forces in exacerbating stress concentrations at the crack tip, thereby intensifying the potential for crack propagation.

This material is reserved for educational use only, not allowed for commercial use.

Forbidden to modify the content, and cite the document when use.

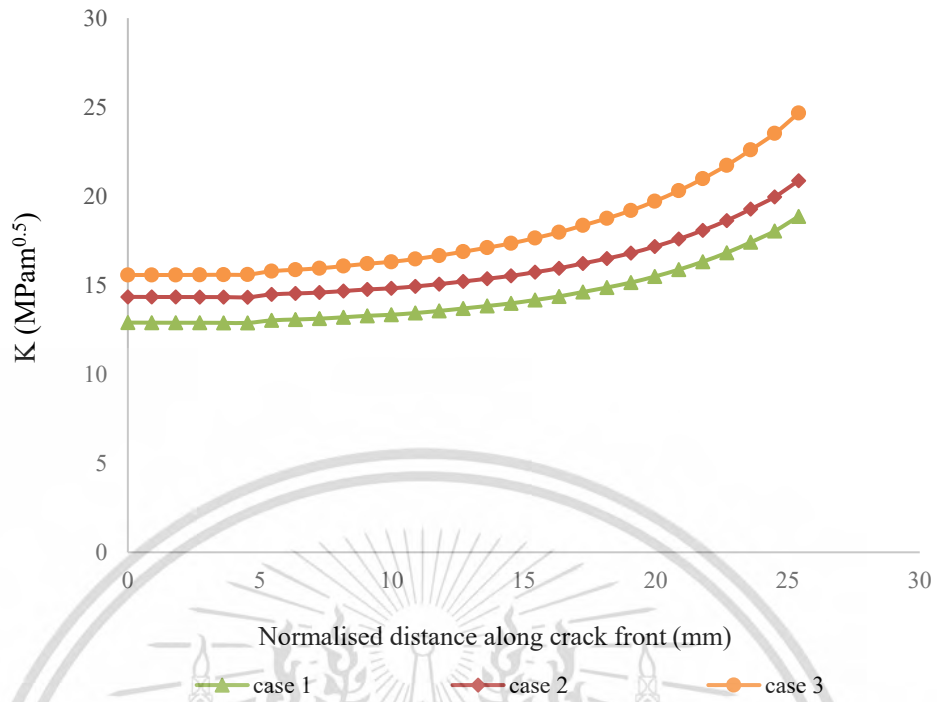


Figure 7.13 Comparison of Stress Intensity Factor (SIF) along the crack front under the different loading conditions.

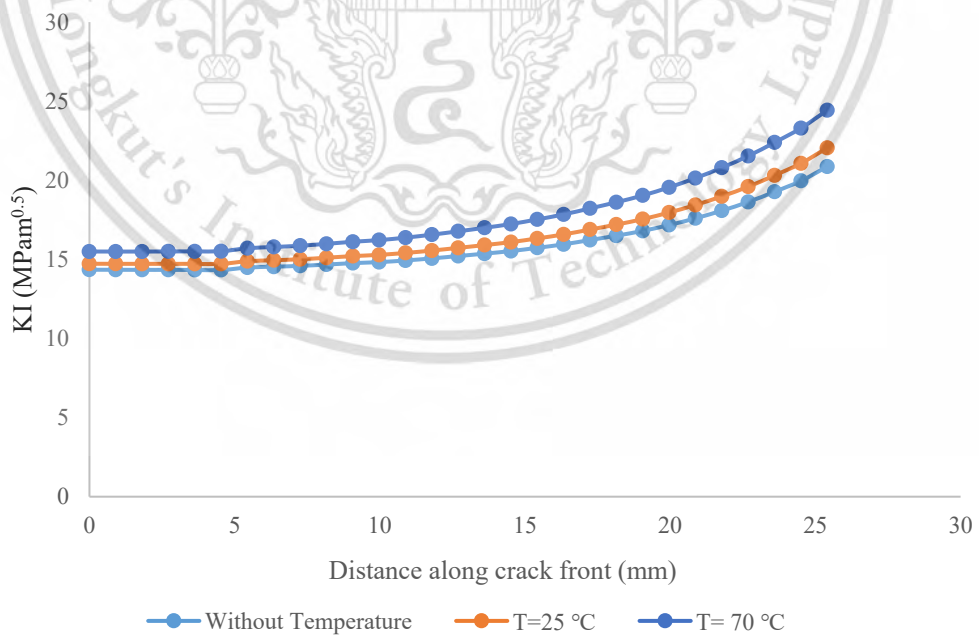


Figure 7.14 Comparison of Stress Intensity Factor (SIF) along the crack front under the different temperature load.

This material is reserved for educational use only, not allowed for commercial use.

Forbidden to modify the content, and cite the document when use.

The influence of temperature on the stress intensity factor (SIF) was investigated to understand its impact on structural integrity. The results reveal a clear correlation between temperature variations and the SIF. Initially, when temperature was not taken into account, the maximum SIF was determined to be  $20.87 \text{ MPam}^{0.5}$ . This baseline value provides a crucial reference point for evaluating the subsequent effects of temperature loading. Upon introducing a temperature load of  $25 \text{ }^{\circ}\text{C}$ , a noticeable increase in the SIF was observed, reaching  $22.054 \text{ MPam}^{0.5}$ . This escalation indicates the sensitivity of the structural response to thermal changes. Furthermore, as the temperature was raised to  $70 \text{ }^{\circ}\text{C}$ , the SIF experienced a further elevation, reaching  $24.43 \text{ MPam}^{0.5}$ , as depicted in Figure 7.14. This significant augmentation underscores the pronounced effect of temperature elevation on the structural integrity, highlighting the importance of accounting for thermal variations in structural analysis and design processes.

### 7.3.7 Crack Growth and Residual Lifetime

The analysis of crack growth rate and residual lifetime prediction has yielded several important findings. Initially, the stress intensity factors (SIF) were evaluated at the surface point and deepest point using finite element (FE) analysis. The crack increments at these locations were then calculated based on the Paris law, considering the cyclic interval range  $N$ . In Figure 7.15, fatigue crack life prediction diagrams are shown for different crack dimensions and orientations. Figure 7.15(a) represents the fatigue crack life prediction along the depth direction, while Figure 7.15 (b) shows the prediction along the length direction.

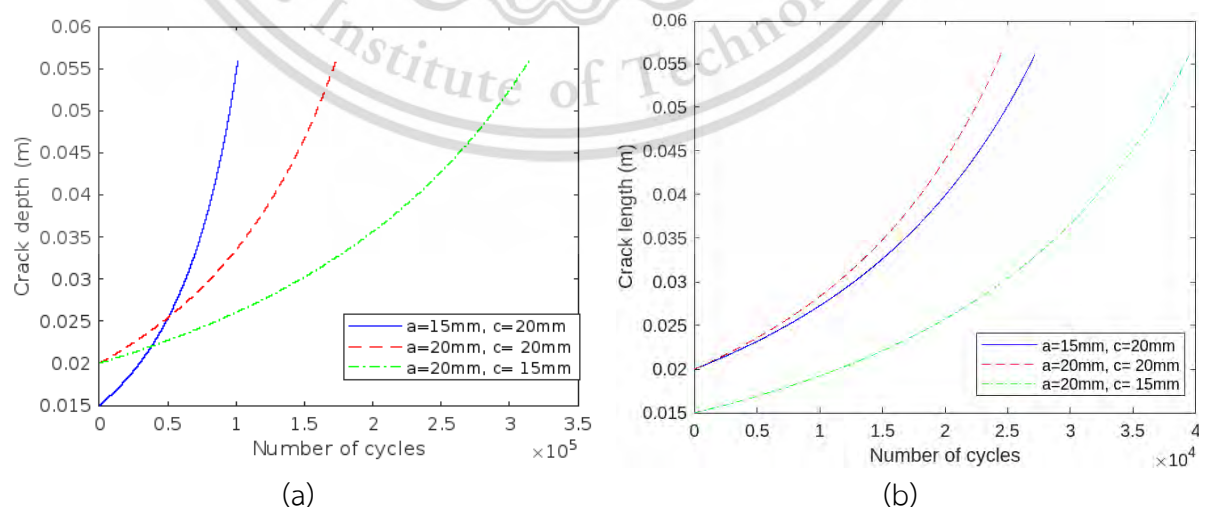


Figure 7.15 Fatigue crack life prediction diagrams based on the crack shape (a) along depth direction and (b) along length direction.

This material is reserved for educational purposes and is not to be used for commercial use.

Forbidden to modify the content, and cite the document when use.

Analyzing the results, it is evident that crack dimensions significantly influence the fatigue life of the structure. In terms of crack depth, case (a) ( $a=15\text{mm}$ ,  $c=20\text{mm}$ ) exhibits the shortest fatigue life, while case (b) ( $a=20\text{mm}$ ,  $c=15\text{mm}$ ) demonstrates the longest fatigue life. Conversely, in terms of crack length, case (b) ( $a=20\text{mm}$ ,  $c=20\text{mm}$ ) has the shortest fatigue life, while case (c) displays the longest fatigue life.

These observations can be explained by considering the crack shape and dimensions. In terms of crack depth, case (a) with a smaller crack depth ( $c$ ) experiences higher stress concentrations, leading to a shorter fatigue life. Conversely, case (c) with a larger crack depth exhibits lower stress concentrations and, consequently, a longer fatigue life. In terms of crack shape comparison, case (c) consistently demonstrates the longest fatigue life for both crack depth and length. This indicates that the specific crack dimensions and shape in case (c) result in a more favorable stress distribution and a higher resistance to crack growth, leading to an extended fatigue life.

Overall, these findings highlight the importance of considering crack dimensions and shape when predicting residual lifetime and estimating fatigue crack growth. The results from fatigue life prediction diagrams aid in understanding the critical areas prone to crack growth and allow for proactive maintenance and inspection strategies to ensure the structural integrity and safety of components subjected to cyclic loading.

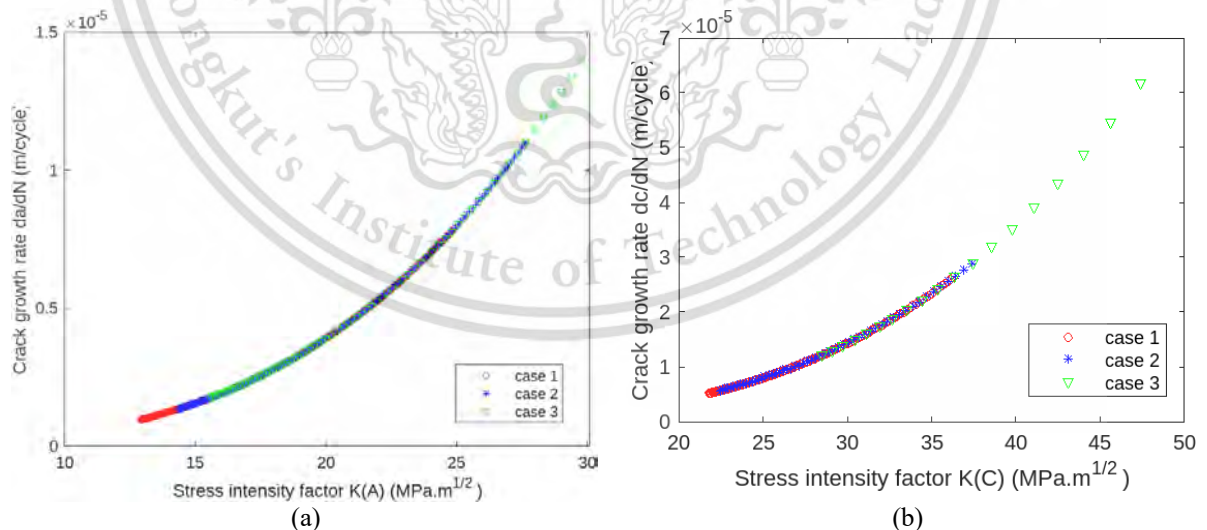


Figure 7.16 The comparison of the crack growth rate as a function of stress intensity factor upon different loading conditions (a) crack deepest point A and (b) crack surface point C.

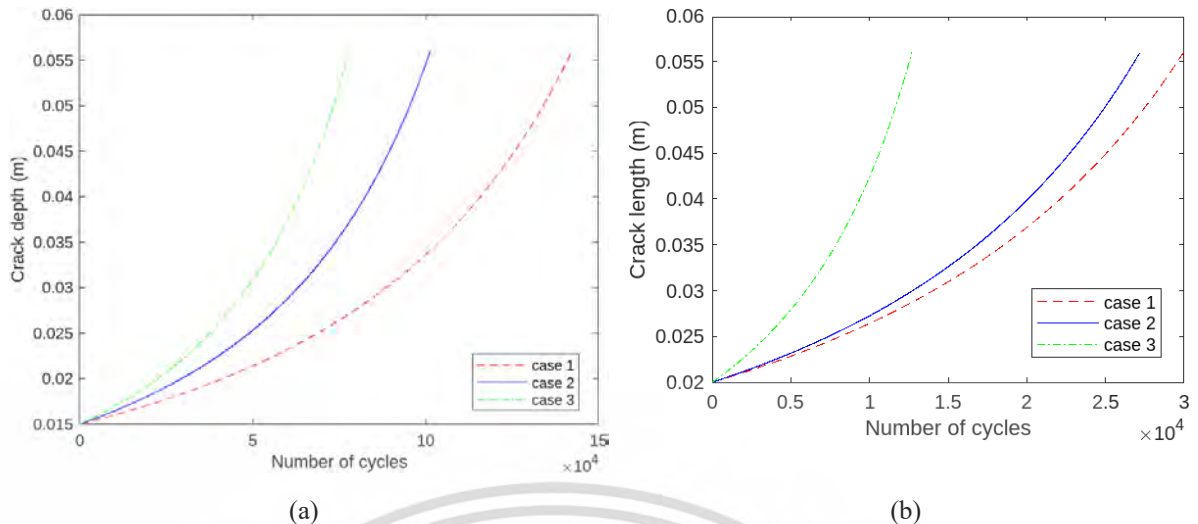


Figure 7.17 The comparison of the predicted life of the axle upon different loading conditions (a) crack deepest point A and (b) crack surface point C.

Figures 7.16 and 7.17 present comparisons of crack growth rate and residual lifetime prediction under three loading cases. The results reveal insights into the behavior of railway axles under different operational conditions. The presence of thermal loading and braking was found to significantly increase the surface crack growth rate in railway axles. In Case 1 with no braking effect, a surface crack with a depth ( $a=15\text{mm}$ ) exhibited a residual fatigue life of approximately  $1.4 \times 10^5$  cycles. However, when incorporating the braking effect, Case 2, in the analysis, the same crack depth ( $a=15\text{mm}$ ) showed a substantially prolonged residual fatigue life of  $1.0 \times 10^5$  cycles. The combination of thermal load and braking Case 3 further reduced the residual fatigue life to  $7.8 \times 10^4$  cycles.

Similarly, Case 1, neglecting the braking effect, a surface crack with a length ( $c=20\text{mm}$ ) had a residual fatigue life of approximately  $2.9 \times 10^4$  cycles. Nevertheless, when accounting for the braking effect, Case 2, the same crack length ( $c=20\text{mm}$ ) exhibited a significantly prolonged residual fatigue life of  $2.7 \times 10^4$  cycles. Addition of thermal loading (Case 3) further reduces the life to  $1.2 \times 10^4$  cycles. These findings underscore the crucial role of both thermal loading and braking effects in influencing crack growth rates in railway axles.

## 7.4 Discussion

This chapter engages in a comprehensive discussion of the key findings presented in the previous chapter. It provides an opportunity to contextualize the results within the broader framework of structural integrity assessment, fracture mechanics, and railway engineering. The

This material is reserved for educational use only, not allowed for commercial use.

Forbidden to modify the content, and cite the document when use.

discussions include insights into the implications of the findings, the limitations of the study, and avenues for future research.

#### *7.4.1 Impact of Running Conditions*

The study delves into the effect of stable and adverse running conditions on the stress intensity factor (SIF) of railway axles. Results have demonstrated that SIF under adverse running conditions is significantly higher than under stable conditions. Adverse conditions introduce increased loads, including asymmetric bending loads and contact lateral forces between the wheel and the rail. These factors lead to crack initiation and propagation, contributing to increased SIF values.

Implications:

- Railway operators must be aware of the potential for increased SIF under adverse running conditions, necessitating more frequent inspections and maintenance.
- Further research may explore advanced materials and designs to mitigate the effects of adverse running conditions on axles.

#### *7.4.2 Press Fitting Effect*

The investigation of the press-fitting effect on SIF values reveals that press fitting increases the SIF by 13%. Press fit creates contact stresses that cause component deformation and residual stresses, ultimately enhancing component stiffness and strength.

Implications:

- The findings underscore the importance of considering the press-fitting effect in the design and analysis of wheelset assemblies.
- Engineers and designers should explore ways to optimize press-fitting processes for improved component performance.

#### *7.4.3 Effect of Crack Shape*

The study systematically explores the impact of different crack shapes, including semi-elliptical, circular, and elongated semi-elliptical cracks. The findings indicate that deeper cracks exhibit lower SIF values, while longer cracks experience a decrease in SIF due to stress redistribution around the crack.

Implications:

This material is reserved for educational use only, not allowed for commercial use.

Forbidden to modify the content, and cite the document when use.

- These insights are valuable for proactive maintenance and inspection strategies, which can be tailored to specific crack geometries.
- The research encourages the development of materials and designs that resist stress concentration based on crack shape.

#### *7.4.4 Braking Effect*

The research has highlighted the substantial influence of braking forces on the SIF and fatigue life of railway axles. The presence of braking forces increases SIF and reduces the residual fatigue life, emphasizing the importance of considering braking effects in structural assessments.

Implications:

- Railway operators should integrate braking effects into their maintenance and inspection schedules.
- This research underlines the need for optimizing brake systems to minimize the impact on structural integrity.

#### *7.4.5 Influence of Thermal Load*

Thermal loading has been explored in this study, revealing a significant increase in SIF when subjected to temperature variations. Thermal loading is found to exacerbate stress concentrations at the crack tip, further intensifying the potential for crack propagation.

Implications:

- Railway systems in regions with significant temperature variations should incorporate thermal effects into their safety assessments.
- The research encourages the development of materials and coatings that mitigate thermal-induced stress concentrations.

#### *7.4.6 Further Research*

The complexity of assessing the structural integrity of railway axles under dynamic loads highlights the need for further research. Future investigations in this area can explore advanced numerical methods, experimental validation, and innovative design approaches to enhance the safety and reliability of railway systems.

This material is reserved for educational use only, not allowed for commercial use.

Forbidden to modify the content, and cite the document when use.

Recommendations for Future Research:

- Conduct experimental studies to validate the numerical findings and to gain insights into real-world structural behavior.
- Explore innovative design approaches, such as the use of composite materials and advanced manufacturing techniques, to improve axle durability.
- Investigate the effects of combined loading conditions on different components of the railway system, including wheels, tracks, and bearings.

## 7.5 Conclusion

In conclusion, this research has presented a comprehensive examination of the factors influencing the stress intensity factor (SIF) and residual lifetime of railway axles under various operational conditions. The findings demonstrate the significant impact of various factors, including running conditions, press fitting, crack shape, braking effect, and thermal load, on the structural integrity and performance of axles.

These results have practical implications for the design, maintenance, and inspection of railway axles. They underscore the need for a comprehensive approach to fracture mechanics analysis that accounts for different operational factors and highlight the importance of proactive maintenance strategies.

As the railway industry continues to evolve, this research paves the way for further investigations into advanced numerical methods, experimental validation, and innovative design approaches. Such endeavors are essential to enhance the safety and reliability of railway systems and to meet the growing demands of high-speed and heavy-load transportation.

Overall, the study contributes to a deeper understanding of the structural behavior of railway axles under dynamic loading conditions and offers valuable insights for the design, maintenance, and inspection of these critical components. The findings presented here serve as a foundation for future research and advancements in railway engineering, ensuring the continued safety and efficiency of railway systems.

## CHAPTER 8

# 8 MULTI-OBJECTIVE OPTIMIZATION OF LIGHTWEIGHT INBOARD BEARING DESIGN FOR HIGH-SPEED RAILWAY AXLE

### 8.1 Overview

#### 8.1.1 Introduction to Inboard Bearing Design

Within the realm of high-speed rail transportation, the role of axles is pivotal for ensuring both the safety and efficiency of train operations. The design of these axles necessitates a delicate balance between durability and weight. Heavier axles can result in elevated energy consumption, affect riding comfort and stability performance, and reduce operational efficiency. Wheelset configurations for high-speed trains can be classified into two primary types: inboard and outboard bearing wheelsets. The utilization of inboard bearings within bogies has gained significant attention and development in recent times.

Inboard bearing axles have garnered interest due to their elongated design, which offers improved design adaptability as a result of greater available space surrounding the axle. It's worth noting that low track force bogies commonly adopt an inboard bearing arrangement, leading to lighter bogie assemblies with reduced structural demands. These bearings present distinct advantages, including diminished total and unsprung mass, as well as reductions in lateral forces and moments of inertia. Such attributes not only enhance vehicle maneuverability along curves but also bolster track compatibility. Additionally, the adoption of inboard bearing axles proves beneficial in addressing specific maintenance challenges associated with conventional wheelsets.

In the context of high-speed rail transportation, the weight of rail vehicle components is of paramount importance. A substantial proportion of a rail vehicle's overall mass, up to 41%, resides within the railway bogie, with the axle accounting for approximately 35% of a standard wheelset's total mass. This scenario underscores a considerable potential for weight reduction. However, the endeavor of reducing weight in axles is intricate due to the continuous stresses and loads imposed on them during their operational life, including cyclic bending fatigue.

### 8.1.2 Multi-Objective Optimization

The principal challenge lies in achieving weight reduction while simultaneously ensuring durability, especially for high-speed trains. To address this challenge, the application of multi-objective optimization techniques has emerged as a valuable approach. These techniques facilitate the development of lightweight yet resilient axle designs that align with the criteria of enduring fatigue performance. Previous research in this field has predominantly concentrated on individual aspects of axle design, such as structural or material strength, vibration resistance, and fatigue performance. However, many of these studies have lacked a comprehensive strategy that considers both weight reduction and durability as complementary objectives.

This research work aims to illuminate the intricate balance between axle weight reduction and structural integrity while satisfying the infinite-life fatigue criterion. It seeks to provide valuable insights into the development of high-speed railway transportation systems. The specific objectives of this research are as follows:

- To comprehensively investigate the advantages of inboard bearing axles in terms of mass reduction, deflection, and stress mitigation, with a focus on high-speed rail transportation.
- To leverage multi-objective optimization techniques for axle design, seeking to achieve a substantial reduction in mass while minimizing stress levels.
- To assess improvements in fatigue resistance and durability in axle designs.
- To establish a finite element model using ABAQUS and develop Python scripts for analysis.
- To utilize the Pointer algorithm in Isight for optimization and Fe-safe for the assessment of infinite fatigue life.

By adeptly navigating the trade-off between weight reduction and structural integrity, this research significantly contributes to the advancement of railway transportation systems and addresses the challenges posed by high-speed rail operations. The subsequent sections

This material is reserved for educational use only, not allowed for commercial use.

Forbidden to modify the content, and cite the document when use.

of this dissertation will delve into the methodology, analysis, findings, and discussions that contribute to achieving these objectives.

### 8.1.3 Finite element model

Using Python script, the FE model is implemented in Abaqus/CAE to parameterize the geometric dimensions and automatically apply the contact and boundary conditions as the geometry is modified during the optimization procedure. The wheelset model in this work has two versions: one is an inboard bearing axle model and the other is an outboard bearing axle model. As illustrated in Figure 8.1, C3D8R hexahedral solid element type is chosen to ensure convergence and minimize computational cost by carefully meshing the contact of the wheelset. The EA4T steel, which is commonly used in modern railroad axles, is a linear elastic body with a Young's modulus of  $E=206$  GPa and a Poisson's ratio of 0.3.

Master-slave contact type with the user-defined specific radial interference fit technique [25] was used to represent the press fittings. In the context of highly nonlinear contact analyses, the interference is assumed to be 0.2 millimeters [32] and a friction coefficient of 0.1 is chosen as a consistent parameter to strike a balance between efficiency and accuracy. Using this procedure, solely normal contact is established. The behavior in the tangential direction adheres to the conventional Coulomb approach, wherein the maximum permissible shear stresses are associated with the contact pressure arising from the press fit between the contacting parts on the contact surfaces[25] .

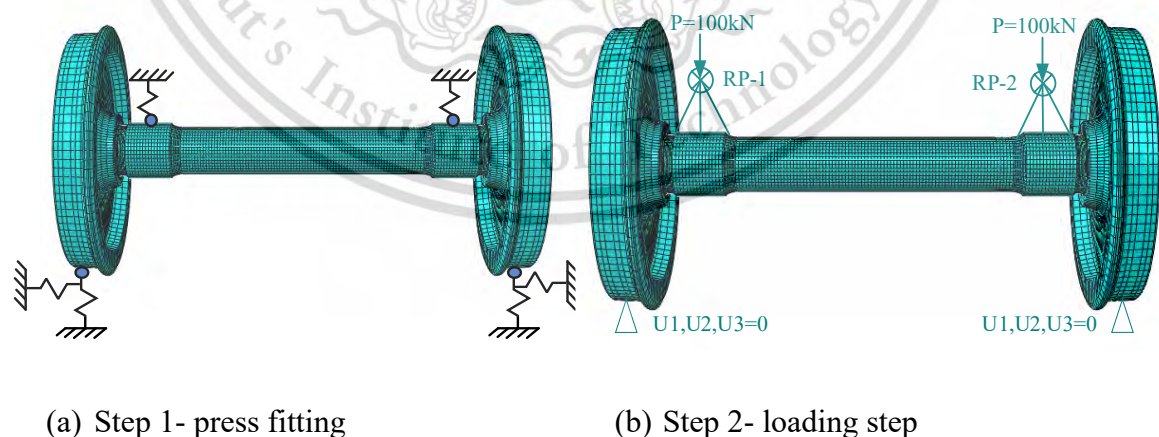


Figure 8.1 Mesh, loading and boundary conditions of FE model.

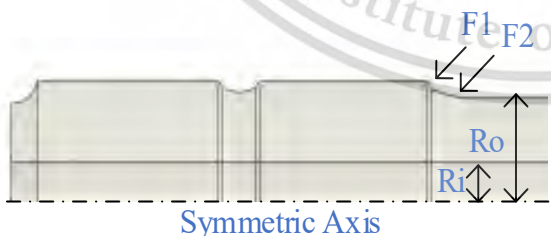
A strategic numerical approach was employed to address the issue, involving a two-step analysis: the first stage encompassing the press fitting; second step followed by loading. To

stabilize the wheelset model, spring elements were implemented Figure 3 (a). Specifically, the axle is confined by two springs exerting forces in directions 1 and 3, while the wheels encounter constraint through springs in three directions. The stiffness of these spring elements was assigned as 1 N/mm, a value devoid of physical meaning. After constructing the residual stress field within the axle owing to press-fitting, necessitating the deactivation of all spring elements. The loading P owing to the bogie and train was applied to the journal bearings' middle plane Figure 8.1 (b). Lateral forces and braking forces were neglected in the current case because the vertical axle load is the most critical factor.

### 8.1.4 Parametric design optimization algorithm

In the context of optimizing the design of an inboard bearing for railway axle, the primary objective is to minimize the maximum mises stress while simultaneously minimizing the mass. This inherently gives rise to a multi-objective problem, where the ideal design should achieve a balance between minimizing mass and stress while satisfying the infinite life fatigue criterion. To address these challenges, the present research defines the mises stress parameter as an upper limit, set at half of the yield stress, to ensure a safety factor greater than 2. The maximum permissible stresses for hollow axles at transition fillets of EA4T steel is 145 MPa. This constraint formulation captures the safety and functionality aspects of the design while considering stress-induced failure modes. The objective, constraint and design variable are as shown in Table 8.1.

Table 8.1. Objective, constraint, and design variable at initial design (all dimensions in mm)

 <p>The diagram shows a cross-section of a railway axle with a central 'Symmetric Axis'. Two forces, F1 and F2, are applied to the top surface. Two dimensions, Ri and Ro, are indicated with arrows pointing to the inner and outer radii of a fillet on the axle's surface.</p>	<p>Optimization – Min {mass, S_mises_max}</p> <p>Constraint – Max {S_Mises_max &lt; 72.5 MPa (max: permissible stress / 2)}</p> <p>Starting Design Points</p> <p>F1 = 75.0 [60.0 &lt; x &lt; 90.0]</p> <p>F2 = 15.0 [12.0 &lt; x &lt; 18.0]</p> <p>Ri = 30.0 [24.0 &lt; x &lt; 36.0]</p> <p>Ro = 85.0 [ 68.0 &lt; x &lt; 102.0]</p>
--	---

For the optimization process, the Pointer Automatic Optimizer is selected due to its ability to effectively handle diverse optimization scenarios. This selection allows the optimizer to adapt to different optimization landscapes. It provides the flexibility to employ a single

This material is reserved for educational use only, not allowed for commercial use.

Forbidden to modify the content, and cite the document when use.

algorithm or all four simultaneously. Throughout the optimization process, the optimizer continually assesses the performance of each algorithm and dynamically adjusts internal parameters such as step sizes and iterations to achieve optimal results. This capability ensures that the optimization process is efficient and effective in discovering high-quality designs.

## 8.2 Findings

The study has produced several key findings that contribute to the understanding of inboard bearing design in the context of high-speed railway axles:

### 8.2.1 Analysis of an inboard and outboard bearing wheelset FEA results

Comparing an inboard and outboard bearing wheelset highlight that the inboard bearing configuration results in a lighter wheelset compared to the conventional trailer bogie axle setup. The investigation, comprising both comprehensive finite element (FE) simulations and assessments based on the EN 13103/4 standard for outboard bearing wheelset and the inboard bearing wheelset follows BS 8535 standard calculations [33,36,37], underscores a remarkable similarity in longitudinal stress distribution patterns between the calculated and FEM results ( Figure 8.2). The minor 8% divergence observed can be attributed to residual stress originating from the press fitting process. The axle's most prominent bending stress emerges at the stress concentration fillet area, situated farthest from the natural axis.

The location of the highest bending stress within the axle is notable; it occurs at the stress concentration fillet area, farthest from the natural axis as shown in Figure 8.3. The utilization of inboard bearings in a wheelset is advantageous from the perspective of axle stress. This is attributed to the mitigation of lateral forces, resulting in a reduction of the bending moment experienced by the axle. Under similar loading conditions, the maximum bending stress encountered by the inboard bearing is notably 38% lower than that experienced by the outboard bearing. An interesting contrast between the two bearing types is observed in their deflection behavior as shown in Figure 8.4. The inboard bearing experiences a negative deflection 0.59 mm, while the outboard bearing demonstrates a positive deflection 0.70 mm. This phenomenon can be explained by differences in the load distribution and structural arrangement of the two bearing configurations. The weight of the inboard bearing axle is 8% lower than outboard bearing axle. This distinction can be reasoned by taking into account the varying structural layouts and load dispersion characteristics inherent to the two distinct bearing types.

This material is reserved for educational use only, not allowed for commercial use.

Forbidden to modify the content, and cite the document when use.

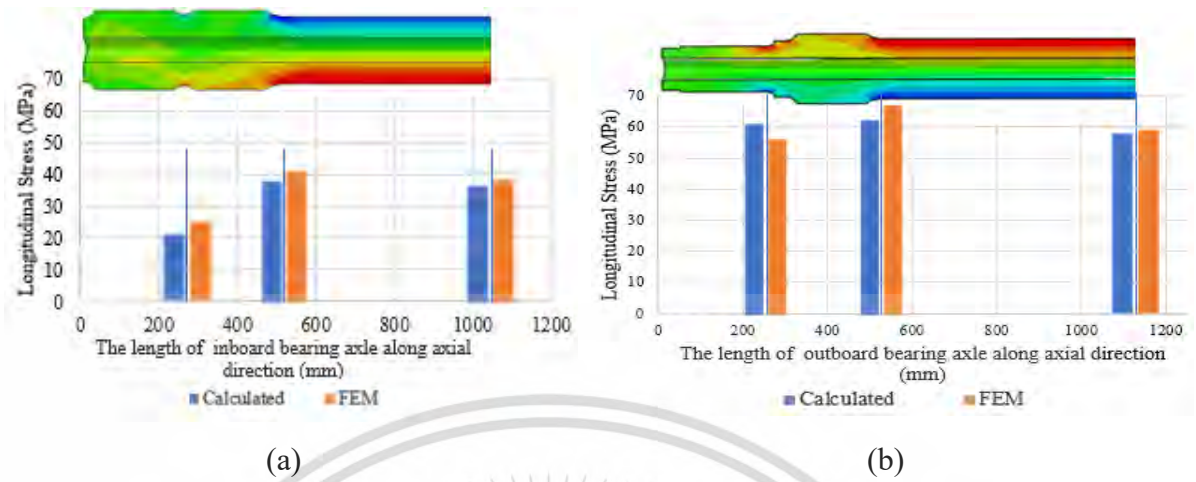


Figure 8.2 Comparison of longitudinal stresses of calculated and FEM (a) inboard bearing axle and (b) outboard bearing axle.



Figure 8.3 Comparison the deflection of the axle under the loading (a) for the assembled inside axle boxes (b) for the assembled outside axle boxes.

### 8.2.2 Identification of optimal design

Figure 8.4 shows the Pareto Front of Pareto-Optimal designs generated by plotting the mass objective vs. the  $S_{mises\_max}$  objective. The green dot corresponds to the optimal solution composing the Pareto front, blue dots are the possible optimum points while the black plots are the dominated solutions. From Figure 8.4, it can be seen that the mass of the wheelset is almost linear and the coefficient of determination  $R^2$  for this linear relationship is calculated to be 0.9115, indicating a strong correlation between the two objectives.

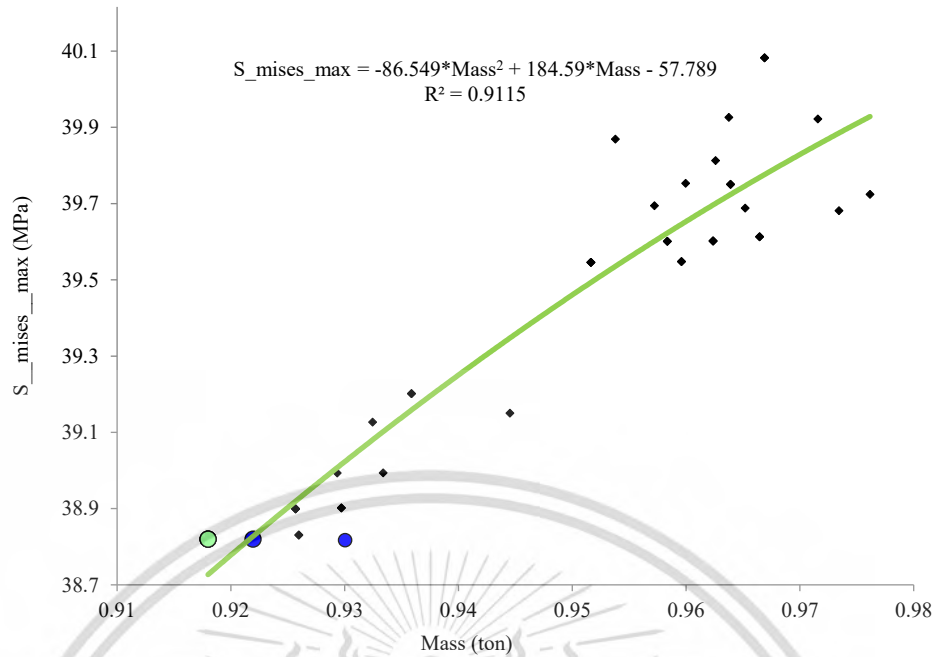


Figure 8.4 Pareto plot of  $S_{mises\_max}$  vs. mass from optimization.

Figure 8.5 illustrates a 3D contour graph that depicts the relationship between design feasibility,  $S_{mises}$ -stress, and mass. The contours on the graph serve as insightful indicators of the interaction between these three factors. Points closer to the peak of the contour correspond to regions of higher design feasibility as the contour lines shift towards lower values of design feasibility. Correlation map (Figure 8.6) shows the impact of model parameters on target objectives and solid lines represent stronger correlations than dash lines. It can be used to calculate the rank and linear correlation values for every pair of parameters in a model. The inner radius parameter (Ri) and  $S_{mises\_max}$  have the strongest inverse linear correction (Rank = -0.978 and Linear coefficient = -0.998) among other parameters.

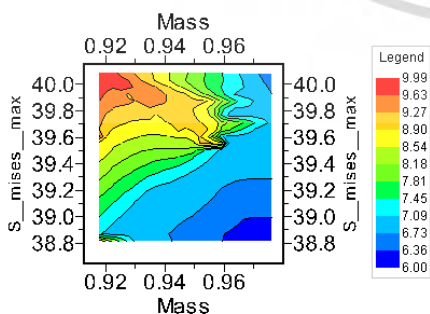


Figure 8.5 3D contour graph of design feasibility vs mass,  $S_{mises\_max}$ .

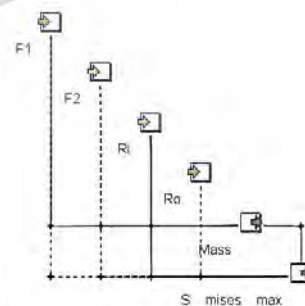


Figure 8.6 Correlation map of input and output parameters.

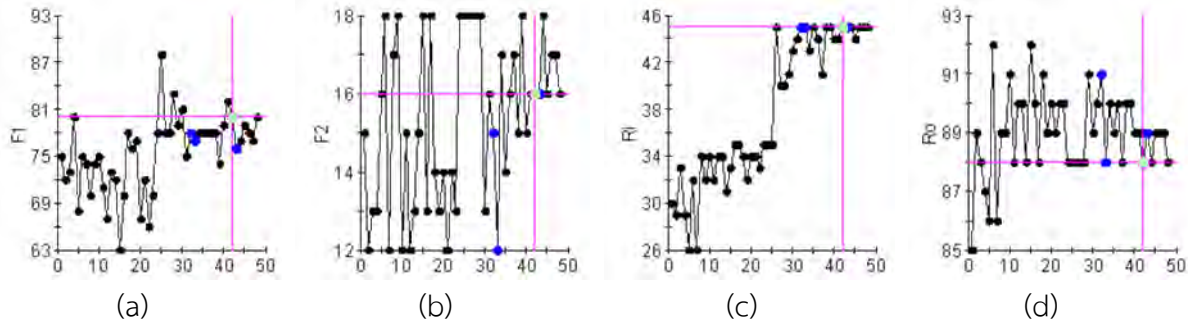


Figure 8.7 History of design variable optimization process (a) F1, (b) F2, (c) Ri, (d) Ro.

Figure 8.7 illustrates the design variable optimization process history for F1, F2, Ri, and Ro. Graphs show the change of such parameters during the analysis run by run and provide an insight into the convergence of the results. Table 2 presents a comparison between initial and optimum design points, indicating reductions in mass of axle 4% (0.315 to 0.302 tons) and stress 4% (40.39 to 38.82 MPa) achieved through optimization.

Table 8.2 Comparison of the starting design points and optimum design points of inboard bearing axle.

	F1(mm)	F2(mm)	Ri(mm)	Ro(mm)	Mass(ton)	S_mises_max(MPa)
Starting design points	75	15	30	85	0.315	40.39
Optimal design points	80	16	45	88	0.302	38.82

### 8.2.3 Assessment of infinite life

Figure 8.8 presents the results of the radial fatigue reverse factor (FRF) contour analysis before and after an optimization process. The analysis is focused on the inboard bearing axles, particularly their shoulder fillets, with the goal of enhancing their fatigue performance. The key observation is that both of the design points satisfy the infinite fatigue life condition and the minimum DV Radial FRF value, which was initially 4.59, has increased to 4.64 after the optimization process. This improvement in the FRF indicates that the axles' fatigue resistance under radial loading conditions has been enhanced due to the optimization method applied.

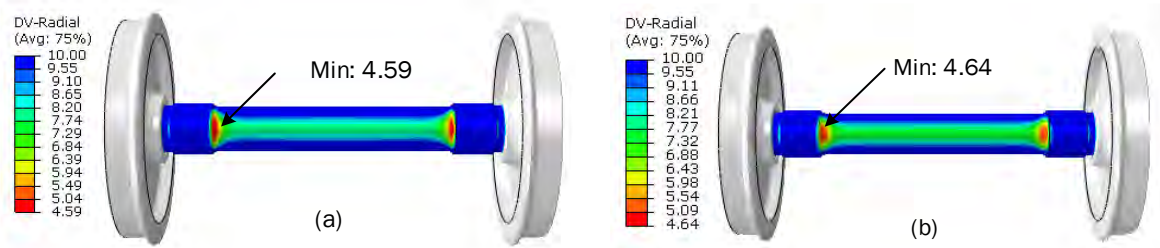


Figure 8.8 Radial FRF contour of (a) before optimization and (b) after optimization.

### 8.3 Discussion

The findings from this research offer valuable insights into the multi-faceted aspects of inboard bearing design for high-speed railway axles. Notably, inboard bearing axles exhibit several advantages, including reduced weight, lower stress levels, and enhanced fatigue resistance compared to outboard bearing axles. These advantages are crucial for the efficiency and performance of high-speed train operations.

Furthermore, the application of multi-objective optimization techniques demonstrates the potential for significant improvements in axle design. The optimization process results in reduced mass and stress levels, making the axles more efficient and durable. The linear relationship between mass and stress, as indicated by the strong correlation ( $R^2$ ), suggests that optimizing for one objective can lead to improvements in the other.

The assessment of infinite life highlights that the optimization process does not compromise the axles' ability to withstand fatigue under radial loading conditions. The improved FRF values indicate that the axles' fatigue resistance is enhanced through optimization.

### 8.4 Conclusions

#### 8.4.1 Key Insights from Multi-Objective Optimization

The primary findings resulting from the multi-objective optimization of inboard bearing design can be summarized as follows:

- Inboard bearing axles offer substantial weight reduction (8%) compared to outboard bearing axles, contributing to improved train efficiency and reduced aerodynamic forces.
- Stress levels in inboard bearing axles are significantly lower (38%) than in outboard bearing axles, enhancing their durability and fatigue resistance.
- Multi-objective optimization techniques can effectively reduce axle mass (4%) and

This stress levels (4%), leading to more efficient and durable axle designs.

Forbidden to modify the content, and cite the document when use.

- The optimization process does not compromise the axles' ability to withstand fatigue under radial loading conditions, as indicated by improved FRF values.

#### 8.4.2 Recommendations for High-Speed Rail Industry

The findings of this research have several implications and recommendations for the high-speed rail industry:

**Preference for Inboard Bearing Axles:** The high-speed rail industry should consider a preference for inboard bearing axles due to their advantages in weight reduction, stress mitigation, and fatigue resistance. Inboard bearing axles are well-suited for high-speed train operations.

**Utilization of Multi-Objective Optimization:** The industry can benefit from the utilization of multi-objective optimization techniques to enhance axle design. These techniques can lead to more efficient, lightweight, and durable axles, contributing to the overall performance of high-speed trains.

**Continuous Improvement:** Ongoing research and development efforts should focus on continuously improving axle design, with an emphasis on reducing weight and enhancing structural integrity. The findings of this research provide a foundation for further advancements in high-speed rail transportation systems.

In conclusion, this research sheds light on the intricacies of axle design for high-speed rail transportation, highlighting the advantages of inboard bearing axles and the potential for multi-objective optimization. The insights and recommendations presented in this study can significantly contribute to the development of more efficient and reliable railway transportation systems.

## CHAPTER 9

# 9 CONCLUSION

In this chapter, we offer a comprehensive conclusion to this doctoral dissertation by summarizing the key findings of the seven research papers, highlighting their contributions to the field of railway axle engineering, discussing their implications for the railway industry, acknowledging study limitations, suggesting areas for future research, and concluding with a reflection on the research's significance.

### 9.1 Summary of Key Findings

#### 9.1.1 *Effect of Press-Fitting Interference on Railway Wheel and Axle Assemblies*

This research has investigated the impact of press-fitting interference on railway wheel and axle assemblies. The findings indicate that press fitting significantly influences the stiffness and strength of the assembly, leading to enhanced structural performance. Press fitting increases the holding torque capacity, emphasizing its importance in maintaining the integrity of the assembly.

#### 9.1.2 *Press-Fitting Force Characteristics and Holding Torque Capacity*

The analysis of press-fitting force characteristics and holding torque capacity provides an insight into the mechanics of the assembly. It highlights the need for optimal press-fitting interference for achieving desired stiffness and strength, a crucial aspect of railway axle design.

#### 9.1.3 *Influence of Press-Fitting on Fatigue Life*

The research has explored the influence of press fitting on the fatigue life of railway axles. It emphasizes that press fitting can enhance the axle's durability, mitigating the risk of fatigue failure. Understanding the impact of press fitting is instrumental in designing robust railway axle systems.

#### 9.1.4 *Multiaxial Fatigue-Life Prediction Considering Braking Effects*

Multiaxial fatigue-life prediction, considering the effects of braking, is essential for ensuring the safety of railway systems. The findings reveal the significance of considering

multiaxial loading conditions, particularly the impact of braking forces, in predicting the fatigue life of railway axles.

### *9.1.5 Assessing the Impact of Press-Fitting, Running Conditions, Braking and Axle Hot Box Bearing Temperature on the Stress Intensity Factor and Residual Lifetime of Railway Axles*

This research investigates the influence of various operational conditions on the stress intensity factor (SIF) and residual lifetime of railway axles. It finds that adverse running conditions, press fitting, crack shape, braking effects, and thermal loading significantly impact axle integrity. The research underscores the importance of proactive maintenance and innovative design approaches to enhance the safety and reliability of railway systems, emphasizing the need for further research in advanced numerical methods and experimental validation.

### *9.1.6 Multi-Objective Optimization of Lightweight Inboard Bearing Design*

The multi-objective optimization of lightweight inboard bearing design provides innovative solutions for enhancing railway axle systems. It showcases how advanced engineering methods can lead to lighter, yet more robust, axle components.

## **9.2 Contributions to Knowledge**

### *9.2.1 Advances in Railway Axle Engineering*

The collective research presented in this dissertation contributes significantly to the field of railway axle engineering. It provides a deeper understanding of the complex interplay of factors affecting axle performance, offering engineers valuable insights into structural design and safety.

### *9.2.2 Innovative Solutions*

The research papers have introduced innovative solutions, methodologies, and insights that can be applied to enhance the safety, durability, and performance of railway axle systems. These innovations have the potential to revolutionize railway engineering practices.

## 9.3 Implications for the Railway Industry

### 9.3.1 Safety Enhancements

The findings of this research have direct implications for enhancing the safety of railway operations. By considering the influence of press fitting, multiaxial fatigue, and adverse running conditions, railway operators can implement advanced safety measures to prevent failures and accidents.

### 9.3.2 Maintenance and Durability

The research also provides insights into the maintenance and durability of railway axle systems. The multi-objective optimization and fatigue-life prediction findings suggest proactive maintenance strategies for prolonged durability and reduced maintenance costs.

## 9.4 Limitations and Future Research

### 9.4.1 Study Limitations

Despite the valuable insights gained, this research is not without limitations. These include the simplifications made in numerical models, assumptions related to materials, and the exclusion of certain environmental factors. Future research can address these limitations to refine our understanding further.

### 9.4.2 Areas for Future Research

Several potential areas for future research are suggested. These encompass the development of more accurate numerical models, comprehensive material studies, and a focus on the environmental impact of railway axle systems. Investigating advanced materials, manufacturing methods, and smart monitoring systems also hold promise for the future.

## 9.5 Concluding Remarks

In conclusion, the research papers presented in this dissertation collectively provide a substantial contribution to the field of railway axle engineering. The findings offer innovative solutions for enhancing the safety and durability of railway axle systems, taking into account factors such as press fitting, multiaxial fatigue, adverse running conditions, and the impact of braking forces and thermal effects.

This material is reserved for educational use only, not allowed for commercial use.

Forbidden to modify the content, and cite the document when use.

This research underscores the vital importance of considering a comprehensive set of variables in the design and maintenance of railway axles. The implications of this work extend to railway operators, maintenance personnel, and engineers, providing valuable insights into how to improve the safety, performance, and longevity of railway systems.

The limitations of the study acknowledge the inherent challenges of modeling complex systems accurately. However, these limitations serve as a foundation for future research endeavors, providing new directions for innovation in railway engineering.

In conclusion, this doctoral dissertation serves as a cornerstone for the advancement of railway axle engineering and the ongoing quest for safer, more reliable railway systems. It is our hope that the knowledge and innovations presented here will inspire further research, leading to enhanced safety and efficiency in the world of rail transportation.



## REFERENCES

- [1] Zerbst U, Mädler K, Hintze H. Fracture mechanics in railway applications - An overview. *Eng Fract Mech.* 2005;72:163–94. <https://doi.org/10.1016/j.engfracmech.2003.11.010>.
- [2] European Railway Agency(ERA). *Railway safety in the european union.* 2011.
- [3] Wikipedia. (2023). “Meudon 1842.jpg.” *Wikipedia, The Free Encyclopedia* 1842. [https://en.wikipedia.org/wiki/Versailles\\_rail\\_accident#/media/File:Meudon\\_1842.jpg](https://en.wikipedia.org/wiki/Versailles_rail_accident#/media/File:Meudon_1842.jpg).
- [4] Eschede Train Disaster, 1998." *DW.com.* Accessed in 2023. n.d. [https://static.dw.com/image/44054924\\_906.jpg](https://static.dw.com/image/44054924_906.jpg).
- [5] National Transportation Safety Board. *Collision of Metrolink Train 111 with Union Pacific Train LOF65-12 Chatsworth, California, September 12, 2008 - Accident Report.* 2010.
- [6] Transportation Safety Board of Canada. (2013). *The 2013 Lac-Mégantic Train Derailment and Fire.* n.d. <https://www.tsb.gc.ca/eng/rapports-reports/rail/2013/r13d0054/r13d0054.html>.
- [7] TransportCanada. *Rail transportation safety investigation report R20W0031.* 2020.
- [8] YAMAMOTO. M. *NIPPON STEEL & SUMITOMO METAL TECHNICAL REPORT No. 105.* n.d.
- [9] G Belloni, M Bocciolone and ALC. *Fatigue test bench for railway bogies and superstructures.* 2015.
- [10] Kowalski S. *Failure analysis of the elements of a forced-in joint operating in rotational bending conditions.* *Eng Fail Anal.* 2020;118:104864. <https://doi.org/10.1016/j.engfailanal.2020.104864>.
- [11] Kowalski S. *Fretting wear in selected elements of rail vehicles.* *Teh Vjesn.* 2018;25:481–6. <https://doi.org/10.17559/TV-20160601144609>.
- [12] Japanese Industrial Standard (JIS) / Japanese Standards Association (JSA). *JIS E 4504:2015-Rolling stock - Wheelsets - Quality requirements.* Mita MT Bldg., Minato-Ku, Tokyo, JAPAN: JSA; n.d.
- [13] European Committee For Standardization. *EN 13260:2009+A1:2010: Railway applications - Wheelsets and bogies - Wheelsets - Product requirements.* London,United Kingdom: BSI; 2010.
- [14] ISO 1005-7:1982. *Railway rolling stock material; Part 7 : Wheelsets for tractive and trailing stock; Quality requirements.* First Edit. CP 401 - 1214 Vernier, Geneva, Switzerland: International Organization for Standization; 1982.

This document is intended for personal use only. It is not to be distributed, copied, or used for commercial purposes without the explicit permission of the copyright holder.

Forbidden to modify the content, and cite the document when use.

- [15] AAR. Manual of Standards and Recommended Practices Section G-II Wheel and Axle Manual. Washington, D.C, United States: Association of American Railroads; 2019.
- [16] European Committee for Standardization. BS EN 13261 : 2020 Railway applications - Wheelsets and bogies - Axles - Product requirements. London,United Kingdom: BSI; 2020.
- [17] European Committee for Standardization. BS EN 13262 : 2020 Railway applications Wheelsets and bogies - Wheels - Product requirements. London,United Kingdom: BSI; 2020.
- [18] P.BORESI RJS. Advanced Mechanics of Material 6 th Edition. 2013. <https://doi.org/10.1093/acprof:oso/9780199670857.001.0001>.
- [19] Budynas, Nisbett. Shingley's Mechanical Engineering Design. Eighth Edi. 1221 Avenue of the Americas, New York, United States: McGraw-Hill; 2006. <https://doi.org/10.5948/upo9781614441052.029>.
- [20] Benuzzi D, Donzella G. Prediction of the press-fit curve in the assembly of a railway axle and wheel. Proc Inst Mech Eng Part F J Rail Rapid Transit. 2004;218:51–65. <https://doi.org/10.1243/095440904322804439>.
- [21] Simulia. FATIGUE THEORY REFERENCE. Dassault Systèmes Simulia Corp.,; 2018.
- [22] Simulia. fe - safe USER GUIDE. 2020.
- [23] Simulia DSC. Abaqus Analysis User's Manual. 2016.
- [24] Rice JR. A Path Independent Integral and the Approximate Analysis of Strain Concentration by Notches and Cracks. J Appl Mech. 1968;35:379–86.
- [25] Abaqus. Abaqus Theory Manual. vol. IV. 2013.
- [26] Carolina N, Engine E. Isight 4.0 Getting Started Guide. 2009.
- [27] Dr. Alex Van der Velden and Dr. Pat Koch. Isight Design Optimization Methodologies. SIMULIA; 2019.
- [28] Yamamoto M, Ishiduka H. Stress concentration of transition groove induced by a press-fitted part in railway axles. Int J Fatigue. 2017;97:48–55. <https://doi.org/10.1016/j.ijfatigue.2016.12.025>.
- [29] SIMULIA. Abaqus Analysis user's manual. Vol I-IV. Providence, RI, USA: Dassault Systèmes Simulia Corp.,; 2010.
- [30] Hibbeler RC. Mechanics of Materials. EIGHTH EDI. New Jersey, United States: Prentice Hall; 2010.
- [31] Ferdinand P. Beer,E. Russell Johnston, Jr. JTD, Hibbeler RC. Mechanics of Materials.

This material is reserved for educational use only, not allowed for commercial use.

Forbidden to modify the content, and cite the document when use.

- EIGHTH EDI. New Jersey, United States: Prentice Hall; 2012.
- [32] European Committee For Standardization. BS EN 13260 : 2020 Railway applications - Wheelsets and bogies - Wheelsets - Product Requirements. London,United Kingdom: BSI; 2020.
- [33] European Committee For Standardization. BS EN 13104:2009+A2:2012: Railway applications — Wheelsets and bogies — Powered axles — Design method. BSI Standards; 2012.
- [34] Han S-W, Son S-W, Jung H-S. Weight Reduction of an Urban Railway Axle Based on EN Standard. *Trans Korean Soc Mech Eng A*. 2012;36:579–90. <https://doi.org/10.3795/ksme-a.2012.36.5.579>.
- [35] Paris P, Erdogan F. A critical analysis of crack propagation laws. *J Fluids Eng Trans ASME*. 1963;85:528–33. <https://doi.org/10.1115/1.3656900>.
- [36] European Committee For Standardization. BS EN 13103-1:2017:Railway applications - Wheelsets and bogies - Part 1: Design method for axles with external journals. 2011.
- [37] British Standards BSI 8535:2011, Railway applications – Wheelsets and bogies – Powered and non-powered axles with inboard bearings – Design method. n.d.



This material is reserved for educational use only, not allowed for commercial use.

Forbidden to modify the content, and cite the document when use.



This material is reserved for educational use only, not allowed for commercial use.

Forbidden to modify the content, and cite the document when use.

PAPER • OPEN ACCESS

## Effect of interference on the press fitting of railway wheel and axle assemblies

To cite this article: Theingi Nwe and Monsak Pimsarn 2021 *IOP Conf. Ser.: Mater. Sci. Eng.* **1137** 012051

View the [article online](#) for updates and enhancements.



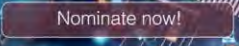


**The Electrochemical Society**  
Advancing solid state & electrochemical science & technology

The ECS is seeking candidates to serve as the  
**Founding Editor-in-Chief (EIC) of ECS Sensors Plus,**  
a journal in the process of being launched in 2021

The goal of ECS Sensors Plus, as a one-stop shop journal for sensors, is to advance the fundamental science and understanding of sensors and detection technologies for efficient monitoring and control of industrial processes and the environment, and improving quality of life and human health.

*Nomination submission begins: May 18, 2021*



This content was downloaded from IP address 171.7.24.135 on 13/06/2021 at 19:31

This material is reserved for educational use only, not allowed for commercial use.

Forbidden to modify the content, and cite the document when use.

## Effect of interference on the press fitting of railway wheel and axle assemblies

Theingi Nwe<sup>1</sup>, Monsak Pimsarn<sup>2,\*</sup>

<sup>1,2</sup>Department of Mechanical Engineering, Faculty of Engineering,  
 King Mongkut's Institute of Technology Ladkrabang, Thailand 10520

\* Corresponding Author: [monsak.pi@kmitl.ac.th](mailto:monsak.pi@kmitl.ac.th)

### Abstract

Press fitting is one of the common fastening methods used to assemble mechanical components. It has also received considerable critical many industrial applications, for example, railway wheel and axle are usually assembled by press-fitting. This process generates high stress on the axle-fillet area and fatigue is generally initiated due to the stress concentration. This paper attempts to propose the stress distribution and deformation of a railway axle. Various interference clearances were analyzed using finite element method. The contact pressure at the axle wheel seat along the axial direction was examined as it significantly influences the press-fitted components life. The analytical results from Lamé's theory [1] were compared with finite element analysis results for the wheel and axle press-fitting process. The results obtained from both methods were in good agreement and the maximum relative error of the contact pressure is by 11.08 %. Additionally, the results show that the Von-Mises stresses on the axle wheel seat and fillet areas were found to be increased if the interference increased.

**Keywords:** Press Fitting, Railway Axle, Interference, Lamé's Theory

### 1. Introduction

Railway axle is the vital security component in railway vehicles, and it is assembled with the wheel by the press-fitting method. The axle might be damaged by any of excessive pressure, excessive interference, or improper lubricant. The damage could evolve into fatigue cracks and these cracks are easily initiated on the axle due to fretting behaviors. Thus, the reliability of interference fits is crucial to ensure the railway wheelset is safe in service. Press fitting is a traditional method for assembly of interference fitting parts, and the quality of the assembly has been extensively studied. The contact pressure in press-fitting produces residual stresses, for example, tangential and radial stresses in the wheel and the axle. The residual stress greatly influences the occurrence of fatigue on the parts in operation.

Previous research has established that interference can have an effect to the interface between the two parts by finite element analysis. However, far too little attention has been paid to railway wheelsets. Lamé's theory for thick-walled cylinder has been commonly used to predict the contact pressure of interference fit and deformation. However, the use of interference in the press-fitting has not been investigated. Partly, such an analytical theory is not adequate to predict residual stresses in press-fitting.



Content from this work may be used under the terms of the [Creative Commons Attribution 3.0 licence](https://creativecommons.org/licenses/by/3.0/). Any further distribution of this work must maintain attribution to the author(s) and the title of the work, journal citation and DOI.  
 Published under licence by IOP Publishing Ltd

Sarabandi et al. [1] estimated the residual stress in railway wheels, due to press fitting, based on the nonlinear structural analysis and the nonlinear transient thermal analysis of the wheelset. They found that the stress distribution, due to thermal loading, is important and sensitive. Naderi [2] studied the stress intensity factor in railway wheelset by press fitting process. Hannemann and Sander [3] analyzed stress intensity factor and crack propagation, considering the effects of rotary bending and press-fitting. It was found that the press-fit load is important for the SIF solution. Marshall et al. [4] measured ultrasonic reflections to non-destructively determine contact conditions in the interference fit and investigated the wheel and axle interface with large contacts and gradual pressure variations. Zehsaz and Shahriary [5] investigated the effects of the coefficient of friction and interference on fretting fatigue strength of axles by using fretting damage parameters.

This research gives an account of the effect of interference on the wheelset press-fitting and variation of residual stresses with different interference clearances. The contact pressure and residual stresses were also evaluated analytically. The finite element analysis results confirmed that the analytic estimations can be employed to predict the stress distribution in the axle.

## 2. Materials and Methods

### 2.1 Interference Fit

Interference fits are widely used for mechanical attachment mechanisms because they are cost-effective and flexible. Concerning the wheelset assembly, shrink fitting or press-fitting can be used. However, press fitting is commonly used for assembling the wheel and axle because it is cheaper and faster. During the press-fitting, the axle wheel seat diameter is larger than that of the wheel hub bore. The assembled wheel and axle should meet the geometric requirements of some standard, e.g., EN 13261, EN 13262. The maximum and a minimum interference between the axle wheel seat and wheel hub bore are as follows [6]:

For shrink fitting,

$$0.0009dm \leq 2\delta \leq 0.0015dm \quad (1)$$

For press-fitting,

$$0.001dm \leq 2\delta \leq 0.0015dm + 0.06 \quad (2)$$

where  $dm$  is the mean diameter and  $\delta$  is the radial interference in mm.

### 2.2 Lamé's Theory for Thick-Walled Cylinder

Assuming the cylinder subjected to internal pressure is the wheel hub bore and the cylinder subjected to external pressure is the axle wheel seat, the stresses can be calculated by Lamé's theory.

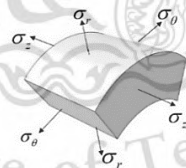


**Figure 1.** Stresses in a thick-walled cylinder element

Consider a small section of the cylinder, radial stresses  $\sigma_r$  and  $\sigma_\theta$  tangential stresses can be achieved as a function of radius:

$$\sigma_r = \frac{r_i^2 P_i - r_o^2 P_o}{r_o^2 - r_i^2} - \frac{(P_i - P_o) r_i^2 r_o^2}{(r_o^2 - r_i^2) r^2} \quad (3)$$

$$\sigma_\theta = \frac{r_i^2 P_i - r_o^2 P_o}{r_o^2 - r_i^2} + \frac{(P_i - P_o) r_i^2 r_o^2}{(r_o^2 - r_i^2) r^2} \quad (4)$$

When the wheel and axle are press-fit assemblies, it can be assumed that pressure  $P$  is exerted all over the surface of the contact at the nominal radius,  $r$ . The magnitude of contact pressure, due to press-fitting assembly, can be calculated by summing the radial displacements of the inner and outer parts [7]. It was designated  $r_i$  is the inside radius of the cylinder,  $r_o$  is the outside radius,  $P_i$  is the inner pressure and  $P_o$  is the outer pressure. Where the subscripts  $o$  and  $i$  on Young's modulus  $E$  and Poisson's ratio  $\nu$  represent the inner and outer cylinder.

$$P = \frac{\delta}{r \left[ \frac{1}{E_o} \left( \frac{r_o^2 + r^2}{r_o^2 - r^2} + \nu_o \right) + \frac{1}{E_i} \left( \frac{r^2 + r_i^2}{r^2 - r_i^2} - \nu_i \right) \right]} \quad (5)$$

If the two members are the same material,  $E_o = E_i = E$ ,  $\nu_o = \nu_i$ , equation (3) simplifies to

$$P = \frac{E\delta}{2r^3} \left[ \frac{(r_o^2 - r^2)(r^2 - r_i^2)}{(r_o^2 - r_i^2)} \right] \quad (6)$$

### 3. Finite Element Analysis

In this article, finite element analysis was employed to evaluate the stress distribution and deformation of the press-fit interference on the railway wheel and axle. The geometric model of the wheel and axle assembly is shown in figure 2. The S1002 wheel profile and hollow axle were used in the analysis. The inside diameter of the axle is 60 mm and the wheel hub diameter is 190 mm. The axle length is 2300 mm and the wheel and axle contact length is 185 mm.

The wheel and axle quarter model were established using the symmetric boundary condition to reduce the running simulation time. A linear elastic material behavior with Young's modulus of 210 GPa and Poisson's ratio of 0.3 [8] is defined for both wheel and axle material properties. A three dimensional (C3D8R) 8-node linear brick (hexahedral), reduced integration, hourglass control was used for the element type. The wheel and axle contact area have meshed with a refine mesh until the stress and contact pressure changed lower than 1%. The total number of elements are 31,305 and 36,322, for the wheel and axle, respectively.

The contact surface interaction between the axle wheel seat and wheel hub was defined using a master-slave contact algorithm; the wheel hub surface was the master surface, and the axle wheel seat surface was the slave. A surface-to-surface interaction was defined with a finite sliding in the initial step. It is also required to be defined as an initial over-closure at the initial step. In the first step, the interference was resolved by automatic shrink-fit with a gradually removed slave node over closure during the step. A contact interaction property was defined as a penalty and the coefficient of friction was set to 0.6 to ensure tangential behavior. The sliding formulation was selected as "finite sliding" because the installation displacement was large. The flag indicating a non-linear geometry, Nlgeom, in the software, was set ON [9].

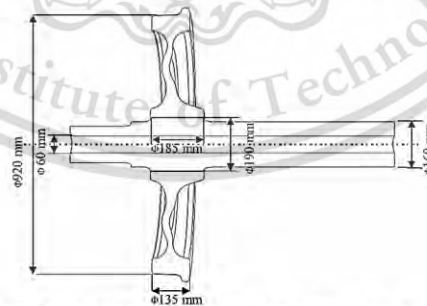


Figure 2. The geometry of the wheel and axle assembly

Figure 3 shows the boundary conditions of the symmetric finite element model: the symmetries of the wheel and axle assemblies used in the finite element analysis are: in the X-Y plane,  $U_z, \theta_x, \theta_y = 0$ , in the X-Z plane,  $U_y, \theta_x, \theta_z = 0$  and at the right end of the axle YZ plane was constrained in the longitudinal direction,  $U_x, \theta_y, \theta_z = 0$ .

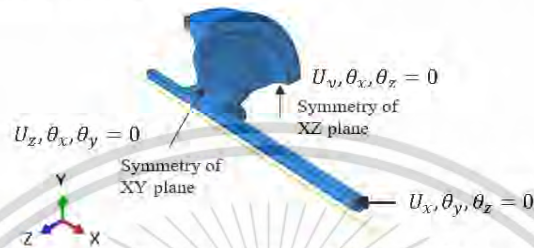


Figure 3. Boundary conditions for wheel and axle assembly

#### 4. Results and Discussion

Several different interference clearances, ranging from 190  $\mu\text{m}$  to 345  $\mu\text{m}$ , obtained from Equations (1) and (2), were modeled and examined. The Equation (5) was used to determine the contact pressure distribution over the interface area. Analytical results and finite element analysis results were compared to determine whether the finite element analysis was acceptable and accurate. Table 1 shows the relative error in contact pressure for various interferences, between the finite element method and Lamé's theory. It also compares the maximum deformations of the wheel and axle between modeling and theory. The axle was compressed, and the wheel was expanded since the contact pressures were equal and opposite at the interface surfaces. When the interference continuously increases, the deformation of the wheel and axle get higher. The lowest relative error of maximum contact pressure was 1.64% with the same mesh size. The Von Mises stress distribution on press-fitted wheelset between FEM and the analytical methods can be compared in Figure 4. The Von Mises stress variation along the wheelset center radial axis from both results were similar and the values rapidly increased at the wheel hub inner surface and then gradually decreased towards the wheel rim outer surface. It can be noticed that FEM shows the maximum Von Mises stress at the wheel hub inner surface, but analytical results showed it at the axle hollow inner surface. Finite element and analytical results for the radial and tangential stress distribution along the central axis of the wheelset are shown in Figures 5 and 6. The radial stresses are zero at the inner surface of the hollow axle and outer surface of the wheel because they are unpressurized surfaces. The tangential stresses on the axle are maximum at the outer surface and minimum at the inner surface. However, maximum tangential stresses were at the inner surface and minimums were at the wheel outer surface. It can be seen the axial, radial, and tangential stress distribution of the wheelset in Figures 8 to 10.

Table 1. Contact pressure and maximum deformations along the radial direction for various interferences by finite element method (FEM) and Lamé's theory.

Interference ( $\mu\text{m}$ )	Contact Pressure (MPa)		Relative Error %	Wheel Deformation ( $\mu\text{m}$ )		Shaft Deformation ( $\mu\text{m}$ )	
	Lamé's Theory	FEM		Lamé's Theory	FEM	Lamé's Theory	FEM
200	96	107	11.08%	60.1	68.2	-30.3	-31.7
240	115	127	10.43%	72.1	77.3	-36	-38.1
280	134	136	1.64 %	84.2	85.7	-42	-38.1
320	153	168	9.8%	96.2	103	-48	-50.8

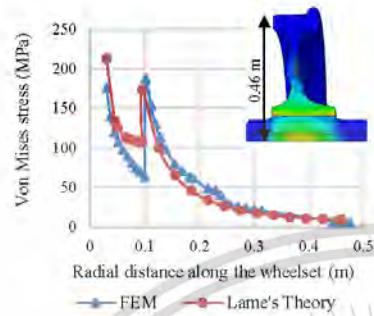


Figure 4. Von Mises stress along the centre of the wheelset radial axis.

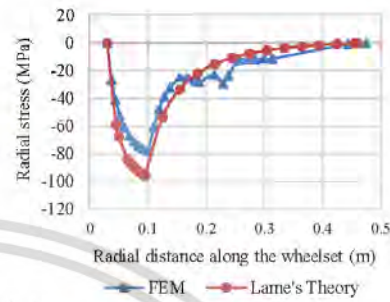


Figure 5. Radial stress distribution along the centre of the wheelset radial axis.

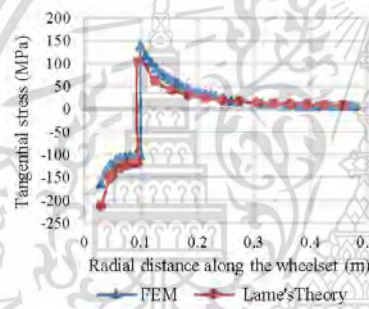


Figure 6. Tangential stress distribution along the centre of the wheelset radial axis.

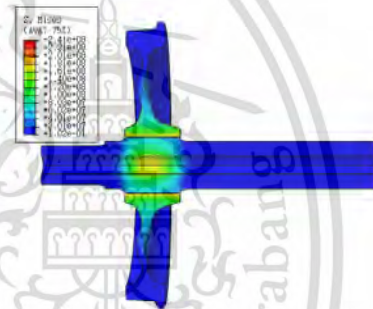


Figure 7. Von Mises stress distribution along the centre of the wheelset radial axis.

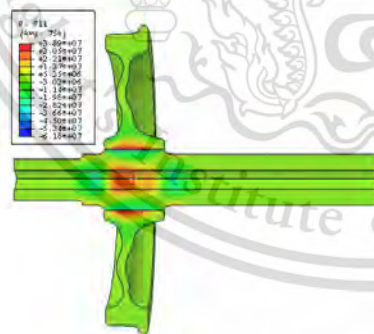


Figure 8. Axial stress distribution for wheel and axle assembly along the radial axis.

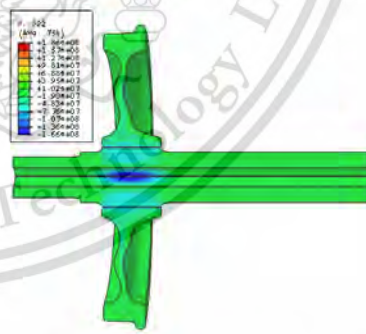


Figure 9. Radial stress distribution for wheel and axle assembly along the radial axis.

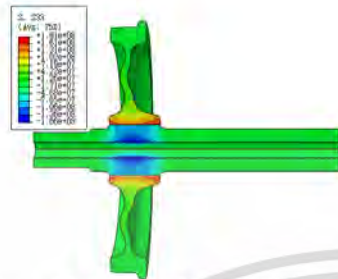


Figure 10. Tangential stress distribution for wheel and axle assembly along the radial axis.

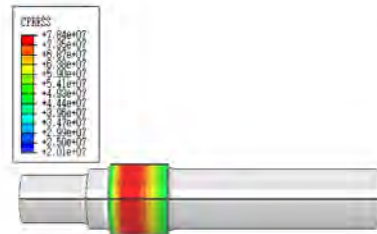


Figure 11. Contact pressure at axle wheel seat.

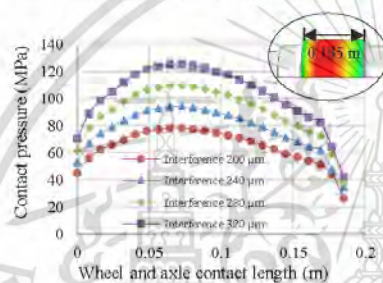


Figure 12. Contact pressure distribution along the contact length vs interference clearance.

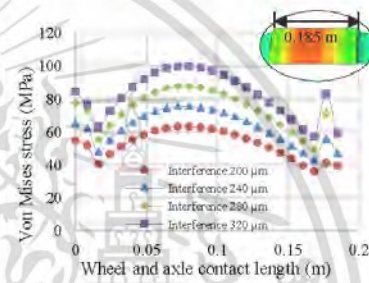


Figure 13. Von Mises stress distribution along the contact length vs interference clearance.

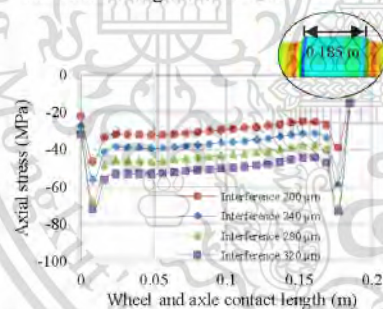


Figure 14. Axial stress distribution along the contact length vs interference clearance.

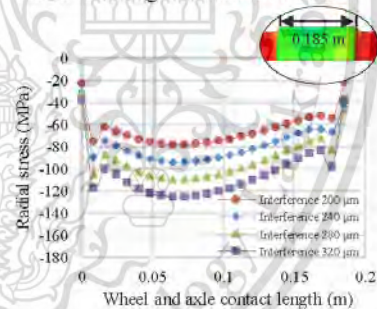


Figure 15. Radial stress distribution along the contact length vs interference clearance.

The variations of contact pressure along the axle wheel seat length vs interference are presented in Figure 12. By increasing the interference, the contact pressure was also increased with the same mesh size. Although the contact pressure, between the wheel and axle, was constant along the axle wheel seat length. Following Lamé's theory, the contact pressure obtained from the FEM varied along the contact length. The maximum contact interference pressure was in the middle of the axle wheel seat contact length for all interferences. This was explained by the assumption that, in Lamé's theory, the cylinder thickness was constant, but in the wheel model it was not. The Von Mises stress variation on the axle wheel seat is presented vs interference values in Figure 13. The axial, radial and Von Mises stresses

were significantly affected by interference clearances as set out in Figures 13 to 15. The results revealed that the maximum Von Mises stress occurred in the middle of the axle wheel seat contact area similar to the contact pressure.

## 5. Conclusion

This paper has discussed the reasons for the wheel and axle press-fitting assembly had a significant impact on the lifetime of the wheelset components. The stress distribution and deformation due to the press-fit interference effect were compared with the finite element method and Lamé's theory. The following conclusion can be drawn from this research:

The FEM model agree well with the theory to within 15% relative error, the maximum relative error of contact pressure is 11.08% and the minimum value is 1.64%, which means the results is considered acceptable. Therefore, Lamé's theory for a thick-walled cylinder was effective for the wheel and axle press-fitting analysis. However, the finite element method was more accurate and comprehensive than Lamé's theory. The comparing results show the results obtained from the FEM are greater than the analytical results because the wheel and axle are considered ideal cylinder surface for analytical calculation and the assembly parts had a complex geometry. These results confirmed that the critical stress occurred at the contacting surfaces of the wheel hub and the tangential stress was greatest among the three principal stresses.

Deformation during press-fitting along the radial axis was unfavorably affected and strongly depended on the contact pressure at the wheel and axle interface. One of the more significant findings to emerge from this study is that increasing amount of interference caused deformation to increase, smaller clearances benefit to press-fitted parts. Taken together, these results suggest that the press-fit effect should be accounted for a railway axle design.

## Acknowledgements

This work was supported by King Mongkut's Institute of Technology Ladkrabang. The author would like to thank the State Railway of Thailand for providing valuable data.

## References

- [1] Budynas R and Nisbett J K 2006 *Shigley's Mechanical Engineering Design 8<sup>th</sup> ed* (New York: MC Graw Hill Education)
- [2] Sarabandi S Soleimani H and Mahmoudi H 2019 *Sci. Iran* **26**(1) 367-374
- [3] Naderi A 2018 *Eng. Fail. Anal* **94**(7) 78-86
- [4] Madia M Beretta B and Zerbst U 2008 *Eng. Fract. Mech* **75**(8) 1906-1920
- [5] Marhsall MB Lewis R Dwyer-Joyce R S Demilly F and Flament Y 2004 *Proc. 14th International Wheelset Congress* (Orlando, USA) **2**(41) 17-21
- [6] Zehsaz M and Shahriary P 2013 *UPB Sci. Bull. Ser. D Mech. Eng* **75**(4) 71-84
- [7] *EN 13260:2009+A1:2010: Railway applications - Wheelsets and bogies - Wheelsets - Product requirements.*
- [8] Boresi R P 2013 *Advanced Mechanics of Material 6<sup>th</sup> Edition* (USA: John Wiley & Sons, Inc)
- [9] Yamamoto M and Ishiduka H 2017 *Int. J. Fatigue* **97** 48-55
- [10] *Abaqus Analysis user's manual* vol I-IV.2010 (USA: Dassault Systèmes)

Article

# Railway Axle and Wheel Assembly Press-Fitting Force Characteristics and Holding Torque Capacity

Theingi Nwe and Monsak Pimsarn \* 

Department of Mechanical Engineering, School of Engineering, King Mongkut's Institute of Technology, Ladkrabang, Bangkok 1052, Thailand; 62601033@kmitl.ac.th

\* Correspondence: [monsak.pi@kmitl.ac.th](mailto:monsak.pi@kmitl.ac.th); Tel.: +65-897-655-778

**Abstract:** Nowadays, press-fitting is widely used in the manufacturing industry because it allows easy and fast installation and is repetitive, strong, and inherently reliable. The quality of a press-fitting assembly can be verified from the press-fitting curves and forced monitoring. This study aims to investigate the characteristics of the press-fitting curve with various interference railway wheelset models and determine the interference limit that axles can withstand at the maximum holding torque without slipping and without plastic deformation. A three-dimensional finite element analysis examined the maximum press-fitting force and stress distributions using Abaqus FEA software. The press-fitting curves of the railway wheel and axle assembly obtained from finite element simulation were classified following European Standard EN 13260. The press-fitting curves showed whether they fell within the boundary limits in the EN standard to allow their practical application. This study also showed when plastic deformation would occur, within the recommended interferences in the EN standard. Moreover, the effect of interference was numerically simulated for the maximum holding torque capacity within the EN standard interference range. Numeric simulation was compared with the theory; the deviation was 15–6%.



**Citation:** Nwe, T.; Pimsarn, M. Railway Axle and Wheel Assembly Press-Fitting Force Characteristics and Holding Torque Capacity. *Appl. Sci.* **2021**, *11*, 8862. <https://doi.org/10.3390/app11198862>

Academic Editor: José A. F. O. Correia

Received: 11 August 2021  
Accepted: 16 September 2021  
Published: 23 September 2021

**Publisher's Note:** MDPI stays neutral with regard to jurisdictional claims in published maps and institutional affiliations.



**Copyright:** © 2021 by the authors. Licensee MDPI, Basel, Switzerland. This article is an open access article distributed under the terms and conditions of the Creative Commons Attribution (CC BY) license (<https://creativecommons.org/licenses/by/4.0/>).

**Keywords:** railway wheelsets; press-fitting curve; interference; torque capacity; EN standard

## 1. Introduction

A railway wheelset is an assembly consisting of an axle and two wheels fitted with interference and, where necessary, applicable associated components, e.g., gear-shaft, bearing bushing, etc. Wheelsets need to be safe because failures could lead to derailment and potentially to major safety issues, including loss of life and heavy damage to railway vehicles. Therefore, it is important to assemble the wheelset correctly to reduce accidents and derailments. Wheelsets are assembled to remain attached to all components while in operation. Wheels may be press-fitted or shrink-fitted to the axles. Press-fit, or interference fit, tightens two parts together by relying on friction and joining the parts that can take a different form. This is commonly used in the industry because the process is reliable, simple, and does not require heating, cooling, or soldering. One problem with railway wheelsets is their failure due to excessive interference in press-fitting, and this can result in a slip between the wheel and axle. Fretting wear takes place at the interface of the axle wheel seat and the wheel hub surface, and it can cause surface fatigue, adhesion, oxidation, exfoliation, and scratching [1,2]. If a press-fit is used for assembling the wheels onto the axle, the wheel mounting peak press force limits and the press-fitting curve must be considered. Furthermore, many standards have been defined for railway wheelset assembly; for example, JIS E 4504 [3], EN 13260 [4], ISO 100-5 [5], and AAR [6]. Railways tend to follow national standards, so the authors followed the State Railway of Thailand's practice and used the European standard EN 13260 for the assembly of wheels and axles [4]. Following the standard improves the quality of the wheelset, and this would also help to standardise production.

Very few publications were found in the literature that discussed the characteristics of the press-fitting curve for railway wheelsets. Benuzzi and Donzella analysed the contact pressure and speed related to lubrication and predicted a press-fitting curve using an FEM model and a simplified theoretical model [7]. Lu et al. constructed and tested a mathematical model for the press-fit curve based on the AAR standard [8]. Saad et al. predicted the residual stress and plastic strain for forging, machining, and assembling [9]. Stamenković et al. addressed the effect of the strength of the wheelset press-fit joint and recommended a frictional coefficient value that resisted sliding between the interface for specific conditions by comparing experiment and theory [10]. Michnój and Guzowski investigated fretting wear in a wheelset press-fit joint and conducted contact surface and fretting wear tests; they found that the adhesion phenomenon played a critical part in the initiation of fretting wear in a press-fit joint [11]. Booker and Truman reviewed the factors affecting the interference fit joints' strength and discussed the modelling and limitations related to the friction coefficient, boundary condition, geometry, and material [12]. Zhao et al. have also discussed the relationship of radial interference and holding torque capacity, the friction coefficient of camshaft based on the finite element analysis and experiment [13].

Lame's equation can also be used to determine the contact pressures at the interface of the assembly parts and to estimate the maximum holding torque capacity of a press-fit. A major challenge of press-fit assembly is to choose reasonable interference values that would ensure the safety of the assembled components. Too large an interference may damage the part being assembled, and less resistance may result in plastic deformation. To prevent slipping, the wheelset maximum holding torque capacity must be known. The magnitude of the press-fit force depends on the geometry, friction coefficient, material properties, and operating conditions [14].

With this in mind, the authors studied the effects of interference on the press-fitting force because it is important to predict the pressing quality of the wheel and axle assembly. The stress on the axle wheel seat contact area was analysed using simulation, and the state of the stress-strain effects are discussed. Moreover, the interferences needed for wheelset press-fitting without slipping were determined. The press-fitting curve, maximum press-fit force, and maximum holding torque capacity were evaluated using the finite element method using Abaqus FEA software [15].

## 2. Theoretical Analysis of Press-Fitting

In general, wheels and axles should meet the geometric requirements before being assembled, as defined in EN 13261 for axles and EN 13262 for wheels [16,17]. The wheelset can be formed by press-fitting or shrink-fitting. In press-fitting, pressure is applied to the wheel hub to force it onto a slightly larger diameter axle, thus leading to contact. External pressure acts on the axle wheel seat, and the internal pressure acts on the wheel hub (Figure 1).

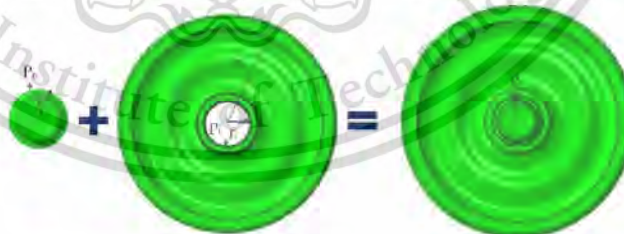


Figure 1. Assembly of an axle and a wheel.

$P_i$  and  $P_o$  are equal and opposite at the contact surface in the wheelset because it is assumed that the axle and wheel are composed of the same material. Lame's equation for

contact pressure distribution in thick-walled cylinders [18] was used for calculating the contact pressure,  $P$ .

$$P = \frac{E\delta}{2r^3} \left[ \frac{(r_o^2 - r^2)(r^2 - r_i^2)}{(r_o^2 - r_i^2)} \right] \quad (1)$$

Equation (1) shows that the contact pressure depends on the interference,  $\delta$ ; nominal diameter,  $d$ ; inner diameter of the axle,  $r_i$ ; outer diameter of the wheel,  $r_o$ ; and Young's modulus of elasticity,  $E$ . The wheel and axle were idealized as thick-walled cylinders, and the wheel was divided into five sections (Figure 2). The average contact pressure was calculated using Equation (2).

$$\bar{p} = \frac{\sum_{i=1}^N P_i L_i}{\sum_{i=1}^N L_i} \quad (2)$$



Figure 2. Simplified model of a wheelset for theoretical analysis [7].

### 2.1. Characteristics of the Press-Fitting Curve

EN 13260 specified that the interference for press-fitting should be 0.2–0.36 mm, which was based on the geometric tolerances of the axle wheel seats. The factors that mainly influenced the maximum press-fitting force and characteristics of the press-fitting curve were the geometry, coefficient of friction, material strength, and operating conditions. During press-fitting, the wheelset could be damaged by insufficient or excessive press-fitting force. Therefore, the press-fitting curve is very important to determine that the assembly has not been damaged along the contact surfaces. If the press-fitting curve is not within the limits specified in the standard, the wheelset needs to be reassembled or rejected. Figure 3 depicts a press-fitting curve, showing the fitting force versus the displacement. In general, this displacement is the axial displacement of a wheel since the axle is fixed to the clamping head of a machine. The standard requires that the final fitting force lies in the range [4]

$$0.85 F < \text{Final Fitting Force} < 1.45 F$$

The axial force,  $F$ , in kN is

$$F = 4 d \quad (3)$$

where  $d$  is the mean diameter of the axle wheel seat (mm), and  $L$  is the axial displacement of the fitting (mm), which must be within the range

$$0.8 d < L < 1.1 d$$

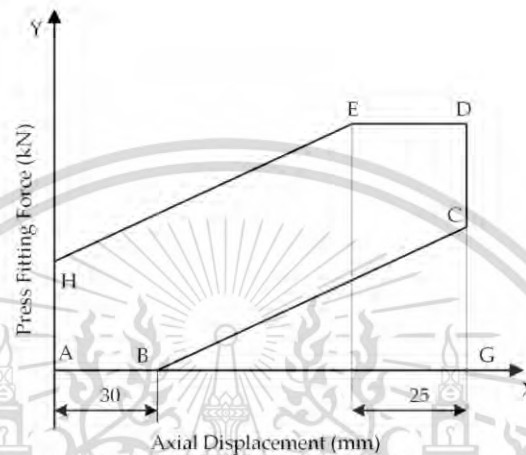


Figure 3. Press-fitting curve for a railway wheelset: force vs axial displacement [4].

The lines, AB, BC, HE, and ED define the boundaries of the press-fitting curve. The contact length is the X-axis, AG, in the diagram. The points labelled in Figure 3 can be found by using the following equations:

$$Y_H = 1.3 \phi;$$

$$Y_C = 0.85 F;$$

$$Y_D = Y_E = 1.45 F;$$

where  $\phi$  is the nominal diameter of the wheel seat in millimetres.

### 2.2. Determination of the Press-Fitting Force

The press-fitting force is related to many factors, including interference, friction coefficient, and elasticity of the assembled parts. These factors could significantly change the press-fitting force. The press-fitting force to the wheel on the axle,  $F_p$ , can be calculated from

$$F_p = \mu \int_A P dA \quad (4)$$

where  $P$  = contact pressure ( $N/m^2$ ),  $\mu$  = coefficient of friction, and  $A$  = contact surface area ( $m^2$ ). Thus, to obtain the press-fit force, the contact pressure between the two assembly parts must be known.

## 3. Finite Element Modelling and Simulation

### 3.1. Materials

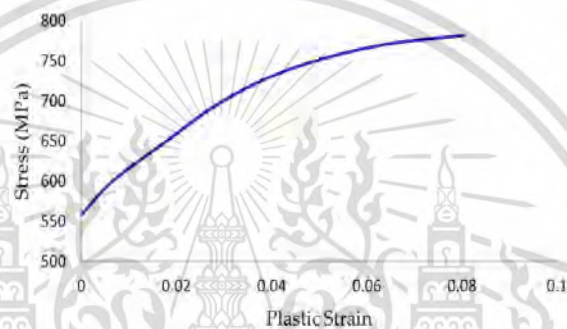
Following the EN standard, the EA1N and EA4T steel grades are widely used for railway axles. The chemical composition and mechanical characteristics of EA4T steel are in Tables 1 and 2. The materials of the wheel and axle were the same, homogeneous, and isotropic, with ideal elastic-plastic behaviour. The stress versus plastic strain graph for EA4T steel is shown in Figure 4.

**Table 1.** Chemical composition of EA4T steel [19].

Grade	C	Mn	Si	S	P	Cr	Cu	Ni	Mo	V
EA4T	0.29	0.8	0.4	0.015	0.02	1.2	0.3	0.3	0.3	0.06

**Table 2.** Mechanical properties of EA4T steel [19].

Material	Young's Modulus (GPa)	Poisson Ratio	Ultimate Tensile Strength (MPa)	Yield Strength (MPa)	Elongation (%)	Absorbed Energy
EA4T	206	0.3	650–800	≥420	≥24	≥30

**Figure 4.** Stress–plastic strain curve for EA4T steel.

### 3.2. Modelling and Simulation

To determine the press-fitting force, a quarter 3D model of the wheel and axle assembly, their dimensions given in Figure 5, was made using Abaqus FEA (Figure 6). During assembly, the wheel was moved onto the axle wheel seat by a specialized assembly machine so that interference between the assembly was eliminated for the outer diameter of the axle wheel seat, which was larger than the inner diameter. A static structure was analysed, and the boundary conditions were used in the finite element analysis. Taking advantage of the symmetric boundary conditions, the XY and XZ planes were constrained in the finite element model. The end of the axle was fixed, and an axial displacement, 180 mm, was applied to the wheel hub towards the axle wheel seat. A contact pair was defined between the wheel- and axle-contacting surfaces. This analysis determined the press-fitting force and stress distribution at the contact surface between the wheel and axle. A 2 mm mesh was used for the contact surface of the wheelset, and a 10 mm mesh was used for the other surfaces (see Figure 7). The mesh type was a 20-node quadratic brick, reduced integration (C8D20R); 17,402 elements were used for the axle model, and 51,858 elements were used for the wheel model.

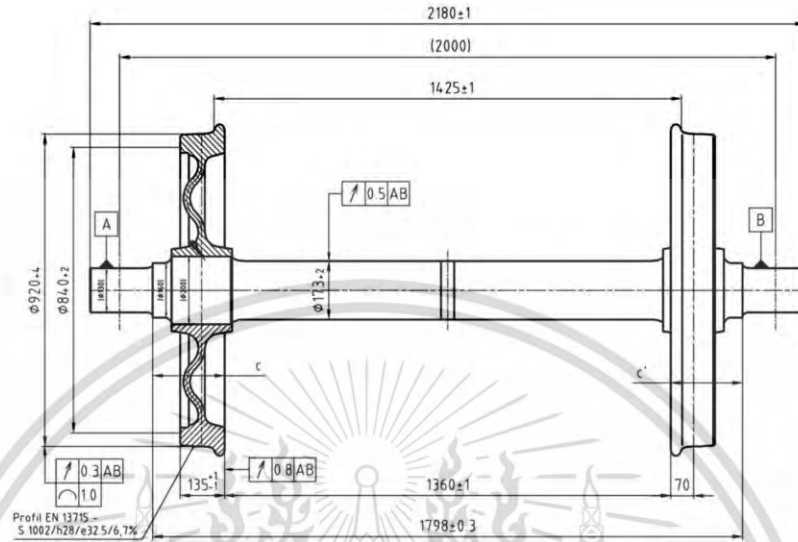


Figure 5. Dimensions of the wheelset [20].

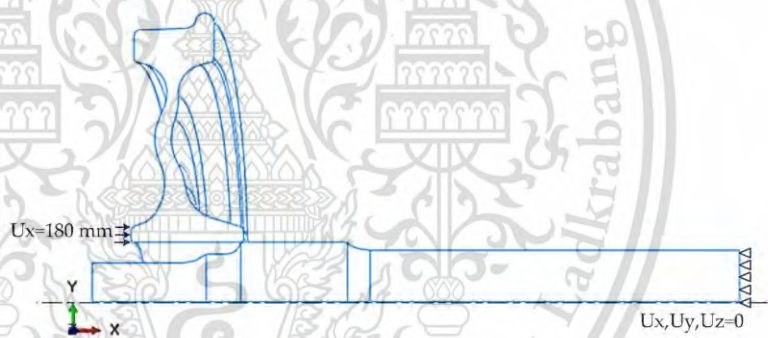


Figure 6. Boundary conditions.

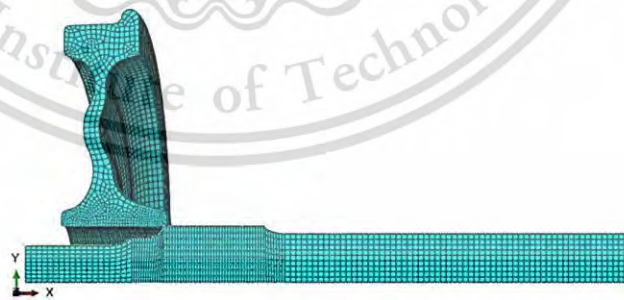


Figure 7. Mesh used by the finite element model.

#### 4. Results and Discussion

##### 4.1. Comparison between the FEA and Theoretical Results

To verify the effectiveness of the numeric model, the finite element results were compared with the calculated theoretical results. The contact pressure between the wheel and axle wheel seat at different sections was determined from Equation (1), and the average contact pressure was calculated by Equation (2). The contact pressure of the axle reached its maximum at the end of the contact edge. The distribution of the contact pressure and average contact pressure along the contact length of the wheelset is shown in Figure 8. The finite element analyses led to higher average contact pressure than the theoretical model because the volume of the 3D model used in the finite element simulation was greater than that of the theoretical model: the finite element results were 3% greater than the theoretical ones. At the start of the wheelset assembly, the two parts did not contact each other because of the taper of the axle. Therefore, the press-fitting force and contact pressure were zero until the end of the taper was reached, and then they suddenly increased. The theory showed that the contact pressure was directly proportional to the outer radius or profile of the wheel and increased in the centre of the contact region. The contact pressure of the axle increased sharply at the start of the contact and decreased towards the centre of the contact length and maximum at the rear end of the edge. The press-fitting force was calculated from the contact length using Equation (4). Figure 9 compares the finite element and theoretical results. The maximum press-fitting force at the end of the assembly was 877 kN from the finite element analysis and 822 kN from the theory, when the interference was 240  $\mu\text{m}$ . The 7% difference between the results was considered acceptable.

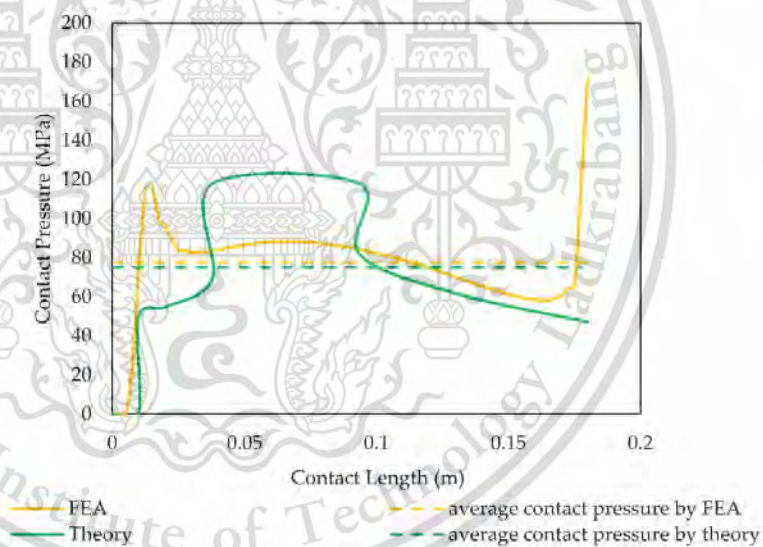
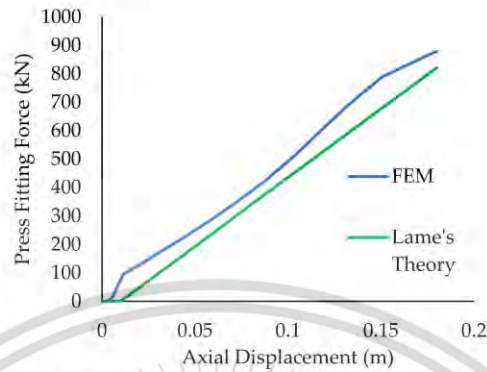


Figure 8. Contact pressure distribution along the contact length.



**Figure 9.** Press-fitting curves obtained from the finite element model (FEM) and Lamé's theory (straight green line).

#### 4.2. Effect of the Interference and Friction Coefficient on Press-Fitting Curves

The interference was a significant factor that affected the press-fitting curve. Simulations used interferences from 160 to 400  $\mu\text{m}$ . The curves are shown in Figure 10. The press-fitting force increased, as expected, with the interference. The boundary of the press-fitting curve was obtained from the EN 13260 standard. The press-fitting curves were used for monitoring the assembly and evaluating its quality. The curves for interferences of 160, 360, and 400  $\mu\text{m}$  did not qualify because they were outside the EN 13260 boundary. One key conclusion from the simulations was that the interferences, specified by the EN standard, fell within the boundary. When the interference increased by 20%, the maximum press-fitting force increased by 12% (Figure 11). Figure 12 shows the press-fitting forces and axial displacements from various friction coefficients obtained from the simulations. Friction coefficients in the range 0.08–0.13 were the only ones acceptable, i.e., led to forces within the boundary shown in Figure 12. Thus, it may be observed that the friction coefficient affected the press-fitting force during the assembly. In general, the greater the friction coefficient, the greater the maximum press-fitting force. Every 0.01 increment in the friction coefficient increased the maximum press-fitting force by 14% (Figure 13).

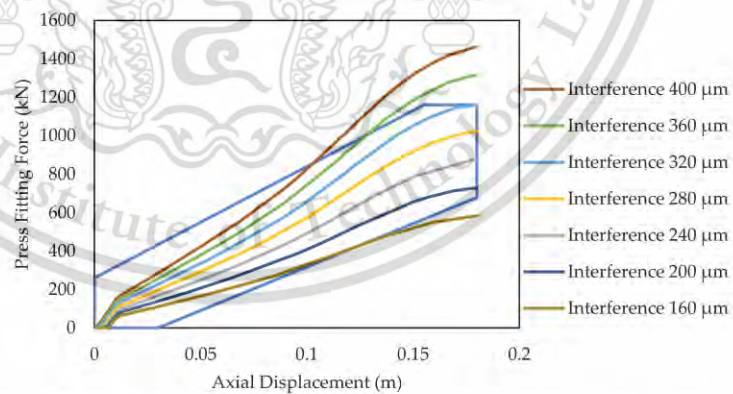


**Figure 10.** Press-fitting curves vs interference derived from the finite element simulations.

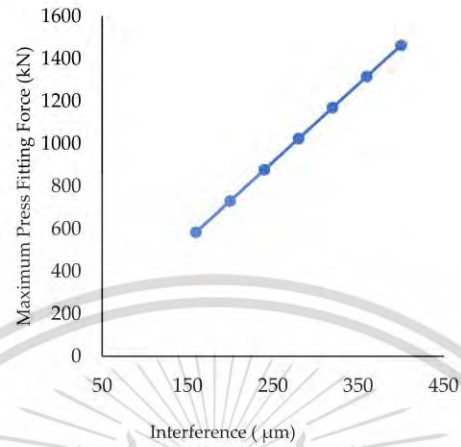


Figure 11. Maximum press-fitting force vs interference.

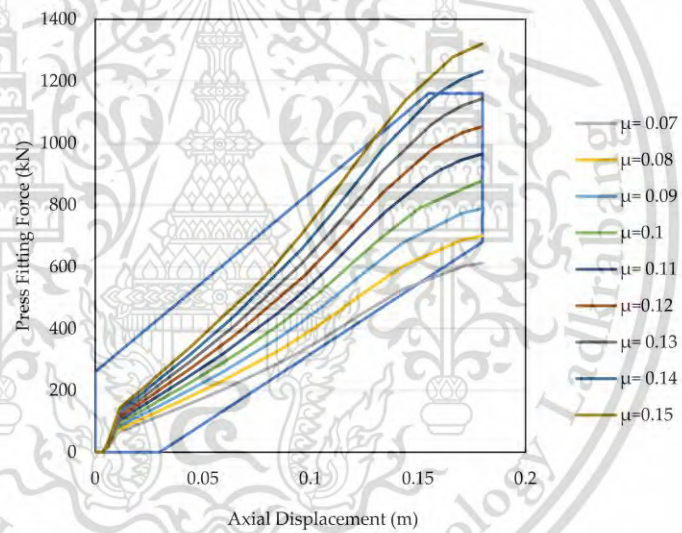


Figure 12. Press-fitting curves with friction coefficient as a parameter.

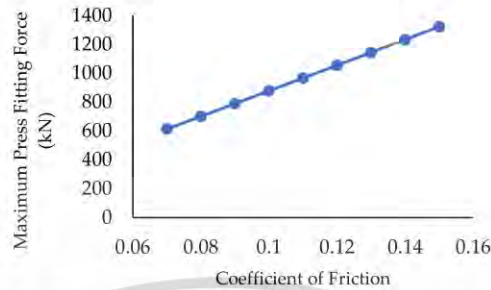


Figure 13. Maximum press-fitting force vs coefficient of friction.

4.3. Contact Strength Analysis

The simulations showed that the maximum von Mises stress took place at the wheel, in contact with the axle wheel seat taper area, in the first simulation time step. The changing of the value and location of the maximum von Mises stress versus the axial displacement and time increment is shown in Figure 14. The von Mises stress was distributed symmetrically on both sides of the wheelset; the maximum stress occurred at the wheel hub bore after assembly. For the axle, the peak stress occurred at the start of the axle wheel seat at the end of the taper area. The maximum stress concentration was localized at the edge of the wheel hub because pressing the wheel to the axle induced critical stress due to the edge effect and abrupt transition in press-fitting. It can be minimized by some geometric characteristics, friction coefficient, contact pressure, and operation conditions. The maximum von Mises stress of the wheelset as a function of interference is shown in Figure 15. The simulations revealed that the interference value significantly affected the stress concentration.

To understand the effect of the interference on the deformation, note that for low values of the interference, up to 360 μm, deformations in the assembly remained in the elastic range. However, for sufficiently large interferences, 380 μm or more, elastoplastic deformation occurred in the wheel. Elastic plastic deformation began at the edge of the wheel hub bore first (Figure 16).

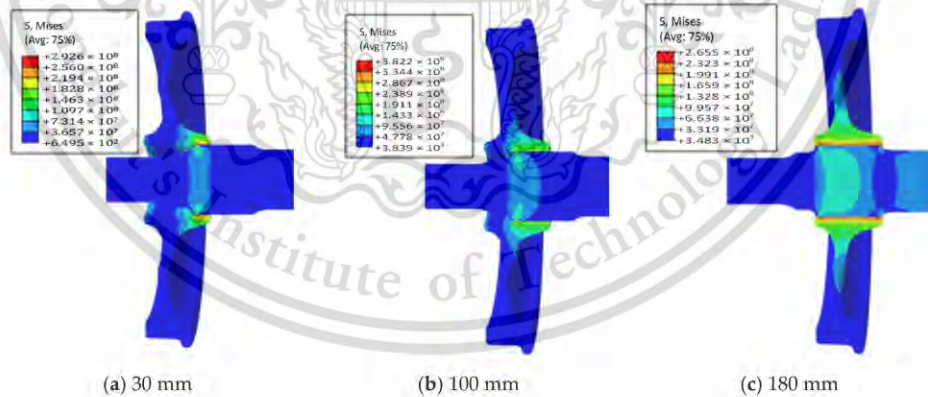


Figure 14. Von Mises stress distribution during simulation (a) axial displacement of 30 mm, (b) axial displacement of 100 mm, and (c) axial displacement of 180 mm.

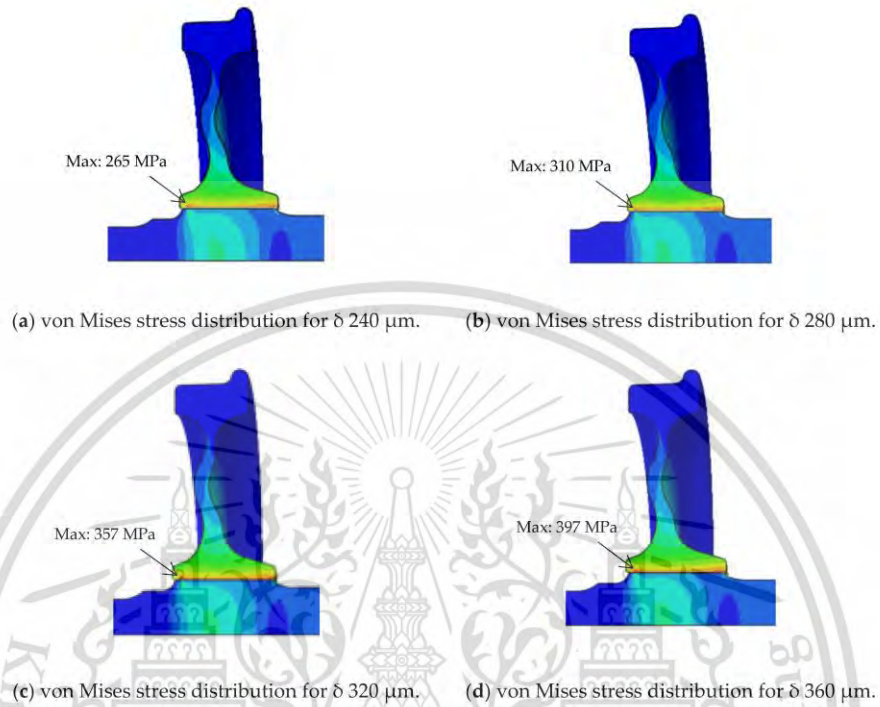


Figure 15. Von Mises stress of the wheel and axle due to radial interference (MPa).

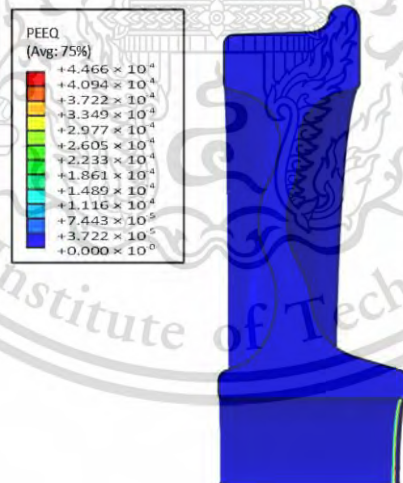


Figure 16. Equivalent plastic strain on the wheel.

## 5. Effect of the Interference on the Holding Torque Capacity

### 5.1. Maximum Holding Torque Capacity Theoretical Analysis

Railway wheelsets are generally running under many loading conditions, for example, vertical static forces of the vehicle, wheel and rail contact forces in longitudinal, vertical, and lateral directions, inertial forces, etc. In operation, the contact force, especially in the longitudinal direction, significantly increases as the train is accelerated (traction) or decelerated (braking). This leads to a torsional moment on the wheelset, which may cause slippage at the wheel hub and axle seat. The maximum holding torque capacity,  $T$ , is the torque required to predict the slip between the wheel and the axle, as it resists the motion of the wheelset at the contact surface. It is transmitted by frictional forces on the wheelset and can be evaluated using Lamé's equation. It was assumed that the contact pressure in the assembly was uniformly distributed. The radial interference was significant for the holding torque capacity since it was related to the contact pressure and frictional force. The holding torque capacity of the wheelset,  $T$ , was thus a function of the frictional coefficient, contact area, and contact pressure [21]

$$T = \mu \frac{D}{2} \int_A P dA \quad (5)$$

where  $\mu$  is the static coefficient of friction,  $D$  is the axle diameter,  $P$  is the contact surface pressure, and  $A$  is the contact surface area. The holding torque capacity derived from Equation (5) was related to the contact length of the press-fit assembly (Figure 17). The maximum holding torque capacities were 71 kNm for the interference of 200  $\mu\text{m}$ , 85 kNm for 240  $\mu\text{m}$ , 99 kNm for 280  $\mu\text{m}$ , and 113 kNm for 320  $\mu\text{m}$ . Clearly, the holding torque capacity increased with the interference.

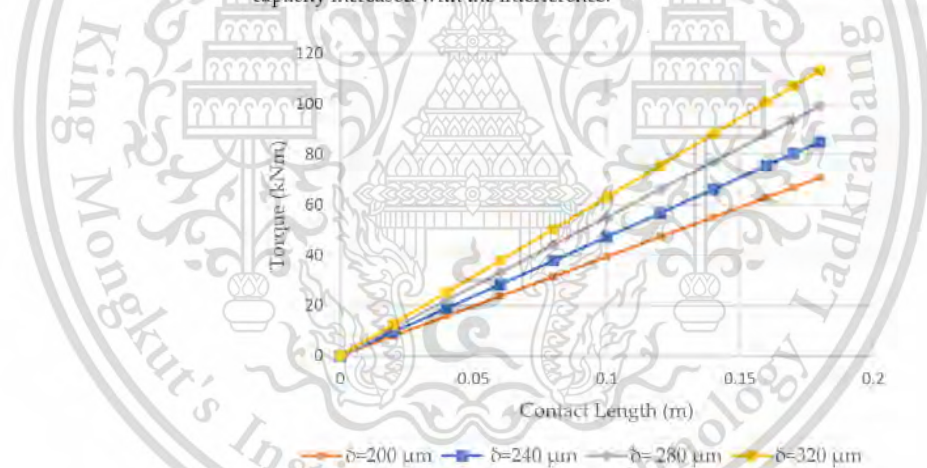


Figure 17. Holding torque capacity vs contact length.

### 5.2. Finite Element Analysis of the Holding Torque Capacity

Finite element analysis was used to examine the effect of the interference on the holding torque capacity for the wheel and axle assembly. The geometry of the 3D models and materials properties were similar to those for the press-fitting finite element analysis. During this analysis, surface-to-surface contact interaction was set between the wheel and axle interface with a contact interference fit option. A penalty frictional coefficient, 0.1, and hard contact were set as the contact properties. It was necessary to define the reference points on the axle at both end sides of the centre point and coupling to the surface that defined the coupling nodes. To obtain more accurate results, a refined mesh was used at

the contact area with a coarse mesh for the other areas. The torque loading was applied to the reference node at the end of the axle, and the outer surface of the wheel was fixed (Figure 18). The value of the applied torque was increased until rotation or 'slip' occurred in the interface.

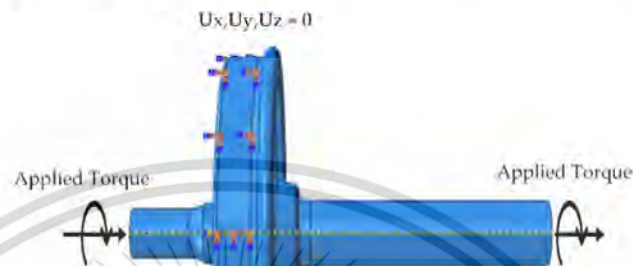


Figure 18. Loading and boundary conditions for the torque analysis.

The torque capacity analysis simulated the wheel and axle assemblies to obtain the curves of the torque and rotational angle, which determined the maximum holding torque capacity for different interference values. The torque and rotational angle curves were needed to decide the torque required to resist the slip between the interference assemblies. In Figure 19,  $T_E$  was the maximum elastic torque, and yielding started at that point. Within the elastic torque region, the shear stress in the axle varied linearly, and the axle showed only elastic deformation. When the torque increased to the plastic region,  $T_P$ , the axle rotated continuously with no further increase in the torque. The maximum elastic torque was equal to 75% of the maximum holding torque capacity at the fully plastic region [22,23]. Therefore, it was evident that the maximum holding torque capacity or plastic torque,  $T_P$ , before slipping was 75 kNm at the twist angle 0.15 rad, and the maximum elastic torque  $T_E$  was 56 kNm at the twist angle 0.029 rad for the interference of 240  $\mu\text{m}$ .  $T_E$  did not exceed the 75% of  $T_P$  for 240  $\mu\text{m}$ , and others were also less than 75% of the maximum holding torque capacity. When the torque increased beyond the maximum holding torque capacity, the axle started slipping. The curves for the torque capacity simulated with different interferences are shown in Figure 20. Table 7 compares the maximum holding torque capacity with theoretical and finite element results. The deviations between the estimated maximum holding torque capacities from the theory and finite element analyses were 15% for 200  $\mu\text{m}$  interference, 12% for 240  $\mu\text{m}$ , 8% for 280  $\mu\text{m}$ , and 6% for 320  $\mu\text{m}$ . Thus, the finite element results agreed with the theory.

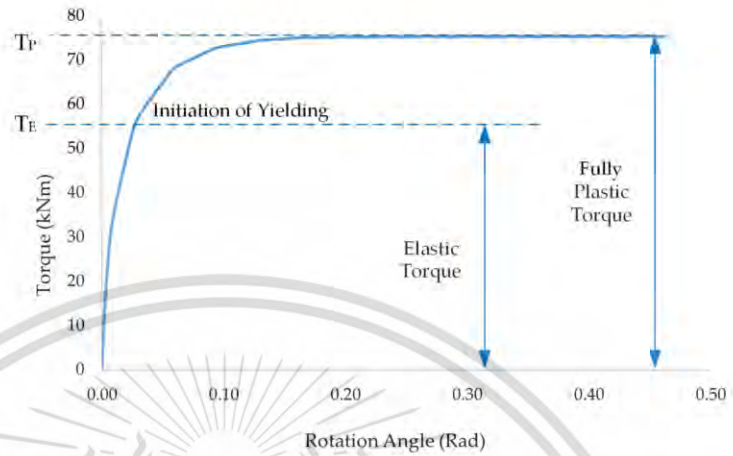


Figure 19. Torque vs. the rotation angle for 240 μm interference.

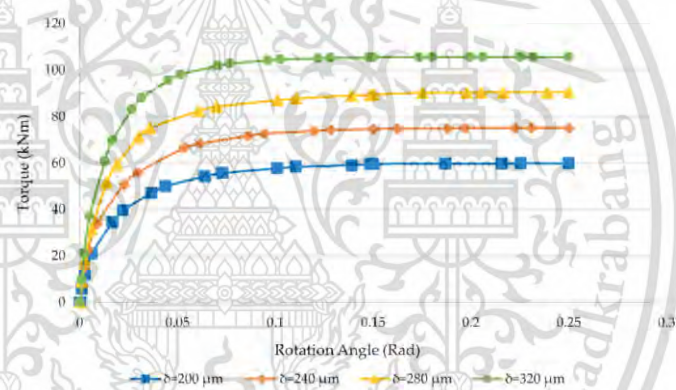


Figure 20. Torque vs rotation angle for four interferences.

Table 3. Maximum holding torque capacity—theory and finite element versus interference.

Interference (μm)	Maximum Holding Torque Capacity		
	Theory (Equation (5)) (kNm)	Finite Element Method (kNm)	Percent Deviation (%)
200	71	60	15
240	85	75	12
280	99	91	8
320	113	106	6

Percent Deviation was calculated as  
 Percent Deviation = [(Theory-FEM)/Theory] × 100%

### 6. Conclusions

Finite element methods and the EN 13260 standard to generate press-fitting curves would provide engineers with valuable information to quickly identify press-fit quality. The authors of this study verified the press-fitting curves and maximum press-fitting forces

obtained from finite element analysis by comparing them with the analytical results. To determine whether the press-fitting curve and maximum press-fitting force were acceptable, the EN 13260 standard was used. From the simulations, the press-fitting curves for assembling the wheel to the axle using the EN 13260 standard criteria were fully satisfied only when the interference ranged from 200  $\mu\text{m}$  to 320  $\mu\text{m}$  and the friction coefficient ranged from 0.08 to 0.13. The difference in the average contact pressure between the finite element and theoretical analyses was 3%. The maximum stress was found at a wheel hub inner surface due to the taper of the axle. The greater the interference, the greater the stress, which was due to the contact force. For interference of less than 360  $\mu\text{m}$ , plastic deformation did not occur, and the EN standard limitation of the interferences for the wheelset could be used in the press-fitting. Furthermore, the maximum holding torque capacity positively correlated to the interference in the elastic range. In the plastic region, the torque is constant even though the twist angle increases. The deviation in the maximum holding torque capacity between the finite element analysis and theory ranged from 15% to 6% for different interferences. Since the maximum elastic torque did not exceed 75% of the maximum holding torque capacity, interferences from 200 to 320  $\mu\text{m}$  were satisfactory. In summary, EN 13260 was very effective and can be used to assess the press-fit quality of the wheelset faster. The holding torque capacity formula (Equation 5) can be used to predict the maximum torque. In a future study, the authors will add experiments to verify the press-fitting curve.

**Author Contributions:** Conceptualization, T.N. and M.P.; methodology, T.N. and M.P.; software, T.N. and M.P.; validation, T.N. and M.P.; investigation, T.N.; resources, T.N.; writing—original draft preparation, T.N.; writing—review and editing, M.P.; visualization, T.N.; supervision, M.P.; project administration, M.P.; funding acquisition, M.P. All authors have read and agreed to the published version of the manuscript.

**Funding:** This research was funded by King Mongkut's Institute of Technology Ladkrabang (Grant No. KDS2019/019).

**Institutional Review Board Statement:** Not applicable.

**Informed Consent Statement:** Not applicable.

**Data Availability Statement:** Not applicable.

**Acknowledgments:** This work was supported by King Mongkut's Institute of Technology Ladkrabang.

**Conflicts of Interest:** The authors declare no conflict of interest.

## References

1. Kowalski, S. Failure Analysis of the Elements of a Forced-in Joint Operating in Rotational Bending Conditions. *Eng. Fail. Anal.* **2020**, *118*, 104864. [CrossRef]
2. Kowalski, S. Fretting Wear in Selected Elements of Rail Vehicles. *Teh. Vjesn.* **2018**, *25*, 481–486. [CrossRef]
3. Japanese Industrial Standard (JIS); Japanese Standards Association (JSA). *JIS E 4504:2015 Rolling Stock—Wheelsets—Quality Requirements*; JSA: Tokyo, Japan, 2015.
4. European Committee For Standardization. *EN 13260:2009+A1:2010: Railway Applications—Wheelsets and Bogies—Wheelsets—Product Requirements*; BSI: London, UK, 2010.
5. ISO 1005-7:1982. *Railway Rolling Stock Material; Part 7: Wheelsets for Tractive and Trailing Stock; Quality Requirements*, 1st ed.; International Organization for Standardization: Geneva, Switzerland, 1982.
6. AAR. *Manual of Standards and Recommended Practices Section G-II Wheel and Axle Manual*; Association of American Railroads: Washington, DC, USA, 2019.
7. Benuzzi, D.; Donzella, G. Prediction of the Press-Fit Curve in the Assembly of a Railway Axle and Wheel. *Proc. Inst. Mech. Eng. Part F J. Rail Rapid Transit* **2004**, *218*, 51–65. [CrossRef]
8. Lu, J.; Xiao, J.; Gao, D.J.; Zong, S.Y.; Li, Z. Research on Standard and Automatic Judgment of Press-Fit Curve of Locomotive Wheel-Set Based on AAR Standard. In *IOP Conference Series: Materials Science and Engineering*; IOP Publishing Ltd.: Bristol, UK, 2018; Volume 326. [CrossRef]
9. Saad, S.; Magnier, V.; Dufrenoy, P.; Charkaluk, E.; Demilly, F. Numerical Chain of Forging Railway Axle and Wheel Press Fitting Operation. *Lect. Notes Mech. Eng.* **2015**, *789*, 115–127. [CrossRef]

10. Stamenković, D.; Milošević, M.; Mijačlović, M.; Banić, M. Recommendations for the Estimation of the Strength of the Railway Wheel Set Press Fit Joint. *Proc. Inst. Mech. Eng. Part F J. Rail Rapid Transit* **2012**, *226*, 48–61. [CrossRef]
11. Michnej, M.; Guzowski, S. Fretting Wear Simulation in a Clamped Joint Based on the Example of a Rail Vehicle Wheel Set. *Wear* **2019**, *438*, 102654. [CrossRef]
12. Booker, J.D.; Truman, C.E. Strengthening And Weakening Mechanisms in Interference-Fitted Joints. In Proceedings of the IRF2020: 7th International Conference Integrity-Reliability-Failure, Funchal, Portugal, 6–10 September 2020; pp. 405–418.
13. Zhao, J.; Wang, J.-X.X.; Yu, C.; Tang, S.-Q.Q.; Yao, J. Influence of Radial Interference on Torque Capacity of Shrink-Fit Camshaft. *Adv. Mech. Eng.* **2019**, *11*, 1–10. [CrossRef]
14. Joannides, T.; Leggoe, J.; Sercombe, T.; McArthur, J. *Effects of Surface Topography and Interference on the Mounting Curve of Railway Wheel-Set Press-Fit Assembly*; CEED: Crawley, Australia, 2017; pp. 25–30.
15. SIMULIA. *Abaqus Analysis User's Manual*; Dassault Systèmes Simulia Corp.: Providence, RI, USA, 2010; Volume I-IV.
16. European Committee for Standardization. *BS EN 13261: 2020 Railway Applications—Wheelsets and Bogies—Axles—Product Requirements*; BSI: London, UK, 2020.
17. European Committee for Standardization. *BS EN 13262: 2020 Railway Applications Wheelsets and Bogies—Wheels—Product Requirements*; BSI: London, UK, 2020.
18. Budynas, R.G.; Nisbett, J.K. *Shigley's Mechanical Engineering Design*, 8th ed.; McGraw-Hill: New York, NY, USA, 2006. [CrossRef]
19. Son, S.-W.; Jung, H.-S.; Kwon, T.-S.; Kim, J.-S. Fatigue Life Prediction of a Railway Hollow Axle with a Tapered Bore Surface. *Eng. Fail. Anal.* **2015**, *58*, 44–55. [CrossRef]
20. Uni Rail. *Wheelset Catalogue*; UniRail Ltd.: Sofia, Bulgaria, 2003.
21. Rothbart, H. *Mechanical Design Handbook*, 2nd ed.; McGraw-Hill Education: New York, NY, USA, 2006.
22. Hibbeler, R.C. *Mechanics of Materials*, 8th ed.; Prentice Hall: Hoboken, NJ, USA, 2010.
23. Beer, F.P.; Johnston, E.R.; DeWolf, J.T.; Mazurek, D.F. *Mechanics of Materials*, 6th ed.; McGraw-Hill: New York, NY, USA, 2012.



**Multiaxial Fatigue-Life Prediction of Railway Axles with Consideration of Braking Effects**
Theingi Nwe<sup>✉</sup>, Monsak Pimsarn<sup>✉</sup>

Department of Mechanical Engineering, School of Engineering, King Mongkut's Institute of Technology, Ladkrabang 10520, Thailand

Corresponding Author Email: [monsak.pi@kmitl.ac.th](mailto:monsak.pi@kmitl.ac.th)<https://doi.org/10.18280/mmep.100320>**ABSTRACT****Received:** 9 January 2023**Accepted:** 2 April 2023**Keywords:***braking, fatigue life, multiaxial loading, railway axle, strain-life*

Ensuring safety in the design of railway infrastructure and rolling stock is a critical aspect of railway operations. Railway axles are subjected to fluctuating bending and torsion loads, which often lead to the development of plastic stresses in the vicinity of fillets and notches, even though they are designed to withstand nominal elastic loads. This study aims to provide an accurate fatigue-life prediction for a motor bogie axle, taking into account the braking effects in conjunction with press fitting and the influence of masses in motion on the axle. Initially, the stress and deflection of the axle under combined loadings are calculated in accordance with the EN 13104 standard. Subsequently, a comparative simulation analysis is conducted using ABAQUS commercial software, with particular emphasis on specific loading conditions. A strain-based approach is employed to estimate fatigue life under multiaxial loading and variable amplitude overloading scenarios, utilizing fe-safe commercial fatigue analysis software. The results reveal a strong correlation between the theoretical and finite element analyses. The braking effects are found to reduce fatigue life by 50% compared to the influences of press fitting combined with masses in motion. This research highlights the significance of considering braking effects in fatigue-life predictions of railway axles to ensure safe and robust design.

**1. INTRODUCTION**

Axles are a vital component in locomotive systems' rolling stock, serving to support rotating elements and transmit rotational motion and power. They must withstand various combined loads, which can result in extensive fatigue damage during operation. Railway axles are subjected to complex loads, such as vertical forces due to wagon mass and payload, lateral forces, and braking forces. An axle drives a vehicle by transmitting power from an electric motor to the vehicle wheels and by managing the rotational speed of the axle or stopping the vehicle using brake discs [1, 2]. Consequently, a railway axle must absorb braking forces and be designed to operate safely with a known fatigue life.

Two types of brakes are commonly employed: adhesion-dependent and independent brakes, consisting of a tread and brake disc that can be mounted either on the axle or the wheel [1, 2]. Owing to limited space in bogies, axle-mounted disc brakes are typically used on trailers, while wheel-mounted disc brakes are utilized on motor bogies, where the braking force is transferred through the wheel to the axle [3, 4]. Although traction forces generated by power transmission must be considered according to applicable standards, they are deemed unnecessary in this analysis since traction and braking forces are not applied to an axle simultaneously. Hence, moments caused by traction forces are not considered.

Fatigue due to cyclic loading is the most common cause of railway axle failure. Even well-designed axles may experience mechanical failure when subjected to repeated loading or overloading. Fatigue-life evaluation is a crucial technique

often used to develop or improve product designs. Complete information regarding component shape, material, load condition, work environment, and work limitations is required for fatigue-failure analysis. Traditional uniaxial models are insufficient for addressing actual axle loads, as axles experience combined multiaxial loading of direct and shear stresses under service conditions [5, 6]. Testing is expensive, and the load spectrum of a railway axle is random, necessitating the development of a novel approach to calculate axle fatigue life. Accordingly, this study focuses on examining railway axle fatigue under variable amplitude cyclic overloading due to track irregularities, including curves, alignment, longitudinal level, switches, and crossovers, using a strain-life method.

Recent studies have not considered the braking effect as a significant issue for design calculation and fatigue-life prediction [7-10]. Nonetheless, contemporary research on railway axle design calculation and fatigue-life prediction offers a more comprehensive understanding of materials, manufacturing, design methods, and press fitting effects. Parametric research on the composite railway axle lightweight design concept has been reported, revealing a potential 75% reduction in unsprung mass compared to a conventional hollow steel axle [11]. Son et al. [12] proposed a new material and taper bore axle geometry to predict fatigue life under various service conditions as a novel design approach. Hirakawa and Kubota [13] explored a fatigue design method comparing Japanese and European design philosophies and examined fretting fatigue damage of press-fitted parts. Other studies [14-17] emphasized the importance of accounting for

the press-fitting effect in railway axle design and demonstrated how research findings have been applied to improve axle manufacturing. A systematic review by Günay et al. [1] investigated various braking systems used in railway vehicles, as well as design and material selection. A parametric study was conducted on wheel tread damage resulting from repeated braking concerning braking temperature and field tests. Wear simulation methodologies for brake blocks and wheel treads were developed [18, 19].

This research aims to investigate the impact of braking on the fatigue crack initiation life of railway axles, an area that has been largely underexplored. All forces due to press fitting, masses in motion, and braking effects are combined according to the EN 13103/4 standard. Stress acting on an axle is calculated in various transition sections where stresses are concentrated for analytical calculations. The finite element (FE) method was employed for numerical modeling and validation of the analytical calculation results. Based on the stress histories of FE analysis, fatigue-life prediction was performed multiaxially, employing a variable amplitude overload history with a strain-based approach.

**2. ANALYTICAL STRENGTH EVALUATION OF RAILWAY AXLES**

This study followed the EN 13104 standard for determining the bending moment and stress along an axle configuration using a specific load on a powered motor bogie wheelset. Figures 1 and 2 show schematic free-body diagrams of the wheelset induced by masses in motion and braking defined by the EN standards.

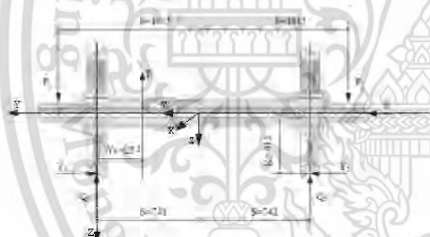


Figure 1. A schematic free-body diagram of a motor bogie wheelset due to masses in motion (measurements are in mm)

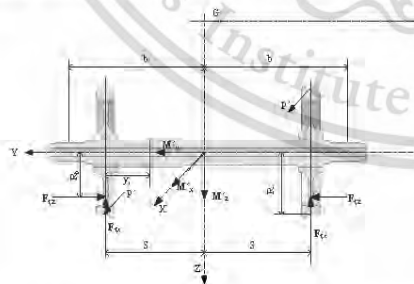


Figure 2. A schematic free-body diagram of a motor bogie wheelset due to braking (measurements are in mm)

**2.1 Loads acting on an axle**

An operating wheelset experiences three forces, those generated by masses in motion, braking and traction. For a powered motor bogie axle with an asymmetric vertical force loaded on its journal bearings, the force due to the masses of the unsprung parts, wheel-rail contact force, lateral force and braking are the most prominent acting on an axle. An axle can be subjected to torsional loading during driving, accelerating, and braking. A railway axle with two brake discs attached to its wheel hub is considered in the calculations of the current study. Type of the rolling stock used in this study is high-speed motor bogies and long-distance trains. The maximum normal design payload for a vehicle is 239.136 kN, and the weight of the vehicle body is 283.755 kN. The maximum braking force used in this study is for emergency braking under a deceleration of 1.25 m/s<sup>2</sup>. The specific load values used to calculate the internal and external stresses on a motor bogie axle are shown in Table 1 [20].

Table 1. Loads for an axle of a motor bogie

Load	Magnitude (kN)
Vertical force on the more loaded side= $P_1$	101.300
Vertical force on the less loaded side= $P_2$	75.528
Wheel-rail horizontal contact force on the more loaded side= $Y_1$	49.509
Wheel-rail horizontal contact force on the less loaded side= $Y_2$	24.754
Vertical rail contact reaction force on the more loaded side= $Q_1$	112.430
Vertical rail contact reaction force on the less loaded side= $Q_2$	63.171
Balancing force between $Y_1$ and $Y_2$ = $H$	24.775
Un-sprung force= $F_1$	-1.215
Friction force between the wheel and brake disk= $F$	0.250
Maximum braking force= $F_f$	39.200
The proportion of $P$ braked by the braking system= $P'$	75.000

**2.2 Stress evaluation along an axle**

The stress concentration factor of an axle,  $K$ , is proportional to the ratio of the fillet or groove radius, the diameter of a cylindrical part, and the ratio of two different adjacent cylindrical parts at the transition fillet or groove (Figure 3). In the current study, these parameters were calculated according to the appropriate standards [3, 4]. Table 2 shows the stress concentration factor at various transition zones of a motor bogie axle. The bore of the hollow axle and other parts that did not change the section and the stress concentration factor was 1.

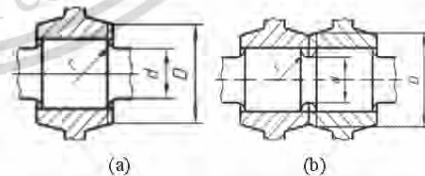
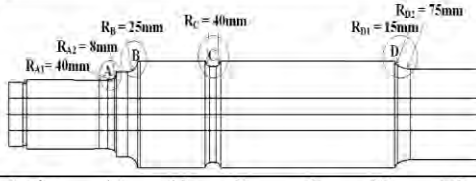


Figure 3. Expression of a stress concentration factor (a) bottom of the transition between two cylindrical parts and (b) groove bottom [1, 2]

**Table 2.** Stress concentration factor in various axle sections



Region	A1	A2	B	C	D1	D2
R (mm)	40	8	25	40	15	75
d (mm)	130	130	160	180	184	170
D (mm)	138	152	266	266	200	200
K	1.01	1.16	1.19	1.21	1.06	1.02

The bending and torsional moments generated by the vertical reaction and braking forces acting on the wheelset were calculated using beam theory. Eqns. (1) and (2) [3, 4] are the bending moments generated by the masses acting on the journal bearings and braking forces acting between the load plane and wheel.

$$M_x = Ry \tag{1}$$

$$M'_x = F_{rx} \Gamma y \tag{2}$$

where,  $M_x$  is the bending moment generated by masses in motion,  $M'_x$  is the bending moment caused by braking forces acting on the x axis,  $F_{rx}$  is the maximum braking force acting vertically,  $\Gamma$  is the friction force between the brake disk and wheel, and  $y$  is the distance for any axle section from the vertical force  $P$ .

Eqns. (3) and (4) [3, 4] are the bending moments generated by the masses in motion and braking forces between two wheels.

$$M_y = Py - Q_b(y - b + S) + YR - \sum_i F_i(y - b + S - y_i) \tag{3}$$

$$M'_y = F_{rx} \Gamma (b - S + y_i) \tag{4}$$

where,  $b$  is the distance between the vertical centerline and the vertical force on axle journals,  $S$  is the distance between the wheel tread and the vertical centerline,  $R$  is the nominal radius of the wheel tread, and  $y_i$  is the distance between one wheel's tread and the force  $F_i$ .

Eq. (5) is the torsional moment between two wheels generated by braking forces acting tangentially to the wheels. The torsional moment between the vertical force load plane and the wheel is zero.

$$M'_y = 0.3P'R \tag{5}$$

where,  $M'_y$  is the torsional moment due to braking,  $P'$  is the proportion of  $P$  from the braking system, and  $R$  is the nominal wheel radius.

Eq. (6) is the bending moment between the vertical force load plane and wheel generated by braking forces acting along the x-axis.

$$M'_z = F_{rz} \Gamma \frac{R_b}{R} y \tag{6}$$

Eq. (7) is the bending moment between two wheels generated by braking forces acting along the x-axis.

$$M'_z = F_{rz} \Gamma (b - S) \frac{R_b}{R} \tag{7}$$

where,  $M'_z$  is the bending moment due to braking acting on the z axis,  $F_{rz}$  is the maximum braking force acting horizontally and  $R_b$  is the radius of applied brake force.

The resultant moment,  $M_R$ , is given by Eq. (8).

$$M_R = \sqrt{MX^2 + MY^2 + MZ^2} \tag{8}$$

where,  $MX$  is the sums of the bending moment acting on the x axis and  $MZ$  are the sums of the bending moments acting on the z axis,  $MY$  is the summation of torsional moments.

The current study considered normal, shear, and equivalent stresses at various sections along a hollow axle. The normal and shear stresses are respectively expressed by Eqns. (9) and (10).

$$\sigma_n = \frac{32 \times \sqrt{MX^2 + MZ^2} d}{\pi(d^4 - d'^4)} \tag{9}$$

$$\tau = \frac{16 \times MY \times d}{\pi(d^4 - d'^4)} \tag{10}$$

Eq. (11) [3, 4] is the equivalent stress on the surface of an axle.

$$\sigma = \frac{K \times 32 \times MR \times d}{\pi(d^4 - d'^4)} \tag{11}$$

where,  $K$  is the stress concentration factor,  $d$  is the external diameter for an axle section and  $d'$  is the bore diameter of a hollow axle.

Eq. (12) [3, 4] is the equivalent stress on the bore surface of an axle.

$$\sigma = \frac{K \times 32 \times MR \times d'}{\pi(d^4 - d'^4)} \tag{12}$$

Eqns. (13) and (14) [3, 4] are the stress concentration factor of a bottom of the transition between two cylindrical parts and groove bottom.

$$K = \frac{(4 - D/d)(D/d - 1)}{5(10(r/d))^{(2.5(r/d)+1.5-0.5(D/d))}} + 1 \tag{13}$$

$$K = \left[ \frac{(4 - D/d)(D/d - 1)}{5(10(r/d))^{(2.5(r/d)+1.5-0.5(D/d))}} \right] \left[ \frac{-1.2(r/d)^2 - 37(r/d)}{(D/d)^3} + 1.74 \right] + 1 \tag{14}$$

where,  $r$  is the transition fillet or groove radius,  $d$  is the diameter of the axle in which the stress concentration is calculated,  $D$  is the diameter of the wheel hub as shown in Figure 3.

### 3. NUMERICAL SIMULATION OF A RAILWAY AXLE

The methodology for predicting railway axle fatigue life consists of two main steps. First, numerical simulation of the railway axle loading must be done in ABAQUS. Then, the loading spectrum is transferred and repeated up to the fracture point in fe-safe, which is a powerful fatigue life prediction software for FE models.

#### 3.1 Finite element method

Finite element analysis of the railway motor bogie wheelset assembly was performed to examine stress history after press fitting and loading. A three-dimensional FE half-symmetry model of the wheelset was developed using ABAQUS software. As demonstrated in Figure 4, the FE model consists of two components, wheel and axle. A railway wheel and axle are press fitted with an interference 0.2 millimetres, calculated following EN 13260 [21]. The material used in this study is EA4T steel, Young's modulus ( $E$ ) is 206 GPa and Poisson's ratio ( $\nu$ ) is 0.3, which are frequently employed in railroad wheelsets. To achieve precise and accurate FE modelling results, the mesh sensitivity analysis was conducted, and the element size was carefully chosen. Based on the results of the comparison of different mesh sizes, we determined the optimal mesh size that provides a reasonable trade-off between accuracy and computational cost. Specifically, the element size was set to 2 mm at the fillet and notch groove transition, 5 mm at the contact area between the wheel and axle, 10 mm at other parts of the axle, and a 20 mm expected contact area for the wheel. This approach allows for accurate results with a minimal number of elements. The model consists of 256,456 elements (C3D8R), as demonstrated in Figure 4. First-order reduced integration elements are utilized by controlling the hourglass effect to improve the accuracy of results. This prevents potential singularities due to reduced integration and increases computational efficiency in numerical simulations.



Figure 4. FE meshing model of the wheelset.

The mating surface between the wheelset was defined as a surface-to-surface contact, where the wheel's contact surface was the master surface due to its greater stiffness. The master surface nodes could penetrate the slave surface, where the axle's contact surface was the slave. Small sliding contact formulation was used to ensure that motion between surfaces was small and accurately simulated the press-fitting procedure. The coefficient of friction for the wheelset contact was 0.1 to account for tangential behaviour. A hard contact model was proposed to ensure normal behaviour.

The boundary conditions and loading of the wheelset were set following the EN 13103/4 design standard (Figure 5). The

wheel-rail contact nodes were fixed,  $U_x = U_y = 0$ , to the contact plane of the wheel and track. In this analysis, the loading was applied in a multi-step case. We defined three load steps using a multi-load case function. Step 1 involves applying an interference fit. The second step is an analysis that adds vertical loading and lateral force to the model. Step 3 includes braking forces and torsion loading.

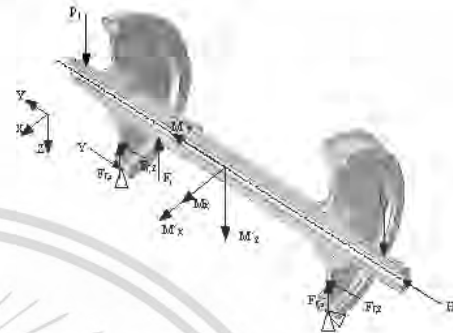


Figure 5. Boundary condition of the FE model wheelset.

#### 3.2 Multiaxial strain-life analysis method

A multiaxial strain-life method was used in the current study. It is applicable to both high- and low-cycle fatigue problems with complicated forces and moments that produce multiaxial stress and strain states. The fatigue performance of the axle was examined under various loading conditions to investigate the discrepancy between the results of considering braking effect and not. A typical strain-life analysis has several basic steps. First, the stress determined from numerical analysis using the ABAQUS program is necessary. It is important in obtaining actual fatigue-life estimates. These FE results are then imported into fe-safe. The fatigue material properties, loading history, fatigue algorithm selection, and mean stress correction all have a significant impact on fatigue-life prediction. Figure 6 illustrates the fatigue analysis procedure used in this investigation.

The loading history to which the component has been subjected affects the fatigue-life prediction model. Imported FE results contain multiple linear elastic stress datasets. Each dataset contains the results of a unit-load scenario for a specific load direction. The estimated stress tensor at each node is multiplied by the load history in fe-safe. Moreover, the load ratios are easily assignable. The load case per load ratio is shown in Table 3. Figures 7 and 8 give the loading history diagram applied to each stress dataset. The load histories are assumed to be repeated until the axle fails. Railway axles in service are exposed to variable amplitude loading, which causes variable fatigue damage and overloading due to additional dynamic forces. The bending stresses obtained from FE analysis were utilized as the base load and set with a cyclic amplitude of variable overloading that was applied every fifth cycle, both upward and downward, during axle rotation. A torsional stress load history was set up as a sinusoidal function with a magnitude range of 0 to 1, since torsion is steady [22]. Press fitting is a constant load ratio [23]. Under Neuber's law [24], elastic stress is converted into elastic-plastic stress-strains, which are then utilized in a strain-life fatigue calculation.

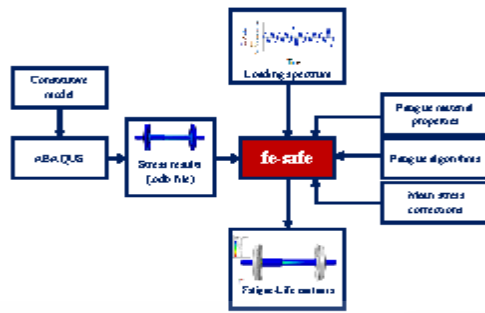


Figure 6. Fatigue analysis procedure

Table 3. Load case vs. load ratio

Load Case	Load Ratio (R)
Press Fitting Force	Constant
Vertical Force	R=-1
Lateral Force	R=0
Braking Force	R=0
Torsional Moment	R=0

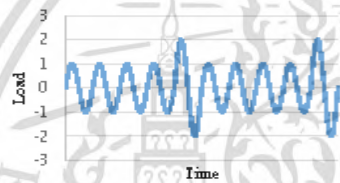


Figure 7. Load spectra for fatigue prediction (R=-1)

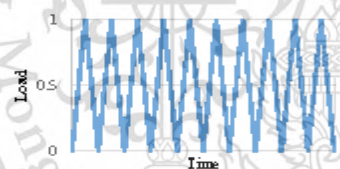


Figure 8. Load spectra for fatigue prediction (R=0)

This study used the Brown-Miller method and Morrow mean stress correction with biaxial strain-life algorithm. The Brown-Miller criterion [25] is widely accepted for analysis of ductile metals and provides the highest accuracy estimates of fatigue-life. The Brown-Miller equation (Eq. (15)) states that the critical plane where maximum fatigue damage occurs is determined by the maximum shear strain amplitude ( $\Delta\gamma_{max}/2$ ) and normal strain amplitude ( $\Delta\epsilon_{max}/2$ ). Therefore, the Brown-Miller equation suggests that the combination of shear and normal strain is the primary cause of severe fatigue damage in materials. The complete Brown-Miller equation can be written as a result of the mean stress correction.

$$\frac{\Delta\gamma_{max}}{2} + \frac{\Delta\epsilon_{max}}{2} = 1.65 \frac{\sigma'}{E} (2N_f)^b + 1.75 \epsilon_f' (2N_f)^c \quad (15)$$

where,  $N_f$  = the number of cycles to failure,  $\frac{\Delta\gamma_{max}}{2}$  = shear strain amplitude,  $\frac{\Delta\epsilon_{max}}{2}$  = normal strain amplitude.

Fatigue damage is determined on each plane using a Rainflow cycle algorithm and Palmgren-Miner rule [26]. For variable amplitude loading, fatigue damage is calculated by dividing the design life by its available life, and overall damage is summed up. The crack initiation plane is defined as the plane with the shortest life. Values greater than one indicate failure prior to reaching the design life. Table 4 provides information on the EA4T steels fatigue materials properties.

Table 4. Fatigue properties of the EA4T material

Ultimate tensile strength	650.0 MPa
Fatigue strength coefficient ( $\sigma'$ )	811.1 MPa
Cyclic yield strength ( $\sigma_{yc}$ )	385.2 MPa
Cyclic fatigue strength coefficient ( $K'$ )	806.3 MPa
Fatigue strength exponent (b)	-0.069
Fatigue ductility exponent (c)	-0.641
Fatigue ductility coefficient ( $\epsilon_f'$ )	0.658
Surface finish factor ( $K_s$ )	1

#### 4. RESULTS

Figure 9 shows a moment diagram of an axle evaluated using the EN 13103/4 standard employing Eqns. (1) to (8). The wheelset was assumed to run on a curved track, considering lateral and braking forces. The bending moment  $M_x$  due to the vehicle's mass between the loading plane and the rolling wheel was also calculated using Eq. (1). It was computed between the two wheels using Eq. (3). The braking system generates moments as three components, x, y and z, which are calculated separately depending on the braking method. Brake imbalance, curvature effects and wheelset hunting generate torque along the y-axis. Frictional braking forces on the disc produce braking moments along the x- and z-axes. Bending moments of the x- and z-components are smaller than the torsional moment in the y-direction. The maximum moment occurred at the axle wheel seat with the transmission of track reaction forces to the axle through the wheel, causing the side of the axle to become more loaded.

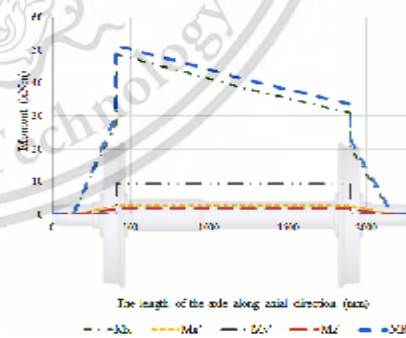
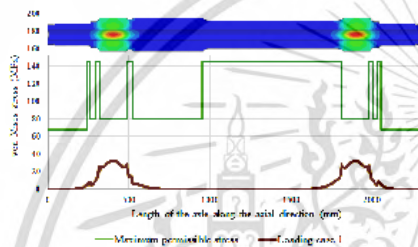


Figure 9. Moment diagram of the axle along the longitudinal axis

**4.1 Effect of loading cases on the stress concentration of a railway axle**

Several static stress analyses were performed and defined considering only the press fitting effect in Loading Case 1, combined press fitting and masses in motion in Loading Case 2 and further combining them with the braking effect in Loading Case 3. Figures 10, 11, and 12 present graphical representations of the corresponding von Mises stress variation and counter plot of the von Mises stress variation of the axle 3D model for each loading condition. The distribution of von Mises stress throughout the axles generated by press fitting is plotted in Figure 10. During the press fitting, displacement and deformation occur on the press fitted seats and wheel hub because the contact pressure increases, causing stress, and the stress concentration rises. The calculated von Mises stress distribution based on FE analysis was zero, except for the wheel seat contact areas, fillets, and groove transitions near the interference fit. As a result, press fitting significantly affected the wheelset's initial residual stresses.



**Figure 10.** von Mises stress variation of an axle along the longitudinal axis generated by Loading Case 1

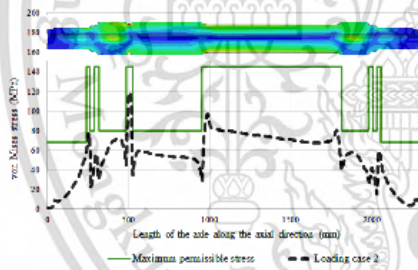


**Figure 11.** von Mises stress variation of an axle along the longitudinal axis generated by Loading Case 2

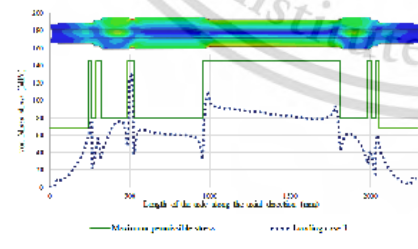


**Figure 12.** von Mises stress variation of an axle along the longitudinal axis generated by Loading Case 3

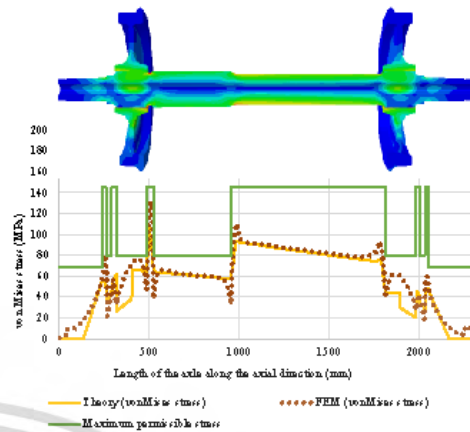


**Figure 13.** Comparison of von Mises stress variation of an axle along the longitudinal axis

The von Mises stress from FE analysis throughout the axles generated by the combined loading cases is shown graphically in Figures 11 and 12. The surface of the axle furthest from the natural axis and notch groove, where the most significant stress concentration resided, experienced the highest von Mises stress. In both loading cases (2 and 3), the maximum stress concentration is located at the notch groove transition zone, with values of 114 and 127 MPa. Comparing the analytical and FE analysis results (Figure 13), the maximum stress value of the notch groove transition from FE analysis was 43% higher than the value calculated using the EN standard. These values vary depending on various axle geometry parameters, as described in Section 2.2. Furthermore, the standard does not consider the press-fitting effect. The other sections of both results are very good agreements except for the location of the wheelset contact place and adjacent transitions places.

This was done to validate the safety factor following the EN 130 13/4 standard, depending on the type and specific zone of the axle. The results from both theoretical and numerical methods indicate that the stress values are below the maximum permissible stress, as illustrated in Figure 13. Furthermore, the FE numerical method yielded a safety factor of 1.2 at the groove notch transition, indicating that the design is safe and can withstand the applied load. The combination of the braking effect increases stress to the axle by 10%. Thus, it would be misleading to design the axle based on only the masses in motion.

**4.2 Multiaxial fatigue-life prediction of a railway axle**

Multiaxial fatigue-life prediction was implemented in fe-safe, a commercial software that functions as a post-processor for structural FEA results, which reads data from a .odb file. Since fatigue cracks typically start at component surfaces, only surface nodes of the axle 3D model were examined. The FE analysis results are output as multiple load cases to accurately account for the effects of various stress histories on axle life. It was necessary to scale the stress to almost the yield-stress because the axle was designed to have an infinite life, and the working stress was below the

permissible level.

Three loading scenarios were taken into consideration to examine the effects of loading conditions and impact of variable amplitude overload on the fatigue-crack initiation. Figure 14 compares the lowest fatigue life between three loading conditions at specific locations with comparative results. The estimated fatigue safety factors show fatigue durability throughout an infinite life cycle in Figure 15. It was calculated as the product of the stress amplitude and the fatigue strength of the material. Figure 16 demonstrates the fatigue damage obtained through fatigue analysis using fe-safe.

The effect of press fitting in Loading Case 1 showed no fatigue in the motor axle design. It has an infinite fatigue life because of endurance cycle reached  $10^7$ . Its factor of strength (FOS) was larger than 2 because the stress amplitude was below the permissible level, and the calculated life was greater than the design life. Figure 16 shows no damage will be caused due to that loading.

The generated fatigue-life results showed that fatigue began in Loading Case 2 at the groove notch, location 3, for the motor axle. It resulted from the combined press fitting and masses in motion with overloading applied every fifth cycle. Figure 14 shows the fatigue-life prediction results of axles as log10(life) contours, where life is in cycles, and the minimum value is ( $10^{5.906} = 8.05E+05$  cycles). As is evident in Figure 14, at location 3, the groove notch region shows the minimum life, and crack initiation occurred here, at the highest stress level. This was determined by the stress at a node for all loading conditions. The crack initiation location is indicated by the red zone in the stress contour where the highest level of stress is present. The minimum factor of strength (FOS) was 0.715 at location 3. The damage contour plot gives the fatigue damage values of a specific plane at a given design life (Figure 16). It shows the maximum fatigue damage was  $3.830E-07$  and the crack initiation will occur when the fatigue damage is equal to 1 because fatigue life is inverse of the damage.

For Loading Case 3, with three loading conditions, the lowest fatigue life will endure  $10^{5.609} = 4.06E+05$  cycles at location 3 before failing. Loading Case 3 for of the log(life-repeat) cycle was 5% less that of Case 2 at location 3. The factor of strength (FOS) was 0.678 and the percentage difference between the two loading cases remained the same as the log(life-repeat) cycle. Additionally, in a specific scenario where braking is applied, the maximum damage value experienced a 70% increase (Figure 16).

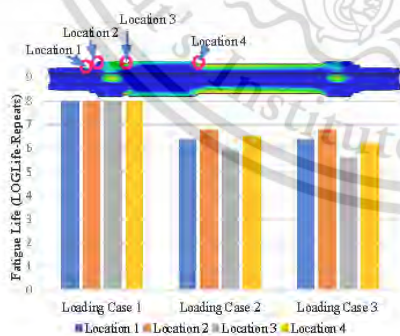


Figure 14. Estimated fatigue life of a railway axle

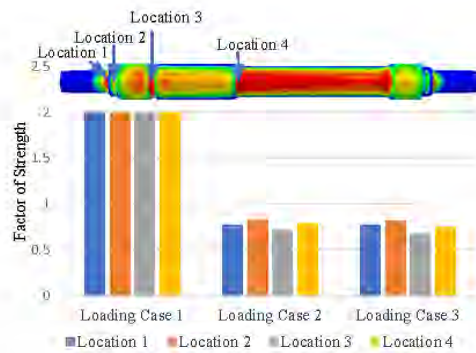


Figure 15. Estimated factor of strength of railway axle

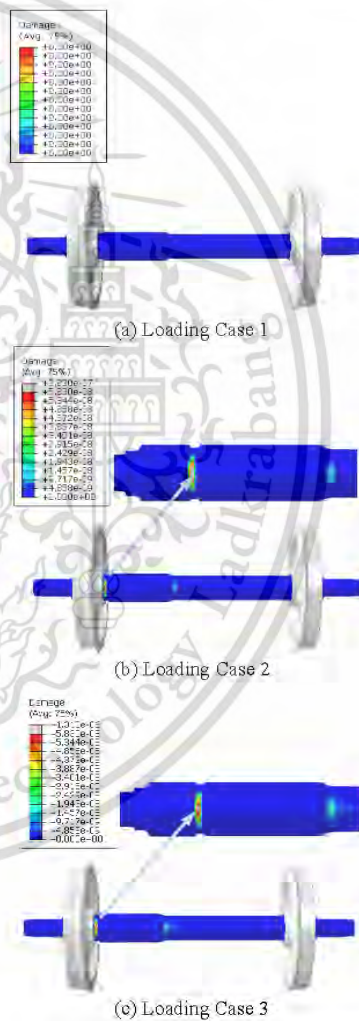


Figure 16. The estimated fatigue damage of railway axle

## 5. CONCLUSIONS

The current paper presents a methodology for analytical and numerical calculation of the strength of railway motor bogie axles according to European standards, which considers the masses of a rail vehicle, lateral forces, and the braking force effect to ensure accurate fatigue-life predictions.

The main results are the following:

- Press fitting caused compression stress on the wheel seat of axle and tensile stress on the adjacent fillet or groove notch transition zone.
- The groove notch is a critical part of the axle, with the operating stress close to the allowable stress. The obtained analytical results are verified by FE calculation results, with deviations of the maximum stress at the groove notch and the FE results due to the residual stress of press fitting.
- Applying several load scenarios and variable amplitude overloading improves the reliability of fatigue-life predictions for accurately assessing fatigue damage under complex multiaxial loading of railway axles.
- The torsional stress does not produce a significant impact on axle fatigue. Nevertheless, the combined bending and torsion stress caused by braking reduces axle fatigue life cycles by 50% (5% in log scale). Therefore, the effect of braking should not be neglected and can be evaluated using the EN method.
- It can be concluded that an axle has an infinite life design because its fatigue life under a combination of various loading scenarios exceeded  $10^7$  cycles. When a rotational bending load defined as a variable amplitude and overload was scaled-up by a factor of two and applied at every fifth cycle, the minimum fatigue crack initiation life is  $4.06E+05$  ( $1.1E+03$  km).

Overall, the presented methodology provides a reliable approach to assessing the fatigue life of railway axles and can aid in the design of new axles with longer life cycles.

## ACKNOWLEDGMENT

This work was financially supported by King Mongkut's Institute of Technology Ladkrabang (Grant No.: KDS2019/019).

## REFERENCES

- [1] Günay, M., Korkmaz, M.E., Özmen, R. (2020). An investigation on braking systems used in railway vehicles. *Engineering Science and Technology, an International Journal*, 23(2): 421-431. <https://doi.org/10.1016/j.jestch.2020.01.009>
- [2] Bosso, N., Gugliotta, A., Magelli, M., Oresta, I.F., Zampieri, N. (2019). Study of wheel-rail adhesion during braking maneuvers. *Procedia Structural Integrity*, 24: 680-691. <https://doi.org/10.1016/j.prostr.2020.02.060>
- [3] BS EN 13103-1: 2017: Railway Applications - Wheelsets and Bogies - Part 1: Design Method for Axles with External Journals, 2011.
- [4] European Committee for Standardization. BS EN 13104: 2009+A2:2012: Railway applications — Wheelsets and bogies — Powered axles — Design method. BSI Standards, 2012.
- [5] Beretta, S., Carboni, M. (2011). Variable amplitude fatigue crack growth in a mild steel for railway axles: Experiments and predictive models. *Engineering Fracture Mechanics*, 78(5): 848-862. <https://doi.org/10.1016/j.engfracmech.2010.11.019>
- [6] Zerbst, U., Beretta, S., Köhler, G., Lawton, A., Vormwald, M., Beier, H.T., Klingbeil, D. (2013). Safe life and damage tolerance aspects of railway axles—A review. *Engineering Fracture Mechanics*, 98: 214-271. <https://doi.org/10.1016/j.engfracmech.2012.09.029>
- [7] Lundén, R., Vernersson, T., Ekberg, A. (2010). Railway axle design: to be based on fatigue initiation or crack propagation? *Proceedings of the Institution of Mechanical Engineers, Part F: Journal of Rail and Rapid Transit*, 224(5): 445-453. <https://doi.org/10.1243/09544097JRRRT384>
- [8] Náhlik, L., Pokorný, P., Ševčík, M., Fajkoš, R., Matušek, P., Hutař, P. (2017). Fatigue lifetime estimation of railway axles. *Engineering Failure Analysis*, 73: 139-157. <https://doi.org/10.1016/j.engfailanal.2016.12.014>
- [9] Nguyen-Tajan, T.M.L., Lorang, X. (2017). EURAXLES-A global approach for design, production and maintenance of railway axles: WP1-Advances in fatigue load analysis and reliability assessment of railway axles: EURAXLES-Ein umfassender Ansatz für Auslegung, Herstellung und Instandhaltung von Eisenbahnachsen: WP1-Fortschritte in der Analyse von Ermüdungslasten und Verlässlichkeitsbewertung von Eisenbahnachsen. *Materialwissenschaft und Werkstofftechnik*, 48(7): 666-686. <https://doi.org/10.1002/mawe.201700582>
- [10] Mancini, G., Corbizi, A., Lombardo, F., Cervello, S. (2006). Design of railway axle in compliance with the European Norms: high strength alloyed steels compared to standard steels. In *Proceedings of WCRR, Italy*.
- [11] Mistry, P.J., Johnson, M. S., Li, S., Bruni, S., Bernasconi, A. (2021). Parametric sizing study for the design of a lightweight composite railway axle. *Composite Structures*, 267: 113851. <https://doi.org/10.1016/j.compstruct.2021.113851>
- [12] Son, S.W., Jung, H.S., Kwon, T.S., Kim, J.S. (2015). Fatigue life prediction of a railway hollow axle with a tapered bore surface. *Engineering Failure Analysis*, 58: 44-55. <https://doi.org/10.1016/j.engfailanal.2015.08.031>
- [13] Hirakawa, K., Kubota, M. (2001). On the fatigue design method for high-speed railway axles. *Proceedings of the Institution of Mechanical Engineers, Part F: Journal of Rail and Rapid Transit*, 215(2): 73-82. <https://doi.org/10.1243/0954409011531413>
- [14] Nwe, T., Pimsarn, M. (2021). Railway axle and wheel assembly press-fitting force characteristics and holding torque capacity. *Applied Sciences*, 11(19): 8862. <https://doi.org/10.3390/app11198862>
- [15] Nwe, T., Pimsarn, M. (2021). Effect of interference on the press fitting of railway wheel and axle assemblies. In *IOP Conference Series: Materials Science and Engineering*, 1137(1): 012051. <https://iopscience.iop.org/article/10.1088/1757-899X/1137/1/012051>
- [16] Hirakawa, K., Toyama, K., Kubota, M. (1998). The analysis and prevention of failure in railway axles. *International Journal of Fatigue*, 20(2): 135-144. [https://doi.org/10.1016/S0142-1123\(97\)00096-0](https://doi.org/10.1016/S0142-1123(97)00096-0)

- [17] Traupe, M., Jenne, S., Lütkepohl, K., Varfolomeev, I. (2016). Experimental validation of inspection intervals for railway axles accompanying the engineering process. *International Journal of Fatigue*, 86: 44-51. <https://doi.org/10.1016/j.ijfatigue.2015.09.020>
- [18] Walia, M.S., Esmacili, A., Vernersson, T., Lundén, R. (2018). Thermomechanical capacity of wheel treads at stop braking: A parametric study. *International Journal of Fatigue*, 113: 407-415. <https://doi.org/10.1016/j.ijfatigue.2018.04.031>
- [19] Walia, M.S., Vernersson, T., Lundén, R., Blennow, F., Meinel, M. (2019). Temperatures and wear at railway tread braking: Field experiments and simulations. *Wear*, 440: 203086. <https://doi.org/10.1016/j.wear.2019.203086>
- [20] Han, S.W., Son, S.W., Jung, H.S. (2012). Weight reduction of an urban railway axle based on EN standard. *Transactions of the Korean Society of Mechanical Engineers A*, 36(5): 579-590. <http://dx.doi.org/10.3795/KSME-A.2012.36.5.579>
- [21] European Committee for Standardization. BS EN 13260: 2020 Railway applications - Wheelsets and bogies - Wheelsets - Product Requirements. London, United Kingdom: BSI, 2020.
- [22] Robert, L.N. (2006). *Machine Design an Integrated Approach*. USA: Pearson Prentice Hall Publishers, pp. 558-560.
- [23] Gokhale, N.S. (2008). *Practical finite element analysis. Finite to Infinite*.
- [24] Simula. *fe-safe 2018 Fatigue Theory Reference*. Dassault Systèmes Simulia Corp.; 2018.
- [25] Kandil, F.A., Brown, M.W., Miller, K.J. (1982). Biaxial low-cycle fatigue failure of 316 stainless steel at elevated temperatures. In *Mechanical Behaviour and Nuclear Applications of Stainless Steel at Elevated Temperatures*.
- [26] Meyers, M.A., Chawla, K.K. (2008). *Mechanical Behavior of Materials*. Cambridge University Press.



## Numerical Analysis of the Influence of Press-Fitting on the Fatigue Life of Railway Axle

Theingi Nwe<sup>1,a)</sup> and Monsak Pimsarn<sup>1,b)</sup>

<sup>1</sup> *Department of Mechanical Engineering, School of Engineering, King Mongkut's Institute of Technology Ladkrabang, 10520, Thailand*

<sup>a)</sup> [62601033@kmitl.ac.th](mailto:62601033@kmitl.ac.th)

<sup>b)</sup> Corresponding author: [monsak.pi@kmitl.ac.th](mailto:monsak.pi@kmitl.ac.th)

**Abstract.** This study investigated the influence of press-fitting on the stress concentration and fatigue life of axles. Models of finite element analysis (FEA) with and without the press-fitting effect were developed using Abaqus software. These models were used to analyze the axle strength and profile the stress histories under various loads and running conditions, such as bending load, wheel-rail contact force, lateral force, and press-fitting force. Their combined loads were responsible for the axle fracture. Also, the prediction of fatigue life was extended to a three-dimensional stress state under fully reversed cyclic loading and variable overload spectra using the commercial Fe-safe software with strain-based Brown-Miller Morrow fatigue algorithm. With the press-fitting effect, the maximum von Mises stress at the groove notch transition zone of the axle was 6% higher than without the press-fitting effect. Press-fitting reduced the fatigue life of an axle by 37% compared to the without press-fitting, and the most damage happened at the same node as the maximum von Mises stress.

**Keywords:** fatigue life, press-fitting, railway axle, strain-life.

### INTRODUCTION

Railway axles transmit driving torques to the wheel and are typically designed to provide an infinite service life. Meanwhile, corrosion, impact load, and cyclic fatigue loading through time on the axle cause axle failure. The primary cause of the varied amplitude loading applied to the railway axle is the vertical weight of the train, which during operation generates a rotating bending moment. Advanced Finite Element Analysis is necessitated for identifying axle deformation mechanisms, facilitating well design, and enhancing fatigue life to improve performance. Stress and strain-based fatigues are analyzed using Fe-safe software by SIMULIA incorporated with various fatigue algorithms. For example, this software uses tensorial stresses to calculate fatigue. The biaxial strain-based model for fatigue life prediction is implemented as a post-processor in the Fe-safe that processes the structural results of finite element analysis (FEA). Assessing the fatigue lifetime for railway axles is under intensive research.

Our previous studies investigated the press-fitting effect on the axle, the quality of the press-fitting curve, and the maximum capacity for holding torque [1], [2]. Another study [3] analyzed the stress concentration of press-fitted axles numerically using small-scaled specimens and full-scale axles. Many studies suggested that fretting fatigue might damage the axle wheel seat. Based on the multiaxial stress and non-linear frictional characteristics, A. Ekberg[4] identified four possible locations for fretting fatigue initiation of the wheelset assembly. It was discovered that the wheelset fretting damage at the higher speed was more severe, leading to a noticeably lower fatigue life by conducting small-scale simulation tests with various rotator speeds[5]. The authors investigated the impact of several parameters on fretting development in press-fit joints. [6], [7]. Critical areas susceptible to railway axle fatigues are the press-

fitted wheel seat, the T transition and the S transition fillet [8]. Also, the stress intensity factor and fatigue fracture crack growth due to the impact of press-fitting on the railway axle were extensively investigated [9]. In particular, the fatigue strength of an axle with hollow tapered bored surfaces was evaluated using the EN standard [10].

Although several studies investigated the fatigue life and strength analysis of railway axles [11]–[16], little is known about the effect of press-fitting on the fatigue life, particularly on the wheelset. Therefore, this study investigated the influence of press-fitting on stress concentration and fatigue life of railway axles. Specifically, this study focused on finite element analyses of axles to quantify the stresses by comparisons with the stable and adverse conditions to define general recommendations for the axles. Furthermore, the fatigue life prediction model under various load spectra was performed using the strain-based Brown-Miller-Morrow fatigue algorithm.

## METHODOLOGY

To determine the fatigue life of the axle, several steps were required. First, two types of running conditions are analyzed: stable and adverse. For the stable condition, the wheelset was assumed to run on the straight track with symmetric vertical forces and neglect the lateral force. For the adverse condition, the wheelset was assumed to run on a curve track, which resulted in an asymmetric distribution of vertical forces and lateral forces. Secondly, with and without press-fitting effects based on the different contact methods on the axle were analyzed. Lastly, stress history was used with Fe-safe to predict the life of the axle for determining the interval of maintaining the wheelset.

### Numerical Simulation

FEA is essential to compute the stress caused by applied loads while assessing the residual press-fitting effect on the axle. This study used two kinds of FE simulations to examine the effect of running conditions and press-fitting on axles' stress concentration. There were two different contact techniques: tie contact for without the press-fitting effect and interference fit contact for taking the press-fitting effect into account. For numerical simulation, this study used a linear elastic isotropic EA4-T material which is commonly used in railway axles with a modulus of elasticity 206 GPa and a Poisson ratio of 0.3.

The 3D FE models of wheels and axles were created as a press-fitted assemblage. The refined mesh was used for a higher resolution at the contact area, fillet, and the notch transition zone, where the stress concentrated. The element size was 2 mm at the fillet and the notch groove transition, 5 mm at the contact area of the wheel and axle, 10 mm at other parts of the axle, and the wheel is a 20 mm<sup>2</sup> expected contact area (Figure 1,2). The element of the first-order-reduced integration hexagonal type (C3D8R) was used with a controlled hourglass effect [17].

The analysis consisted of two steps: press-fitting and applying the loading for the simulated case by taking into account the residual stress from the press-fitting. Surface-to-surface contact with an interference fit was used. For without press-fitting effect, the tie contact was used between two contact surfaces of the wheelset to ensure no relative motion between them. The master surface was the wheel bore, while the wheel seat of the axle outer surface was the slave surface. The wheel and axle were press-fitted with an allowable radial interference value of 0.2 mm according to EN 13260 [18]. The frictional coefficient of 0.1 was assigned, encompassing the tangential behavior and the hard-contact model to ensure the normal behavior using the method of Augment Lagrange constraint enforcement. Besides, a small sliding was used to simulate the press-fitting. Figure 1,2 shows the boundary conditions of the motor bogie wheelset based on the EN 13104 standard [19]. Table I shows the specific load values used to calculate the internal and external stress on the motor bogie axle, and they were adopted from another study [20]. For stable condition with symmetric vertical forces (88.4 kN) loaded on the journal bearings, other forces are negligible.



Figure 1. Meshing and boundary conditions of the motor bogie wheelset for stable condition.

Figure 2. Meshing and boundary conditions of the motor bogie wheelset for adverse condition.

TABLE I. Loads for an axle of a motor bogie.

Load	Magnitude (kN)
Vertical force on the more loaded side = $P_1$	101.300
Vertical force on the less loaded side = $P_2$	75.528
Wheel-rail horizontal contact force on more loaded side = $Y_1$	49.509
Wheel-rail horizontal contact force on less loaded side = $Y_2$	24.754
Vertical rail contact reaction force on more loaded side = $Q_1$	112.430
Vertical rail contact reaction force on less loaded side = $Q_2$	63.171
Balancing force between $Y_1$ and $Y_2 = H$	24.775
Un-sprung force = $F_i$	-1.215

### Fatigue Simulation

Fe-safe commercial software utilizes the stress history from the results of the FE numerical simulation as input to predict the fatigue life. The loading history, fatigue algorithm method, and mean stress correction are crucial factors during the fatigue analysis. The biaxial strain-based model for fatigue life prediction was chosen as a post-processor that processes the FEA structural results. If elastic FEA stress results are used, a multiaxial elastic-plastic correction utilizing Neuber's rule is used to evaluate the elastic-plastic stress-strains from these results[21]. The cyclic stress occurred in a rotating axle, the stress would alternate between tension and compression, causing fatigue fracture in structures. We investigated the fatigue life of a railway axle under several load spectrums, emphasizing the constant loading and overloading applied every five cycles and three cycles as indicated in Figure. 3, to better understand the effect of the press-fitting contact fatigue behavior and overload spectra. These conditions, however, may not be indicative of the actual load spectra acting on the railway axle in service, which is typically complex variable amplitude loading. We used a simple method to scale-up the load taking into account the impact overload applied to the cycles and simulated the fatigue life by using three sets of repetitive load spectra.

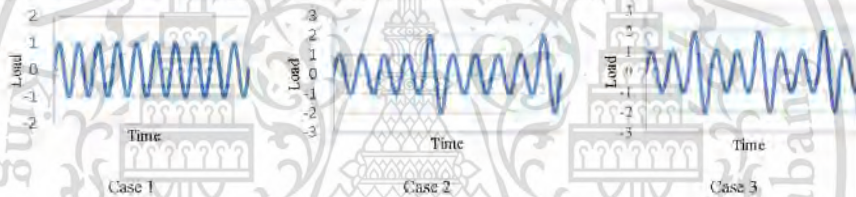


Figure 3. Load spectra for fatigue prediction

This study used Brown-Miller strain-based algorithms with Morrow mean stress correction which was widely used for ductile metals, with the most realistic lifetime prediction [22]. This is the critical plane analysis, which determined the maximum damage plane, and that the damage is a function of both normal and shear strain to this plane. The complete Brown-Miller strain-life equation is represented in Equation 1. The fatigue strength of axles depended on material properties, local stress conditions at individual axle areas, and manufacturing technology. Presumptively, the surface of the axle was mirror-polished with no scratches. Table III shows the fatigue material parameters extracted from other studies [23].

$$\frac{\Delta\gamma_{max}}{2} + \frac{\Delta\epsilon_{max}}{2} = 1.65 \frac{\sigma'}{E} (2N_f)^b + 1.75 \epsilon_f' (2N_f)^c \quad \text{equation (1)}$$

Where,  $N_f$  = the number of cycles to failures

$$\frac{\Delta\gamma_{max}}{2} = \text{shear strain amplitude}$$

$$\frac{\Delta\epsilon_{max}}{2} = \text{normal strain amplitude}$$

TABLE II. Fatigue properties of the EA4T material.

Ultimate tensile strength	650.0 MPa
Fatigue strength coefficient ( $\sigma'$ )	811.1 MPa
Cyclic yield strength ( $\sigma_{yc}$ )	385.2 MPa
Cyclic fatigue strength coefficient ( $K'$ )	806.3 MPa
Fatigue strength exponent ( $b$ )	-0.069
Fatigue ductility exponent ( $c$ )	-0.641
Fatigue ductility coefficient ( $\epsilon_f'$ )	0.658
Strain hardening coefficient ( $n'$ )	0.102
Surface finish factor ( $K_s$ )	1

## RESULTS

### Comparison of numerical results with running conditions

Figure. 4 shows the bending stress variation of the motor bogie axle along the axial direction for stable and adverse conditions evaluated by the numerical FE simulation. The variation of bending stress was different for stable and adverse conditions. The maximum bending stress occurred on the surface of the axle farthest from the natural axis and notch groove, where the maximum stress concentration was. The maximum bending stress of the adverse condition was 72% higher than that of stability. Thus, it would be misleading to design the axle base on the stable condition.

### Comparison of numerical results with press-fitting effect

The press-fitting effect was studied under adverse running conditions. Figure. 5 shows the distribution of von Mises stress throughout the axles and the effects of press-fitting, tie contact type with loading and interference fit contact type with loading. In this study, combining press-fitting and loading showed that press-fitting created the corresponding von Mises stress at the contact area of the wheelset and the transition zone near the wheel seat. However, the stress distribution of other parts remained constant. Therefore, the press-fitting substantially influenced the residual stresses of the wheelset's initial conditions. In other words, the residual stress of press-fitting remained vulnerable to cracking at places such as fillet, groove transition, and axle wheel seat.

Figure. 6 shows that stresses at the contact of wheel seat, fillet, and groove transition near the wheel seat from the finite element method differed between the with and without press-fitting effect. At the groove transition zone, the maximum von Mises stress occurred as expected, and the combined stress with the press-fitting effect was 6% higher than the value of applied loading without the press-fitting effect. The nature of interference fit, and tie contacts differed substantially. Therefore, the stress distribution at the contact area of the wheel seat was different.

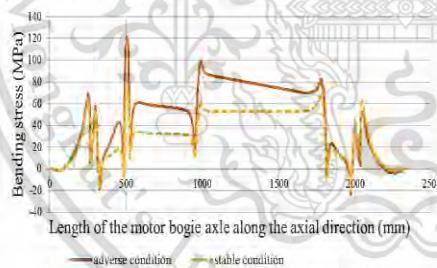


Figure 4. Comparison of bending stress along the axial direction of the motor bogie axle.

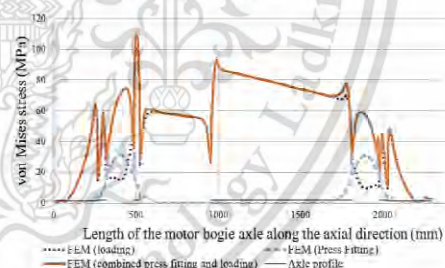


Figure 5. Comparison of von Mises stress along the axial direction of the motor bogie axle.

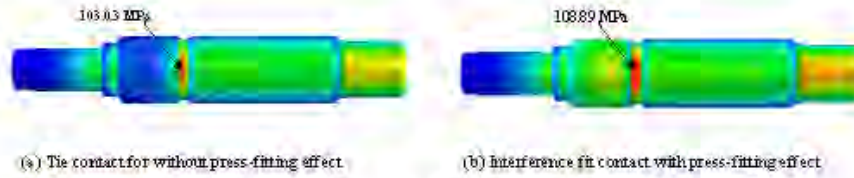


Figure 6. Comparison of the maximum von Mises stress for the motor bogie axle.

### Fatigue Analysis Results

To examine the press-fitting effect and impact of variable amplitude overload on the fatigue life, three loading scenarios are taken into consideration. The load scale factor 1 showed no damage in the motor axle design. The axle was designed to have an infinite life, and the working stress was below the permissible level. Therefore, it was necessary to scale the stress to almost yield stress. Expectedly, the fatigue life results showed that damage began at the loading case 2, overloading was applied every five cycles for the motor axle and the fatigue life decreased when the overloading repeated cycle increased. Table III compares the shortest fatigue life and the safety factor between the interference fit and tie contact for motor bogie axle. The interference fit contact for the worst life-repeat cycle, and the safety factor was less than tie contact. The weakest failure position of the motor axle was the grooved notch. Figure 7 and 8 show the fatigue life and factor of strength as a contour in the worst element.

Table III. Comparison of fatigue life of the motor bogie axles.

Loading Case	Without press-fitting effect		With press-fitting effect	
	Worst life-repeat cycle	FOS*	Worst life-repeat cycle	FOS*
1	No damage	1.609	No damage	1.492
2	2.409E+7	0.935	1.513E+7	0.875
3	1.205E+7	0.889	7.568E+6	0.834

\* FOS = Factor of strength

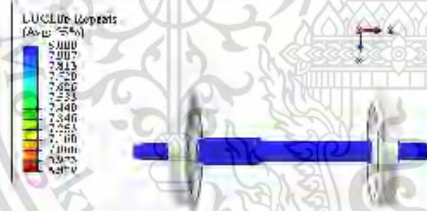


Figure 7. Fatigue-life assessment of the motor bogie wheelset.

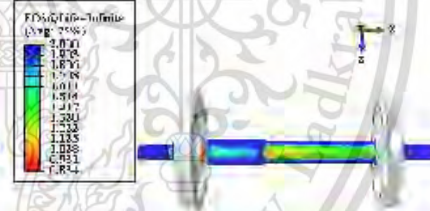


Figure 8. Safety factor assessment of the motor bogie wheelset.

## CONCLUSION

The bending stress of a railway motor bogie axle was compared under two different running conditions, and the influence of press-fitting on fatigue life under two different contact methods was investigated using simple several load spectra. Based on the findings from this study, the following conclusion can be drawn;

- The adverse condition of the wheelset, rather than the stability condition, should be deliberated when designing the axle.
- Press-fitting substantially influenced the stress concentration at the axle wheel seat and adjacent transitions.
- The maximum von Mises stress with and without press-fitting at the grooved notch differed by 6%.
- The safety factor with press-fitting was 6% lower than without the press-fitting effect and fatigue life was 37% lower either, i.e., the fatigue failure was strongly related to the press-fitting.
- According to the findings, fatigue life is also strongly related to the overloading repeated load cycle.
- The proposed method, which considered press-fitting, could be advantageous for designing the railway axle, and the fatigue-life assessments were of direct practical relevance.
- Also, numerical modelling was crucial for assessing the press-fitting effect on the fatigue life of railway axles.

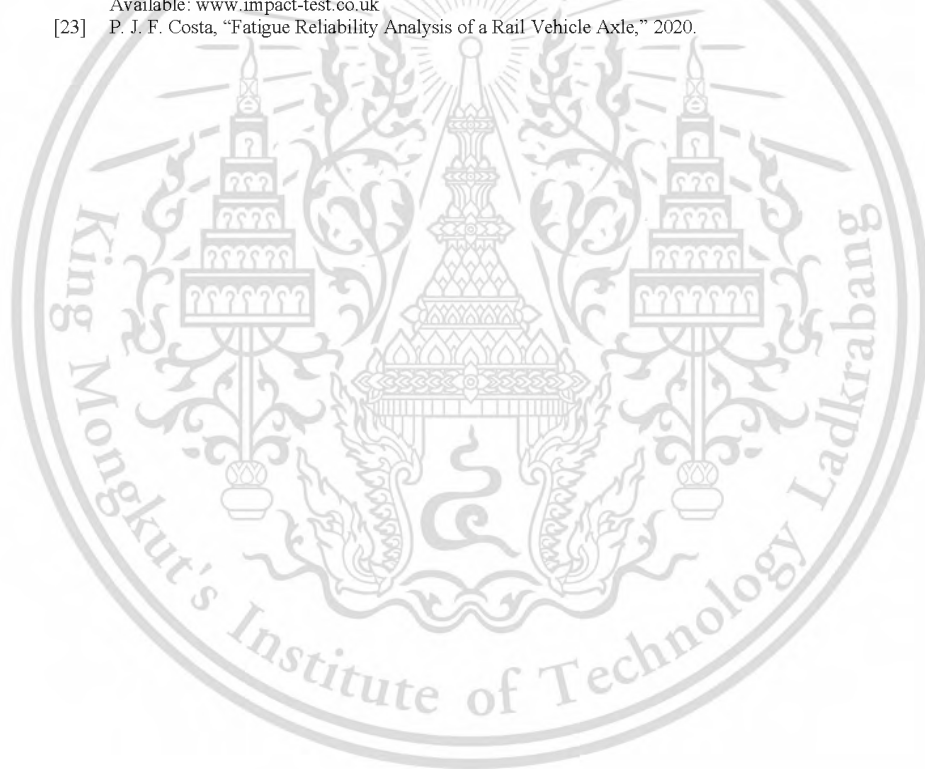
## ACKNOWLEDGMENTS

We would like to thank King Mongkut's Institute of Technology Ladkrabang for the financial support under the grant No. KDS2019/019.

## REFERENCES

- [1] T. Nwe and M. Pimsarn, "Effect of interference on the press fitting of railway wheel and axle assemblies," *IOP Conf. Ser. Mater. Sci. Eng.*, vol. 1137, no. 1, p. 012051, May 2021, doi: 10.1088/1757-899X/1137/1/012051.
- [2] T. Nwe and M. Pimsarn, "Railway axle and wheel assembly press-fitting force characteristics and holding torque capacity," *Appl. Sci.*, vol. 11, no. 19, p. 8862, Sep. 2021, doi: 10.3390/app11198862.
- [3] M. Yamamoto and H. Ishiduka, "Stress concentration of transition groove induced by a press-fitted part in railway axles," *Int. J. Fatigue*, vol. 97, pp. 48–55, 2017, doi: 10.1016/j.ijfatigue.2016.12.025.
- [4] A. Ekberg, "Fretting fatigue of railway axles - A review of predictive methods and an outline of a finite element model," *Proc. Inst. Mech. Eng. Part F J. Rail Rapid Transit*, vol. 218, no. 4, pp. 299–316, 2004, doi: 10.1243/0954409043125905.
- [5] C. Song, M. X. Shen, X. F. Lin, D. W. Liu, and M. H. Zhu, "An investigation on rotatory bending fretting fatigue damage of railway axles," *Fatigue Fract. Eng. Mater. Struct.*, vol. 37, no. 1, pp. 72–84, 2014, doi: 10.1111/ffe.12085.
- [6] M. Zehsaz and P. Shahriary, "The effects of friction coefficient and interference on the fretting fatigue strength of railway axle assembly," *UPB Sci. Bull. Ser. D Mech. Eng.*, vol. 75, no. 4, pp. 71–84, 2013.
- [7] S. G. M. Michnej, "Fretting wear simulation in a clamped joint based on the example of a rail vehicle wheel set," *Wear*, vol. September, no. 438–439, p. 102654, 2019, [Online]. Available: <https://doi.org/10.1016/j.wear.2018.12.083>
- [8] V. Grubisic and G. Fischer, "Railway axle failures and durability validation," *Proc. Inst. Mech. Eng. Part F J. Rail Rapid Transit*, vol. 226, no. 5, pp. 518–529, 2012, doi: 10.1177/0954409712442325.
- [9] M. Madia, S. Beretta, and U. Zerbst, "An investigation on the influence of rotary bending and press fitting on stress intensity factors and fatigue crack growth in railway axles," *Eng. Fract. Mech.*, vol. 75, no. 8, pp. 1906–1920, 2008, doi: 10.1016/j.engfracmech.2007.08.015.
- [10] S.-W. wan Son, H.-S. seung Jung, T.-S. soo Kwon, and J.-S. sung Kim, "Fatigue life prediction of a railway hollow axle with a tapered bore surface," *Eng. Fail. Anal.*, vol. 58, no. P1, pp. 44–55, Dec. 2015, doi: 10.1016/j.engfailanal.2015.08.031.
- [11] P. Hutař, P. Pokorný, J. Poduška, R. Fajkoš, and L. Náhlík, "Effect of residual stresses on the fatigue lifetime of railway axle," 2017, doi: 10.1016/j.prostr.2017.07.005.

- [12] M. Filippini, M. Luke, I. Varfolomeev, D. Regazzi, and S. Beretta, "Fatigue strength assessment of railway axles considering small-scale tests and damage calculations," *Procedia Struct. Integr.*, vol. 4, no. December, pp. 11–18, 2017, doi: 10.1016/j.prostr.2017.07.013.
- [13] L. Náhlik, P. Pokorný, M. Ševčík, R. Fajkoš, P. Matušek, and P. Hutař, "Fatigue lifetime estimation of railway axles," *Eng. Fail. Anal.*, vol. 73, pp. 139–157, 2017, doi: 10.1016/j.engfailanal.2016.12.014.
- [14] M. Bayraktar, N. Tahrali, and R. Guclu, "Reliability and fatigue life evaluation of railway axles," *J. Mech. Sci. Technol.*, vol. 24, no. 3, pp. 671–679, Mar. 2010, doi: 10.1007/s12206-009-1219-1.
- [15] O. Yasniy, Y. Lapusta, Y. Pyndus, A. Sorochak, and V. Yasniy, "Assessment of lifetime of railway axle," *Int. J. Fatigue*, vol. 50, pp. 40–46, 2013, doi: 10.1016/j.ijfatigue.2012.04.008.
- [16] J. Luo, S. Wang, X. Liu, and S. Geng, "Fatigue life prediction of train wheel shaft based on load spectrum characteristics," *Res. Artic. Adv. Mech. Eng.*, vol. 13, no. 2, pp. 1–10, 2021, doi: 10.1177/1687814021992153.
- [17] SIMULIA, *Abaqus Analysis user's manual. Vol I-IV*. Providence, RI, USA: Dassault Systèmes Simulia Corp., 2010.
- [18] European Committee For Standardization, *BS EN 13260 : 2020 Railway applications - Wheelsets and bogies - Wheelsets - Product Requirements*. London, United Kingdom: BSI, 2020.
- [19] European Committee For Standardization, *BS EN 13104:2009+A2:2012: Railway applications — Wheelsets and bogies — Powered axles — Design method*, no. May 2009. BSI Standards, 2012.
- [20] S.-W. Han, S.-W. Son, and H.-S. Jung, "Weight Reduction of an Urban Railway Axle Based on EN Standard," *Trans. Korean Soc. Mech. Eng. A*, vol. 36, no. 5, pp. 579–590, 2012, doi: 10.3795/ksme-a.2012.36.5.579.
- [21] Simulia, *fe-safe 2018 FATIGUE THEORY REFERENCE*. Dassault Systèmes Simulia Corp., 2018.
- [22] L. Vallance, "Quick Fatigue Tool for Matlab User Guide," no. September. pp. 169–232, 2018. [Online]. Available: [www.impact-test.co.uk](http://www.impact-test.co.uk)
- [23] P. J. F. Costa, "Fatigue Reliability Analysis of a Rail Vehicle Axle," 2020.



## Deterministic Stress Intensity Factor of a Railway Axle under Adverse Running Condition

Theingi Nwe<sup>1,a</sup>, Monsak Pimsarn<sup>1,b,\*</sup>

<sup>1</sup>Department of Mechanical Engineering, School of Engineering, King Mongkut's Institute of Technology Ladkrabang, 10520, Thailand

<sup>a</sup>62601033@kmitl.ac.th, <sup>b</sup>monsak.pi@kmitl.ac.th

**Keywords:** railway axle, stress intensity factor, press-fitting, adverse running condition, rotary bending

**Abstract.** Although railway axles are a crucial part of railway vehicles, they are susceptible to long-term failure because of repeated loads. The aim of this research is to investigate the stress intensity factor (SIF) of a surface elliptical crack on a high-speed railway axle under various operating conditions. The study employs numerical analysis to explore the impact of press-fitting, rotary bending, stable and adverse running conditions on the SIF solutions. The main findings demonstrate that adverse running conditions, such as the press-fitting force, asymmetric vehicle weight, lateral force and wheel-rail contact force, can significantly increase the SIF values and result in axle failure. The press-fitting effect and rotary bending also have a significant impact on the SIF values, highlighting their importance in the railway axle design and analysis. The outcome of this research emphasizes the significance of accurately estimating SIF values to ensure the safe and reliable performance of railway axles in adverse operating conditions.

### Introduction

Railway axles are crucial parts of railway systems and require a high level of reliability to ensure safe operations. The axles are subjected to various loading conditions, including cyclic loading due to rolling contact fatigue and other adverse running conditions. Such adverse running conditions can cause stress concentrations, which can initiate and propagate cracks, resulting in axle failure. Thus, it is necessary to evaluate the stress intensity factor (SIF) of railway axles under adverse running conditions. The stress intensity factor (SIF) is a key parameter used to assess the risk of structural failure due to cracks. The SIF provides information about the maximum stress at the tip of a crack, and it is affected by factors such as geometry, material properties, and load. This information is critical to ensure the safe operation of railway axles. Generally, cracks initiate at several locations, mostly around the axle wheel seat, S-transition, T-notch, U-notch, due to the rotating bending [1]. In the railway axle, the crack formed an elliptically which was distributed circumferentially along the axle body [2,3]. When more accuracy is required in life expectancy predictions, SIF can be used in conjunction with other methods such as fracture mechanics or finite element analysis to provide a comprehensive assessment.

Previous research has established the SIF solution for semi-elliptical cracks in railway axles [4-9]. It has been reported that the press-fitting effect significantly influences the residual stress, and thus should be accounted for in axle design [10]. Although literature on SIF solutions for railway axles has mainly focused on symmetric loads and stable running conditions, it is crucial to investigate the effects of adverse conditions to ensure the safe and reliable performance of railway axles. While some studies have investigated the influence of rotary bending and press-fitting on stress intensity factors and fatigue crack growth [5], others have compared SIF solutions for cracks under rotating bending and their impact on the propagation lifetime of railway axles [6]. Analytical and numerical crack growth analysis has also been performed on 1:3 scaled railway axle specimens [7]. Stress intensity factor solutions for cracks in railway axles have been determined [8], and SIF solutions for cracks in railway axles under rotating bending have been investigated [9]. Recently, the effect of interference on the press-fitting of railway wheel and axle assemblies has been studied [10].

This study aims to make a novel contribution to the field by considering the effects of adverse running conditions and press-fitting on the SIF. The press-fitting process used to assemble the wheel and axle is also a critical factor in determining the fatigue life of railway axles. Press-fitting can introduce residual stresses, which can significantly affect the SIF and residual fatigue life of the axle. Therefore, this research will also consider the effects of press-fitting on the axle's SIF. To achieve the research objectives, numerical analysis was performed using ABAQUS commercial finite element analysis (FEA) software to simulate the adverse running conditions and the press-fitting process.

#### Numerical Approaches of Evaluation Stress Intensity Factor

The numerical approaches for evaluating the SIF through the J-integral using the contour integral method provide a powerful tool for predicting the various crack geometries and loading conditions. The ABAQUS[11] finite element software package is capable of computing the stress intensity factor,  $K$ , and the J-Integral,  $J$  along paths that encircle a crack. The method involves defining a contour around the crack tip (Figure 1) and quantifying the energy absorbed by a crack and computing the stress field at the crack tip, was initially developed by Rice in 1968 [12].

$$J = \int_{\Gamma} (W dy - \bar{T} \frac{\partial u}{\partial x} ds) \quad (1)$$

Where  $W$  is a strain energy density,  $\bar{T}$  is the traction vector,  $u$  the displacement vector of a contour element  $ds$  respectively.

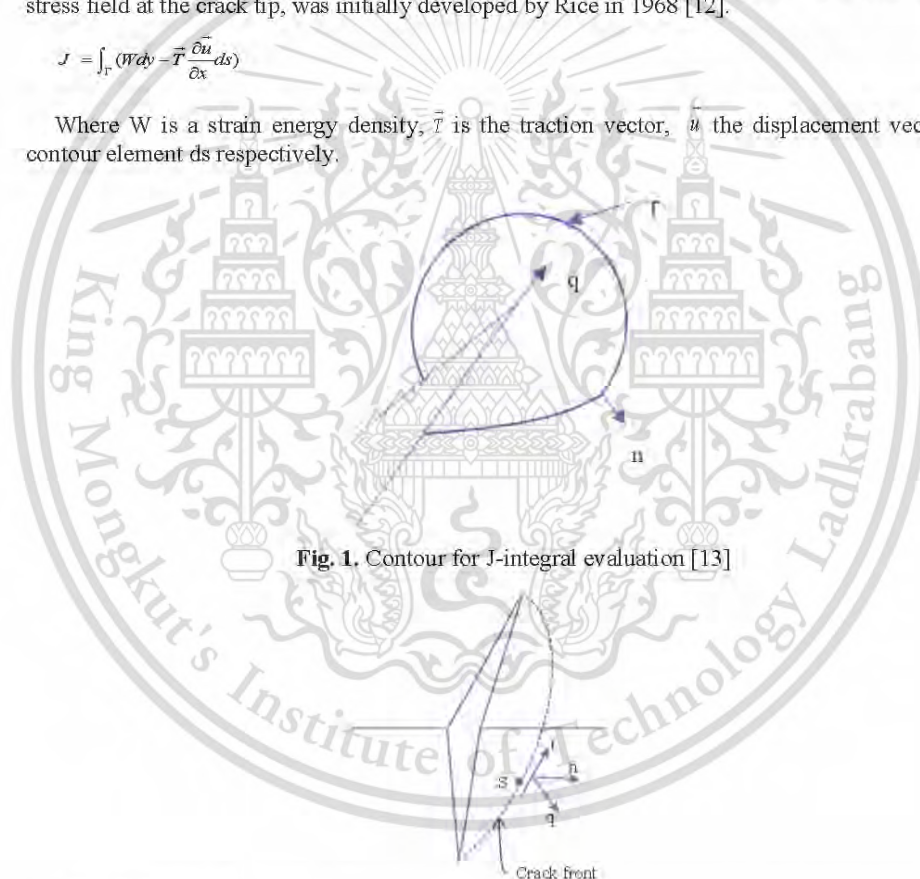


Fig. 1. Contour for J-integral evaluation [13]

Fig. 2. Local orthogonal Cartesian coordinates are defined at point  $s$  on the crack front [13]

In order to extend the J-integral to three dimensions, it is necessary to examine a crack that has a tangential contour front, as illustrated in Figure 2. The direction of virtual crack propagation is denoted by  $q$ , which runs perpendicular to the local crack front and lies within the crack plane,  $n$  and  $t$  are assigned as normals and tangent of the crack front, respectively.

For homogeneous, isotropic materials, the crack front stress intensity factor,  $K$ , can be related to the J integral,  $J$ , using the following equation:

$$J = \frac{1}{E}(K_I^2 + K_{II}^2) + \frac{1}{2G}K_{III}^2 \quad (2)$$

where  $J$  is the J-integral,  $G$  is the shear modulus of a material,  $K_I$ ,  $K_{II}$ ,  $K_{III}$  are the three stress intensity factor modes for general crack opening.

For the plane stress,  $\bar{E} = E$  and the plane strain,  $\bar{E} = E/(1-\nu^2)$ , the conditions are axisymmetric, and three dimensions. Where  $E$  is the elastic modulus of the material,  $\nu$  is the Poisson ratio.

Regarding the linear elastic condition, the J-integral is equivalent to the rate of energy release when considering a single mode condition. Moreover, it is possible to calculate  $K$  from J-integral by using the following equation.

$$J = \frac{(1-\nu^2)K_I^2}{E} \quad (3)$$

### Finite Element Modeling and Simulation

The crucial initial crack location becomes assumed on the notch of the railway axle between the wheel seat and gear seat, and modelled at the maximum excessive loading. A semi-elliptical shape is a common form for cracks found in railway axles [14], as depicted in Figure 3 which shows a semi-elliptical crack in a hollow cylindrical bar. Due to its usage in modern railway axles, EA4T steel was selected as a linear elastic material with Young's modulus 206 GPa and Poisson's ratio 0.3. By taking into consideration the press-fitting effect, the interference between the wheel and axle is assumed to be 0.24 mm.

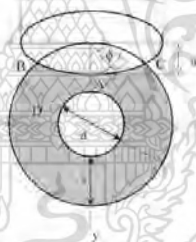
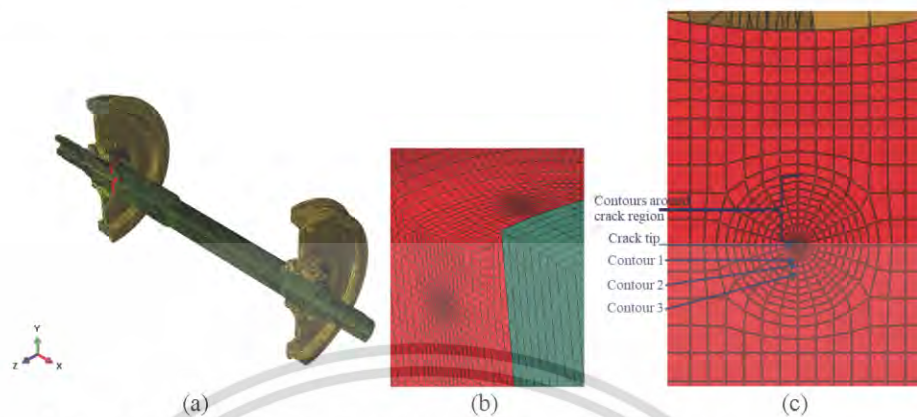


Fig. 3. Semi-elliptical crack in a hollow cylindrical bar

**Meshing, Loadings, and Boundary Conditions.** Firstly, create a wheel and axle 3D half model of a wheelset for the sake of symmetry. The present study investigated the sensitivity of the stress intensity factor (SIF) calculation to mesh parameters such as element size and contour number around a surface crack so that the finding is independent of the mesh size. Full integration of hexahedral solid elements of type C3D8 is employed to obtain SIF values from both the deepest and surface points.

By refining the mesh near areas of the crack tip, more accurate and reliable results can be obtained, as demonstrated in Figure 4. For a reliable and precise assessment, an element size of 2.0 mm was selected for the regions surrounding the surface crack, whereas a larger size of 5.0 mm was implemented for other regions. Several concentric rings of mesh elements were utilized around the crack's edge to compute the contour integral necessary for the calculation of the stress intensity factor ( $K$ ). The mesh size around the surface crack front was controlled by adjusting the number of contours and their divisions, as shown in Figure 4 (c).



**Fig. 4.** Three-dimensional wheelset mesh model with a semi-elliptical crack: (a) global geometry (b) insertion of the crack into the sub-model (c) refinement of the structural mesh surrounding the crack

The contact between the wheelset components was configured as a master-slave interaction, with the axle-wheel seat acting as the slave and the wheel bore as the master. An interference fit option was included for a press-fitting effect. In order to investigate the contact without the press-fitting effect, a tie contact was utilized. Two types of operation conditions were carried out, one being stable and the other adverse. The stable simulation involved assuming that the wheelset runs on a straight track, experiencing symmetrical vertical forces (88.4 kN) while disregarding any lateral force. Assuming an adverse condition where the wheelset runs on a curved track, an asymmetric distribution of vertical and lateral forces results. Assuming an adverse condition where the wheelset runs on a curved track, an asymmetric distribution of vertical and lateral forces are subjected to the wheelset in the current study. The contact point of the wheel and rail was constrained by displacement. The asymmetric vertical loading force applied to the middle plane of bearing journals was caused by the maximum weight of the train and passenger. The analysis is carried out in two stages: first, press-fitting is done, followed by the implementation of boundary constraints and loads, as indicated in Figure 5.

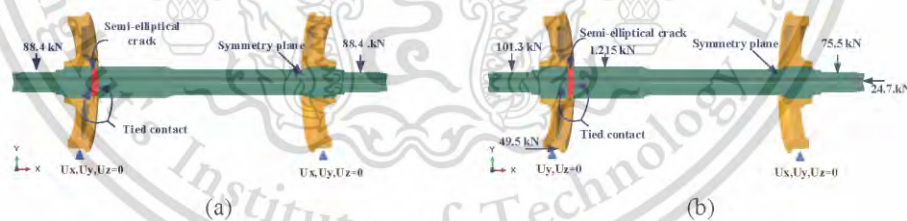


**Fig. 5.** Loading and boundary conditions of the wheelset (a) stable running condition and (b) adverse running condition

**Results**

**Studying the Effect of Stable and Adverse Running Conditions on SIF Solutions.** Figure 6 shows the variation of stress intensity factors along the crack front, which are determined under stable and adverse running conditions. As can be seen, the results show that SIF under adverse conditions is much greater than the stable condition. There is a remarkable finding that the maximum SIF takes place at the surface of crack point B and minimum at the deepest point A for relative depths ( $a/t=0.25$ )

and aspect ratios ( $a/c=0.75$ ), the SIF values decreased gradually as the distance from the crack tip increased. The SIF value of a railway axle under adverse running conditions is greater than under stable conditions due to several factors because of results in increased loads, including asymmetric bending loads, the contact lateral force between the wheel and the rail of the axle. These factors can lead to crack initiation and propagation in the axle, which can increase the SIF value. In Figure 7, the distribution of longitudinal stress for the semi-elliptical crack under combined press-fitting and the adverse loading of a wheelset is shown, and it is evident that the stress concentration is higher at the crack surface point B. The higher stress concentration at the crack tip can further increase the SIF value, resulting in a more critical structural state.

**Studying the Effect of Press-fitting on SIF Solutions.** In Figure 8, the SIF values along the crack front are compared with and without the press-fitting effect of the wheelset assembly. The results indicate that the SIF value with the press-fitting effect is 13% greater than the one without it. The press fit creates contact stresses that cause the deformation of the components and that can lead to residual stresses. As a result, the press-fitting effect can increase the stiffness and strength of the component, which in turn increases the SIF values along the crack front. This suggests that the press-fitting effect should be considered in the design and analysis of the wheelset assembly to ensure its safe and reliable operation.

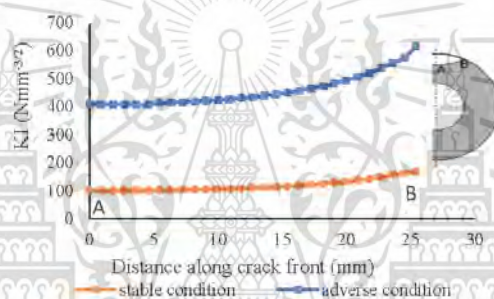


Fig. 6. Comparison of stress intensity factor for stable and adverse running conditions

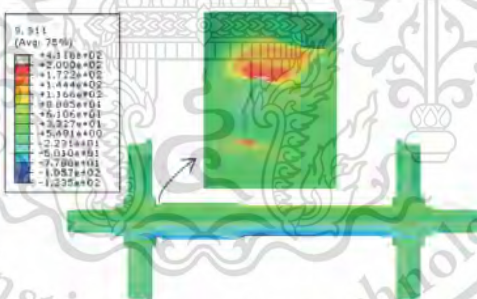


Fig. 7. Distribution of the longitudinal stress for the semi-elliptical crack under combined press-fitting and the bending load of a wheelset in FEM

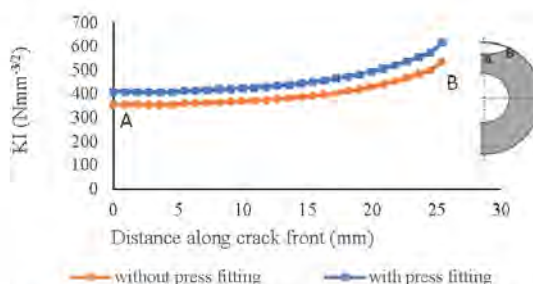


Fig. 8. Stress intensity factor comparison for the press-fitting effect

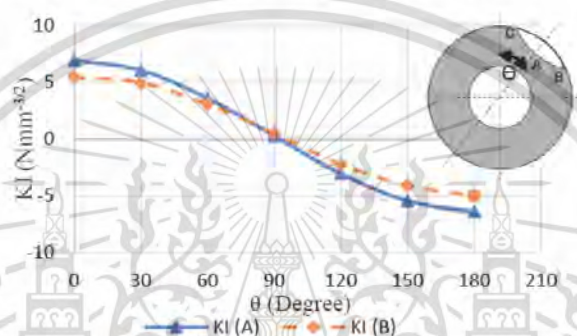


Fig. 9. Stress intensity factor of the finite element model versus rotation angle

**Studying the Rotary Bending Effect on SIF Solutions.** In this section, stress intensity factors were evaluated under the rotation of the axle to understand the effect of rotary bending, according to the same procedure used for the previous section. Figure 9 shows the variation of the stress intensity factor as a function of rotational angle. It can be seen that when  $\theta = 0^\circ$ , the crack is fully open and positive because the maximum tensile stress is located at the crack front. On the other hand, the crack is fully closed when the rotation angle reaches the ( $\theta = 180^\circ$ ), and the SIF is negative because of the maximum compressive stresses. This shows the principle of opening and closing the crack of the axle. The SIF values of crack surface point B are almost zero at  $\theta = 90^\circ$ .

### Conclusion

Based on the investigation of different operating conditions, including stable and adverse running conditions, press-fitting, and rotary bending, this research paper aimed to determine the impact of these factors on the stress intensity factor (SIF) values of a high-speed railway axle. The findings of this study suggest that adverse running conditions can significantly increase SIF values by four times and lead to crack initiation and propagation. Additionally, the press-fitting effect can increase SIF values by 13%, and rotary bending can also contribute to increasing SIF values. Therefore, it is essential to consider these factors in component design and analysis to ensure the safe and reliable operation of components under different operating conditions. Overall, this study emphasizes the importance of accurately predicting SIF values and highlights the need for further research in this area.

### Acknowledgments

We would like to thank King Mongkut's Institute of Technology Ladkrabang for the financial support under the grant No. KDS2019/ 019.

---

**References**

- [1] European Committee for Standardization. BS EN 13261 : 2020 Railway applications - Wheelsets and bogies - Axles - Product requirements. London, United Kingdom: BSI; 2020.
- [2] Zerbst U, Vormwald M, Andersch C, Mädler K, Pfuff M. The development of a damage tolerance concept for railway components and its demonstration for a railway axle. *Eng Fract Mech*. 2005 Jan;72(2):209–39.
- [3] Zerbst U, Beretta S, Köhler G, Lawton A, Vormwald M, Beier HT, et al. Safe life and damage tolerance aspects of railway axles – A review. *Eng Fract Mech [Internet]*. 2013 Jan [cited 2019 Sep 6];98(1):214–71. <https://doi.org/10.1016/j.engfracmech.2012.09.029>
- [4] DE Freitas M, François D. Analysis of Fatigue Crack Growth in Rotary Bend Specimens and Railway Axles. *Fatigue Fract Eng Mater Struct*. 1995;18(2):171–8.
- [5] Madia M, Beretta S, Zerbst U. An investigation on the influence of rotary bending and press-fitting on stress intensity factors and fatigue crack growth in railway axles. *Eng Fract Mech*. 2008;75(8):1906–20.
- [6] Pourheidar A, Beretta S, Ragazzi D, Baykara C. Comparison of SIF solutions for cracks under rotating bending and their impact upon propagation lifetime of railway axles. *Procedia Struct Integr [Internet]*. 2018;8:610–7. <https://doi.org/10.1016/j.prostr.2017.12.060>
- [7] Simunek D, Leitner M, Maierhofer J, Ganser HP, Pippan R. Analytical and numerical crack growth analysis of 1:3 scaled railway axle specimens. *Metals (Basel)*. 2019;9(2).
- [8] Madia M, Beretta S, Schödel M, Zerbst U, Luke M, Varfolomeev I. Stress intensity factor solutions for cracks in railway axles. *Eng Fract Mech [Internet]*. 2011 Mar [cited 2019 Nov 7];78(5):764–92. <http://dx.doi.org/10.1016/j.engfracmech.2010.03.019>
- [9] Milano P, Meccanica D. SIF SOLUTIONS FOR CRACKS IN RAILWAY AXLES UNDER ROTATING BENDING. :2–7.
- [10] Nwe T, Pimsarn M. Effect of interference on the press-fitting of railway wheel and axle assemblies. 2021; <https://iopscience.iop.org/article/10.1088/1757-899X/1137/1/012051>
- [11] Simulia DSC. Abaqus Analysis User's Manual [Internet]. Abaqus Documentation. 2016. 1137 p. [http://www.maths.cam.ac.uk/computing/software/abaqus\\_docs/docs/v6.12/pdf\\_books/BENCHMARKS.pdf](http://www.maths.cam.ac.uk/computing/software/abaqus_docs/docs/v6.12/pdf_books/BENCHMARKS.pdf)
- [12] Rice JR. A Path Independent Integral and the Approximate Analysis of Strain Concentration by Notches and Cracks. *J Appl Mech*. 1968;35:379–86.
- [13] Abaqus. Abaqus Theory Manual. Vol. IV. 2013.
- [14] Zerbst U, Mädler K, Hintze H. Fracture mechanics in railway applications - An overview. *Eng Fract Mech*. 2005;72(2):163–94.

AECXXX

(this number will be assigned after full manuscript is accepted)

## Multi-Objective Optimization of Lightweight Inboard Bearing Design for High-Speed Railway Axle

Theingi Nwe<sup>1</sup>, Akapot Tantrapiwat<sup>1</sup>, Monsak Pimsarn<sup>1,\*</sup>

<sup>1</sup>Department of Mechanical Engineering, School of Engineering, King Mongkut's Institute of Technology Ladkrabang, 10520, Thailand

\* Corresponding Author: [monsak.pi@kmitl.ac.th](mailto:monsak.pi@kmitl.ac.th)

**Abstract.** In this research article, the intricate balance between axle weight reduction and structural integrity within the realm of high-speed rail transportation is explored. The objective is to achieve a reduction in weight, a crucial factor in high-speed axle design, while simultaneously minimizing the occurrence of maximum stress to satisfy the infinite-life fatigue criterion. By utilizing comprehensive finite element simulations and standard calculations, the study systematically explores the distinct attributes of inboard and outboard bearing wheelsets, shedding light on their characteristics. An essential highlight of this study is the examination of inboard bearing axles, which reveals compelling advantages in terms of reducing mass, deflection, and mitigating stress. The weight of the inboard bearing axle is 8% lower than the outboard bearing axle. Leveraging multi-objective optimization techniques, the research demonstrates remarkable improvements in axle design, substantiated by the findings from Pareto front analysis, 3D contours graphs, and a correlation map of optimization outputs. Specifically quantified, the optimization process attains a commendable 4% reduction in mass and an associated 4% decrease in stress levels, making it possible to achieve a 12% reduction in mass compared to the traditional outboard bearing axle. The study also identifies enhancements in fatigue resistance, as evidenced through radial fatigue reverse factor (FRF) analysis, thereby underlining the study's comprehensive assessment of axle performance. The paper details the establishment of a finite element model using ABAQUS, Python script development, utilization of the Pointer algorithm in Isight for optimization, and Fe-safe for infinite fatigue life assessment. By adeptly navigating the trade-off between weight reduction and structural integrity, this study significantly contributes to the advancement of railway transportation systems.

**Keywords:** optimization, inboard bearing axle, outboard bearing axle, infinite fatigue life, lightweight design.

### 1. Introduction

Within the realm of rail transportation, the role of axles is crucial for ensuring both the safety and efficiency of train operations. The design of these axles necessitates a delicate equilibrium between durability and weight, as heavier axles can lead to elevated energy consumption, enhanced riding

comfort and stability performance and reduced operational efficiency. Wheelset configurations can be classified into two main types: inboard and outboard bearing wheelsets, as illustrated in Figure 1. The utilization of inboard bearings within bogies has undergone substantial growth in recent times. The elongated design of an outboard solution offers enhanced design adaptability due to the greater available space encircling the axle. Nevertheless, existing literature highlights that low track force bogies commonly adopt an inboard bearing arrangement, leading to lighter bogie assemblies with reduced structural demands [1]. These bearings present distinct advantages, including diminished total and unsprung mass, as well as lateral force and moments of inertia [2]. Such attributes not only enhance vehicle manoeuvrability along curves but also bolster track compatibility. Additionally, the adoption of inboard bearing axles proves beneficial in addressing specific maintenance challenges tied to conventional wheelsets.

Notably, a substantial proportion of a rail vehicle's overall mass (up to 41%) resides within the railway bogie [3], with the axle accounting for approximately 35% of a standard wheelset's total mass. This scenario underscores considerable potential for weight reduction. However, this endeavour is intricate due to the axle is constantly subjected to both combined loads and the stresses caused by cyclic bending fatigue throughout its operational life. The principal challenge involves achieving weight reduction while upholding durability especially for the high-speed train. To address this challenge, the application of multi-objective optimization techniques has emerged as a valuable approach, facilitating the development of lightweight yet resilient axle designs that align with the criteria of enduring fatigue performance. Previous research has concentrated mostly on individual aspects of axle design, such as structural or material strength, vibration resistance, and fatigue performance, and has lacked a complete strategy that considers both weight reduction and durability as complementary objectives [1,4–6]. This study aims to illuminate the intricate balance between axle weight reduction, structural integrity and satisfy the infinite-life fatigue criterion, thus contributing to the development of high-speed railway transportation systems.



Figure 1. Trailer bogie wheelset with (a) inboard bearing axle and (b) outboard bearing axle.

## 2. Multi-Objective Optimization Methodologies

This study involves an investigation of a railway inboard and outboard bearing axle, employing the commercially available software Abaqus/CAE integrated into an Isight simulation workflow to attain an optimized design focusing on both durability and weight performance aspects. The schematic representation of the specific optimization workflow procedure is depicted in Figure 2. Initially, a Python script is used to generate a finite element model, which is subsequently executed in Abaqus/CAE as a pre- and post-processor. A parametric design optimization targeting the inboard bearing wheelset model is carried out using the Isight commercial optimization tool. Isight's integration of the Sim Code module facilitates the organization of input, output, and execution processes within the program [7]. This module operates by accepting a Python script as input, capturing all relevant parameters, and then modifying the code to extract data from the generated file and output it in TXT format. Moreover, an Abaqus module accepts the output file from Sim Code as input, subsequently generating an output database file. Lastly, the fatigue life assessment of the inboard axle is conducted using the commercial

Fe-Safe software. This is executed post the extraction of load history data from the optimized finite element model and subsequent comparison with the existing model.



Figure 2. Structural analysis and optimization process workflows chart

### 2.1. Finite element model

Using Python script, the FE model is implemented in Abaqus/CAE to parameterize the geometric dimensions and automatically apply the contact and boundary conditions as the geometry is modified during the optimization procedure. The wheelset model in this work has two versions: one is an inboard bearing axle model and the other is an outboard bearing axle model. As illustrated in Figure 3, C3D8R hexahedral solid element type is chosen to ensure convergence and minimize computational cost by carefully meshing the contact of the wheelset. The EA4T steel, which is commonly used in modern railroad axles, is a linear elastic body with a Young's modulus of  $E=206$  GPa and a Poisson's ratio of 0.3.

Master-slave contact type with the user-defined specific radial interference fit technique [8] was used to represent the press fittings. In the context of highly nonlinear contact analyses, the interference is assumed to be 0.2 millimeters [9] and a friction coefficient of 0.1 is chosen as a consistent parameter to strike a balance between efficiency and accuracy. Using this procedure, solely normal contact is established. The behavior in the tangential direction adheres to the conventional Coulomb approach, wherein the maximum permissible shear stresses are associated with the contact pressure arising from the press fit between the contacting parts on the contact surfaces[8].

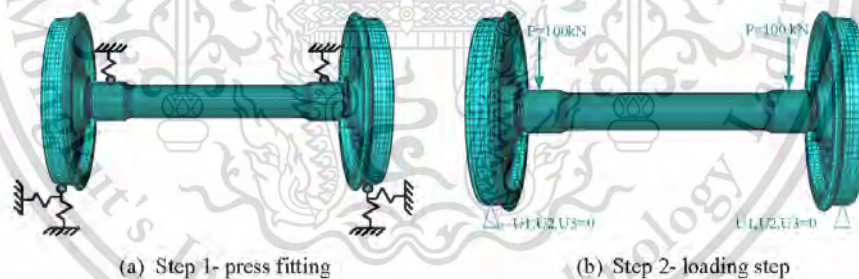


Figure 3. Mesh, loading and boundary conditions of FE model.

A strategic numerical approach was employed to address the issue, involving a two-step analysis: the first stage encompassing the press fitting, second step followed by loading. To stabilize the wheelset model, spring elements were implemented Figure 3 (a). Specifically, the axle is confined by two springs exerting forces in directions 1 and 3, while the wheels encounter constraint through springs in three directions. The stiffness of these spring elements was assigned as 1 N/mm, a value devoid of physical meaning. After constructing the residual stress field within the axle owing to press-fitting, necessitating the deactivation of all spring elements. The loading  $P$  owing to the bogie and train was


applied to the journal bearings' middle plane Figure 3 (b). Lateral forces and braking forces were neglected in the current case because the vertical axle load is the most critical factor.

## 2.2. Parametric design optimization algorithm

In the context of optimizing the design of an inboard bearing for railway axle, the primary objective is to minimize the maximum mises stress while simultaneously minimizing the mass. This inherently gives rise to a multi-objective problem, where the ideal design should achieve a balance between minimizing mass and stress while satisfying the infinite life fatigue criterion. To address these challenges, the present research defines the mises stress parameter as an upper limit, set at half of the yield stress, to ensure a safety factor greater than 2. The maximum permissible stresses for hollow axles at transition fillets of EA4T steel is 145 MPa. This constraint formulation captures the safety and functionality aspects of the design while considering stress-induced failure modes. The objective, constraint and design variable are as shown in Table 1.

For the optimization process, the Pointer Automatic Optimizer is selected due to its ability to effectively handle diverse optimization scenarios. It integrates various algorithms, including an evolutionary algorithm, Nelder and Mead simplex downhill method, sequential quadratic programming (NPQL), a linear solver, and the TABU method [10]. This selection allows the optimizer to adapt to different optimization landscapes. It provides the flexibility to employ a single algorithm or all four simultaneously. Throughout the optimization process, the optimizer continually assesses the performance of each algorithm and dynamically adjusts internal parameters such as step sizes and iterations to achieve optimal results. This capability ensures that the optimization process is efficient and effective in discovering high-quality designs.

**Table 1.** Objective, constraint, and design variable at initial design (all dimensions in mm)

	<p>Optimization – Min {mass, <math>S_{mises\_max}</math>}</p> <p>Constraint – Max {<math>S_{Mises\_max} &lt; 72.5</math> MPa (max. permissible stress /2)}</p> <p><u>Starting Design Points</u></p> <p>F1 = 75.0 [60.0 &lt; x &lt; 90.0]</p> <p>F2 = 15.0 [12.0 &lt; x &lt; 18.0]</p> <p>Ri = 30.0 [24.0 &lt; x &lt; 36.0]</p> <p>Ro = 85.0 [ 68.0 &lt; x &lt; 102.0]</p>
---	---

## 3. Infinite Fatigue Life Analysis

Railway axles experiencing multiaxial cyclic loading at high rotational speeds tend to reach their high cycle fatigue limit quickly during operation. Traditional fatigue analysis, which establishes a minimum number of cycles to failure, is inadequate for such scenarios. The focus is on determining the possibility of fatigue damage occurring during the component's entire loading history. The absence of damage indicates infinite life potential for the axle.

To address this, the Dang Van is an endurance criterion and employed for high cycle fatigue analysis subject to complex multiaxial stresses. In most cases, fatigue crack initiation takes place at stress concentration zones like fillets and notches. The Dang Van criterion has demonstrated considerable efficacy in assessing infinite fatigue life[11]. This methodology incorporates a multi-scale perspective, establishing a connection between the macroscopic stress derived from finite element analysis (FEA) and the microscopic stress within grain boundaries. Instead of directly calculating fatigue life, a novel approach involves the determination of the fatigue safety factor, denoted as the Fatigue Reverse Factor (FRF), utilizing a simplified pass/fail algorithm. Achieving an infinite life design necessitates ensuring that the FRF surpasses a value of 1 for all elements. To perform a Dang Van analysis, endurance limit stresses and corresponding R values need to be defined (Figure 4), the endurance stress is 375 MPa for constant amplitude testing at R=0 and the endurance stress is 290 MPa for R=-1 [12].

The Dang Van Criterion can be expressed as

$$\tau = \alpha S = \tau_0 \quad (1)$$

Where

$\tau$  = local shear stress

$S$  = hydrostatic stress

$\alpha, \tau_0$  are material-specific constants at a specific endurance.

The microscopic stress can be expressed as

$$\sigma_{ij}(P,t) = \sum_{ij} \sigma_{ij}(P,t) + S_{ij}(P,t) \quad (2)$$

$\sigma_{ij}$  = microscopic stress tensor

$\sum_{ij}$  = macroscopic stress tensor

$S_{ij}$  = residual stress tensor

$P,t$  are position and time co-ordinates.

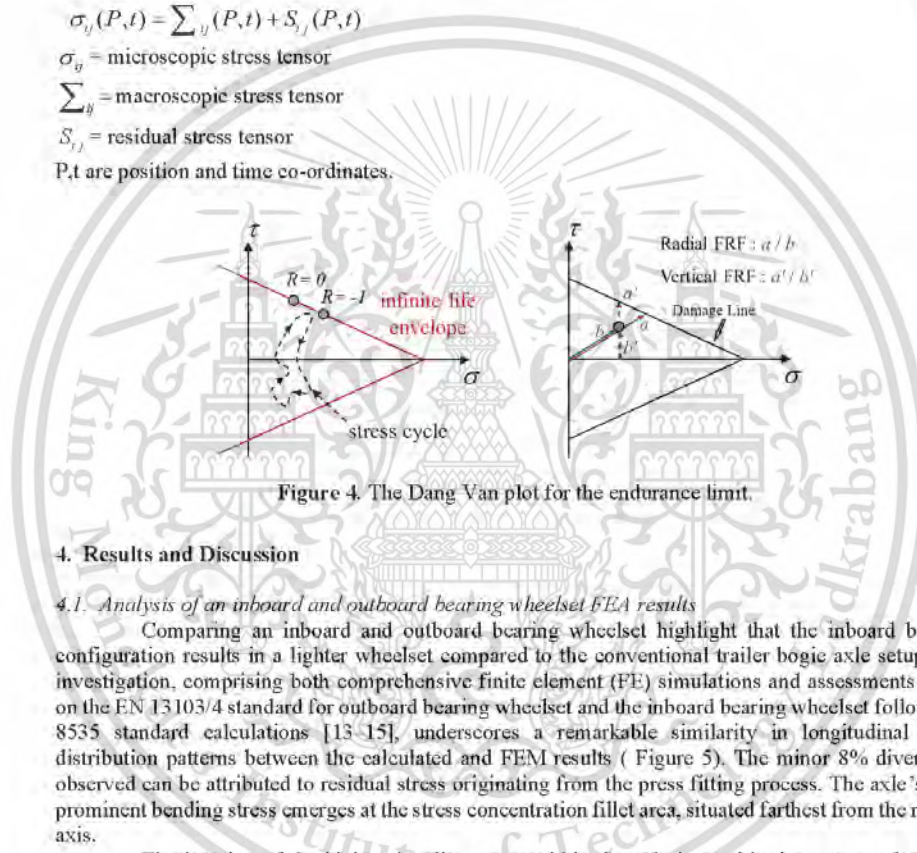


Figure 4. The Dang Van plot for the endurance limit.

#### 4. Results and Discussion

##### 4.1. Analysis of an inboard and outboard bearing wheelset FEA results

Comparing an inboard and outboard bearing wheelset highlight that the inboard bearing configuration results in a lighter wheelset compared to the conventional trailer bogie axle setup. The investigation, comprising both comprehensive finite element (FE) simulations and assessments based on the EN 13103/4 standard for outboard bearing wheelset and the inboard bearing wheelset follows BS 8535 standard calculations [13–15], underscores a remarkable similarity in longitudinal stress distribution patterns between the calculated and FEM results ( Figure 5). The minor 8% divergence observed can be attributed to residual stress originating from the press fitting process. The axle's most prominent bending stress emerges at the stress concentration fillet area, situated farthest from the natural axis.

The location of the highest bending stress within the axle is notable; it occurs at the stress concentration fillet area, farthest from the natural axis as shown in Figure 5. The utilization of inboard bearings in a wheelset is advantageous from the perspective of axle stress. This is attributed to the mitigation of lateral forces, resulting in a reduction of the bending moment experienced by the axle. Under similar loading conditions, the maximum bending stress encountered by the inboard bearing is notably 38% lower than that experienced by the outboard bearing. An interesting contrast between the two bearing types is observed in their deflection behavior as shown in Figure 6. The inboard bearing experiences a negative deflection 0.59 mm, while the outboard bearing demonstrates a positive deflection 0.70 mm. This phenomenon can be explained by differences in the load distribution and

structural arrangement of the two bearing configurations. The weight of the inboard bearing axle is 8% lower than outboard bearing axle. This distinction can be reasoned by taking into account the varying structural layouts and load dispersion characteristics inherent to the two distinct bearing types.

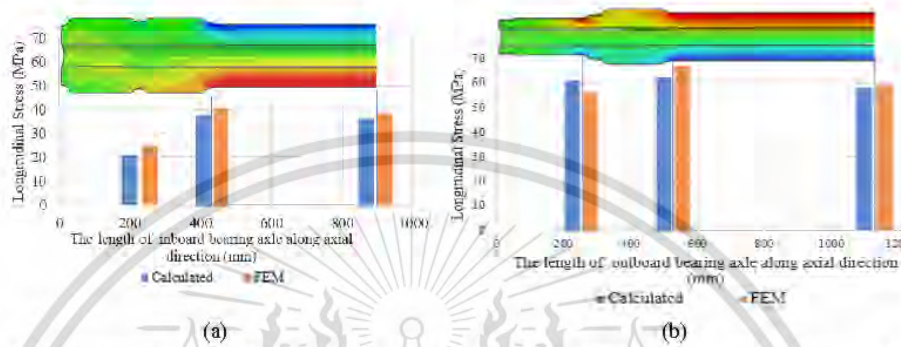


Figure 5. Comparison of longitudinal stresses of calculated and FEM (a) inboard bearing axle and (b) outboard bearing axle.

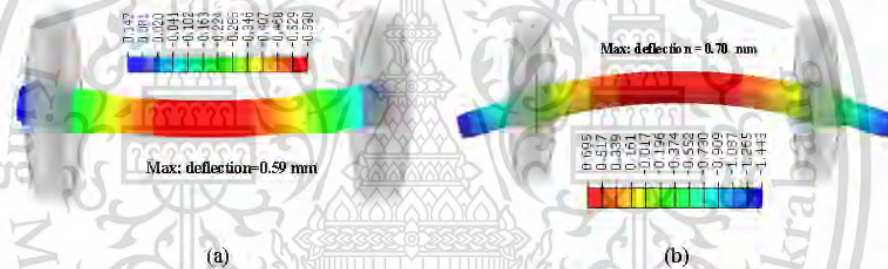


Figure 6. Comparison the deflection of the axle under the loading (a) for the assembled inside axle boxes (b) for the assembled outside axle boxes.

4.2. Identification of optimal design

Figure 7 shows the Pareto Front of Pareto-Optimal designs generated by plotting the mass objective vs. the  $S_{mises\_max}$  objective. The green dot corresponds to the optimal solution composing the Pareto front, blue dots are the possible optimum points while the black plots are the dominated solutions. From Figure 7, it can be seen that the mass of the wheelset is almost linear and the coefficient of determination  $R^2$  for this linear relationship is calculated to be 0.9115, indicating a strong correlation between the two objectives.

Figure 8 illustrates a 3D contour graph that depicts the relationship between design feasibility,  $S_{mises\_stress}$ , and mass of the wheelset. The contours on the graph serve as insightful indicators of the interaction between these three factors. Points closer to the peak of the contour correspond to regions of higher design feasibility as the contour lines shift towards lower values of design feasibility. Correlation map (Figure 9) shows the impact of model parameters on target objectives and solid lines represent stronger correlations than dash lines. It can be used to calculate the rank and linear correlation values for every pair of parameters in a model. The inner radius parameter ( $R_i$ ) and  $S_{mises\_max}$  have the strongest inverse linear correction (Rank = -0.978 and Linear coefficient = -0.998) among other parameters.

Figure 10 illustrates the design variable optimization process history for F1, F2, Ri, and Ro. Graphs show the change of such parameters during the analysis run by run and provide an insight into the convergence of the results. Table 2 presents a comparison between initial and optimum design points, indicating reductions in mass of axle 4% (0.315 to 0.302 tons) and stress 4% (40.39 to 38.82 MPa) achieved through optimization.

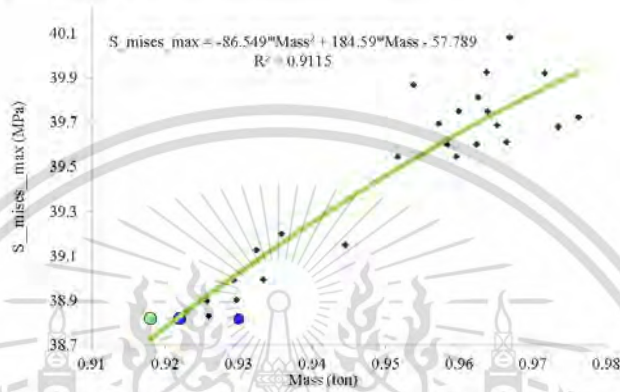


Figure 7. Pareto plot of S\_mises\_max vs. mass from optimization.

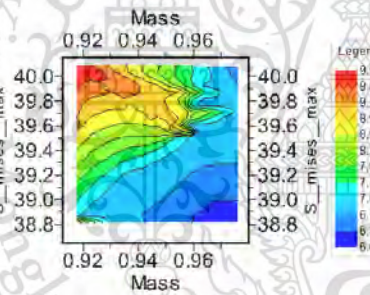


Figure 8. 3D contour graph of design feasibility vs. mass, S\_mises\_max.

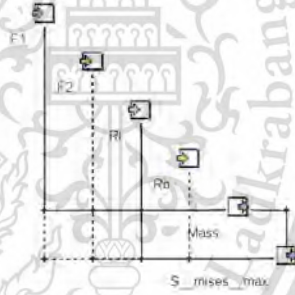


Figure 9. Correlation map of input and output parameters.

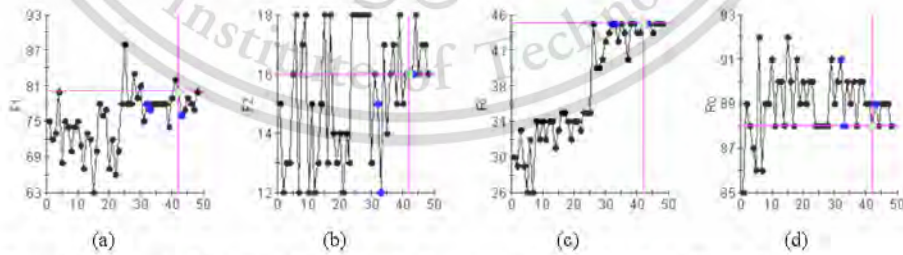


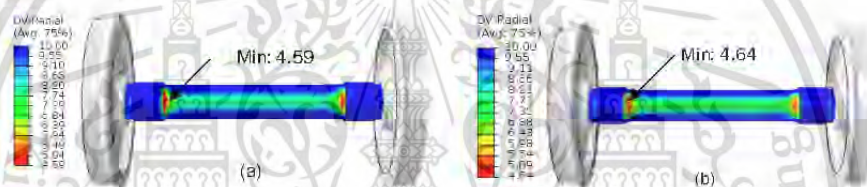
Figure 10. History of design variable optimization process (a) F1, (b) F2, (c) Ri, (d) Ro.

**Table 2.** Comparison of the starting design points and optimum design points of inboard bearing axle.

	F1(mm)	F2(mm)	Ri(mm)	Ro(mm)	Mass(ton)	S mises max(MPa)
Starting design points	75	15	30	85	0.315	40.39
Optimal design points	80	16	45	88	0.302	38.82

#### 4.3. Assessment of infinite life

Figure 11 presents the results of the radial fatigue reverse factor (FRF) contour analysis before and after an optimization process. The analysis is focused on the inboard bearing axles, particularly their shoulder fillets, with the goal of enhancing their fatigue performance. The key observation is that both of the design points are satisfy the infinite fatigue life condition and the minimum DV Radial FRF value, which was initially 4.59, has increased to 4.64 after the optimization process. This improvement in the FRF indicates that the axles' fatigue resistance under radial loading conditions has been enhanced due to the optimization method applied.

**Figure 11.** Radial FRF contour of (a) before optimization and (b) after optimization.

## 5. Conclusion

This study highlights the intricate interactions between reducing axle weight at high speeds and maintaining structural integrity in rail transportation. Lightweight high-speed train axles are required to reduce aerodynamic forces, enhance performance, and ensure track compatibility and durability. Through comprehensive finite element simulations and assessments based on EN 13103/4 and BS 8535 standard calculations, the study illuminates the distinct characteristics of inboard and outboard bearing wheelsets. Comparative analysis reveals a noteworthy 8% reduction in weight for inboard bearing axles compared to their outboard counterparts, along with a significant 38% decrease in bending stress and 14% decrease in deflection. Evidently, the design of inboard bearing axles emerges as more favourable considering these findings. The subsequent pursuit of multi-objective optimization techniques leads to significant improvements in inboard bearing axle design, as evident in the Pareto front analysis, 3D contour graphs, correlation map and design variable optimization history. Particularly remarkable is the achievement of a 4% mass reduction and a corresponding 4% decrease in stress levels through the optimization process. The research also highlights enhancements in fatigue resistance via radial FRF analysis. By navigating the balance between weight reduction and structural robustness, this study contributes valuable insights to the development of railway transportation systems.

### Acknowledgments

We would like to thank King Mongkut's Institute of Technology Ladkrabang for the financial support under the grant No. KDS2019/019.

## References

1. Bracciali A, Megna G. Inside Frame Bogies & Air Wheelset : a Winning Marriage. 2016;12–5.
2. Bracciali A. Railway Wheelsets: History, Research and Developments. *Int J Railw Technol*. 2016;5(1):23–52.
3. Carruthers JJ, Calomfirescu M, Ghys P, Prockat J. The application of a systematic approach to material selection for the lightweighting of metro vehicles. *Proc Inst Mech Eng Part F J Rail Rapid Transit*. 2009;223(5):427–37.
4. Johnson MS, Evans R, Mistry PJ, Li S, Bruni S, Bernasconi A, et al. Structural analysis for the design of a lightweight composite railway axle. *Compos Struct*. 2022;290(November 2021).
5. Mistry PJ, Johnson MS, Li S, Bruni S, Bernasconi A. Parametric sizing study for the design of a lightweight composite railway axle. *Compos Struct* [Internet]. 2021;267(January):113851. <https://doi.org/10.1016/j.compstruct.2021.113851>
6. Wu SC, Liu YX, Li CH, Kang GZ, Liang SL. On the fatigue performance and residual life of intercity railway axles with inside axle boxes. *Eng Fract Mech* [Internet]. 2018;197(December 2017):176–91. <https://doi.org/10.1016/j.engfracmech.2018.04.046>
7. Carolina N, Engine E. *Isight 4.0 Getting Started Guide*. 2009. pg. 1-179.
8. Abaqus. *Abaqus Theory Manual*. Vol. IV. 2013.
9. European Committee For Standardization. BS EN 13260 : 2020 Railway applications - Wheelsets and bogies - Wheelsets - Product Requirements. London,United Kingdom: BSI; 2020.
10. Simulia 3ds. *Isight documentation* [Internet]. 2019. <http://www.3ds.com/fileadmin/PRODUCTS/SIMULIA/PDF/whitepapers/SIMULIA-Isight-Design-Optimization-Methodologies.pdf>
11. Simulia. *FATIGUE THEORY REFERENCE*. Dassault Systemes Simulia Corp.; 2018.
12. Simulia. *fe - safe USER GUIDE*. 2020.
13. European Committee For Standardization. BS EN 13104:2009+A2:2012: Railway applications — Wheelsets and bogies — Powered axles — Design method. BSI Standards; 2012.
14. European Committee For Standardization. BS EN 13103-1:2017:Railway applications - Wheelsets and bogies - Part 1: Design method for axles with external journals. 2011.
15. British Standards BSI 8535:2011, Railway applications – Wheelsets and bogies – Powered and non-powered axles with inboard bearings – Design method.

## AUTHOR'S BIOGRAPHY

- Author's Name: Ms. Theingi Nwe
- Date of Birth: 13<sup>th</sup> July 1988
- Address: 300/91 Chalong Krung Soi 2, Khwaeng Lam Prathew, Khet Lat Krabang, Krung Thep Maha Nakhon 10520.
- Educational History: 2009: Bachelor of Mechanical Engineering, Technological University (Myitkyina), Kachin State, Myanmar.  
2018: Master of Mechanical Engineering, Yangon Technological University, Yangon, Myanmar.
- Scholarship: 2009-2022: KMITL Doctoral Scholarship,  
She got a scholarship to study Doctor of Engineering in Mechanical Engineering at School of Engineering, King Mongkut's Institute of Technology Ladkrabang from August, 2019 till May 2022 which supported the monthly stipend, tuition fees and research cost during the scholarship period.
- Work Experience 2010 – present, a full-time lecturer in the department of mechanical engineering, Technological University (Myitkyina) Myitkyina, Kachin State, Myanmar.
- Publications: [1] Nwe, T., Pimsarn, M. (2021). Effect of interference on the press fitting of railway wheel and axle assemblies. IOP Conference Series: Materials Science and Engineering. 1137. 012051. <https://doi.org/10.1088/1757-899X/1137/1/012051>  
[2] Nwe, T., Pimsarn, M. (2021). Railway axle and wheel assembly press-fitting force characteristics and holding torque capacity. Applied Sciences, 11(19): 8862. <https://doi.org/10.3390/app11198862>  
[3] Nwe T, Pimsarn M. Multiaxial Fatigue-Life Prediction of Railway Axles with Consideration of Braking Effects. Math Model

This material is reserved for educational use only, not allowed for commercial use.

Forbidden to modify the content, and cite the document when use.

Eng Probl. 2023;10(3): 897–905.

<https://doi.org/10.18280/mmep.100320>

[4] Nwe T, Pimsarn M. Deterministic Stress Intensity Factor of a Railway Axle under Adverse Running Condition. MSF 2023;1109:165–71. <https://doi.org/10.4028/p-k75d6r>

[5] Nwe, T., Pimsarn, M. (2022). Numerical Analysis of the Influence of Press-Fitting on the Fatigue Life of Railway Axle. In AIP Conference Proceeding on [The12th International Conference on Mechanical Engineering (TSME-ICOME 2022)], 2022, Phuket, Thailand. (Accepted for Publication)

[6] Nwe, T., Pimsarn, M., Tantrapiwat, A. (2024). Multi-Objective Optimization of Lightweight Inboard Bearing Design for High-Speed Railway Axle. Journal of Research and Applications in Mechanical Engineering, X(X), JRAME-24. (Accepted for Publication).

[7] Nwe, T., Pimsarn, M. Assessing the Impact of Braking and Axle Hot Box Bearing Temperature on the Stress Intensity Factor and Residual Lifetime of Railway Axles. (Under Review)

